Karlsruhe Institute of Technology

Pascal Kiefer

On Next-Generation Multi-Focus 3D Laser Printing

2023
Dissertation



This document is licensed under a Creative Commons Attribution 4.0 International License
(CC BY 4.0): https://creativecommons.org/licenses/by/4.0/deed.en

On Next-Generation Multi-Focus 3D Laser Printing

Zur Erlangung des akademischen Grades eines
DOKTORS DER NATURWISSENSCHAFTEN (Dr. rer. nat.)
von der KIT-Fakultät für Physik des
Karlsruher Instituts für Technologie (KIT)

genehmigte

DISSERTATION

von

M. Sc. Pascal Kiefer
geboren in Karlsruhe

Tag der mündlichen Prüfung: 8. Dezember 2023
Referent: Prof. Dr. Martin Wegener
Korreferent: Prof. Dr. Martin Bastmeyer

Contents

Publications . . . 1

1 Introduction . . . 3

2 Fundamentals of 3D Laser Printing . . . 9
- 2.1 Photopolymerization 3D Printing . . . 10
- 2.2 The Two-Photon Exposure Dose . . . 12
- 2.3 Power Scaling . . . 23
- 2.4 3D Printing Speed Overview . . . 28

3 Methods . . . 31
- 3.1 Sensitive Photoresist Development . . . 32
- 3.2 Optimization of Micro-Optical Components . . . 35
- 3.3 Multi-Focus 3D Laser Printing of Large-Scale Microstructures . . . 39

4 Development of Highly Sensitive Photoresists . . . 43
- 4.1 A Figure-of-Merit for the Photoresist Sensitivity . . . 44
- 4.2 Enhancing DETC-Containing Photoresists . . . 51
- 4.3 Development of a New Photoinitiator With Record-High Photoresist Sensitivity . . . 56
- 4.4 Discussion and Conclusion . . . 61

5 Fabrication of Micro-Optical Components for Beam Splitting 63
- 5.1 Beam-Splitting Approaches for Multi-Focus 3D Laser Printing . . . 64
- 5.2 Component Design for Hybrid Diffractive-Refractive Beam Splitting 69
- 5.3 Maximizing Optical Quality by Iterative Pre-compensation . . . 77
- 5.4 Discussion and Conclusion . . . 95

6 A Next-Generation Multi-Focus 3D Laser Printer . . . 99
- 6.1 An Optical Setup for High-Speed Multi-Focus 3D Laser Printing . 100
- 6.2 Low-Aberration Scan Optics . . . 104
- 6.3 Voxel Size Characterization . . . 110
- 6.4 Summary and Discussion . . . 113

7 Multi-Focus Manufacturing of Large-Scale Microstructures 115
7.1 Millions of Carrier Particles for Respiratory Drug Delivery . . . 116
7.2 Centimeter-Scale Metamaterial Samples 124
7.3 Large-Scale Structures for Potential Scintillator Applications in Particle Physics 130
7.4 Discussion 134

8 Conclusions and Outlook 137

A Appendix 145
A.1 Further Data on Sensitive Photoresists 145
A.2 Lens Data for the Next-Generation Setup 149

Bibliography 153

Acknowledgments 173

Publications

Parts of this thesis have already been published ...
... in scientific journals:

- V. Hahn, **P. Kiefer**, T. Frenzel, J. Qu, E. Blasco, C. Barner-Kowollik, and M. Wegener, "Rapid Assembly of Small Materials Building Blocks (Voxels) into Large Functional 3D Metamaterials", *Adv. Funct. Mater.* **30**, 1907795 (2020).
- **P. Kiefer**, V. Hahn, M. Nardi, L. Yang, E. Blasco, C. Barner-Kowollik, and M. Wegener, "Sensitive Photoresists for Rapid Multiphoton 3D Laser Micro- and Nanoprinting", *Adv. Opt. Mater.* **8**, 2000895 (2020).
- T. Frenzel, V. Hahn, P. Ziemke, J. L. G. Schneider, Y. Chen, **P. Kiefer**, P. Gumbsch, and M. Wegener, "Large characteristic lengths in 3D chiral elastic metamaterials", *Comms. Mater.* **2**, 4 (2021).
- **P. Kiefer**, V. Hahn, S. Kalt, Q. Sun, Y. Eggeler, and M. Wegener, "A multi-photon (7×7)-focus 3D laser printer based on a 3D-printed diffractive optical element and a 3D-printed multi-lens array", *Light Adv. Man.*, accepted.
- J. Weinacker[1], S. Kalt[1], **P. Kiefer**[1], P. Rietz[1], and M. Wegener, "On Iterative Pre-Compensation of 3D Laser-Printed Micro-Optical Components Using Confocal-Optical Microscopy", *Adv. Funct. Mater.*, 2309356 (2023).
- P. Serles, J. Yeo, M. Haché, P. G. Demingos, J. Kong, **P. Kiefer**, J. Surjadi, B. Kumral, K. Jia, T. Feng, C. Jia, C. Portela, M. Wegener, P. Ajayan, J. Howe, C. V. Singh, Y. Zou, S. Ryu, and T. Filleter, "Multi-Objective Bayesian Optimized Carbon Nanolattices", in preparation.

... at scientific conferences (only own presentations):

- **P. Kiefer**, V. Hahn, M. Nardi, L. Yang, E. Blasco, C. Barner-Kowollik, and M. Wegener, "Sensitive multi-photon photoresists: Overview and recent advances" (invited talk), SPIE Photonics West (online conference), March 2021.

[1] These authors have contributed equally.

- **P. Kiefer**, V. Hahn, and M. Wegener, "A 7×7-foci 3D laser nanoprinter using a diffractive optical element and an aspheric-lens array made by 3D laser nanoprinting" (invited talk), SPIE Photonics West, United States of America, San Fransisco, January 2023.

ADDITIONAL RELATED WORK HAS ALREADY BEEN PUBLISHED ...
... in scientific journals:

- R. Zvagelsky, **P. Kiefer**, J. Weinacker, and M. Wegener, "In-situ Quantitative Phase Imaging during Multi-photon Laser Printing", *ACS Photonics* **10**, 2901-2908 (2023).

- A. Mauri, **P. Kiefer**, P. Neidinger, T. Messer, N. M. Bojanowski, L. Yang, S. Walden, A.-N. Unterreiner, C. Barner-Kowollik, M. Wegener, W. Wenzel, and M. Kozlowska, "Two- and three-photon processes in photoinitiators for 3D laser printing", under review at *Nat. Commun.*

Chapter 1

1 Introduction

In 1965, Gordon E. Moore, Fairchild Semiconductor's director of research and development, was *"given the chore of predicting what would happen in silicon components in the next 10 years for the 35th anniversary edition of Electronic Magazine"* [1]. This occurred just eight years after he left the Shockley Semiconductor Laboratory under the leadership of Nobel Prize winner Wilhelm Shockley and co-founded Fairchild Semiconductor together with seven other previous co-workers[1]. Two years after the foundation, the first monolithic integrated circuit was realized by co-founder Robert Noyce. In his article for Electronic Magazine addressing this topic[2], Moore *"blindly extrapolated"* [1] the progress in the early days of the integrated circuit for the upcoming ten years and wrote: *"The complexity for minimum component costs has increased at a rate of roughly a factor of two per year [...]. That means by 1975, the number of components per integrated circuit for minimum cost will be 65,000."* [2]. Moore's prediction proved right within a percent when a new memory chip series released in 1975 counted 65,536 transistors. In the same year, the forecast was revised to doubling biannually instead of annually and eventually was dubbed "Moore's Law" by Moore's friend and professor at Cal Tech, Dr. Carver Mead [1].

Decades later, the continuous trend of increasingly more complex microchips seemed doomed to reach the end of the line several times. However, for each barrier preventing a new technology leap, *"creative engineers [came] up with ways around them"* [1]. Innovations overcoming predicted boundaries for future growth include, for example, the invention of the complementary metal-oxide-semiconductor (CMOS) by Chih-Tang Sah and Frank Wanlass at Fairchild Semiconductor in 1963 [3, 4], the development of dynamic random-access memory (DRAM) by Robert H. Dennard at IBM in 1967 [5], the invention of a chemically-amplified photoresist with a $5-10\times$ higher sensitivity to ultraviolet light by Carlton Grant Willson and Jean M. J. Fréchet at IBM in 1980 [6–8], and the invention of Deep UV excimer laser photolithography by Kanti Jain at IBM in 1980 [9–11].

[1] They were later called the "traitorous eight" due to Shockley calling their leaving a betrayal.
[2] Intel, founded by Moore and Noyce in 1968, announced a $10,000 reward in 2005 for the original article in good condition.

In an effort to emulate Moore's law, many other industries and fields of research have tried to formulate their own regularities. For example, Swanson's Law says that for each doubling of solar panel cumulative volume, the price of the respective photovoltaic modules drops by 20 % [12]; Kryder's law projects that the storage density of magnetic hard drive discs annually increases by 40 % [13, 14], and Nielsen's law states that the internet connection speed of high-end users grows by 50 % per year [15]. In the field of additive manufacturing, similar principles can be found. For example, the technological improvement rate for industrial stereolithography, i.e., a combination of speed, accuracy, and system cost, is empirically found to be 38 % per year [16].

Like electronics, especially in the early decades, additive manufacturing has become a megatrend, enabling breakthrough innovations by offering a production-oriented technology [17]. With an increasing demand for customized specifications in a world of rapidly changing needs, new manufacturing approaches are the key enablers for customized components [17]. Furthermore, they enable the fabrication of components that simply could not be manufactured before [17].

One specific approach of additive manufacturing, 3D laser printing, developed particularly rapidly and allows for 3D printing of components with micro- and nanometer resolution [18]. Using this technique, a typically femtosecond-pulsed laser is focused into a liquid photoresist to solidify the material into a polymer. This allows for smallest printable 3D volume elements, so-called voxels, in the sub-micrometer range. By scanning this laser focus along a certain trajectory, the desired structure can be fabricated. In the early days of 3D laser printing in 1999, the laser focus was typically scanned with a focus velocity of $10\,\mu m\,s^{-1}$ [19]. Translating this into a rate of how many voxels can be printed per second, one ends up with roughly $50\,voxels\,s^{-1}$. Naturally, with such a small throughput, the fabrication of, e.g., popular photonic crystal structures required quite some time and ultimately limited the maximum sample size that could be produced with high resolution in a reasonable time span. In the following years, the demand of increasingly larger and more complex structures pushed the development of 3D laser printing to yield increasingly higher total peak printing rates while keeping sub-micrometer resolution.

Consequently, the available peak printing rate grew over time in a similar fashion to the number of components per integrated circuit in Moore's law. Figure 1.1 illustrates the available total peak printing rates of 3D laser printing technologies from early years until the beginning of my thesis in 2020 in a logarithmic plot. Following all data points contributing to a technology leap, i.e. increasing the available total peak printing rate, a clear trend can be observed. The printing rate

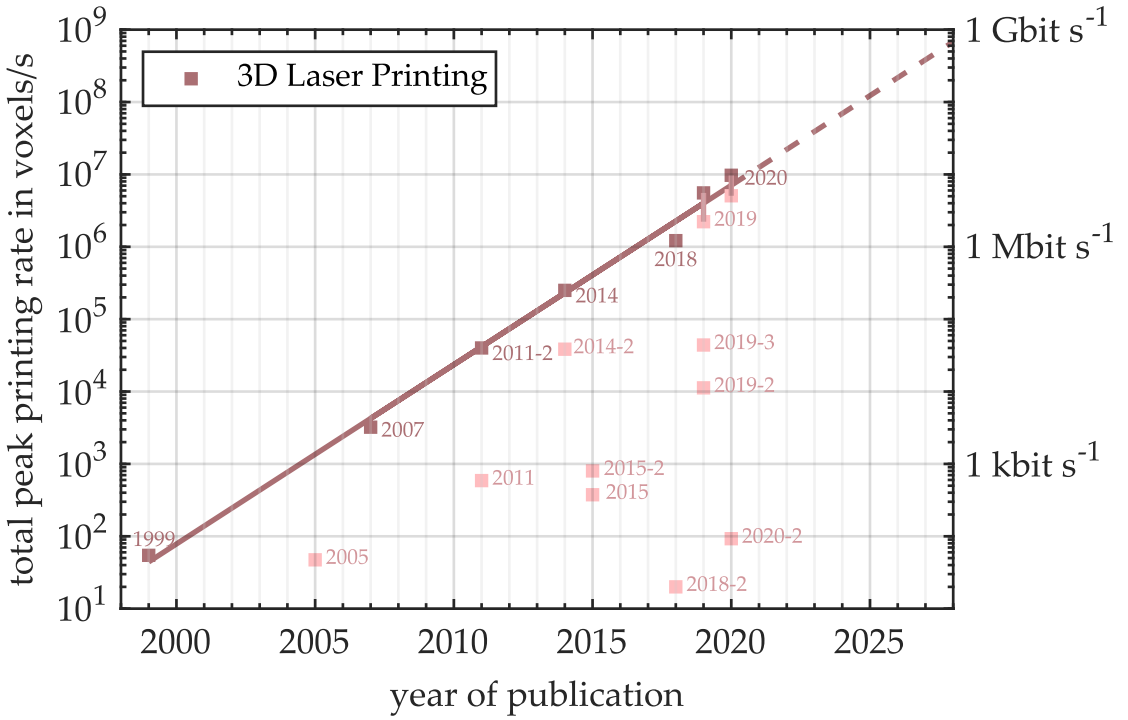

Figure 1.1: Printing speed evolution of 3D laser printing. The data is sorted by peak printing rate and publication year. Data points in dark red mark technology leaps that increased the total peak printing rate of the field. Data points in light red mark publications that used 3D laser printers which did not employ the highest possible printing rate at the time but were added for the sake of completeness. Therefore, only data points in dark red were considered for the linear fit. The printing rate has increased annually by a factor of 1.77, reaching an increase by a total factor of 1.6×10^5 between 1999 and 2020.
References: 1999 [19], 2005 [20], 2007 [21], 2011 [22], 2011-2 [23], 2014 [24], 2014-2 [25], 2015 [26], 2015-2 [27], 2018 [28], 2018-2 [29], 2019 [30], 2019-2 [31], 2019-3 [32], 2020 [33], and 2020-2 [34].

increased by approximately 77 % per year or doubled roughly every 15 months. Clearly, like the history of Moore's law, the increase in available total peak printing rate faced several challenges along the way, potentially stopping the throughput from advancing further. For example, a laser focus cannot be scanned arbitrarily quickly, possibly limiting the available printing rate. However, similar to the advancements that managed to overcome thresholds in electronics production, new approaches in 3D laser printing further enhanced throughput by, e.g., parallelizing the manufacturing process. One recent result connected to the highest total peak printing rate in Figure 1.1 is multi-focus 3D laser printing which used $3 \times 3 = 9$ laser foci at high focus velocities to allow for the manufacturing of sub-micrometer resolved samples with previously inaccessible dimensions [33].

Based on this data, the available total peak printing rate should reach a rate of 10^8 voxels s^{-1}, i.e., 100 million voxels per second, before 2025. However, the new technology was anticipated to approach a limit. In multi-focus 3D laser printing, the laser power required for the multiple foci to solidify the liquid photoresist was approaching the damaging threshold of the focusing lens required for printing. Thus, increasing the number of foci further would divide the total laser power into more and therefore weaker individual foci. Simply increasing the total laser power to counteract this reduction of laser power per focus was not feasible because the system would potentially damage its components. Therefore, blindly extrapolating the trend, as indicated by the dashed line in Figure 1.1, seemed like a dangerous prediction. Yet, in the scope of this thesis, the limitations of multi-focus 3D laser printing were tackled to allow for even higher total peak printing rates while staying in a limited power budget. In the effort of driving the trend of the 3D laser printing equivalent of Moore's law in Figure 1.1, the peak printing rate was increased to a new order of magnitude.

Outline of this thesis

In chapter 2, I describe the necessary fundamentals for 3D laser printing to understand the many limitations of further advancing the printing rate. By focusing on the two-photon exposure dose, I isolate two aspects with heavy influence on the technology's power scaling: (1) photoresist sensitivity and (2) the approach of parallelization. I end the chapter with an overview of the current state of print rates for all 3D printing technologies. Before diving further into these topics, I document the experimental methods used throughout this thesis in chapter 3. This includes the various photoresist formulations I have studied, details on the fabrication and optimization of micro-optical components for beam splitting, and specifics of the structures printed with the newly developed multi-focus 3D laser printing setup, including their lift-off from the substrate.

The following two chapters address the two fundamental limitations of multi-focus 3D laser printing that thus far prevented higher printing rates. In chapter 4, I give an overview of over 80 different photoresists in literature and introduce a metric to allow for the fair comparison of their sensitivity. Next, I present different experiments to enhance the sensitivity of promising photoresist systems and present the development of a new photoinitiator yielding record-high photoresist sensitivities at high focus velocities[3]. This reduced the necessary laser power for printing and

[3]Photoresist sensitivity was a challenge for Moore's law, too. Charlton Grant Willson and Jean M. J. Fréchet resolved this at IBM in 1980 by developing a chemically amplified photoresist as explained on page 3.

eliminated the first barrier in advancing multi-focus 3D laser printing. In chapter 5, I present a novel beam-splitting approach overcoming many limitations of conventional beam splitting. After demonstrating the vulnerability of the required micro-optical elements with respect to manufacturing imperfections, I present a workflow to iteratively enhance the shape accuracy and therefore efficiency of the components and close off by characterizing the final structures.

In chapter 6, I combine the advancements of chapter 4 and chapter 5 in a newly assembled optical setup for next-generation multi-focus 3D laser printing allowing for an order of magnitude larger peak printing rate while featuring a large field of view for printing. Finally, I discuss the optical performance of the setup by raytracing simulations and characterize the obtainable feature size.

To demonstrate the capabilities and need for the new setup, I show applications in respiratory science, material science, and particle physics in chapter 7. Enabled by the high print rate, I show printed samples in voxel numbers and quantities which were inaccessible before and give a brief outlook on the further course of each of the promising collaborations presented.

Finally, I summarize the results of this thesis in chapter 8 and give a brief outlook on further possible advancements in the field of fast 3D laser printing.

Chapter 2

2 Fundamentals of 3D Laser Printing

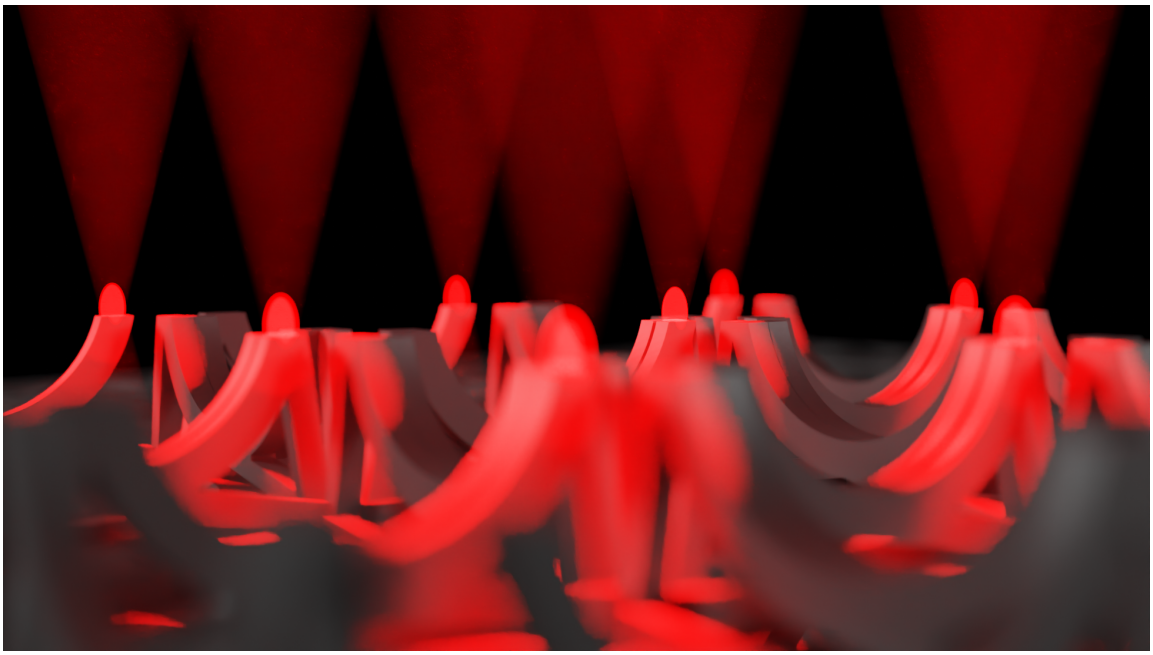

Artistic illustration of many laser foci 3D laser printing a periodic structure.

In this chapter, I will explain the basic concepts of multi-photon 3D laser printing by photopolymerization. After presenting the basic workflow and describing the underlying chemical processes, I will focus on the two-photon exposure dose and the various fabrication characteristics that can be explained by it. Since the fabrication setup developed in this work is heavily limited by the available laser power, I will further discuss power scaling in 3D laser printing before giving an overview of fast 3D printing in the literature and present the printing rate that was achieved within this thesis.

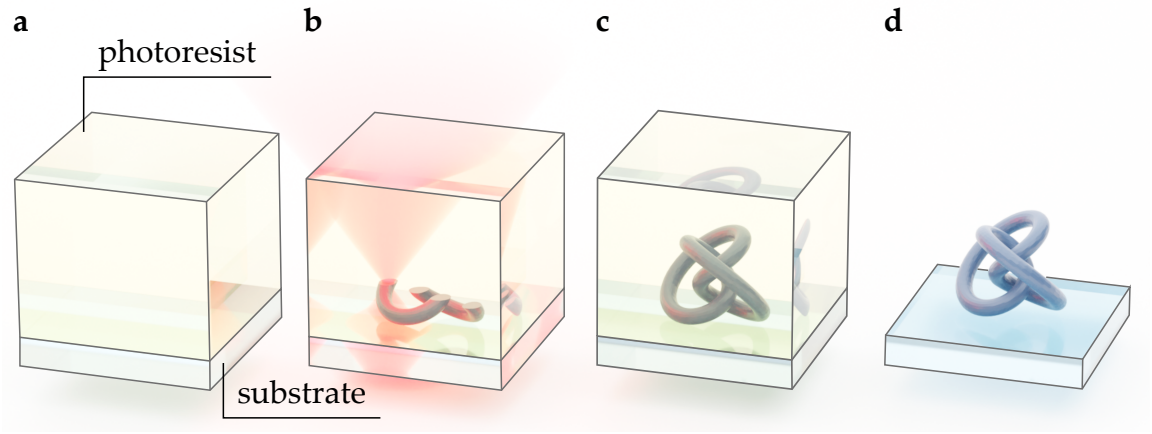

Figure 2.1: Illustration of the photopolymerization 3D laser printing workflow. **a,** a photoresist is applied on the substrate. **b,** exposure of a focused laser beam solidifies the material. **c,** after scanning the laser focus along the desired trajectory, a 3D structure can be fabricated. **d,** after dissolving all remaining liquid photoresist with a developing solvent, the final structure is obtained. Adapted from [35, 36].

2.1 Photopolymerization 3D Printing

The method applied for 3D printing throughout the entire thesis is multi-photon 3D laser printing by photopolymerization. In the following, the workflow and fundamentals of the underlying photochemistry will be discussed.

2.1.1 Methodology

The usual workflow of multi-photon 3D laser printing [19] is schematically depicted in Figure 2.1. A negative-tone photoresist [37] is applied on a substrate. Most photoresists used by this technique are liquid at room temperature [38], allowing for easy handling. During printing, the substrate is positioned in the vicinity of the focal plane of a microscope objective lens where a typically femtosecond-pulsed laser beam is focused into the photoresist [39]. A fraction of the photoresist then undergoes multi-photon absorption [40, 41], which excites photoresist molecules as discussed in the next paragraph. Some applications also use, e.g., picosecond-pulsed lasers [42]. Ultimately, the laser focus has to feature the necessary peak intensity for exciting the photoresist molecules depending on the used photoresist system [43]. In most cases, glass substrates are used. They allow for more flexibility than other intransparent materials with the laser being able to enter the photoresist through the glass side, allowing for sandwich-like configurations [44], or directly entering the photoresist. In the last decade, 3D laser printing in the "dip-in" configuration became a widely-used standard. Here,

the microscope objective lens for focusing is directly immersed into the photoresist [45], allowing for the fabrication of large samples with their height only limited by the travel range of the linear translation stage.

In the vicinity of the laser focus, the photoresist material undergoes a transition from liquid to solid, triggered by a polymer chain reaction [46]. A single point-like illumination therefore creates the smallest 3D element that can be printed with a specific multi-photon 3D laser printing setup: the voxel (stemming from the two words *volume* and *element* in analogy to the pixel) [47]. By scanning the laser focus through the photoresist along a trajectory dependend on the desired sample and translating a linear stage in between, a 3D structure can be obtained [48]. In a last step, the sample is immersed into a developing solution, dissolving any remaining unreacted photoresist and only leaving the final 3D structure [48].

2.1.2 *Polymer Chain Reaction by Photoinitiation*

Liquid negative-tone photoresists typically consist of a liquid monomer and a small amount of photoinitiator mixed into it. In the polymer chain reaction solidifying the photoresist, monomer molecules cross-link to large polymer networks with large molecular weight and solid state of matter. A common reaction which leads to these solid polymer networks is free radical photopolymerization [49]. Nowadays, multi-functional monomers and radical photoinitiators are typically chosen as ingredients for fast printing of still structures and are also used throughout this thesis.

In a first of four steps [50], photoinitiators (I) absorb light, which leads to cleavage of the molecules and the formation of radicals ($R^\bullet$) [51, 52]:

$$I \xrightarrow{h\nu} I^* \longrightarrow R^\bullet. \tag{2.1}$$

With a vast portion of monomers in direct vicinity, the created radical attacks and attaches to one of the functional groups of an available monomer molecule (M), creating a larger resulting molecule which still keeps the radical status condition [50]:

$$R^\bullet + M \longrightarrow RM_1{}^\bullet. \tag{2.2}$$

This molecule marks the first step in creating a large polymer chain. With the radical status condition still intact, the molecule will attack other monomers, incorporating them into the chain growing in size with each iteration:

$$RM_i{}^\bullet + M \longrightarrow RM_{i+1}{}^\bullet. \tag{2.3}$$

Eventually, this process called chain propagation comes to an end by one of several possible termination processes. One scenario is the reaction of the growing polymer chain with another radical molecule, losing the radical status condition. This second molecule can be another growing polymer chain or a cleaved photoinitiator [50]:

$$RM_i^\bullet + RM_j^\bullet \longrightarrow RM_{i+j}R, \tag{2.4}$$

$$RM_i^\bullet + R^\bullet \longrightarrow RM_iR. \tag{2.5}$$

Another potential termination pathway is radical scavenging. An important scavenger is oxygen, which is available in most photoresists as ambient oxygen [53]. Upon reaction with a radical polymer chain part, the scavenger (S) forms a stable peroxy radical:

$$RM_i^\bullet + S \longrightarrow RM_iS^\bullet. \tag{2.6}$$

Peroxy radicals do not further attack monomers and quickly recombine [54]. Scavenging molecules play a crucial role in the excitation of polymerization reactions since initially excited radicals get quickly scavenged until the local scavenger concentration within the focal volume of the laser focus is low enough for some polymer networks to grow in sufficiently cross-linked networks and form a voxel [43]. Only when the degree of cross-linking is high enough, the polymer network will survive the subsequent development process.

For a mono-functional monomer, the described process ends with a long polymer chain. Materials made from these chains typically feature low mechanical stabilities. Therefore, a third ingredient, cross-linking molecules, basically additional multi-functional monomers, were added into the photoresist formulation in the past with the sole purpose of connecting individual polymer chains.

Modern photoresists do not necessarily require cross-linking molecules anymore. They exploit multi-functional monomers that cross-link on their own due to multiple functional groups available for each molecule. A common type of monomers also employed in this thesis are acrylates [50, 55], which feature acrylate groups as functional groups.

2.2 The Two-Photon Exposure Dose

A solidified cross-linked polymer results from incident light triggering a chemical reaction that cures a liquid monomer [38]. The bridging molecule in this reaction is the photoinitiator. The reaction-diffusion kinetics in the photoresist are complex to calculate and still not fully understood [38, 43, 49]. Therefore, several assumptions,

which make the description of the photoresist behavior possible, are introduced in this section and derived following Ref. [38]. These subsequent models will establish the quantity of the two-photon exposure dose to describe effects on a length scale of a few voxels and further allow for describing the evolution of larger prints. The successful simulation implementation of these models is shown in the last part of this section.

2.2.1 *Polymerization Threshold Models*

To enable describing the photoresist behavior, two models are introduced: the threshold model and the accumulation model. Before going into detail, it is important to understand how light energy is deposited in the liquid photoresist. As outlined in section 2.1, an important quantity for the initiation of photoinitiator radicals is the pulse peak intensity [38]

$$I = \frac{P}{R_\mathrm{p} t_\mathrm{p}} \frac{1}{\pi r^2}. \tag{2.7}$$

It depends on the average laser power P of a potentially femtosecond-pulsed laser with wavelength λ_0, repetition rate R_p, pulse duration t_p, and effective spot radius r after focusing with a numerical aperture NA. [38]. When using continuous-wave lasers, the pulse parameter product simplifies to $R_\mathrm{p} t_\mathrm{p} = 1$. To calculate the spatial and temporal peak intensity, the radius r is calculated as the distance of an ideal Gaussian focus' maximum to $1/e^2$ of its peak in the small-angle approximation [38]:

$$r = \frac{\lambda_0}{\pi \mathrm{NA}}, \tag{2.8}$$

$$I = \frac{P}{R_\mathrm{p} t_\mathrm{p}} \frac{(\pi \mathrm{NA})^2}{\pi \lambda_0^2}. \tag{2.9}$$

To express the dose that is deposited in a liquid photoresist with sensitivity s_2[1] by a train of laser pulses in an exposure time $t_\mathrm{exp} \gg t_p$, the two-photon exposure dose is defined [38]:

$$D_\mathrm{exp} = s_2 t_\mathrm{exp} (R_\mathrm{p} t_\mathrm{p}) I^N. \tag{2.10}$$

Employing higher intensities or longer exposure time of the same photoresist volume element with constant intensity therefore yields higher two-photon exposure doses. Notably, for ideal two-photon absorption the photoresist nonlinearity exponent is $N = 2$. However, some photoresists do not follow ideal two-photon absorption and can therefore deviate from this value, even allowing for $N > 2$. This

[1] The sensitivity will be of importance in chapter 4.

characteristic will be of importance throughout this thesis and will be discussed in subsection 2.2.2. The following assumptions will facilitate the understanding on the relation between the two-photon exposure dose and the final structure fabricated by multi-photon 3D laser printing with a given photoresist.

Threshold Model

In the threshold model, the polymerization threshold dose D_{th} [38] is introduced as a new quantity. Exposure doses below the polymerization threshold dose $D_{\text{exp}} < D_{\text{th}}$ will lead to insufficiently cross-linked material not being able to withstand the development step after printing [38]. Only volume elements experiencing exposure doses above the polymerization threshold dose $D_{\text{exp}} > D_{\text{th}}$ lead to sufficiently cross-linked material and produce a sufficiently polymerized structure.

This model is depicted in Figure 2.2 where four different single exposures are studied. Figure 2.2a shows the computed 3D isosurfaces of the respective exposures and allows for visualizing the printed voxel size. Figure 2.2b and Figure 2.2c plot the quotient $D_{\text{exp}}/D_{\text{th}}$ for ideal two-photon absorption, which results in dose profiles following the squared intensity profile I^2. Values calculated this way only sufficiently cross-link the material when exceeding $D_{\text{exp}}/D_{\text{th}} = 1$. Using this model, the calculation of the size of the voxel created by the respective exposure can be calculated. The closer the exposure dose peak approaches the polymerization threshold dose $D_{\text{max}} \approx D_{\text{th}}$, the smaller the resulting voxel becomes. In this model, arbitrarily small voxels can be printed without any diffraction limit of light limiting the minimum size [38, 47, 50]. Notably, the exposure dose depicted in dark gray in Figure 2.2b and Figure 2.2c is below the polymerization threshold (dashed line) and therefore does not lead to the polymerization of a voxel.

Accumulation Model

In the accumulation model, the photoresist accumulates multiple exposure doses over space and time [38]. The fabricated structure is then defined by the accumulated dose exceeding the polymerization dose instead of the individual exposure doses

$$D_{\text{acc}} = \sum D_{\text{exp}}. \tag{2.11}$$

Figure 2.3 illustrates this model by again showcasing four individual exposures, this time at different locations x. Furthermore, the accumulated dose is computed and shown as well. Figure 2.3a and Figure 2.3b show the respective dose profiles with respect to the polymerization threshold dose. Notably, only two out of four individual exposures are strong enough to exceed the polymerization threshold

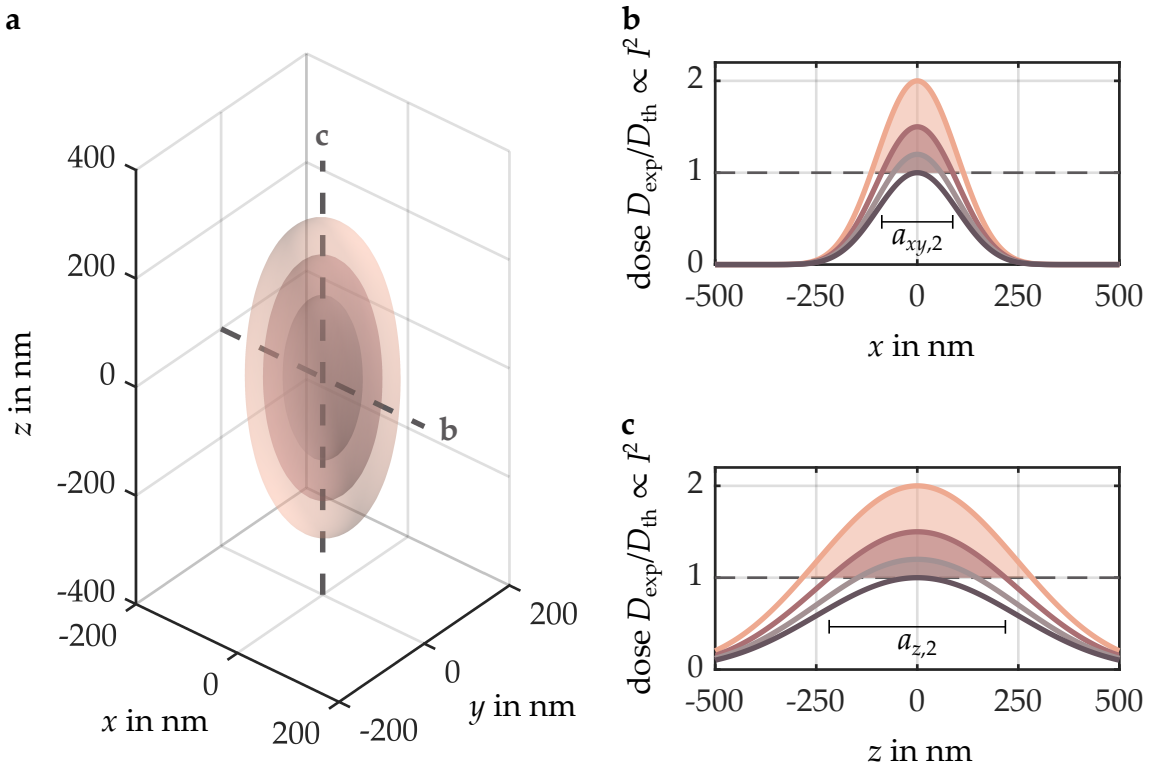

Figure 2.2: Depiction of the polymerization threshold model for a laser beam with wavelength $\lambda = 790\,\text{nm}$ that is propagating in z-direction and focused with an NA $= 1.4$ microscope objective lens. **a,** computed 3D isosurfaces of the two-photon exposure doses. **b,** two-photon exposure dose profiles normalized by the polymerization threshold dose along the x-direction indicated by the dashed line in **a**. The lateral voxel sizes increase with increasing doses with the lowest dose in dark gray and the highest dose in orange. They calculate to $a_{xy,1} = 118\,\text{nm}$, $a_{xy,2} = 176\,\text{nm}$, and $a_{xy,3} = 228\,\text{nm}$. The exposure dose in dark gray is not strong enough to overcome the polymerization threshold and produces no voxel. **c,** two-photon exposure dose profiles normalized by the polymerization threshold dose along the z-direction indicated by the dashed line in **a**. The axial voxel sizes calculate to $a_{z,1} = 294\,\text{nm}$, $a_{z,2} = 436\,\text{nm}$, and $a_{z,3} = 568\,\text{nm}$. Adapted from [36, 56].

dose, as shown in the profile along the x-direction in Figure 2.3a. However, by integrating all exposures according to the accumulation model, the resulting dose shown in orange exceeds the polymerization threshold dose at many locations where there should be no sufficiently cross-linked polymer without dose accumulation. Along the z-direction at $x = -100\,\text{nm}$ shown in Figure 2.3b there should be no sufficiently cross-linked polymer at all without the consideration of dose accumulation. Figure 2.3c shows the computed 3D isosurfaces of all individual exposure doses as well as the accumulated exposure dose. By considering the accumulation effect, the model predicts a larger structure instead of two distinct

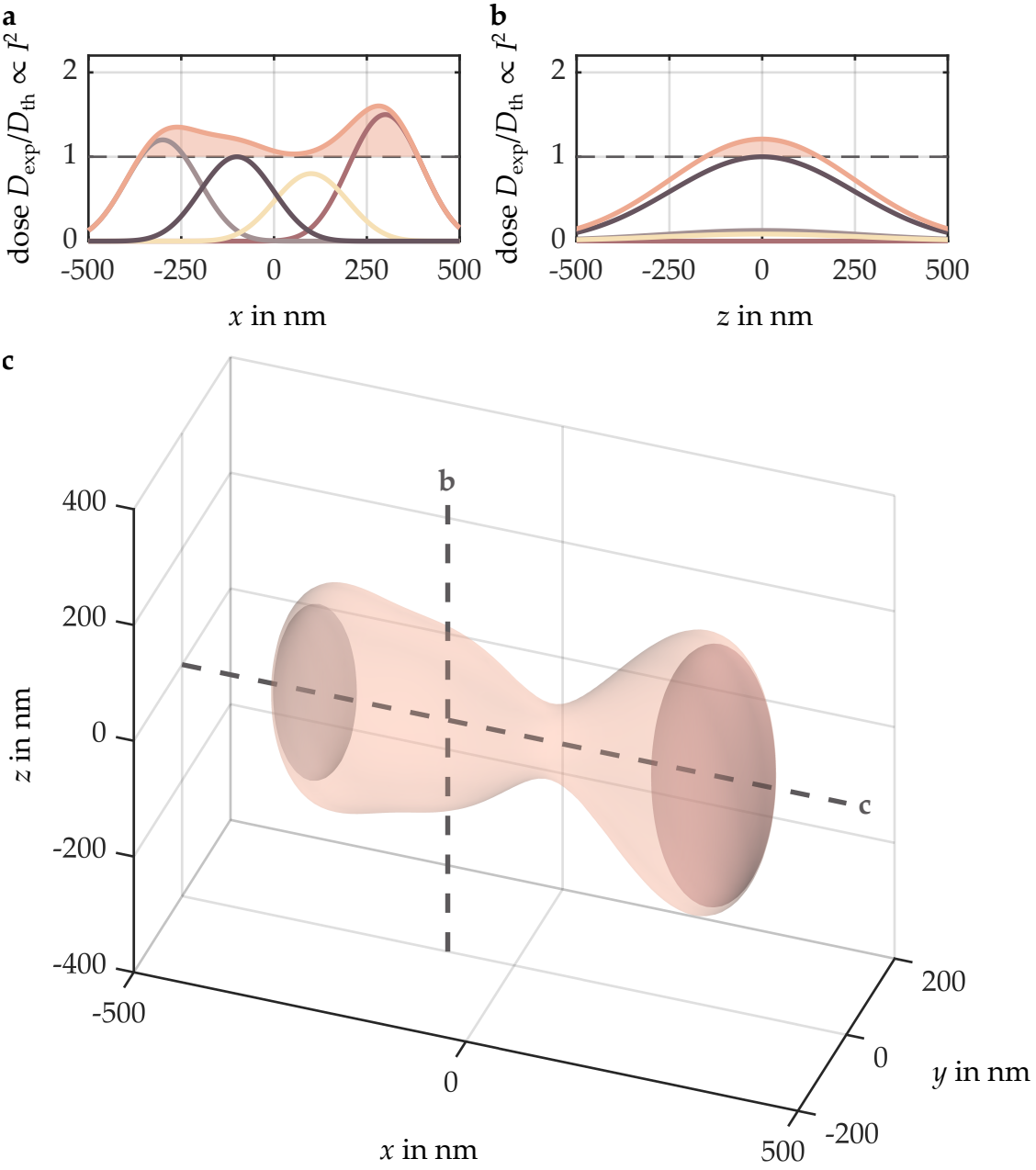

Figure 2.3: Depiction of the polymerization accumulation model for a laser beam with wavelength $\lambda = 790\,\text{nm}$ that is propagating in z-direction and focused with an NA $= 1.4$ microscope objective lens. For multiple exposures, the doses add up and polymerize the material in volume elements that would otherwise not have overcome the polymerization threshold. **a,** individual and accumulated (orange) two-photon exposure dose profiles along the x-direction indicated by the dashed line in **c**. **b,** individual and accumulated (orange) two-photon exposure dose profiles along the x-direction indicated by the dashed line in **c**. **c,** computed 3D isosurfaces of the individual and accumulated (orange) two-photon exposure doses. Based on [36, 56].

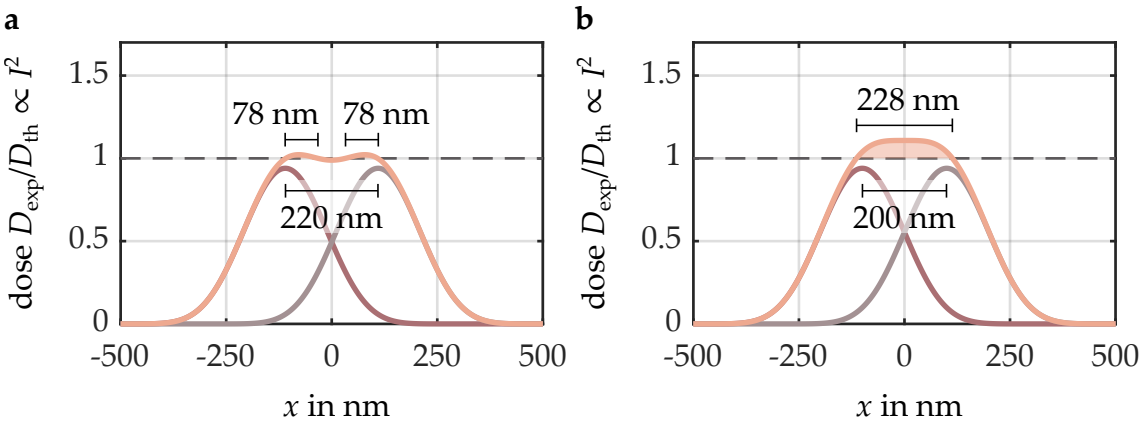

Figure 2.4: Depiction of the Sparrow criterion using a laser beam with wavelength $\lambda = 790\,\text{nm}$ that is propagating in z-direction and focused with an NA $= 1.4$ microscope objective lens. **a,** individual and accumulated (orange) two-photon exposure dose profiles along the x-direction for a focus spacing of 220 nm. The resulting voxels are clearly separated by a local dose minimum. **b,** individual and accumulated (orange) two-photon exposure dose profiles along the z-direction for a focus spacing of 200 nm. The individual doses add up to a integrated structure and show no individual voxels anymore. Based on [47, 57].

voxels which is in accordance to experiments. The accumulation leads to a larger structure without separated voxels. Since this integration is not only performed over space but also over time, the individual exposures can happen at different points in time t and will still lead to the depicted structure.

Importantly, the sole existence of dose accumulation limits the diffraction-limited resolution while only applying the threshold model allows for many infinitesimally small voxels next to each other. This leads to the definition of the two-photon Sparrow criterion [47]. Here, two slightly separated exposure doses still yield two disconnected voxels when the accumulated exposure dose features a local minimum in between [47].

This two-photon Sparrow criterion is illustrated in Figure 2.4 by showing two individual exposures and their accumulated dose. In Figure 2.4a, the two exposures are separated by 220 nm. The accumulated dose shows a local minimum below the polymerization threshold dose and therefore yields two disconnected voxels of finite size. In Figure 2.4b, the exposure separation is further decreased to 200 nm, leading to an accumulated dose without local minima and therefore only producing one piece of polymer. In many works including this thesis, the voxel size is the size corresponding to the two-photon Sparrow criterion [58].

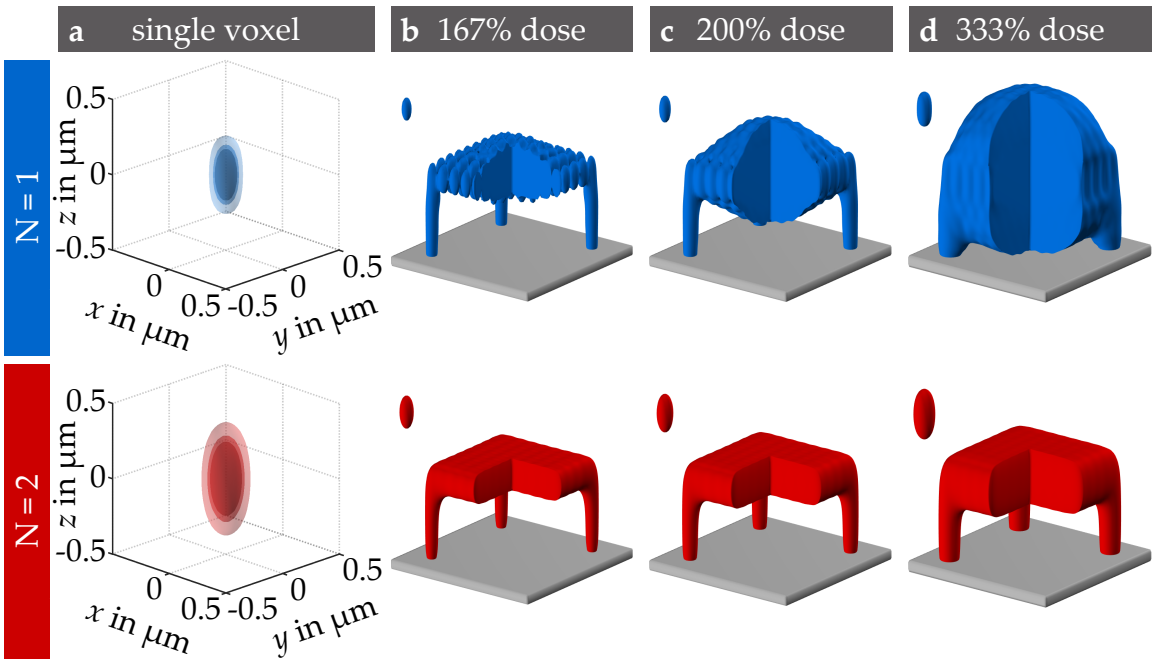

Figure 2.5: Illustration of dose accumulation in 3D laser printing for ideal one-photon absorption and ideal two-photon absorption using laser beams with wavelengths $\lambda_{1PA} = 400\,\text{nm}$ (first row) and $\lambda_{2PA} = 800\,\text{nm}$ (second row), respectively, that are propagating in z-direction and focused with an NA = 1.4 microscope objective lens. For one-photon absorption, the dose is directly proportional to the intensity of light $D \propto I$, while the two-photon absorption dose is proportional to the square of the intensity $D \propto I^2$. **a,** computed 3D isosurfaces of the one-photon and two-photon exposure doses according to the threshold model for single exposures of 167 %, 200 %, and 333 %. A single-voxel exposure dose of 100 % reaches the threshold only at the peak of the dose profile and therefore only produces a singular point. **b-d,** computation of the total exposure doses by summing up the sequential exposure doses presented in **a** according to the accumulation model. The target structure is a table consisting of a plate and four legs. The lateral voxel spacing is 0.2 µm. Despite the voxel size for one-photon absorption being smaller due to the smaller wavelength, the table structures show pronounced proximity effects. Adapted from [38].

2.2.2 *Dose Accumulation and Nonlinearity*

The photoresist's ability to memorize past exposures is the critical motivation to use multi-photon absorption instead of one-photon absorption [38]. As shown in Equation 2.10, the dose of an individual exposure D_{exp} depends on the intensity profile I to the power of the nonlinearity N of the photoresist. During printing of a structure, the several exposure doses necessary for manufacturing accumulate as described in Equation 2.11. The consequences are displayed in Figure 2.5.

In the case of one-photon absorption, the nonlinearity exponent follows $N = 1$, setting a linear proportionality of the exposure dose to the intensity $D_{\text{exp}} \propto I$. For ideal two-photon absorption, the nonlinearity exponent changes to $N = 2$, making the exposure dose follow a quadratic relationship $D_{\text{exp}} \propto I^2$. Figure 2.6a shows voxels resulting from single exposures following one-photon- and two-photon absorption. For one-photon absorption, a wavelength $\lambda_{1\text{PA}} = 400\,\text{nm}$ yielding smaller voxels was used while $\lambda_{2\text{PA}} = 800\,\text{nm}$ was applied for two-photon absorption. Figure 2.6b-d shows the computed result of printing a simple table consisting of one plate and four legs by either one-photon or two-photon absorption using the individual exposure doses $D_{\text{exp},1}/D_{\text{th}} = 167\,\%$, $D_{\text{exp},2}/D_{\text{th}} = 200\,\%$, and $D_{\text{exp},3}/D_{\text{th}} = 333\,\%$ [38]. For the computation, the individual exposures were summed up to the accumulated dose D_{acc} following Equation 2.11. Afterwards, the threshold model was applied on D_{acc}, yielding the illustrated structure.

Large exposure doses increase the size of the individual voxels building up the structure. However, apart from consequences of larger individual voxels, the structures produced by one-photon absorption show large deviations from the envisioned table. The explanation lies in strong dose accumulation governed by linear dependencies of the exposure dose from the intensity $D_{\text{exp}} \propto I$. At some position in the tail of the Lorentzian-shaped intensity distribution along the optical axis, the intensity of an individual exposure dose might only lead to

$$D_{\text{exp,tail}} \propto I_{\text{tail}}^{N=1} = (1\,\%)^{N=1} = 1\,\% \tag{2.12}$$

of D_{th}. However, raster scanning the table shown in Figure 2.6 leads volume elements far from the focal region getting illuminated, e.g., 100 times, leading to

$$D_{\text{acc,tail}} = 100 \times D_{\text{exp,tail}} \propto 100 \times I_{\text{tail}}^{N=1} = 100 \times (1\,\%)^{N=1} = 100\,\% \tag{2.13}$$

of the necessary threshold dose for one-photon absorption [38]. Thereby, dose accumulation leads to the unwanted polymerization of material, explaining the distorted tables. For two-photon absorption, the nonlinearity changes to $N = 2$ and therefore suppresses the influence of these tails of the intensity along the optical axis. This leads to exposure doses in these volume elements of

$$D_{\text{acc,tail}} \propto 100 \times I_{\text{tail}}^{N=2} = 100 \times (1\,\%)^{N=2} = 100 \times 0.01\,\% = 1\,\% \tag{2.14}$$

of the necessary threshold dose for two-photon absorption [38]. In this case, no sufficient polymerization is initiated. Obviously, dose accumulation is not completely negligible and will still lead to slight deformations in the vicinity of the focal regions but it is orders of magnitude weaker than for one-photon absorption.

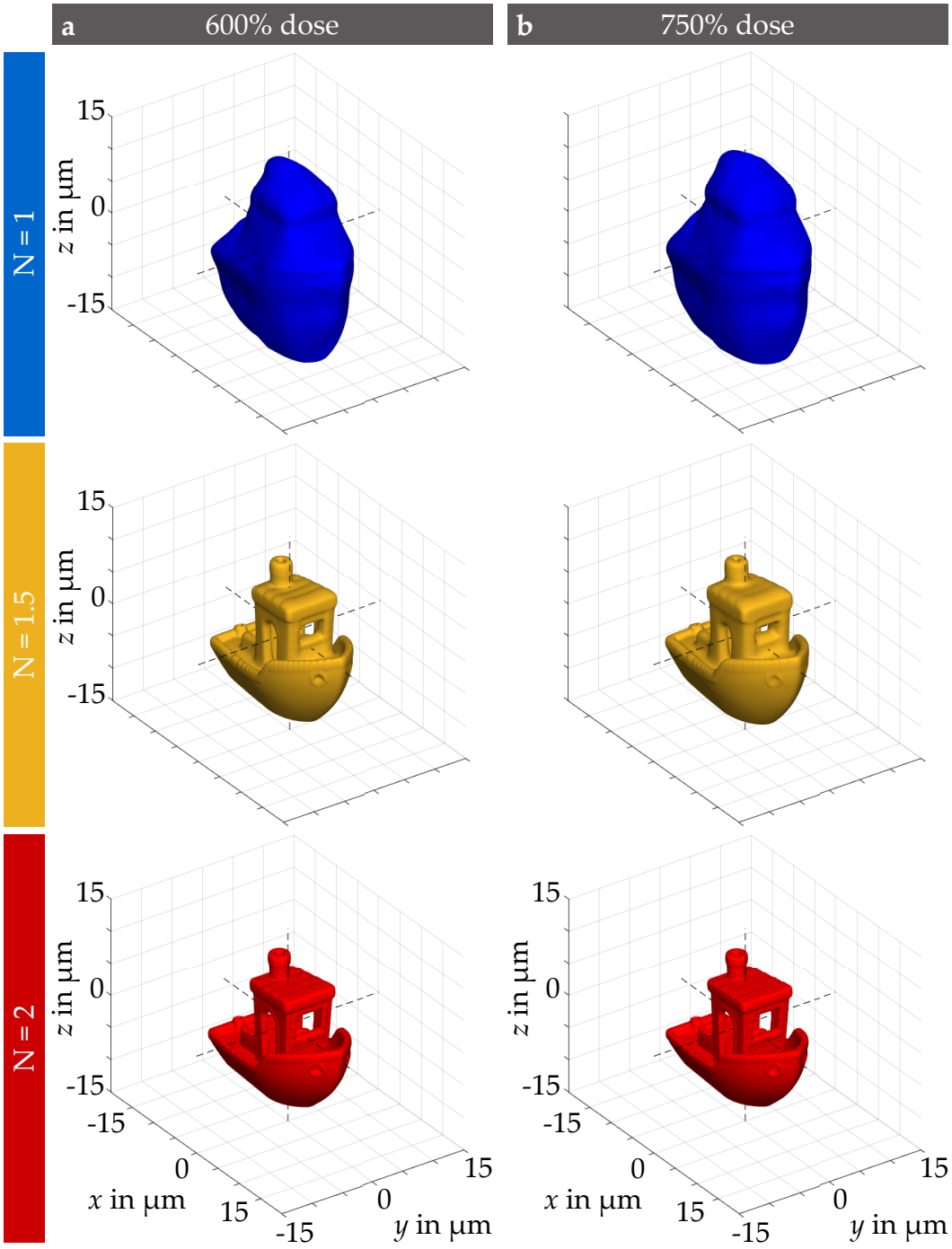

Figure 2.6: Illustration of dose accumulation for different nonlinearities using a laser beam with wavelength $\lambda = 780\,\text{nm}$ that is propagating in z-direction and focused with an NA $= 1.4$ microscope objective lens. The target is a structure with a lateral voxel spacing of $0.1\,\mu\text{m}$. **a-b,** 3D isosurfaces of the total exposure doses according to the accumulation model for single exposures of $D_{\text{exp},1}/D_{\text{th}} = 600\,\%$ and $D_{\text{exp},2}/D_{\text{th}} = 750\,\%$. For $N = 1$, the structure is not identifiable anymore. The accumulation effect is much smaller for $N = 1.5$. The boat can be printed with $N = 2$, revealing a well-resolved chimney and cabin. Adapted from [59].

In principle, the nonlinearity exponent of a given photoresist does not necessarily need to follow integer numbers. For some photoresists, the effective nonlinearity of the underlying process can even lie between one and two [60]. Simulating dose accumulation for a more delicate structure and also including these numbers shows that already slightly larger nonlinearity exponents than $N = 1$ can allow for 3D laser printing of complicated structures without two-photon absorption.

Based on early approaches as in Figure 2.5, Richard Wagner developed a simulation tool in the scope of this Bachelor's thesis [59] to automate the 3D laser printing prediction based on the used objective lens, the photoresist system, the laser source, and printing parameters according to the models described before. This work was supervised by the author. In Figure 2.6, the fabrication of a #3DBenchy[2] boat is simulated for the three nonlinearity exponents $N = 1$, $N = 1.5$, and $N = 2$ using the different individual exposure doses $D_{\mathrm{exp},1}/D_{\mathrm{th}} = 600\,\%$ and $D_{\mathrm{exp},2}/D_{\mathrm{th}} = 750\,\%$. For one-photon absorption ($N = 1$), strong dose accumulation renders the production of the target structure impossible, while the features are nicely reproduced for two-photon absorption ($N = 2$). In the case of $N = 1.5$, features like the boat's chimney or the cabin's window are impaired in comparison to the result obtained by two-photon absorption, however, the structure is resolved way better than for one-photon absorption. In these cases, good control over the accumulated exposure dose is necessary, making the simulation of the printing process highly desirable.

2.2.3 3D Laser Printing Simulations

Until now, the shown simulations referred to an arbitrary photoresist with arbitrary threshold dose. However, these simulations can also be performed with parameters from experimentally characterized photoresists. The accuracy of such simulations is demonstrated in Figure 2.7. Figure 2.7a shows simulated rolling-knot structures using various combinations of focus velocity v and total average laser power P. These parameters influence the individual exposure doses D_{exp} as explained in Equation 2.10. An increase in the focus velocity will decrease the exposure time $t_{\mathrm{exp}} = 2r/v$ while the employed intensity I is directly proportional to the total average laser power P. To account for the used photoresist comprising 2 wt% of the photoinitiator Irgacure 369 in the monomer mixture IP-Dip NPI (Nanoscribe GmbH & Co. KG) [59], the threshold exposure dose D_{th} and the effective nonlinearity exponent N were extracted from earlier characterization experiments performed in Ref. [38]. It is clearly visible that larger laser powers and smaller focus velocities lead to higher individual exposure doses D_{exp} and thereby

[2]Source and background of the 3D model: https://www.3dbenchy.com/.

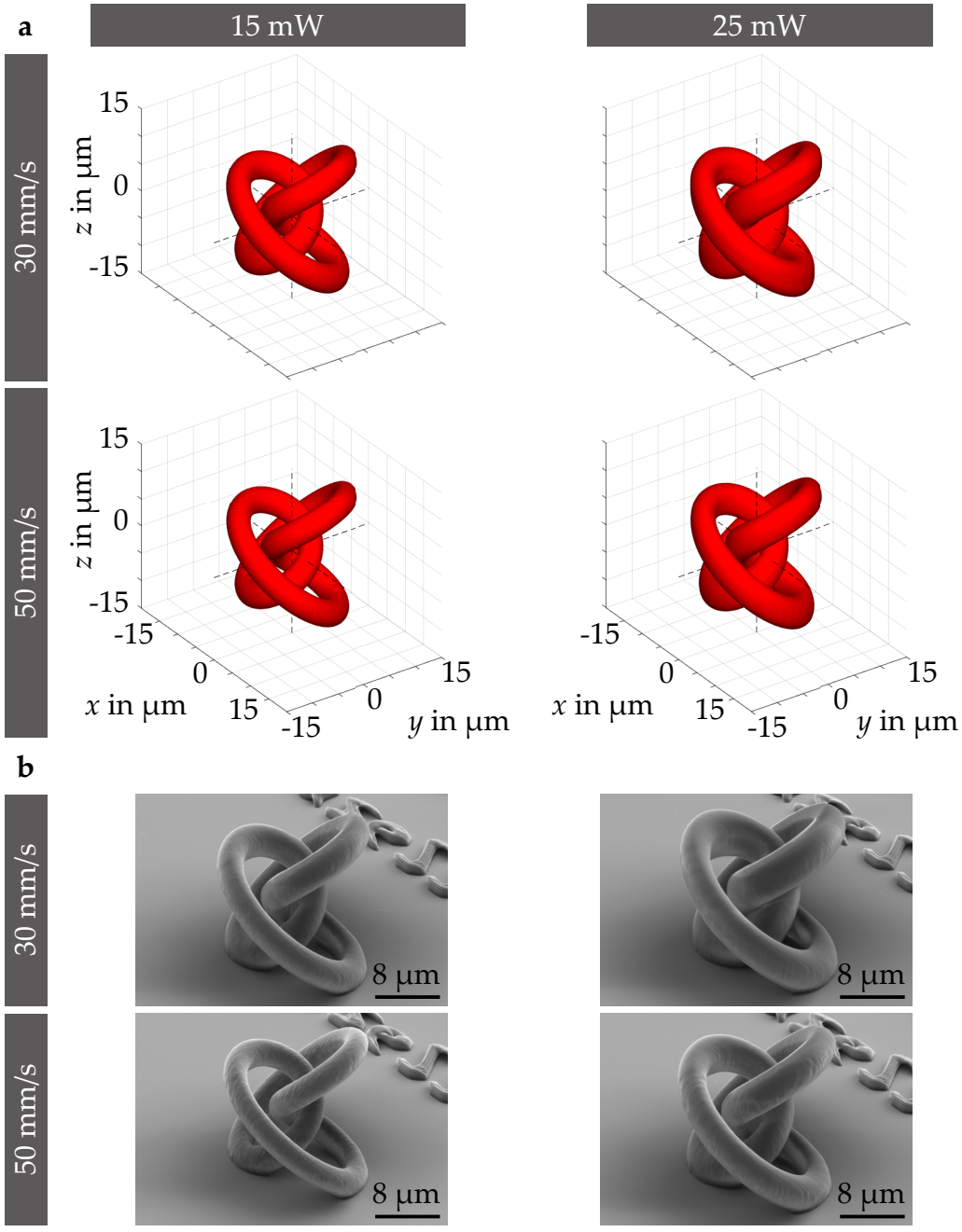

Figure 2.7: Comparison of dose accumulation simulation with 3D laser printed structures using a laser beam with wavelength $\lambda = 780\,\text{nm}$ that is propagating in z-direction and focused with an NA $= 1.4$ microscope objective lens. The target is a rolling knot structure with a lateral voxel spacing of $0.1\,\mu\text{m}$. **a,** 3D isosurfaces of the total exposure doses according to the accumulation model for varying laser powers and focus velocities. High laser powers and low focus scanning speeds lead to united parts that should not be connected. **b,** Scanning-electron micrographs of the same design printed with the same parameters using a commercial system (Photonics Professional GT, Nanoscribe GmbH & Co. KG). The printed structures are in good accordance to the simulation. Adapted from [59].

also to larger accumulated doses D_{acc}, which are reflected in larger features of the structure. On the top right, the bent tubes are almost in contact with each other while they are well separated on the lower left.

Figure 2.7b depicts scanning-electron-microscope images of the same structures using the modeled photoresist system and equal fabrication parameters. They show good accordance to the simulated counterparts. Understanding accumulated and exposure doses therefore is not only important in theory but can reduce the amount of iterations to retrieve a structure with the desired quality.

2.3 Power Scaling

Understanding exposure and accumulated dose does not only play a role to understand influences on the target structure while printing, it is also important to understand power scaling in 3D laser printing. Depending on the target structure, the necessary volume elements of the liquid photoresist must experience sufficient cross-linking by overcoming the threshold dose. Therefore, the necessary total laser power P for printing this structure depends on certain parameters. Especially for fast 3D laser printing, correctly understanding and handling power scaling is vital for successfully increasing the total number of voxels that can be printed per second. After all, the total average laser power P is a very limited resource that, depending on the manufacturing approach, can be used efficiently or inefficiently.

In principle, the manufacturing throughput depends on the employed focus velocity and the degree of parallelization. To understand power scaling for fast focus scanning, the influence of photoresist nonlinearity will be discussed. Furthermore, different parallelization techniques will be touched on and evaluated on their power efficiency.

2.3.1 Photoresist Nonlinearity

For a given photoresist, the proportionality of the exposure dose to the intensity or rather the total average laser power is dependent on the nonlinearity exponent as described in Equation 2.10. The nonlinearity exponent's influence is not only important for the degree of dose accumulation as explained in subsection 2.2.2, it is also crucial for high-speed applications. For a constant exposure dose D_{exp} exceeding the threshold dose, the laser power P and focus velocity v must be constant within the nonlinearity exponent's influence N as well [38]:

$$D_{exp} \propto t_{exp} P^N \propto \frac{P^N}{v} = \text{const.} \tag{2.15}$$

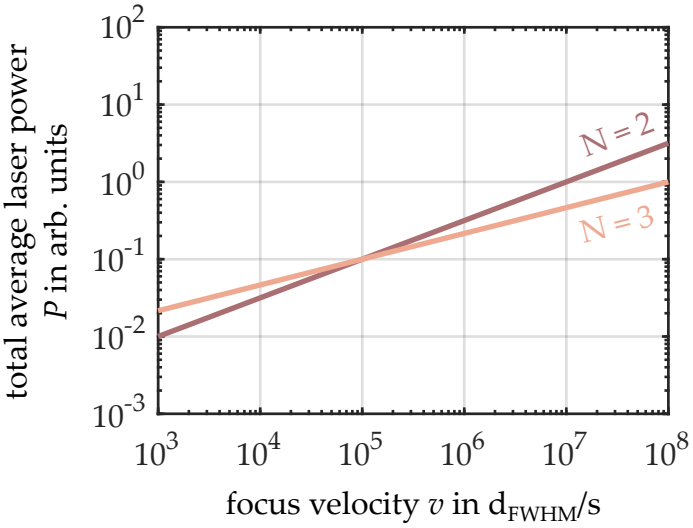

Figure 2.8: Power scaling in 3D laser printing for different nonlinearities. Lines of constant exposure in a double-logarithmic plot of necessary total average laser power versus focus velocity. Simply scanning a laser focus faster decreases the exposure dose and must be compensated by increasing laser power to retrieve equally cross-linked material. The additional laser power necessary depends on the nonlinearity of the photoresist. Adapted from [38].

Solving this equation for the necessary total average laser power P shows that increasing the focus velocity v by, e.g., a factor of ten only increases the necessary total average laser power for keeping a constant exposure dose D_{exp} by a factor $\sqrt[N]{10}$:

$$P \propto \sqrt[N]{v}. \tag{2.16}$$

Figure 2.8 visualizes this relationship by plotting the total average laser power P versus the focus velocity v for the two exemplary nonlinearity exponents $N = 2$ and $N = 3$. To increase the focus velocity with a limited total average laser power available, it is therefore advisable to use photoresists with higher effective nonlinearities $N > 2$ than for ideal two-photon absorption. The photoresist developed in this thesis and presented in chapter 4 features $N \approx 3$ and is therefore highly suitable for the envisioned high-speed application. However, even when using a photoresist sensitive enough to sufficiently cross-link the polymerized material at the highest speeds, the focus velocity will have a technological limit. Should this limit be reached, the printing rate of the corresponding device can be further increased by parallelization.

2.3.2 *Parallelization*

Next to simply scanning a single laser focus rapidly, the straight-forward approach to increase the number of voxels printed per second is printing with multiple foci in parallel. This can be achieved by, e.g., splitting one incident laser beam into many beamlets that eventually get focused down to an array of foci. However, the power budget scales very differently in comparison to changes of the focus velocity. Obviously, when using any number of foci K in parallel, the total average

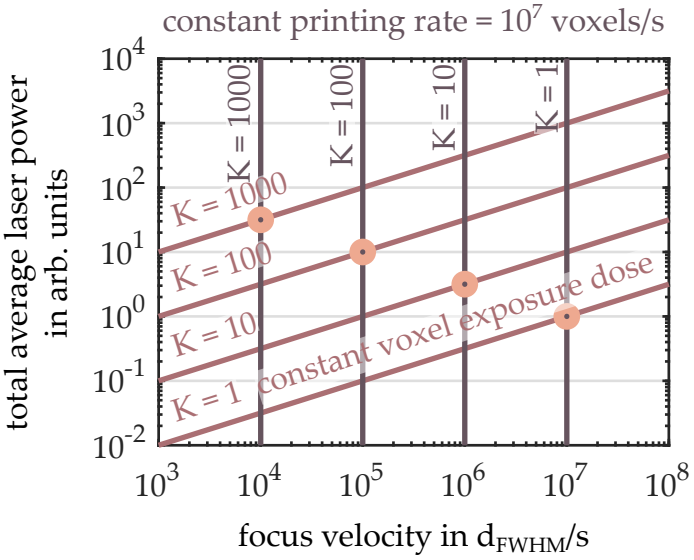

Figure 2.9: Power scaling in 3D laser printing for different numbers K of foci. Lines of constant exposure in a double-logarithmic plot of necessary total average laser power versus focus velocity. Intersections between lines of constant exposure with lines of constant printing rate show possible solutions. Employing the highest possible focus velocity allows for achieving a desired printing rate with the lowest possible total average laser power. Adapted from [38].

laser power must be increased by that factor K as well to keep the laser power per laser focus constant. Combined with Equation 2.16, the power budget can therefore be estimated to [38]

$$P \propto K \sqrt[N]{v}. \tag{2.17}$$

Applying many laser foci K in parallel therefore increases the necessary total average laser power P linearly while the proportionality to the focus velocity v depends on the photoresist nonlinearity N. The printing rate p in units of voxels per second scales linearly with both the number of laser foci K and the focus velocity v

$$p = \frac{Kv}{d}, \tag{2.18}$$

$$v = \frac{pd}{K}, \tag{2.19}$$

with the voxel diameter d [38]. In Figure 2.9, Equation 2.17 and Equation 2.19 are visualized in a diagram of the necessary total average laser power P versus the focus velocity v for an exemplary photoresist nonlinearity $N = 2$, following ideal two-photon absorption.

The absolute necessary total average laser power depends on the sensitivity of the used photoresist, which is why in Figure 2.9, the laser power is given in arbitrary units [38]. The vertical lines specify the necessary focus velocity v to achieve a constant printing rate $p = 10^7\,\text{voxels}\,\text{s}^{-1}$ with different numbers of foci in parallel K. The brown lines also depict cases following different numbers of foci in parallel K, however, this time the necessary total average laser power P is calculated. The crossing points between lines of equal numbers of foci in parallel K are solutions

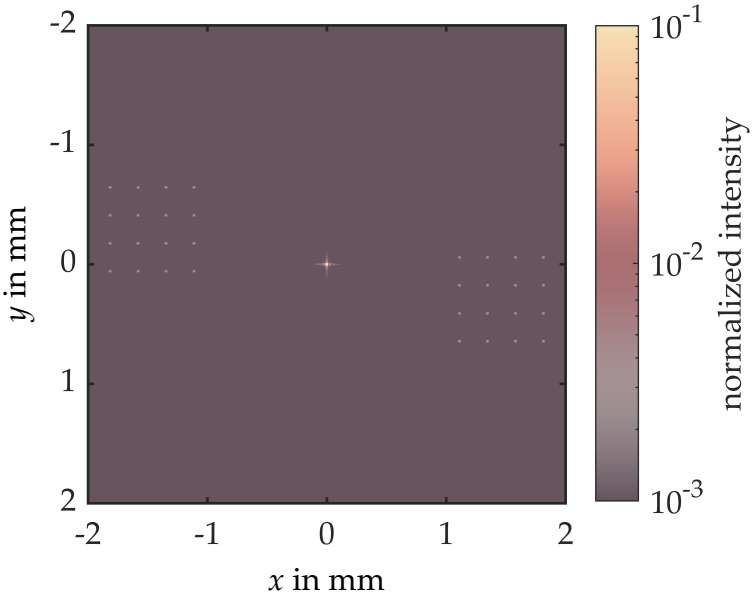

Figure 2.10: Calculated intensity profile in the Fourier plane of an amplitude-modulating digital micromirror device (DMD). For the simulation, a DMD with 1000×1000 micromirrors with a single mirror side length of 5.4 µm was assumed to be uniformly illuminated with a $\lambda = 790\,\text{nm}$ laser. The intensity pattern shows a grid of 4×4 foci twice alongside a strong zeroth order. In this mode, only a small fraction of the incident power can be used for 3D laser printing.

of the problem and are highlighted by circles [38]. Different numbers of foci lead to different solutions with different necessary total average laser powers P.

With arbitrary focus velocities v available, the solution requiring the lowest total average laser power applies only one laser focus $K = 1$ [38]. This can intuitively be understood by the different proportionality of the total average laser power P with the focus scanning speed v for nonlinearities $N > 1$. In terms of power efficiency, it is therefore advisable to apply the maximum focus velocity possible before using multiple foci in parallel. Many approaches already allow for fast scanning, e.g., galvanometric mirror scanning, polygon mirror scanning, or acousto-optic deflection. Parallelizing manufacturing by applying multiple laser foci on the contrary can be achieved by following different static and dynamic approaches, linked to respective advantages and disadvantages.

Dynamic Approaches

Dynamic beam-splitting allows for changing the focus pattern during printing, which offers a lot more flexibility in comparison to its static counterpart and can furthermore combine beam splitting and focus scanning in one device. The incident light can be modified accordingly by either directly projecting the required focus pattern into the writing plane or by placing the corresponding device in the Fourier plane of the microscope objective lens.

Projection-based beam-splitting can be achieved by using, e.g., a liquid-crystal display (LCD) [61, 62] or a digital micromirror device (DMD) [31, 63–65]. Both pixelate the active region of their display that the incident beam is guided on. By activating and deactivating certain pixels of the pixel array, the required focus pattern can be defined. In the case of the LCD, activated and deactivated pixels are realized by locally changing the polarization of the incident beam accordingly. This even allows for true grayscale intensity modulation [62], which expands the potential of LCDs even further than simply fully activating or deactivating certain pixels.

The DMD, on the other hand, comprises many small mirrors, which can be tilted individually. Thereby, certain fractions of the incident beam can be further guided through the optical setup or reflected into a beam dump. Cruicially, the refresh rate as well as the resolution of both devices become critical parameters for the connected multi-focus 3D laser printing approach.

While projection-based approaches benefit from dynamic beam splitting in a straight-forward manner, their power efficiency is a major disadvantage. Even though each pixel can be triggered individually, most pixels will be deactivated most of the time. Since dark pixels are not used for printing, most of the incident intensity is lost. This severely reduces the power efficiency of all projection-based approaches. Even for the fabrication of a solid cube it is disadvantageous to activate all pixels due to interference of coherent foci in close proximity leading to Talbot planes along the optical axis [66, 67]. Furthermore, the resolution along the optical axis can get lost completely when polymerizing a hypothetical infinitely broad plane, leading to a constant intensity along the optical axis.

To overcome wasting most of the incident laser power by only using a fraction of the beam-splitting device at a time, it can be positioned in the Fourier plane. The incident laser beam's amplitude is modulated and arbitrary focus patterns can be created in the writing plane. This time, the incident laser power can be distributed among the activated foci in the writing plane, which is a clear advantage to projection-based beam splitting. However, in this approach, a large fraction of the incident laser power is lost by diffraction. Figure 2.10 depicts the computed 4×4 focus pattern in the Fourier plane [68–70] of a DMD with 1000×1000 micromirrors and the correct amplitude-modulating pattern set to the pixelated display. The amplitude-modulating pattern was calculated using a weighted Gerchberg-Saxton algorithm [71]. The software code for the calculation was put together by Pascal Rietz. The diffraction pattern features a strong zeroth order next to multiple versions of the target focus array. Printing with this approach includes blocking the zeroth order and thereby still wasting a large fraction of the incident laser power.

This strong zeroth order can be suppressed in the diffraction-based approach using a spatial light modulator (SLM) [23, 26, 72]. It also can dynamically change the diffraction pattern and offers flexibility [70] but has a very limited lateral resolution in comparison to the static approach of the diffractive optical element. Additionally, SLMs suffer from phase jitter and therefore can not hold a certain phase topography nicely over time, which ultimately results in a perturbed diffraction pattern [56].

Static Approaches

Static beam-splitting approaches do not have the possibility to change the pattern of the focus array while printing. The introduced focus array is fixed and can only be scanned by further devices in the optical setup. While this is a clear disadvantage in terms of flexibility during printing, static beam splitting benefits from high power efficiency.

By using a diffractive optical element (DOE) or a multi-lens array (MLA), static beam splitting can be achieved both diffractively and refractively, respectively. While an MLA focuses an incident beam into many foci, a DOE splits an incident beam into many beamlets by diffraction. Static-diffractive beam splitting does not introduce a strong zeroth order that cannot be used for printing and offers power efficiencies over 90 % [73]. Since the laser power in highly-parallelized 3D laser printing with maximum focus velocities is severely limited, the next-generation multi-focus 3D laser printing setup developed in this thesis will focus on static beam splitting in combination with rapid scanning. Further advantages and disadvantages of different static beam-splitting approaches are therefore thoroughly discussed in chapter 5.

2.4 3D Printing Speed Overview

A fast 3D printing setup is ultimately characterized by its smallest possible voxel size and its total peak printing rate, which was already introduced in Equation 2.18. Given a constant voxel size, 3D printers with large total peak printing rates excel in rapid manufacturing of unprecedented total numbers of voxels. Given that current research efforts in, e.g., biology, optics, material sciences, and pharmacy demand for increasingly larger and more complex 3D structures in high numbers, record-breaking print rates at the required voxel sizes are needed year after year [74]. To identify these swift 3D printing setups, Figure 2.11 summarizes various 3D printing methods with respect to their total peak printing rate and voxel size.

One leading technology in terms of total peak printing rate with label 2023-2 features acousto-optical deflection as a fast focus-scanning approach and pairs it with beam splitting by a DOE [75]. This advancement thereby directly follows the sequence outlined in subsection 2.3.2. First, the laser focus should be scanned as fast as possible. If the power budget allows for it, further enhancements in print rate can be achieved by parallelization afterwards. While this 3D printer excels in total peak printing rate, it suffers from tiny $34 \times 68\,\mu m^2$-sized fields of view and requires a lot of stitching of individual writing fields to produce larger structures.

Previously, multi-focus 3D laser printing already brought up a rapidly-printing optical setup, depicted with data point 2020 [33]. Here, an array of $3 \times 3 = 9$ laser foci was used in parallel and scanned with focus scanning speeds of up to $0.5\,m\,s^{-1}$ [33]. The second leading technology in terms of total peak printing rate with label 2023-3 [58] comprises the next-generation multi-focus 3D-printing technology presented in this thesis. Its optical setup is presented in chapter 6.

The main goal here was to push the total peak printing rate for multi-focus 3D laser printing to the maximum while working with a limited power budget. The following chapter explains all methods used for achieving this goal. In chapter 4, the first of the necessary advancements is presented. It explains enhancements in photoresist sensitivity and is the first and most crucial step to increase the number of foci in parallel further.

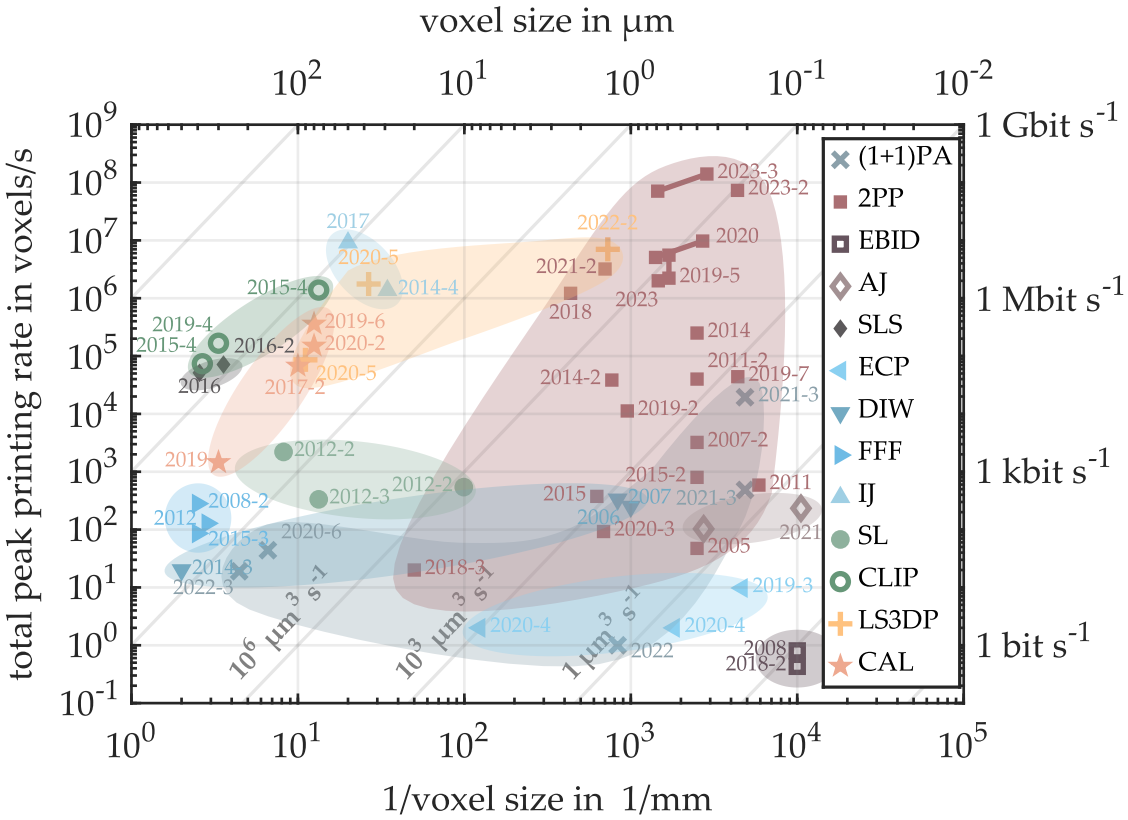

Figure 2.11: Printing speed comparison of different 3D printing technologies by sorting them by their peak printing rate and voxel size. The two leading connected data points (2023-3) refer to the next-generation multi-photon multi-focus 3D laser printing setup presented in this thesis. Its printing rate is approximately 10^8 voxels s^{-1} (right data point) when assuming a diffraction-limited voxel size of approximately 350 nm or slightly below 10^8 voxels s^{-1} (left data point) when using an average measured voxel size across the later introduced array of $7 \times 7 = 49$ foci. The various technologies in this graph are: one-plus-one-photon absorption ((1+1)PA), two-photon printing (2PP), electron-beam-induced deposition (EBID), aerosol-jet 3D nanoprinting (AJ), selective laser sintering (SLS), electrochemical printing (ECP), direct ink writing (DIW), fused filament fabrication (FFF), inkjet printing (IJ), stereolithography (SL), continuous liquid interface printing (CLIP), light-sheet 3D printing (LS3DP), and computed axial lithography (CAL).
References: 2005 [20], 2006 [76], 2007 [77], 2007-2 [21], 2008 [78], 2008-2 [79], 2011 [22], 2011-2 [23], 2012 [80], 2012-2 [81–83] (with data points from ref. [84]), 2012-3 [85], 2014 [24], 2014-2 [25], 2014-3 [86], 2014-4 [87], 2015 [26], 2015-2 [27], 2015-3 [88], 2015-4 [89], 2016 [90], 2016-2 [91], 2017 [92], 2017-2 [84], 2018 [28], 2018-2 [93], 2018-3 [29], 2019 [94], 2019-2 [31], 2019-3 [95], 2019-4 [96], 2019-5 [30], 2019-6 [97], 2019-7 [32], 2020 [33], 2020-2 [98], 2020-3 [34], 2020-4 [99], 2020-5 [100], 2020-6 [101], 2021 [102], 2021-2 [64], 2021-3 [60], 2022 [103], 2022-2 [62], 2022-3 [104], 2023 [63], 2023-2 [75], and 2023-3 [58]. Adapted from [33, 58, 62].

3 Chapter 3
Methods

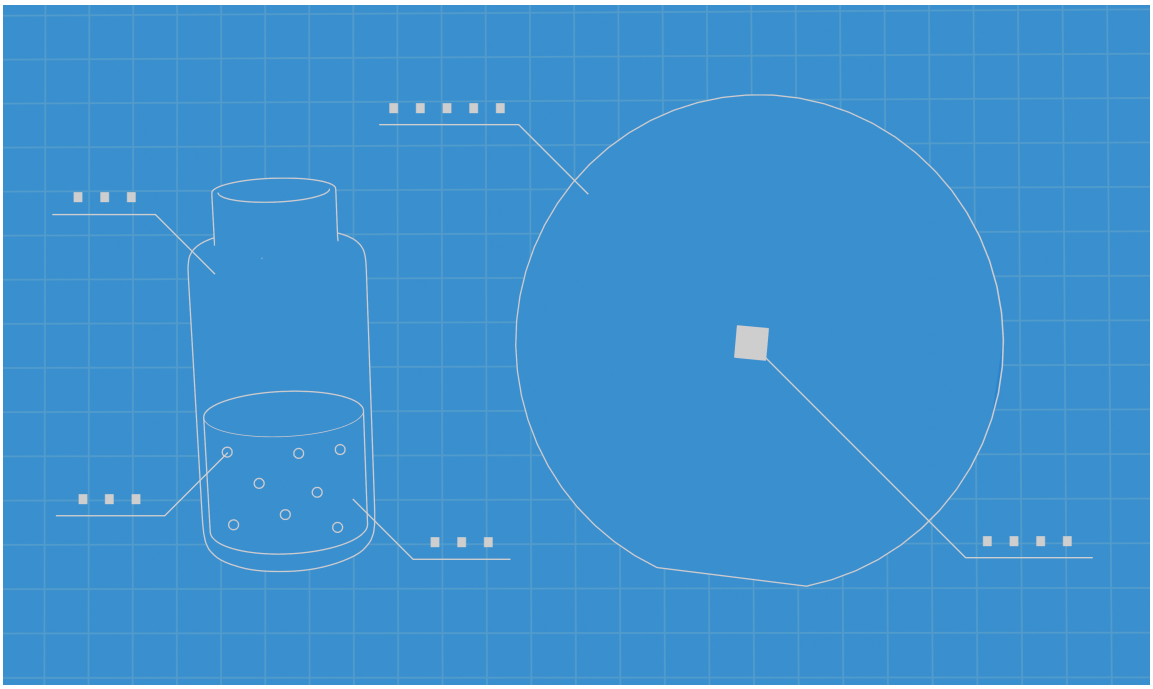

Artistic illustration of a blueprint containing photoresist and substrate information.

In this chapter, the applied methods for the upcoming results chapters are documented. These methods include the composition of characterized photoresists, the optical setups that were used and not developed in the scope of this thesis, and important background information for some processes that were applied in this work.

3.1 Sensitive Photoresist Development

In this section, the different methods used to mix new photoresists and perform polymerization threshold power experiments are explained. Furthermore, the preparation, development, and characterization of the samples shown in chapter 4 is documented.

3.1.1 Photoresist Composition

All photoresists were mixed under yellow-light conditions and using a precision balance (XSR105DU, Mettler-Toledo International Inc.).

PETA + DETC

10 mg 7-diethylamino-3-thenoylcoumarin (DETC, Luxottica Exciton) was dissolved in 1990 mg pentaerythritol triacrylate (PETA, technical grade, Sigma-Aldrich) to obtain a DETC concentration of 0.5 wt%. The resist was treated in an ultra-sonic bath for 30 min and stirred on a hot plate at 40 °C over night.

PETA + DETC + Irgacure 819

10 mg 7-diethylamino-3-thenoylcoumarin (DETC) and 12.8 mg Irgacure 819 (Ciba Specialty Chemicals) were dissolved in 1977.2 mg pentaerythritol triacrylate (PETA) to obtain a DETC concentration of 0.5 wt% with a 1 : 1 molar ratio of Irgacure 819. The resist was treated in an ultra-sonic bath for 30 min and stirred on a hot plate at 40 °C over night.

PETA + DETC + Irgacure 369

10 mg 7-diethylamino-3-thenoylcoumarin (DETC) and 11.2 mg Irgacure 369 (Ciba Specialty Chemicals) were dissolved in 1978.8 mg pentaerythritol triacrylate (PETA) to obtain a DETC concentration of 0.5 wt% with a 1 : 1 molar ratio of Irgacure 369. The resist was treated in an ultra-sonic bath for 30 min and stirred on a hot plate at 40 °C over night.

PETA + DETC + Coinitiators

10 mg 7-diethylamino-3-thenoylcoumarin (DETC), 3.9 mg (7.9 mg) dibutylamine (DBA, $\geq$ 99.5 %, Sigma-Aldrich), and 13.3 mg (26.6 mg, 53.2 mg) diphenyliodonium hexafluorophosphate (DPIHFP, TCI Chemicals) were dissolved in pentaerythritol triacrylate (PETA) yielding a total mass of 2000 mg to obtain a DETC concentration of 0.5 wt% with a 1 : 1 (2 : 1) molar ratio of DBA and a 1 : 1 (2 : 1,

4 : 1) molar ratio of DPIHFP. The resist was treated in an ultra-sonic bath for 20 min and stirred on a hot plate at 30 °C over night.

PETA + MBK

2 mg (2E,6E)-2,6-Bis (4-(dimethylamino)benzylidene)-4-methylcyclohexanone (MBK) was dissolved in 1998 mg pentaerythritol triacrylate (PETA) to obtain an MBK concentration of 0.1 wt%. The resist was treated in an ultra-sonic bath for 30 min and stirred on a hot plate at 40 °C over night.

PETA + BBK

1 mg (8 mg) (2E,6E)-2,6-Bis (4-(dibutylamino)benzylidene)-4-methylcyclohexanone (BBK) was dissolved in 999 mg (1134.9 mg) pentaerythritol triacrylate (PETA) to obtain a BBK concentration of 0.1 wt% (0.7 wt%). The resist was treated in an ultra-sonic bath for 30 min and stirred on a hot plate at 40 °C over night.

3.1.2 3D Laser Printing Setup

For the characterization of the presented photoresists, the optical setup shown in Figure 3.1 was used. It was originally built by Joachim Fischer and heavily modified by Vincent Hahn and Tobias Messer [56]. The setup offers many different laser wavelengths for characterization. However, for this work, only the beam path originating from the Titanium-Sapphire (Ti:Sa) laser (Mai Tai HP, Spectra Physics) with a fundamental wavelength $\lambda = 820\,\text{nm}$ was used.

To determine the threshold laser power, point-exposure experiments were performed. For multiple locations on the sample, the exposure time t_{exp} and laser power P was varied per voxel. The lowest laser power yielding a polymer dot with a sufficient cross-linking density to withstand the development process for each exposure time was defined the polymerization threshold power P_{th}.

3.1.3 Sample Preparation

For the photoresist characterization, glass cover slides with a thickness of 170 µm were used. By using a paper towel, they were cleaned with acetone and 2-propanol. After blow-drying with nitrogen, the surface of the glass cover slides was activated to generate hydroxyl groups by a 20 min treatment in air plasma [57, 105]. To permanently offer covalent binding during photopolymerization, the substrates were silanized by immersing in a 1 mM solution of 3-(trimethoxysilyl)propyl-methacrylate in toluene.

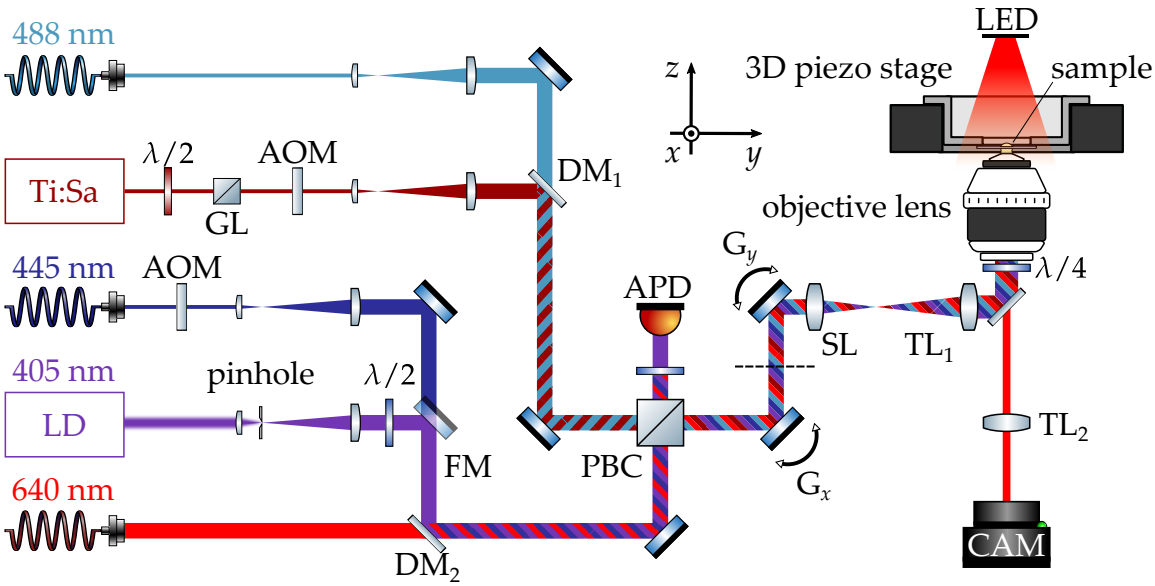

Figure 3.1: Scheme of the optical setup used for the characterization of the polymerization threshold power of various photoresists. The setup features five different beam paths for experiments at vastly different wavelengths. These beam paths are combined by the dichroic mirrors DM_1 and DM_2, the kinematic flip mirror FM, and the polarizing beam combiner PBC. For the experiments in this thesis, only the beam path comprising the Titanium-Sapphire (Ti:Sa) laser is used. Its power can be regulated by both using a half-wave plate with the polarizing PBC as well as the acousto-optical modulator (AOM). Furthermore, a Glan-Laser polarizer (GL) is used. Beam deflection is possible by the two galvanometric mirrors G_x and G_y. After a scan lens (SL) and a tube lens (TL_1), the beam can be focused for printing. The apochromatic quarter-wave plate in front of the objective lens (HCX PL APO 100×/1.4–0.7 Oil CS, Leica) translates the linear polarization to a circular polarisation. The sample can be positioned by both a coarse microscope stage (not shown) and a fine 3D piezo stage. Observation of the sample is possible by a camera (CAM) with a tube lens (TL_2). Adapted with permission from [56].

3.1.4 *Sample Development*

All photoresist-characterization samples were developed vertically by immersing them for 10 min in acetone (UV/IR grade, Carl Roth GmbH + Co. KG). Afterwards, they were dried in a nitrogen gas stream.

3.1.5 *Sample Characterization*

The point-exposure samples were characterized by analyzing the images taken by an optical light microscope to determine the polymer dots printed with the lowest laser power for each exposure time.

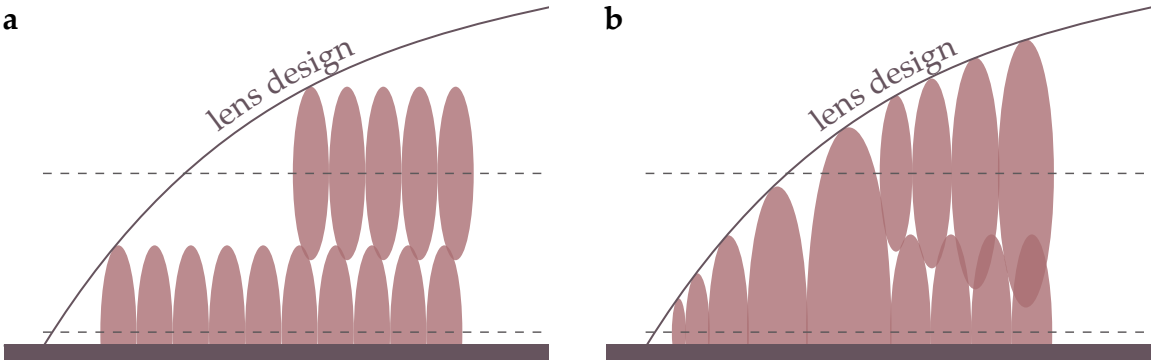

Figure 3.2: Comparison of conventional two-photon lithography and two-photon grayscale lithography (2GL). a, Depiction of a lens shape getting filled with voxels on a substrate during conventional two-photon lithography. The structure is divided into different slices that are indicated by the gray dashed lines. With a constant voxel size, a good approximation of the lens design by voxels is only possible when using minuscule voxel sizes that in turn extends the fabrication time tremendously. **b,** Depiction of the same lens shape like in **a** but with tuned voxel sizes using the 2GL technology. In 2GL, the voxel size gets adjusted during the manufacturing process. Using the same slicing distance the structure can now be approximated precisely without sacrificing fabrication time. Adapted from [106].

3.2 Optimization of Micro-Optical Components

In this section, the different methods that were applied to manufacture and enhance the optical quality of the manufactured diffractive optical element (DOE) and multi-lens array (MLA) presented in chapter 5 are described.

3.2.1 Two-Photon Grayscale Lithography

The micro-optical components for next-generation multi-focus 3D laser printing were fabricated using the commercially available Quantum X lithography system (Nanoscribe GmbH & Co. KG) in combination with a 25x/NA0.8 objective lens (LCI Plan-NEOFLUAR, Zeiss). Instead of applying conventional two-photon lithography, Quantum X employs two-photon grayscale lithography (2GL) [107]. Figure 3.2a schematically depicts the filling of a desired lens profile with voxels in conventional two-photon lithography. Here, any structure gets divided into individual slices, which get filled with voxels that share the same size. This results in a finite surface imperfection. In two-photon grayscale lithography, the voxel size is adjusted during the manufacturing process [106] like depicted in Figure 3.2b, allowing for higher throughput of structures that resemble the design more closely. This approach leads to smooth surfaces which is especially beneficial for optical

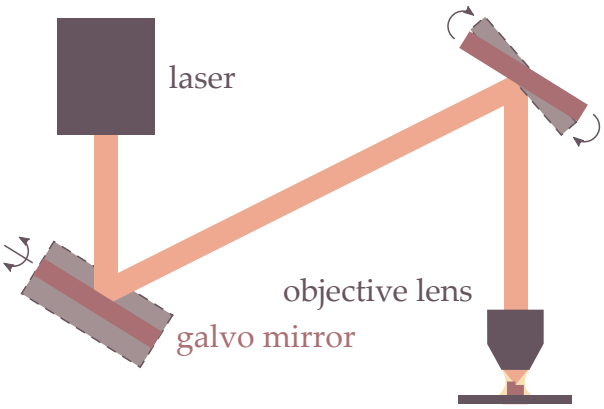

Figure 3.3: Simplified scheme of the Nanoscribe Quantum X lithography setup. A femtosecond-pulsed laser beam gets focused in a liquid photoresin by an objective lens. Beam steering is performed by two galvanometric mirrors. Precise control over the laser power enables the variable voxel sizes during fabrication. Adapted from [106].

components [108, 109].

A simplified schematic of the Quantum X optical setup is shown in Figure 3.3. The power-controlled $\lambda = 780\,\text{nm}$ femtosecond-pulsed laser is laterally scanned by two galvanometric mirrors and eventually focused into the writing plane using an objective lens. For printing, the objective lens is directly dipped into the liquid photoresist. The voxel size is controlled by adjusting the laser power. For printing, the 2GL mode was used with typical parameters for hatching and slicing. For the DOE, a slicing distance of 1 µm and a hatching distance of 0.2 µm was used. For the MLA, a slicing distance of 1 µm and a hatching distance of 0.1 µm was used.

3.2.2 *Photoresist*

The diffractive optical element and the multi-lens array were both fabricated using the commercially available photoresist IP-S (Nanoscribe GmbH & Co. KG).

3.2.3 *Sample Preparation*

All micro-optical components were manufactured on 2-inch diameter fused-silica glass wafers. To increase adhesion, the substrate surfaces were activated in air plasma for 20 min. Afterwards, they were vapor-silanized in an evacuated exsiccator with an ambient pressure of 100 mbar for 2 h. The vapor-silanization takes place by additionally placing a Petri dish with a droplet of pure 3-(trimethoxysilyl)propyl methacrylate (Merck KGaA) next to the substrates in the exsiccator. Following this process, multiple substrates can be vapor-silanized in parallel.

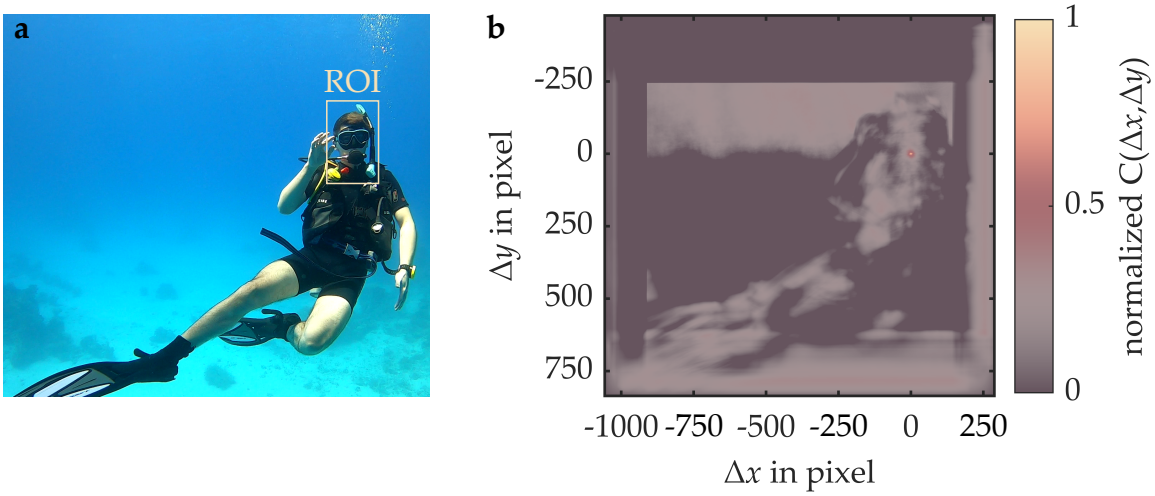

Figure 3.4: Concept of digital image cross-correlation analysis. a, Optical photograph of the author that serves as the base image for the analysis. To locate the author's head, a region of interest (ROI) is defined and depicted by the yellow rectangle. **b,** false-color plot of the computed normalized cross-correlation function $C(\Delta x, \Delta y)$. To retrieve the position of the kernel in the base image, the maximum of the normalized cross-correlation function $C(\Delta x = 0, \Delta y = 0)$ is located. For the analysis, the input image was converted to a grayscale image. Based on [110].

3.2.4 *Sample Development*

All micro-optical component samples were developed upside down by successively immersing them for 2×10 min in propylene glycol methyl ether acetate (PGMEA, $\geq$ 99 %, Carl Roth GmbH + Co. KG) and for 2×5 min in 2-propanol (UV/IR grade, Carl Roth GmbH + Co. KG). Afterwards, they were dried in a nitrogen gas stream.

3.2.5 *Sample Characterization*

To characterize the quality of the fabricated micro-optical components, their topography was retrieved by measuring with an optical spinning-disc confocal microscope (MarSurf CM explorer S/W, Mahr GmbH). Furthermore, the final versions of the diffractive optical element and the multi-lens array were imaged using a digital microscope (Smartzoom 5, Zeiss) and a scanning-electon microscope (Supra 55VP, Zeiss).

3.2.6 *Digital Image Cross-Correlation*

For assessing any imperfections in the surface topography of the fabricated DOEs and MLAs, the surface measurement needs to be overlayed with the initial design. To automate this process with high precision, digital image cross-correlation is used [111–113]. This technique was already exploited to detect and track local displacements in, e.g., mechanical metamaterials [45, 114–116] and can be applied to align measurement and design.

The digital images of the design $\mathrm{DES}(x, y)$ and measurement $\mathrm{MEA}(x, y)$ with coordinates $x = n_x p$ and $y = n_y p$ defined by the pixel size p and the integers n_x, n_y are used to calculate the potential displacement (u_x, u_y) by computing the 2D cross-correlation function

$$C(\Delta x, \Delta y) = \int_{\mathrm{ROI}} \mathrm{DES}(x, y)\mathrm{MEA}(x + \Delta x, y + \Delta y)\mathrm{d}x\mathrm{d}y. \tag{3.1}$$

For this analysis, a small part of the measured topography defined by a region of interest (ROI) or the whole measurement can be aligned. This decision depends on the quality and type of the surface. For periodic structures like the DOE, it makes sense to use the entire measured surface topography to avoid unwanted positive signals due to the recurring unit cells. For the measurement of a single lens of the MLA, it helps to only use a central part of the topography since the lens edges often suffer from manufacturing imperfections that could have a negative impact on the algorithm performance.

Figure 3.4 shows an example of this analysis. In Figure 3.4a, the entire image with a small part of it marked as the ROI is shown. Figure 3.4b shows the evaluated 2D cross-correlation function $C(\Delta x, \Delta y)$ in dependence of different shifts Δx and Δy. Reading out the shift for which the 2D cross-correlation function is maximized enables locating the correct lateral position. In general, the value of this maximum quantifies how similar both images are. Identical images will yield a value of normalized one, while, e.g., a slightly rotated image will lose its similarity and therefore yield a cross-correlation maximum of less than one. Comparing these maximum values of the 2D cross-correlations for varying scenarios therefore allows for finding, e.g., the correct rotation or lateral scale of the measurement, which can be subject to these errors. To perform this, the described routine is executed successively for different small rotations or lateral scales of the measurement. Afterwards, the rotation and scale yielding the largest maximum of the 2D cross-correlation function is chosen for further analysis described in subsection 5.3.2.

3.2.7 *Anti-Reflection Coatings*

To suppress reflection losses at the glass-air interfaces of the micro-optical component samples, a 120 nm thick layer of Al_2O_3 and a 140 nm thick layer of MgF_2 was evaporated on the backside of the DOE and both sides of the MLA sample. For this process, an e-vap CVS-6 device (MDC) was used with evaporation rates of 1.5 Å s^{-1} for Al_2O_3 and 5.0 Å s^{-1} for MgF_2. The intensity reflection losses decreased from 6.38 % (uncoated) to 3.46 % (one side coated) to 0.43 % (two sides coated).

3.3 Multi-Focus 3D Laser Printing of Large-Scale Microstructures

In this section, the methods applied for fabricating structures with next-generation multi-focus 3D laser printing described in chapter 7 are specified.

3.3.1 *Lift-off With a Sacrificial Layer*

To retrieve large numbers of 3D printed carrier particles without damage after the manufacturing step, sacrificial layers are used [117, 118]. These layers dissolve upon contact with, e.g., water, releasing anything that was attached to them. By using glass substrates with a thin sacrificial layer for fabrication, carrier particles can be easily detached from the substrate afterwards.

For the initial sacrificial layer mixture, 7 wt% polyvinyl alcohol (PVA, "Mowiol 4-88", Sigma-Aldrich) was dissolved in de-ionized water. The resulting mixture was then stirred on a hot plate at a temperature of 80 °C for 24 h. For using the solution, all PVA must be dissolved. To create the necessary thin PVA layer on the employed glass substrates, spin coating (KL-SCE-150, Quantum Design GmbH) was performed with a rotation frequency of 67 rps for 60 s. Afterwards, the sample was immediately baked on a hot plate at a temperature of 80 °C for 2 min, resulting in a sacrificial layer with a few 100 nm thickness [119, 120]. After the baking step, the samples can be conveniently stored for later use.

In the subsequent manufacturing step, the sensitive BBK-based photoresist described in chapter 4 was applied, the carrier particles 3D printed, and the structures developed using propylene glycol methyl ether acetate (PGMEA) and isopropyl alcohol (IPA). The development time in IPA was limited to prevent swelling of the sacrificial layer [119, 120]. Samples with structures and the sacrificial layer intact can now be stored and even shipped before detaching the microparticles.

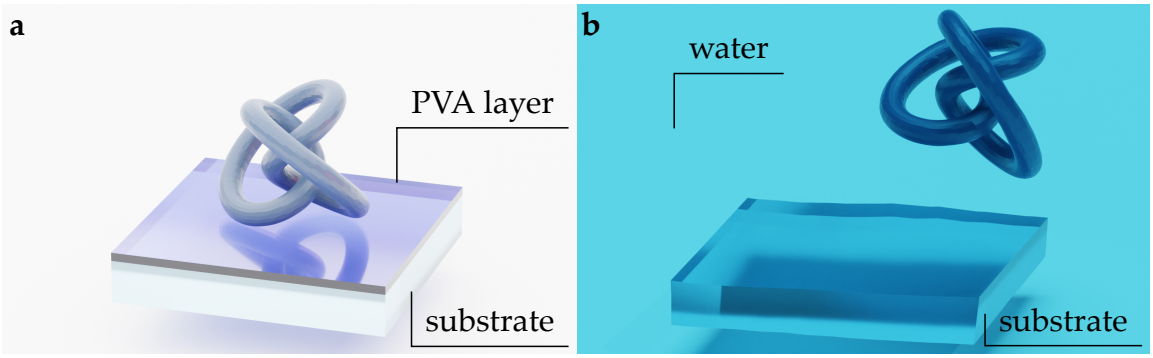

Figure 3.5: Schematic depiction of the lift-off process. a, a structure is 3D printed on a glass substrate with a thin layer of polyvinyl alcohol (PVA). The PVA layer usually measures a thickness of a few 100 nm. **b,** the sample is immersed in warm water, which dissolves the PVA layer and detaches the sample from the substrate. The free-swimming particle has to be filtered out in a subsequent step.

Eventually, the manufactured carrier particles are detached by immersing the substrate in de-ionized water at 40 °C temperature. Figure 3.5 visualizes this procedure using two schematic pictures. Figure 3.5a shows a glass substrate with an intact, thin sacrificial layer employing PVA on top. A rolling-knot carrier particle is printed on the sacrificial layer. Figure 3.5b shows the same scenario but immersed in warm de-ionized water. The sacrificial layer was dissolved and the carrier particle therefore detached. It now swims in water until it is filtered out in a later step. This method was applied for printing carrier particles for respiratory drug delivery and lightweight metamaterials with high compressive strength.

3.3.2 *Photoresist Composition*

All corresponding structures were printed using a resist comprising 0.5 wt% (2E,6E)-2,6-Bis (4-(dibutylamino)benzylidene)-4-methylcyclohexanone (BBK) (synthesized by Maximilian Bojanowski) in the monomer mixture IP-DIP NPI (Nanoscribe GmbH & Co. KG). The photoresist was stirred on a hot plate at 35 °C for 12 h.

3.3.3 *Sample Development*

All samples besides the chiral-roton metamaterial sample were developed by successively immersing them for 2×10 min in PGMEA (propylene glycol methyl ether acetate) and for 2×5 min in IPA (isopropanol). Afterwards, they were dried by placing them in a fume hood. The chiral-roton metamaterial sample was developed, too, by successively immersing it for 2×10 min in PGMEA (propylene

glycol methyl ether acetate) and for 2×5 min in IPA (isopropanol). Instead of placing it in a fume hood, however, it was supercritically dried in CO_2 (EM CPD300, Leica Microsystems) to preserve the delicate connection rods of the metamaterial unit cells.

Chapter 4

4 Development of Highly Sensitive Photoresists



Artistic illustration of highly sensitive photoresists.

Since the total available laser power is limited and the amount that can safely be sent through the microscope objective lens was almost reached in previous multi-focus 3D laser printing efforts, the number of foci that can be used for multi-focus printing was limited by photoresist sensitivity. To overcome this obstacle, this chapter presents the development of the currently most sensitive photoresist at high focus velocities. First, a photoresist-sensitivity figure-of-merit is introduced to quantitatively compare more than 80 different photoresists in the literature. Afterward, two promising photoinitiator candidates are selected for further optimization. Though using coinitiators to boost sensitivity turns out to be limited, a breakthrough in sensitivity is shown by synthesizing a new derivative of an already sensitive photoinitiator with a seven times higher solubility.

4.1 A Figure-of-Merit for the Photoresist Sensitivity

The increasing amount of laser power necessary for high-speed applications with high degrees of parallelization (outlined in section 2.3) can either be tackled by increasingly more powerful laser systems or more sensitive photoresists, which effectively allow for very low polymerization threshold powers. Since arbitrarily high amounts of laser power are not only expensive (and sometimes unavailable) but also quickly exceed the damage threshold of the used microscope objective lens in the optical setup, this chapter focuses on the development of sensitive photoresists to allow for even faster 3D laser printing. Even with laser oscillators offering $3-4\,\mathrm{W}$ laser power, the polymerization threshold power should be low enough to allow for next-generation multi-focus 3D laser printing, making the approach more scalable.

When talking about the sensitivity of a certain photoresist, it is important to understand that every process step from absorbing light by a photoinitiator to the formation of a densely cross-linked polymer network must be efficient on its own. Only improving one isolated aspect, e.g., the two-photon absorption cross-section of a certain photoinitiating molecule, does not necessarily lead to more sensitive photoresists. Many processes come into play after absorption. High fluorescence quantum yields, e.g., will quickly render efforts put into good absorption properties useless. Low photoinitiator solubility in the required monomer mixture on the other hand will yield insensitive photoresists even when using highly efficient photoinitiator molecules [38, 121].

When scanning the literature for sensitive photoresists, there are many claims of having developed highly sensitive photoinitiators for 3D laser printing. However, comparing these data is troublesome since the reported experimental results were obtained using vastly different parameters like different laser wavelengths λ_0, different focus velocities v or exposure times t_{exp}, different laser pulse durations t_{p}, different laser pulse repetition rates R_{p}, or different numerical apertures NA [38]. As derived in section 2.2, these values have a strong influence on the two-photon exposure dose and therefore will show different polymerization laser threshold powers P_{th} corresponding to different threshold doses D_{th}. Therefore, only comparing published polymerization threshold powers will doom the search of finding more sensitive photoresists.

To overcome this problem and establish a fair comparison, a dimensionless photoresist-sensitivity figure-of-merit that takes all of these experimental parameters into account will be derived. Afterwards, an overview of more than 80 different photoresists published in literature will be presented both with respect

to the actually published minimum polymerization threshold power and with respect to the calculated photoresist-sensitivity figure-of-merit.

4.1.1 Derivation

The two-photon exposure dose, which was already derived in section 2.2, serves as the basis for deriving the photoresist-sensitivity figure-of-merit:

$$D_{\mathrm{exp}} = s_2 t_{\mathrm{exp}} (R_{\mathrm{p}} t_{\mathrm{p}}) I^N. \tag{4.1}$$

The focus velocity can be used to calculate an effective exposure time $t_{\mathrm{exp}} = 2r/v$. Inserting the already derived expression for the intensity from Equation 2.9 yields [38]

$$D_{\mathrm{exp}} = s_2 \frac{2\lambda_0}{v\pi \mathrm{NA}} (R_{\mathrm{p}} t_{\mathrm{p}}) \left(\frac{P}{R_{\mathrm{p}} t_{\mathrm{p}}} \frac{(\pi \mathrm{NA})^2}{\pi \lambda_0^2} \right)^N. \tag{4.2}$$

Assuming ideal two-photon absorption and hence inserting $N = 2$, the solution of this equation for the two-photon photoresist sensitivity is [38]

$$s_2 = \text{const.} \frac{v \lambda_0^3 R_{\mathrm{p}} t_{\mathrm{p}}}{P_{\mathrm{th}}^2 \mathrm{NA}^3}. \tag{4.3}$$

Here, the term $D_{\mathrm{exp}}/2\pi = \text{const.}$ was inserted. Importantly, the polymerization threshold power P_{th} is used here instead of any arbitrary laser power. Now, the photoresist-sensitivity figure-of-merit FOM can be expressed by defining [38]

$$\mathrm{FOM} = \frac{s_2}{\tilde{s}_2}. \tag{4.4}$$

This equation makes use of a hypothetical reference two-photon photoresist sensitivity $\tilde{s}_2$ to both eliminate the unknown prefactor in Equation 4.3 and to allow for a dimensionless value. For the calculation of $\tilde{s}_2$, the following parameters are used: $\tilde{v} = 1\,\mathrm{m\,s^{-1}}$, $\tilde{P}_{\mathrm{th}} = 1\,\mathrm{W}$, $\tilde{\lambda}_0 = 1\,\mu\mathrm{m}$, $\tilde{R}_{\mathrm{p}} = 100\,\mathrm{MHz}$, $\tilde{t}_{\mathrm{p}} = 100\,\mathrm{fs}$, and $\tilde{\mathrm{NA}} = 1$ [38]. The final expression for the photoresist-sensitivity figure-of-merit FOM therefore is [38]:

$$\mathrm{FOM} = \frac{v \lambda_0^3 R_{\mathrm{p}} t_{\mathrm{p}}}{P_{\mathrm{th}}^2 \mathrm{NA}^3}. \tag{4.5}$$

In Equation 4.5, v should be inserted in units of $1\,\mathrm{m\,s^{-1}}$, P_{th} in units of $1\,\mathrm{W}$, λ_0^3 in units of $1\,\mu\mathrm{m}$, R_{p} in units of $100\,\mathrm{MHz}$, and t_{p} in units of $100\,\mathrm{fs}$ [38]. With this term for the photoresist-sensitivity figure-of-merit FOM, the sensitivity of different photoresist systems can now be compared even when their experimental results were obtained using different parameters. A large photoresist sensitivity will

yield a large FOM. However, the FOM is only useful when comparing different photoresists. A single FOM value therefore has no meaning [38]. Notably, the FOM does implicitly depend on the photoinitiator concentration n_{PI}. Using a lower concentration than possible might yield higher polymerization threshold powers but is not taken into account in Equation 4.5. However, since the target is achieving the highest overall sensitivity possible, it is highly advisable to dissolve as much photoinitiator into the monomer mixture as possible anyway.

Some publications reporting sensitive photoresists did not perform line scanning experiments using a certain focus velocity $v > 0$ but rather conducted point-exposure experiments with varying exposure times t_{exp} per voxel. For these data, the exposure time was translated into an effective focus velocity [38]

$$v_{\mathrm{eff}} = \frac{2\lambda_0}{\pi \mathrm{NA} t_{\mathrm{exp}}}. \tag{4.6}$$

The reported parameters have several uncertainties that directly translate into an uncertainty of the FOM. These uncertainties include [38]:

1. A Different effective laser pulse duration t_{p} than reported due to group-delay dispersion.
2. A Different effective laser power transmitted into the analyzed photoresist due to an over-illuminated microscope objective lens.
3. A Different effective laser power transmitted into the analyzed photoresist due to the limited transmittance of the microscope objective lens.
4. A Different effective numerical aperture due to an under-illuminated microscope objective lens.

If the laser power was measured in front of the microscope objective lens, an assumed $T = 70\,\%$ transmittance crudely accounts for vignetting (uncertainty 2) and transmittance (uncertainty 3) [38]. Other imperfections reduce the FOM to a lower value than otherwise possible.

4.1.2 Overview of Different Photoresist Systems

To give an overview over the many published results that were taken into account and show what was actually measured, Figure 4.1 plots the measured polymerization threshold power P_{th} against the focus velocity v of the performed experiment. The effective exposure time t_{exp} for the respective focus velocity is plotted in

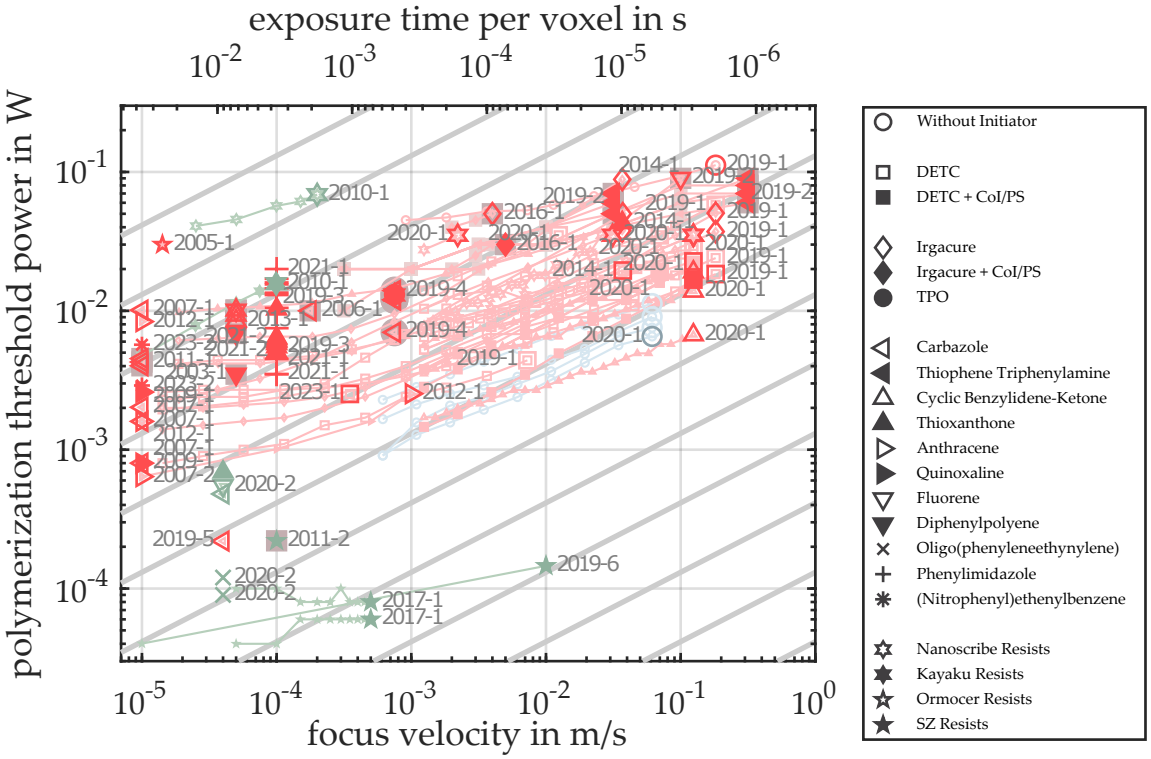

Figure 4.1: Overview of the polymerization threshold power for various multi-photon photoresists. The different values are plotted against the focus velocity or respectively the exposure time per voxel with a lateral voxel size of $a_{xy} = 364\,\text{nm}$, according to an exposure with a $\lambda = 800\,\text{nm}$ wavelength laser and an $\text{NA} = 1.4$. The data points were obtained using different wavelengths, which is indicated by the marker color. The marker shape indicates the corresponding chemical group, which is further specified in the legend. The parallel gray lines indicate the power scaling for ideal two-photon absorption. Some references did not specify the polymerization threshold power but only a power at which a structure could be printed. These data points are marked by a gray background. Multiple characterization experiments at different focus velocities are connected by a line. Here, only one data point of this data set is highlighted by a bright color. Data generated from experiments within this thesis are labeled as 2020-1.
References: 2003-1 [122], 2005-1 [123], 2006-1 [124], 2007-1 [125], 2007-2 [126], 2009-1 [127], 2010-1 [128], 2010-2 [129], 2011-1 [130], 2011-2 [42], 2012-1 [131], 2013-1 [132], 2014-1 [49], 2015-1 [133], 2016-1 [134], 2017-1 [135], 2019-1 [43], 2019-2 [136], 2019-3 [137], 2019-4 [138], 2019-5 [139], 2019-6 [32], 2020-1 [38], 2020-2 [121], 2021-1 [140], 2021-2 [141], 2023-1 [142], 2023-2 [143]. Adapted and updated from [38].

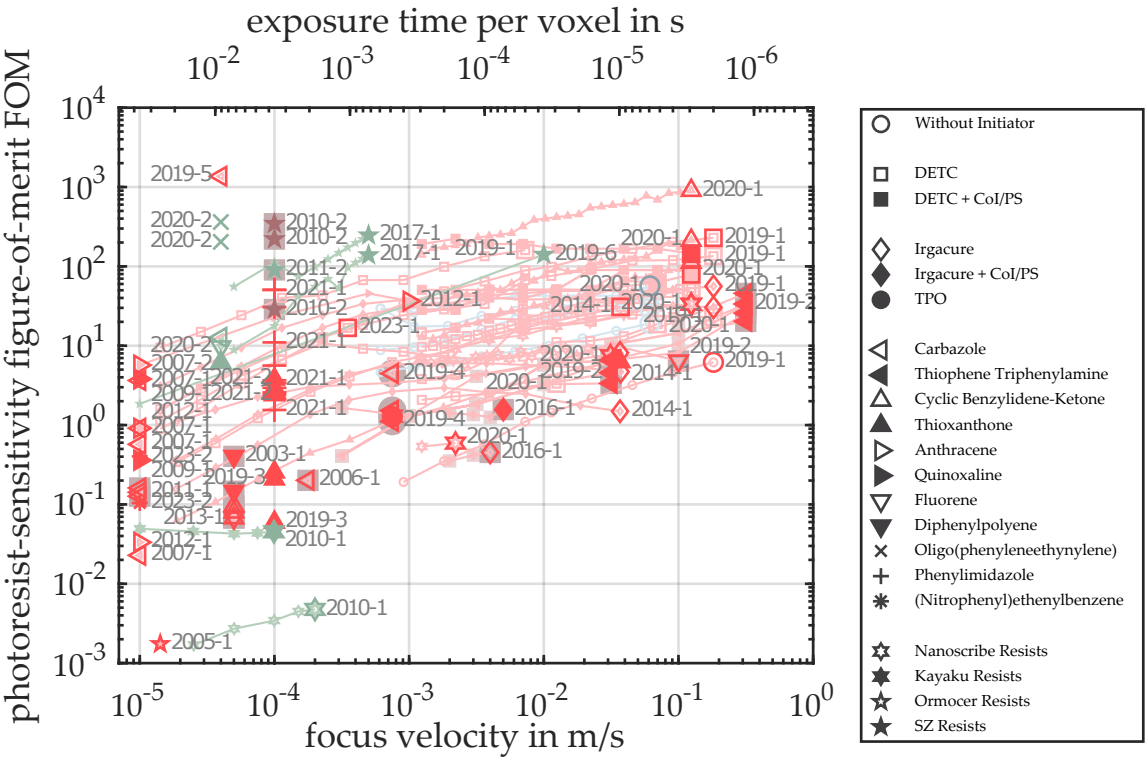

Figure 4.2: Overview of the photoresist-sensitivity figure-of-merit for various multi-photon photoresists. The different values are plotted against the focus velocity or respectively the exposure time per voxel with a lateral voxel size of $a_{xy} = 364\,\mathrm{nm}$, according to an exposure with a $\lambda = 800\,\mathrm{nm}$ wavelength laser and an NA $= 1.4$. The data points were obtained using different wavelengths, which is indicated by the marker color. The marker shape indicates the corresponding chemical group, which is further specified in the legend. Some references did not specify the polymerization threshold power but only a power at which a structure could be printed. These data points are marked by a gray background. Multiple characterization experiments at different focus velocities are connected by a line. Here, only one data point of this data set is highlighted by a bright color. Data generated from experiments within this thesis are labeled as 2020-1.
References: 2003-1 [122], 2005-1 [123], 2006-1 [124], 2007-1 [125], 2007-2 [126], 2009-1 [127], 2010-1 [128], 2010-2 [129], 2011-1 [130], 2011-2 [42], 2012-1 [131], 2013-1 [132], 2014-1 [49], 2015-1 [133], 2016-1 [134], 2017-1 [135], 2019-1 [43], 2019-2 [136], 2019-3 [137], 2019-4 [138], 2019-5 [139], 2019-6 [32], 2020-1 [38], 2020-2 [121], 2021-1 [140], 2021-2 [141], 2023-1 [142], 2023-2 [143]. Adapted and updated from [38].

the upper horizontal axis. The parallel gray lines indicate the development of the polymerization threshold power according to ideal two-photon absorption $P_{\text{th}} \propto \sqrt{v}$ [38].

Did a study not report the polymerization threshold power but only a power to 3D laser print a structure, a gray background was added to the data point [38]. In this case, the real polymerization threshold power could be lower or higher due to dose accumulation.

To allow for a more meaningful comparison, Figure 4.2 shows the same data as before but now displays the corresponding photoresist-sensitivity figure-of-merit FOM. This value is not dependent on the focus velocity v anymore, however, the data are still plotted against v to allow for easy comparison with Figure 4.1 [38].

The different photoresists were grouped in chemical categories that are encoded in the shape of the corresponding marker. To also encode the used wavelength, the markers show different colors. A dark red color indicates a wavelength $\lambda_0 \approx 1000\,\text{nm}$, red color indicates $\lambda_0 \approx 800\,\text{nm}$, green color indicates $\lambda_0 \approx 532\,\text{nm}$, and blue color indicates $\lambda_0 \approx 400\,\text{nm}$. The complete data contributing to Figure 4.1 and Figure 4.2 are compiled in Figure A.1, Figure A.2, and Figure A.3 in the appendix.

The most sensitive photoresists reside at the top of this overview graph. The five most sensitive groups of photoresists (which exceed FOM = 100) are presented in the following paragraphs.

7-Diethylamino-3-Thenoylcoumarin-Containing Photoresists

A widely used photoresist systems consists of the photoinitiator 7-diethylamino-3-thenoylcoumarin (DETC) shown in Figure 4.3a together with the monomer pentaerythritol triacrylate (PETA) [38, 43, 49]. The resist is able to exceed FOM = 200 and features many interesting properties with the most important one lying in its unusual nonlinearity exponent $N \approx 3$ [43], which is not consistent with ideal two-photon absorption. However, as discussed in section 2.3, this property is beneficial for high-speed applications due to the advantageous power scaling in comparison to $N = 2$. Due to this nonlinearity, the FOM increases with increasing focus velocity, making the resist system attractive for setups employing large focus velocities. In the following section 4.2, the interaction of DETC with coinitiators is studied to further enhance the already well-performing resist system.

SZ photoresists

SZ2080 is a monomer mixture that is used with many different photoinitiators and was able to yield sensitivities of FOM > 300 at focus velocities between $10\,\mu m\,s^{-1}$ and $1\,cm\,s^{-1}$ [32, 42, 129, 135]. It is commonly used together with low laser pulse repetition rates R_p and also shows an increase in the FOM with increasing focus velocity, which, again, is a beneficial property. However, there is no source showing this effect for large repetition rates and large focus velocities. Naturally, large repetition rates are vital with fast laser scanning to produce connected voxels. Using a laser pulse repetition rate $R_p = 200\,kHz$ at a focus velocity $v = 0.4\,m\,s^{-1}$ would lead to an adjacent voxel spacing of $2\,\mu m$. Such voxel spacings are not practical when using sub-µm voxel diameters.

Photoresists Containing Oligo(Phenyleneethynylene) Derivatives

The most sensitive photoresist of this class with an FOM exceeding FOM $= 300$ comprises a photoinitiator consisting of three-branched oligo(phenyleneethynylene) derivatives (Oct), the reactive dilutive monomer 1,10-decanediol diacrylate (DDA), and the monomer dipentaerythritol penta-/hexa-acrylate (DPPHA) [121]. These photoinitiators feature long alkyl groups to improve solubility in the monomer mixture [121]. The photoresist is able to fabricate structures with the usual lateral resolution, however, the promising results still need to be reproduced at large focus velocities.

OXE-Containing Photoresists

The resist system showing the largest photoresist-sensitivity figure-of-merit FOM $=$ 1300 comprises the photoinitiator (E)-10-(2-(acetoxyimino)butanoyl)-7-hexyl-4-methylpyrano[3,2-c]carbazol-2(7H)-one (OXE) with the monomer pentaerythritol triacrylate (PETA) [139]. The photoinitiator is based on carbazole and features a chevron-shaped structure, which is associated with an O-acyl-α-oxooxime function [38, 139]. The integrated $N-O$ bond is photocleavable and allows for triggering the necessary polymerization reaction [38, 139].

However, these results were only obtained at the small focus velocity $v = 40\,\mu m\,s^{-1}$ and the low numerical aperture NA $= 0.6$ [38, 139]. It is not clear if these results can be translated to large focus velocities. Furthermore, the achievable spatial resolution of the resist system is unclear, too. Since the photolysis of OXE is rather insensitive to oxygen, the resist could suffer from limited spatial resolution [38]. Oxygen is the main quenching molecule, reducing sensitivity but also enhancing spatial resolution [49]. In an experiment with a photoinitiator batch supplied by the authors of Ref. [139], their results could not be reproduced.

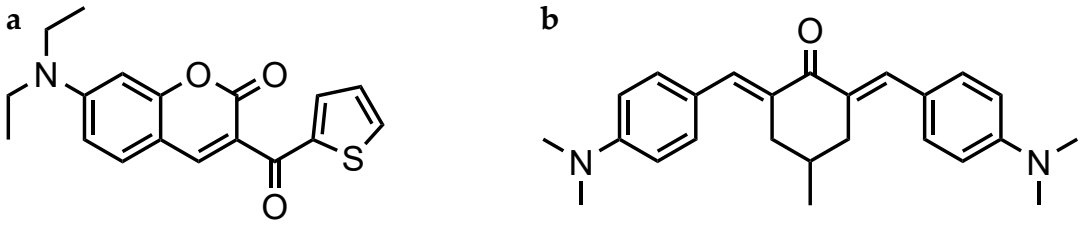

Figure 4.3: Structural formulas of **a,** 7-diethylamino-3-thenoylcoumarin (DETC) and **b,** (2E,6E)-2,6-Bis (4-(dimethylamino)benzylidene)-4-methylcyclohexanone (MBK). The benzylidene ketone-based photoinitiator can be synthesized in one step and was first published in Ref. [132].

Cyclic-Benzylidene-Ketone-Containing Photoresists

A photoresist system showing promising sensitivites FOM $>$ 200 at large focus velocities consists of the photoinitiator (2E,6E)-2,6-Bis (4-(dimethylamino)-benzylidene)-4-methylcyclohexanone (MBK) shown in Figure 4.3b with the monomer ethoxylated bisphenol A diacrylate (BPADA) [132]. The photoinitiator contains donor and acceptor groups that are located in a conjugated backbone and can be synthesized in only one step [132]. Similar to other discussed resists, it shows a nonlinearity exponent $N \approx 3$, making it attractive for high-speed applications due to the advantageous power scaling [38]. Its main downside is its very limited solubility in commonly used monomers like PETA. In the next two sections, enhancements of the highly promising DETC- and MBK-containing photoresists are discussed.

4.2 Enhancing DETC-Containing Photoresists

As already presented in subsection 4.1.2, photoresists containing 7-diethylamino-3-thenoylcoumarin (DETC) offer a high sensitivity and an advantageous nonlinearity exponent, making them highly suitable for high-speed applications like in this work. Therefore, this section focuses on further increasing the sensitivity of DETC-containing photoresists by adding coinitiators to enhance an already well-adapted photoinitiator. The used photoresists and characterization setup are further specified in subsection 3.1.1.

4.2.1 Properties of 7-Diethylamino-3-Thenoylcoumarin

DETC is commonly used as an efficient multi-photon photoinitiator [38, 43, 49] with its chemical structure shown in Figure 4.3a [144]. It . A polymerization threshold power experiment for a resist containing 0.5 wt% DETC in the monomer

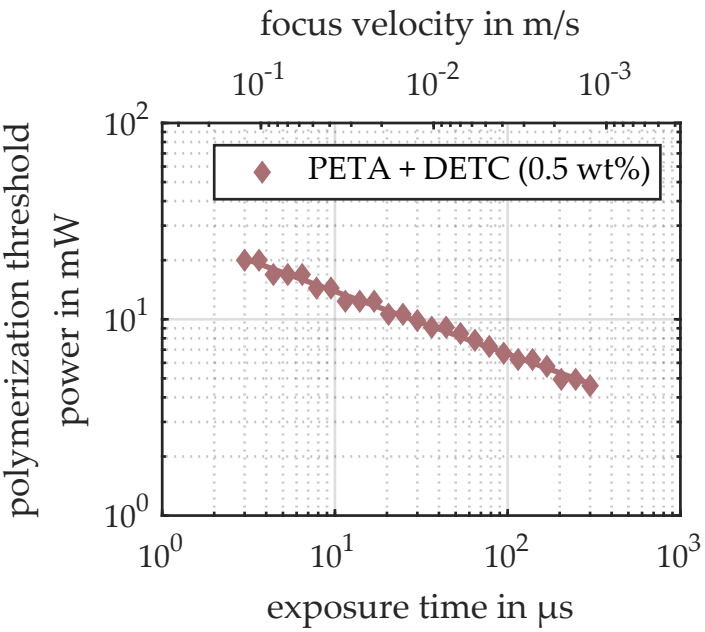

Figure 4.4: Polymerization threshold power for various exposure times of a 7-diethylamino-3-thenoylcoumarin (DETC) photoresist. The experiment was performed using a $\lambda = 820\,\mathrm{nm}$ wavelength laser with repetition rate $R_\mathrm{p} = 80\,\mathrm{MHz}$ and pulse duration $t_\mathrm{p} = 100\,\mathrm{fs}$ as well as a NA $= 1.4$ microscope objective lens. The effective focus velocity for these parameters is shown in the upper horizontal axis. The photoresist contained 0.5 wt% DETC in pentaerythritol triacrylate (PETA). The line fit function yields a nonlinearity exponent of $N \approx 3$.

PETA is shown in Figure 4.4. Besides its already low polymerization threshold power at low focus scanning speeds, the nonlinearity exponent $N \approx 3$ allows for beneficial power scaling in fast printing. Thus, for large focus velocities or low exposure times, respectively, the increase in the necessary polymerization threshold power is weaker than for photoinitiators making use of ideal two-photon absorption. As discussed in section 2.3, increasing the focus velocity by a factor of ten only requires $\sqrt[3]{10} \approx 2.15\times$ more laser power for $N = 3$ in comparison to $\sqrt[2]{10} \approx 3.16\times$ more laser power for $N = 2$.

Even though the photoinitiator is commonly used, the underlying quantum-chemical processes leading to cleavage upon light radiation and the subsequent photopolymerization are still not fully understood and subject to current research [49, 144–147].

4.2.2 Interaction With Additional Photoinitiators

One of the main drawbacks of DETC is its limited solubility in common monomers like PETA. Dissolving more than 0.5 wt% DETC is typically not possible. Therefore, one straight-forward approach to increase the photoresist's sensitivity might be to dissolve additional photoinitiators into the mixture. Figure 4.5 shows the polymerization threshold powers for a resist containing 0.5 wt% DETC and two

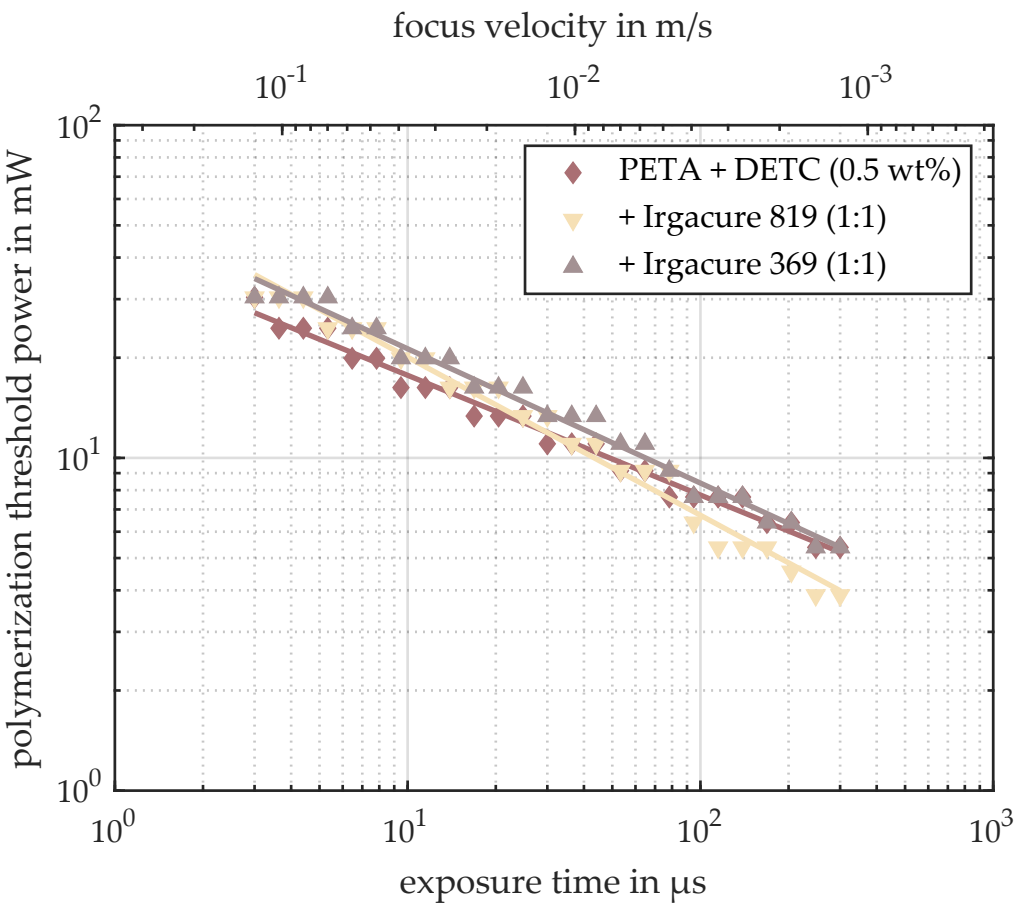

Figure 4.5: Polymerization threshold power for various exposure times of three 7-diethylamino-3-thenoylcoumarin (DETC) photoresists, two partly containing the additional photoinitiators Irgacure 819 and Irgacure 369. The experiment was performed using a $\lambda = 820\,\mathrm{nm}$ wavelength laser with repetition rate $R_\mathrm{p} = 80\,\mathrm{MHz}$ and pulse duration $t_\mathrm{p} = 100\,\mathrm{fs}$ as well as a NA $= 1.4$ microscope objective lens. The effective focus velocity for these parameters is shown in the upper horizontal axis. The basic photoresist contained 0.5 wt% DETC in pentaerythritol triacrylate (PETA). In the two additional photoresists, the additional photoinitiators were added in the same molecular ratio with respect to DETC.

resists additionally containing the photoinitiators Irgacure 819 and Irgacure 369 with a 1 : 1 molar ratio to DETC, respectively.

The polymerization threshold power does not show significant changes. Interestingly, the photoresist containing Irgacure 819 shows a change in slope of the linear fit applied to the experimental data, indicating a change in the effective nonlinearity exponent. This comes to no surprise since the used Irgacure photoinitiators are known to work according to ideal two-photon absorption and

hence featuring $N = 2$ [43]. At short exposure times (or high scanning speeds), the polymerization threshold of the purely DETC-containing photoresist is significantly lower than the threshold of photoresists additionally containing Irgacure photoinitiators, diminishing the effect of the second photoinitiator due to the change in effective nonlinearity. In Figure 4.5, the lowest polymerization threshold power at short exposure times is the pure DETC-containing photoresist. Therefore, this approach delivered no enhancement in photoresist sensitivity.

4.2.3 *Increasing the Photoresist Sensitivity With Coinitiators*

Another route to increase the sensitivity of photoresists is to add coinitiators. Two typical examples from this group are onium salts or amines which can increase the rates of polymerization and conversion [38, 148], potentially enhancing the performance of the dissolved photoinitiator [149]. Furthermore, thiols can increase the photoresists sensitivity as well [134].

Amines work in assistance to the photopolymerization by interacting with dissolved oxygen and forming a charge-transfer complex [38, 150]. This complex can convert into a hydroperoxide by consuming oxygen. After decomposition, this hydroperoxide can then generate further radicals [38, 151]. By consuming oxygen, the concentration of the main scavenging molecule is reduced, which attenuates radical inhibition [38] but could potentially worsen the achievable spatial resolution of 3D laser printed features. Onium salts take a more active coinitiating role. The onium salt diphenyliodonium hexafluorophosphate (DPIHFP) can absorb light and forms unstable diaryl iodine free radicals after a reduction by a formal electron transfer [38, 152].

Within this work, the tertiary amine triethylamine (TEA) and the secondary amine dibutylamine (DBA) were tested as amine coinitiators. While TEA did not show significant improvements, DBA as well as the onium salt DPIHFP alter the photoresists behavior noticeably in the measured polymerization threshold power plot shown in Figure 4.6. The polymerization threshold power of photoresists containing these coinitiators is lower in comparison to the pure DETC-containing photoresist, even at low exposure times or high focus velocities. However, the slope of the linear fit applied to the experimental data changes from $N \approx 3$ for the pristine photoresist to $N \approx 2$ for the photoresists with coinitiators. As discussed above, this behavior is potentially disadvantageous for high-speed applications like in this thesis, severely limiting the decrease in polymerization threshold power for high focus velocities. For low scan speeds, this effect might not lead to less sensitive photoresists.

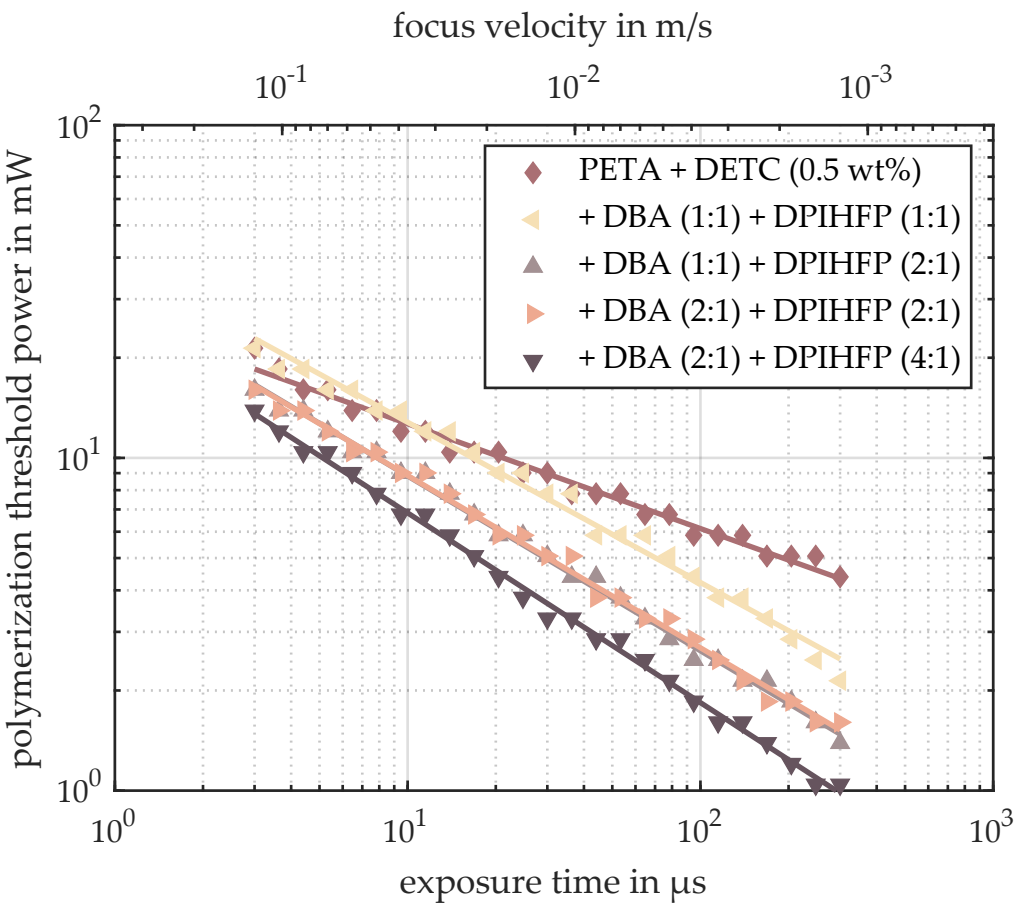

Figure 4.6: Polymerization threshold power for various exposure times of different 7-diethylamino-3-thenoylcoumarin (DETC) photoresists, partly containing coinitiators. The experiment was performed using a $\lambda = 820\,\mathrm{nm}$ wavelength laser with repetition rate $R_\mathrm{p} = 80\,\mathrm{MHz}$ and pulse duration $t_\mathrm{p} = 100\,\mathrm{fs}$ as well as a NA $= 1.4$ microscope objective lens. The effective focus velocity for these parameters is shown in the upper horizontal axis. The basic photoresist contained 0.5 wt% DETC in pentaerythritol triacrylate (PETA). In four additional photoresists, the coinitiators dibutylamine (DBA) and diphenyliodonium hexafluorophosphate (DPIHFP) were added in different molecular ratios with respect to DETC.

Adding thiols as additional ingredients showed promising enhancements in photoresist sensitivites in the past [134], but showed even poorer results for the DETC-containing photoresist than the coinitiators discussed here. The corresponding experimental results can be found in Figure A.4 in the appendix.

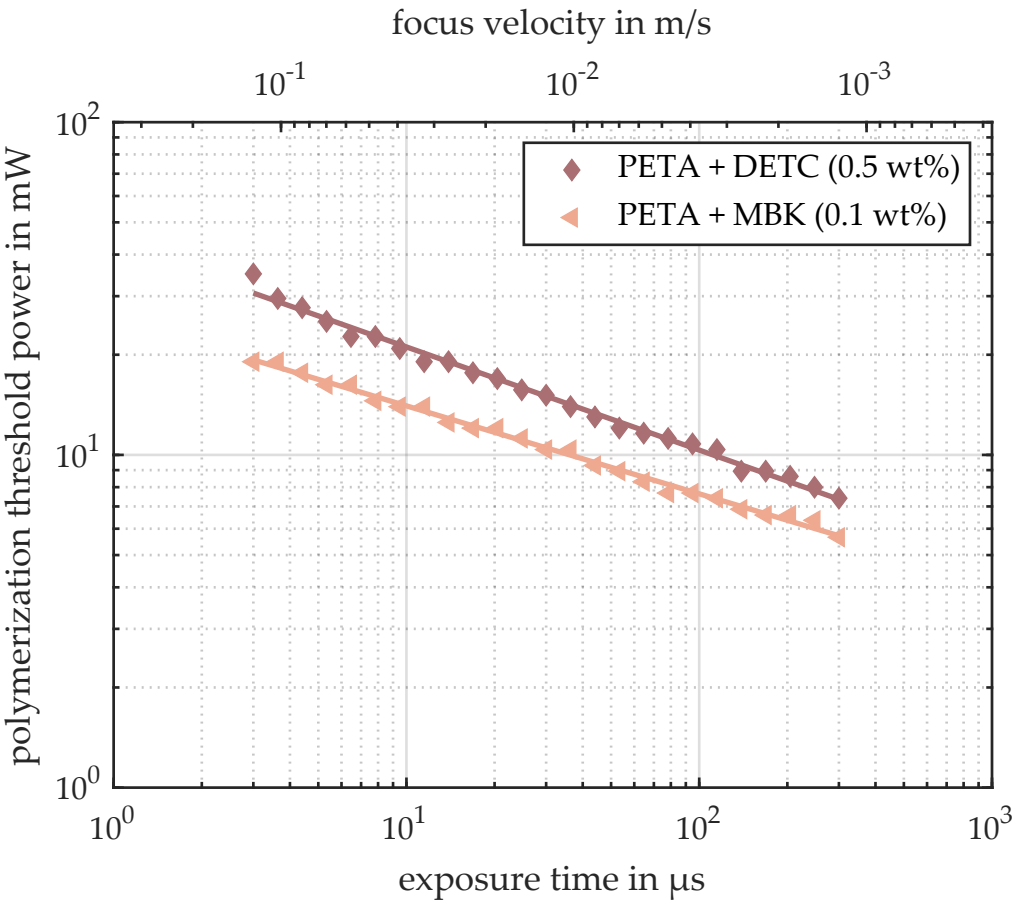

Figure 4.7: Polymerization threshold power for various exposure times of a 7-diethylamino-3-thenoylcoumarin (DETC) and a (2E,6E)-2,6-Bis (4-(dimethylamino)benzylidene)-4-methylcyclohexanone (MBK) photoresist. The experiment was performed using a $\lambda = 820\,\mathrm{nm}$ wavelength laser with repetition rate $R_\mathrm{p} = 80\,\mathrm{MHz}$ and pulse duration $t_\mathrm{p} = 100\,\mathrm{fs}$ as well as a NA $= 1.4$ microscope objective lens. The effective focus velocity for these parameters is shown in the upper horizontal axis. The photoresists contained the respective photoinitiator in pentaerythritol triacrylate (PETA). The line fit functions yield nonlinearity exponents of $N \approx 3$.

4.3 Development of a New Photoinitiator With Record-High Photoresist Sensitivity

Since significant sensitivity improvements of the already well-established DETC-containing photoresists by either additional photoinitiators or coinitiators was not achievable, the development of a new photoinitiator molecule is discussed in the following. The used and characterized photoresists as well as the characterization setup are further specified in subsection 3.1.1.

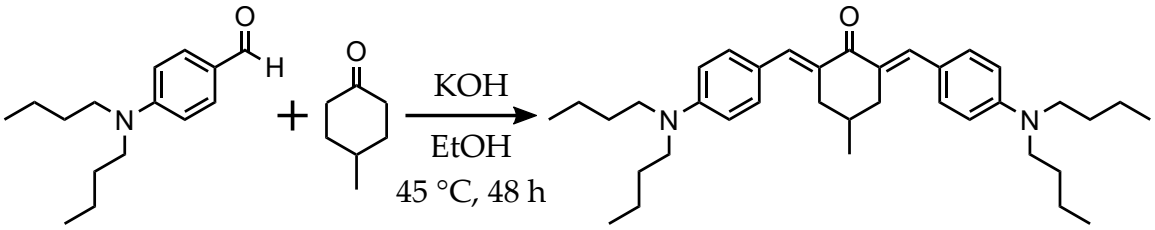

Figure 4.8: Synthesis procedure of (2E,6E)-2,6-Bis (4-(dibutylamino)benzylidene)-4-methylcyclohexanone (BBK). The reagents 4-dibutylaminobenzaldehyde and 4-Methylcyclohexanone react together with potassium hydroxide (KOH) and ethanol (EtOH). Adapted from [38].

4.3.1 Experiments on a Sensitive Benzylidene-Ketone Photoinitiator

In the photoresist overview presented in subsection 4.1.2, photoresists containing the photoinitiator (2E,6E)-2,6-Bis (4-(dimethylamino)benzylidene)-4-methylcyclohexanone (MBK) shown in Figure 4.3b show a high sensitivity next to DETC. However, its solubility is even worse than for DETC. Dissolving as little as 0.1 wt% in the common monomer PETA is already very close to the solubility limit.

However, the sensitivity of the corresponding photoresist is higher than for DETC-containing photoresists with the higher photoinitiator concentration 0.5 wt% as shown in Figure 4.7. Next to the low polymerization threshold power despite the low concentration, the nonlinearity exponent $N \approx 3$ stands out. This unusual behavior is shared with the other highly efficient photoinitiator DETC and rarely reported for any photoresist, making MBK a promising candidate for highly-sensitive photoresists. Therefore, a newly developed derivative of this molecule is presented in the next section that improves the main drawback of limited solubility.

4.3.2 Synthesis of a New Benzylidene-Ketone Derivative With High Solubility

By exchanging the methyl side groups with longer alkyl chains, in this case butyl groups, the derivative (2E,6E)-2,6-Bis (4-(dibutylamino)benzylidene)-4-methylcyclohexanone (BBK) is obtained [38]. The synthetic procedure is shown in Figure 4.8 and was adapted from a published reaction [153] in a collaboration with Prof. Eva Blasco. The synthesis was taken over by the chemists Martina Nardi and Maximilian Bojanowski. Longer side arms improve the solubility in the common monomer PETA by a factor of seven, making it possible to prepare photoresists with a higher concentration of this class of photoinitiators. The exceptional absorption

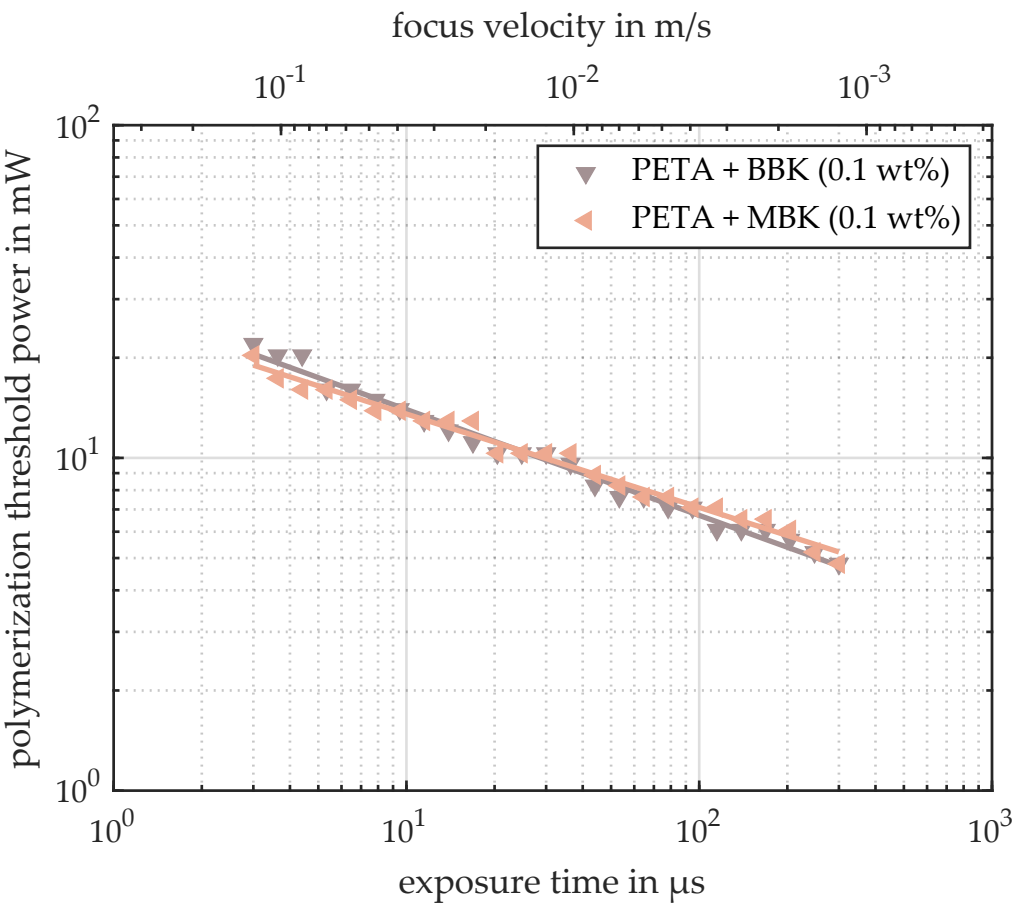

Figure 4.9: Polymerization threshold power for various exposure times of a (2E,6E)-2,6-Bis (4-(dimethylamino)benzylidene)-4-methylcyclohexanone (MBK) and a (2E,6E)-2,6-Bis (4-(dibutylamino)benzylidene)-4-methylcyclohexanone (BBK) photoresist. The experiment was performed using a $\lambda = 820\,\mathrm{nm}$ wavelength laser with repetition rate $R_\mathrm{p} = 80\,\mathrm{MHz}$ and pulse duration $t_\mathrm{p} = 100\,\mathrm{fs}$ as well as a $\mathrm{NA} = 1.4$ microscope objective lens. The effective focus velocity for these parameters is shown in the upper horizontal axis. The photoresists contained the respective photoinitiator in pentaerythritol triacrylate (PETA). The line fit functions yield non-linearity exponents of $N \approx 3$.

properties of the molecule should not be strongly affected since the expectation was that they are mainly determined by the center of the molecular structure.

4.3.3 *Properties of the New Photoinitiator Derivative*

To verify that the optical properties of the parent compound MBK are indeed unaltered, the polymerization threshold power of two photoresists, one containing 0.1 wt% MBK in PETA and one containing 0.1 wt% BBK in PETA, is determined.

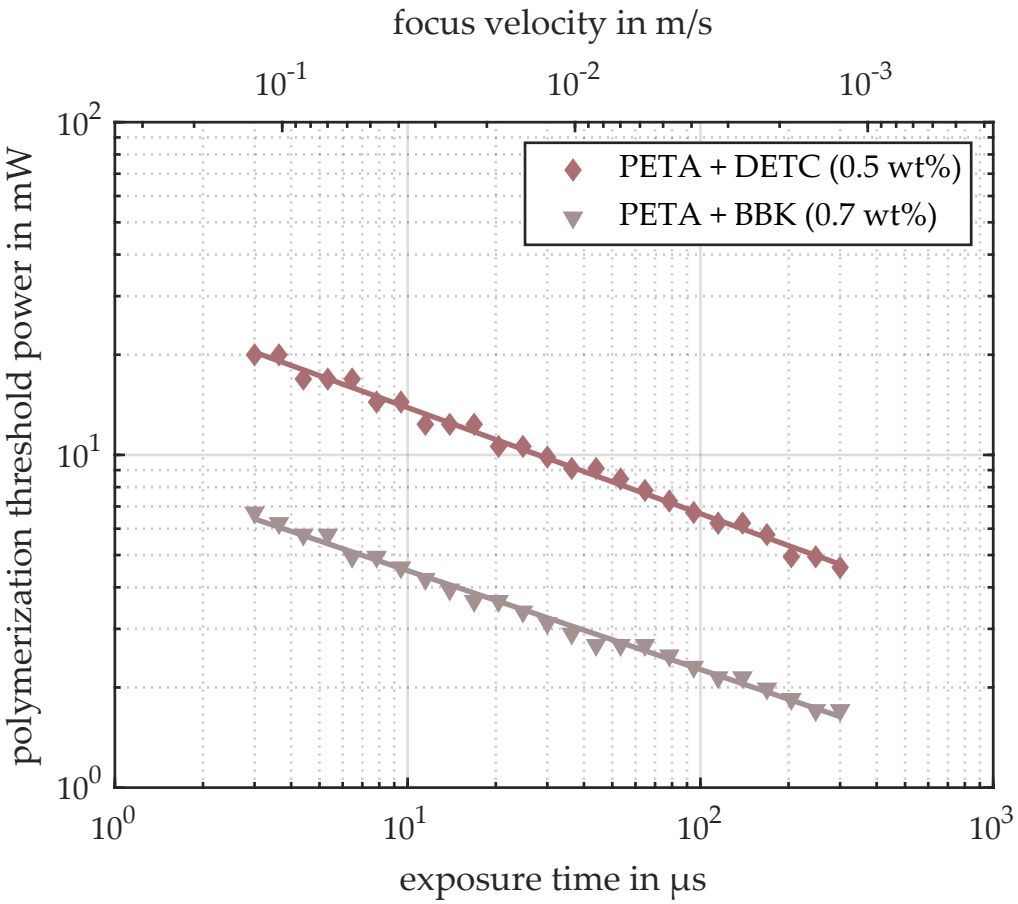

Figure 4.10: Polymerization threshold power for various exposure times of a 7-diethylamino-3-thenoylcoumarin (DETC) and a (2E,6E)-2,6-Bis (4-(dibutylamino)benzylidene)-4-methylcyclohexanone (BBK) photoresist. The experiment was performed using a $\lambda = 820\,\mathrm{nm}$ wavelength laser with repetition rate $R_\mathrm{p} = 80\,\mathrm{MHz}$ and pulse duration $t_\mathrm{p} = 100\,\mathrm{fs}$ as well as a NA $= 1.4$ microscope objective lens. The effective focus velocity for these parameters is shown in the upper horizontal axis. The photoresists contained the respective photoinitiator in pentaerythritol triacrylate (PETA). The line fit functions yield nonlinearity exponents of $N \approx 3$.

The results are shown in Figure 4.9. The polymerization threshold power does not show a significant difference. Furthermore, the slope of the linear fit applied to the experimental data does not change much either, indicating that the beneficial effective nonlinearity of the process remained $N \approx 3$ as well.

To study the capabilities of the new photoinitiator BBK, it was dissolved in PETA with the now enabled increased concentration of 0.7 wt% and its polymerization threshold power compared to a highly-sensitive DETC-containing photoresist

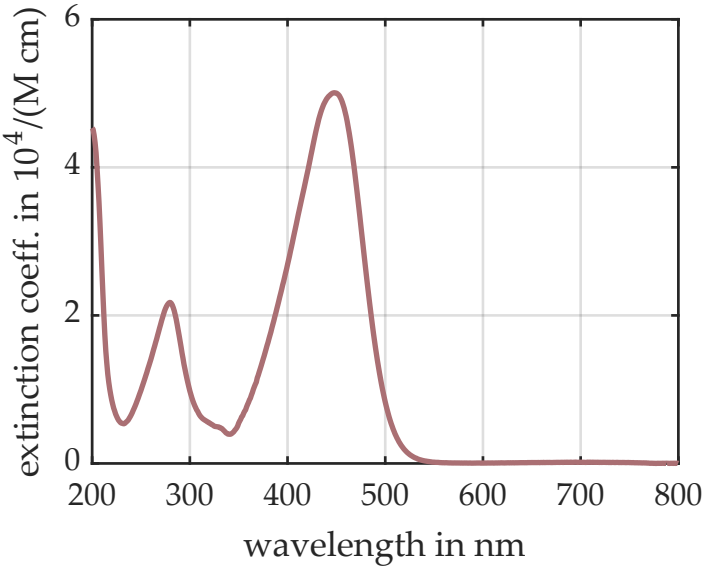

Figure 4.11: Absorption spectrum of (2E,6E)-2,6-Bis (4-(dibutylamino)benzylidene)-4-methylcyclohexanone (BBK). The spectrum was recorded using a Cary 300 Bio UV-VIS spectrophotometer (Agilent Technologies). The photoinitiator was dissolved in spectroscopy-grade acetonitrile and analyzed in a quartz cuvette with 10 mm path length at ambient temperature.

with 0.5 wt% DETC in PETA. Figure 4.10 shows the experimental results. The BBK-containing photoresist shows a roughly three times lower polymerization threshold power in comparison to the DETC-containing photoresist. Importantly, this enhancement is shown for all experimentally studied exposure times due to the similar nonlinearity exponent $N \approx 3$. The photoresist-sensitivity figure-of-merit calculates to FOM = 905 and represents the most sensitive photoresist reported at high focus velocities [38].

To further characterize the optical properties of the new molecule, the absorption spectrum was measured. The resulting extinction coefficients are plotted in Figure 4.11. These can be of interest in processes utilizing ideal 1-photon absorption. Since many applications of rapid 3D laser printing lie in the field of biology [154–158], the potential cell cytotoxicity of BBK for NIH 3T3 cells was studied. For this experiment, a checkerboard-like structure consisting of $160 \times 160\,\mu m^2$ square blocks was 3D laser printed with a photoresist containing 0.5 wt% BBK in the non-cytotoxic monomer mixture IP-Dip NPI. The latter mainly consists of the monomer PETA but has a refractive index that matches the refractive index of the used microscope objective lens, enabling fabrication in the dip-in configuration. In order to not work at the solubility limit of BBK, the concentration 0.5 wt% was chosen. The printed structures were coated with fibronectin prior to culturing and immunocytochemical staining of NIH 3T3 cells. All cell-biological work and imaging was conducted by Kai Weißenbruch. Figure 4.12 shows three regions of the sample after cell culturing, captured with a confocal laser-scanning-microscope. The blue squares indicate the printed polymer structure, which can

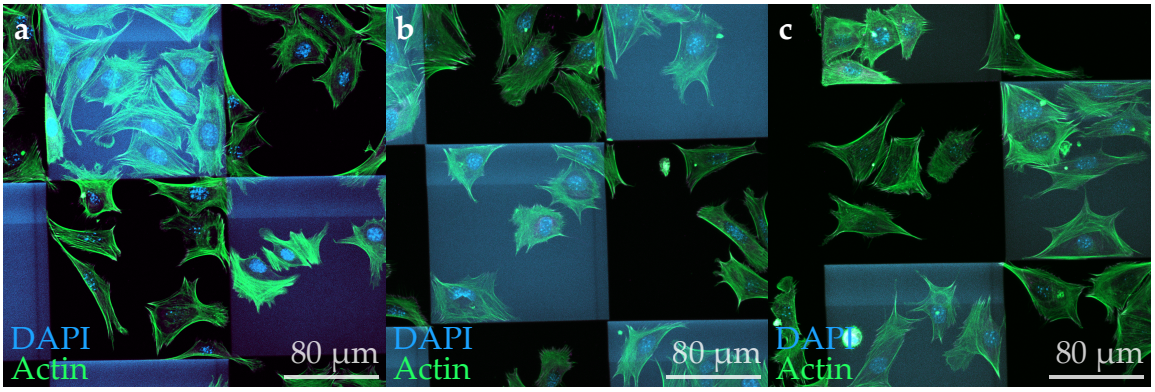

Figure 4.12: Confocal laser-scanning-microscope (LSM) images showing square blocks in a checkerboard-like arrangement printed using a BBK photoresist. The photoresist contained 0.5 wt% BBK in the non-cytotoxic monomer mixture IP-Dip NPI. The printed structures were coated with fibronectin prior to culturing and immunocytochemical staining of NIH 3T3 cells. The actin cytoskeleton is depicted in green, whereas the DAPI-stained nuclei are depicted in blue. **a-c,** images of three different regions of the sample. Cells cultivate on both the polymer and the glass substrate. Cells adhered normally to glass as well as the printed structure and show no morphological irregularities, indicating that no apparent cytotoxic effect was introduced by the use of BBK.

be discriminated from the glass substrate by the autofluorescence in the blue channel. Notably, cells spread on both surfaces, BBK polymer and glass substrate and show no disturbance of the actin cytoskeleton (green) or deformation of the cell nuclei (blue). This indicates that the used concentration of BBK does not introduce apparent cytotoxic properties to the photoresists.

4.4 Discussion and Conclusion

In this chapter, the first step in enabling yet faster multi-focus 3D laser printing was presented. To identify suitable candidates and allow for a fair comparison of many published photoresist mixtures, a photoresist-sensitivity figure-of-merit was defined. Using this value, over 80 different reported photoresists were compared and highly sensitive formulations discussed. This work was the foundation to find a more sensitive photoresist that allows fast printing with more laser foci in parallel.

Afterwards, photoresists containing two promising photoinitiators revealed by this overview were studied and further enhanced. In the case of 7-diethylamino-3-thenoylcoumarin (DETC), the interaction with further ingredients to the formulation was studied. Combining different photoinitiators with varying sensitivity

was shown to yield no significant improvement to the sensitivity, while the combination with amines and onium salts as coinitiators enhanced sensitivity but only for slow scan speeds.

The second promising photoinitiator, MBK, was studied and its sensitivity compared to DETC. Furthermore, its main drawback in limited solubility was successfully diminished by synthesizing the new derivative BBK with improved solubility. This achievement alone allows for three times more laser foci in multi-focus 3D laser printing by just exchanging the DETC-containing photoresist used in the previous version [33] with the newly developed BBK-containing photoresist. Finally, the absorption spectrum of BBK was presented and its non-cytotoxicity studied in an early experiment, indicating that the newly acquired BBK-containing photoresist can also be used for biological applications.

The enhancement in photoresist sensivitiy achieved with the results presented in this chapter are not only vital for developing the next generation of multi-focus 3D laser printing, they also serve the 3D laser printing community in general. Highly sensitive photoresists are desirable. Consequently, BBK was used in several projects [64, 159] since its first publication within the respective publication [38].

The next chapter will change disciplines and address different issues in conventional optical beam splitting and eventually resolves the second challenge that hindered the development of the next generation of multi-focus 3D laser printing. All advancements presented in this and the next chapter will eventually converge in the optical setup presented in chapter 6.

Chapter 5

5 Fabrication of Micro-Optical Components for Beam Splitting

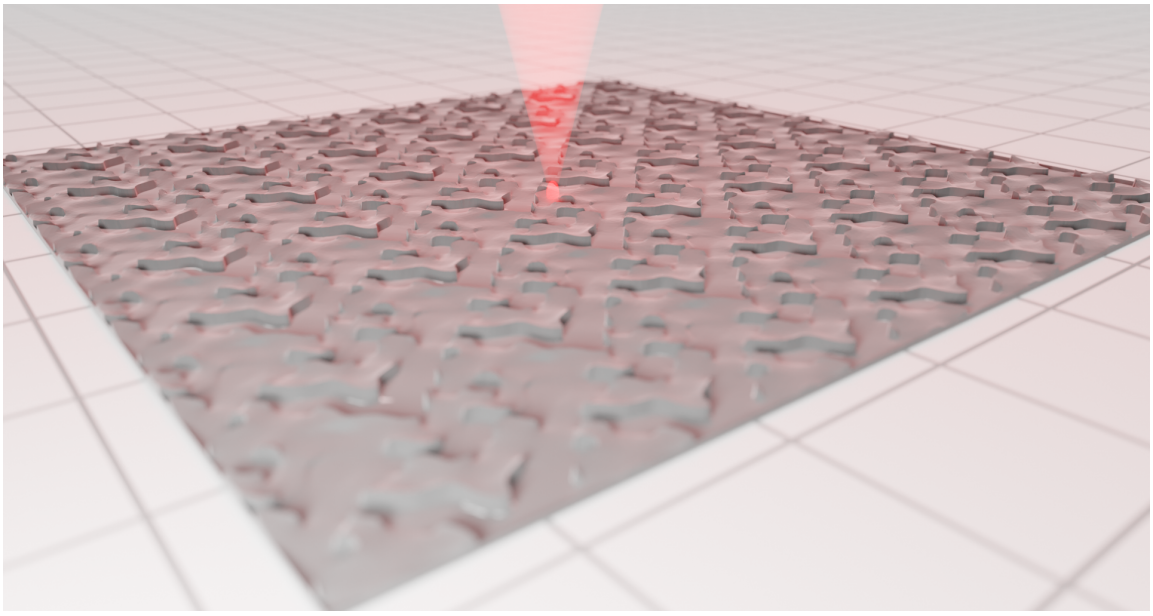

Artistic render of the manufacturing of a diffractive optical element.

In this chapter, I will resolve the second limitation on enhancing multi-focus 3D laser printing further and present the beam-splitting method used in this thesis. To start, I will assess the advantages and disadvantages of various beam-splitting approaches, followed by introducing a hybrid diffractive-refractive beam-splitting technique that overcomes numerous disadvantages. Furthermore, I will introduce the design of the necessary micro-optical components. To explain the need for producing high-quality micro-optical components, I will explore the impact of different fabrication imperfections on the focus array and outline an iterative workflow for achieving optimal manufacturing results.

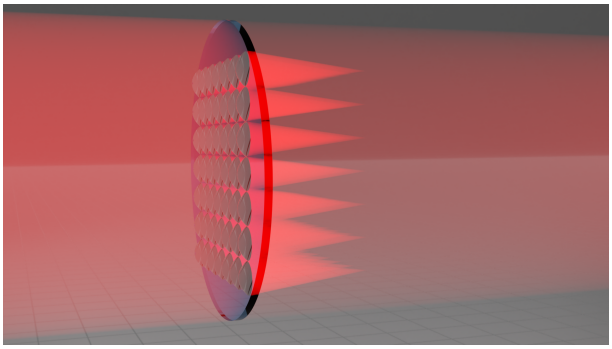

Figure 5.1: Rendering of refractive beam-splitting by a multi-lens array. The device focuses a fraction of an incident red Gaussian laser beam into an array of 7×7 foci. Assuming closely-packed spherical lenses, half of the incoming laser power is transmitted without contributing to the focus array and therefore lost. Adapted from [58].

5.1 Beam-Splitting Approaches for Multi-Focus 3D Laser Printing

To achieve the highest possible total voxel printing rate, it is recommended to first scan a single focus as fast as possible [38, 160] as outlined in section 2.3. If singe-voxel scanning reaches a maximum due to the underlying beam-scanning technology, one solution to further increase throughput is parallelization. In multi-focus 3D laser printing, the parallelization approach uses multiple laser foci instead of just one for manufacturing. This requires the division of the incident laser beam into multiple laser beamlets to create the necessary focus array. Beam-splitting can be accomplished using various refractive and diffractive methods [161]. In the following paragraphs, the advantages and disadvantages of both approaches are discussed and a novel hybrid refractive-diffractive beam-splitting approach that overcomes many of the limitations of both refractive and diffractive methods is presented. This innovative approach was first proposed by Vincent Hahn [56].

5.1.1 *Refractive Beam Splitting*

Refractive beam splitting utilizes an array of lenses to individually focus a fraction of an incident beam into an array of foci [20], as illustrated in Figure 5.1. This is a straight-forward way to introduce the necessary focus array, which will then be further imaged into the printing plane for multi-focus 3D laser printing. Nonetheless, this approach has a number of disadvantages.

First, when illuminating the lens array with a Gaussian beam, the intensity across the array is not homogeneous. This leads an undesirable power variation among the different foci. Severely overilluminating the lens array would help to enhance the homogeneity but at the cost of losing laser power in an already power-limited application. Alternatively, one could use additional optics to generate a flat-top

profile for the illumination of the lens array [162, 163], however, by adding more surfaces with finite reflections, these optics will introduce further losses, too.

Second, even when illuminating the lens array homogeneously, 50 % of the incident laser power is lost when using spherical lenses due to the closest packing in a rectangular array. For power-limited applications like multi-focus printing, this power-inefficient approach limits the maximum number of foci that can be used to sufficiently polymerize the photoresist. One could use square-shaped lenses but these will lead to asymmetric point-spread functions (PSFs) and decrease the effective numerical aperture of the microscope objective lens used to create the focus array in the writing plane by underilluminating it in certain locations.

5.1.2 *Diffractive Beam Splitting*

In diffractive beam-splitting approaches, the incident laser beam is divided by locally changing its phase using an optical element to introduce the desired diffraction pattern [21, 27, 31]. In subsection 2.3.2, various parallelization approaches are discussed and the diffractive optical element (DOE) [33, 34] selected as the most promising one for this work because of its high power efficiency.

The phase profile introduced to the planar wavefront of the laser beam is calculated such that the resulting intensity pattern in the diffraction plane yields, e.g., an array of $7 \times 7 = 49$ diffraction orders of equal intensity. To maximize the amount of laser power diffracted in the desired diffraction orders, i.e. to maximize the diffraction efficiency, high lateral resolution and phase precision of the optical device is needed [73].

Angular Dispersion

Due to their diffractive nature, DOEs introduce issues when using non-monochromatic beams like femtosecond-pulsed laser beams, which are needed for multi-photon absorption. With the spatial period or grating constant of the DOE g, the first-order diffraction angle α for each wavelength λ is given by

$$\sin(\alpha) = \frac{\lambda}{g}. \tag{5.1}$$

This characteristic is illustrated in Figure 5.2 where a broadband light source is split into two diffraction orders of the DOE. Each wavelength contributing to the broadband light is diffracted with a slightly different diffraction angle α, which is

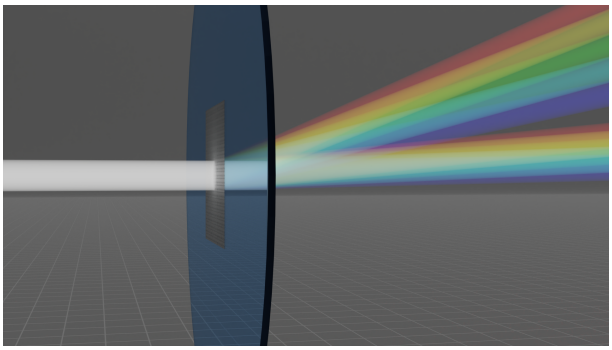

Figure 5.2: Rendering of diffractive beam-splitting by a diffractive optical element. An incident broadband laser beam gets diffracted into two diffraction orders. The generated beamlets can later be focused to create a focus array for printing. The wavelengths contributing to the incident light get fanned out by the wavelength-dependent diffraction angle. Adapted from [58].

referred to as angular dispersion [164]. For instance, when using a femtosecond-pulsed laser beam with a pulse duration $\tau = 140\,\mathrm{fs}$ and sech^2-shaped pulses, the finite bandwidth $\Delta\lambda$ can be calculated to $\Delta\lambda = 4.7\,\mathrm{nm}$. The severity of the angular dispersion introduced by the DOE when illuminated with such a laser beam can then be calculated to

$$\Delta\alpha = \alpha_1 - \alpha_2 \approx \frac{(\lambda_1 - \lambda_2)}{g} = \frac{\Delta\lambda}{g}. \tag{5.2}$$

Eventually focusing the generated beamlets suffering from angular dispersion into an array foci will lead to broadened point-spread functions (PSFs) due to closely but not perfectly overlapping foci of different wavelengths. This effect becomes worse with increasing angular dispersion, which depends on the grating constant and hence the central diffraction angle like described in Equation 5.2. Larger diffraction angles will lead to larger lateral focus displacements in the writing field. For a given lateral focus displacement d_{focus} of a given focus in the focus array generated by a lens with focal length f, the width of this spread-out PSF Δd can be calculated to

$$\frac{\Delta d}{d_{\mathrm{focus}}} = \frac{f\Delta\alpha}{f\lambda/g} = \frac{\Delta\lambda}{\lambda}. \tag{5.3}$$

The broadening of the PSF Δd therefore depends on the spectral bandwidth $\Delta\lambda$ of the chosen laser source and the focus displacement d_{focus}. Choosing a small bandwidth laser together with a small focus spacing will therefore minimize the PSF broadening. However, for multi-photon absorption, a certain pulse duration τ is needed to achieve the necessary pulse peak intensity, which is connected to the spectral bandwidth $\Delta\lambda$. Furthermore, the lateral focus displacement d_{focus} dictates the distance between neighbouring foci of the focus array. When this focus array is used for printing, it is scanned through the writing plane by an additional scan unit. Therefore, all foci print identical structures since the focus array is scanned as a whole. That means that the maximum size of individual structures one of these foci can produce is dictated by the lateral focus displacement d_{focus}. Thus, this quantity should not be chosen to be too small.

DOE Design Impacts

The lateral focus displacement d_{focus} in Equation 5.3 is ultimately determined by the DOE design. Taking the design into account is possible by introducing the quantity M, which describes the lateral focus displacement d_{focus} by the voxel diameter d_{FWHM}. Achieving large lateral focus displacements, i.e. large focus-to-focus distances, while keeping the lateral voxel size constant is therefore possible by employing DOE designs with large quantities M. Inserting these quantities further reveals that M can also be expressed by the number of DOE grating periods g in the objective lens pupil diameter D [165, 166]:

$$M = \frac{d_{\text{focus}}}{d_{\text{FWHM}}} = \frac{f\lambda/g}{0.567\lambda/NA} = 0.88\frac{D}{g}. \tag{5.4}$$

The PSF broadening Δd with respect to the lateral voxel size d_{FWHM} can now be expressed with the DOE design quantity M:

$$\frac{\Delta d}{d_{\text{FWHM}}} = \frac{\Delta\lambda}{\lambda}M. \tag{5.5}$$

A simple example with parameters typically used for multi-photon 3D laser printing employing a lateral focus displacement $d_{\text{focus}} = 60\,\mu\text{m}$ and a spectral bandwidth $\Delta\lambda = 4.7\,\text{nm}$ of a $\lambda = 790\,\text{nm}$ center wavelength femtosecond-pulsed laser beam shows that already the nearest neighbours of the center focus have a PSF broadening of

$$\frac{\Delta d}{d_{\text{FWHM}}} = 178\,\%. \tag{5.6}$$

This change in focal spot size is severe for the power-limited application of multi-focus 3D laser printing. In the previous chapter, a sensitive photoinitiator was developed to still achieve sufficient cross-linking even with low laser powers for the individual foci. Decreasing the peak intensity further by a factor of $1.78^2 = 3.17$ by broadening the PSF will lead to a $(3.17)^2 = 10.0$-fold decrease in two-photon absorption probability. Even when employing sensitive photoresists, the available laser power of typically used laser systems will not be sufficient to allow for multi-focus 3D laser printing with a large number of foci. Furthermore, with increasing diffraction angles, the DOE also lowers the effective numerical aperture of the microscope objective lens due to the spatial chirp at the back of it.

In the past, this wavelength-dependent effect was compensated for by inserting highly-dispersive Keplerian telescopes in the optical setup [33, 164]. However, these telescopes come with two major disadvantages that would constrain multi-focus 3D laser printing with many foci further. First, the available field of view (FOV) would be severely limited. Small FOVs were acceptable when employing

a small number of foci in parallel. However, utilizing, e.g., $7 \times 7 = 49$ laser foci with a small FOV forces small focus-to-focus distances to not clip the focus array. Decreasing the desired focus-to-focus distance $d_{\text{focus}} = 60\,\mu\text{m}$ further would consequently limit the maximum lateral size of an individual 3D structure one focus could print, which is undesirable.

Second, these kinds of telescopes usually add a large amount of group-delay dispersion into the setup. Laser pulses suffering from the resulting group-velocity dispersion have an increased pulse duration and thus a decreased peak intensity, which limits already power-limited applications like multi-focus 3D laser printing. This stretch in pulse duration can be prevented by additionally adding a unit compensating for group-velocity dispersion into the optical setup [33, 167, 168]. However, these units introduce more reflective losses in laser power and make the optical setup more and more complex.

5.1.3 Hybrid Diffractive-Refractive Beam Splitting

As outlined in the previous section, refractive and diffractive beam splitting are accompanied by many disadvantages that prevent multi-focus 3D laser printing to reach the next level. However, these problems can be overcome by combining both micro-optical elements to a hybrid diffractive-refractive beam-splitting approach [56]. The concept is depicted in Figure 5.3. An incident femtosecond-pulsed laser beam is split by a DOE. This time, the DOE is designed to have very small M values to minimize angular dispersion and the PSF broadening connected to it. Consequently, small M values lead to small focus-to-focus distances well below the desired value $d_{\text{focus}} = 60\,\mu\text{m}$ like described in the previous section. However, by individually focusing each beamlet introduced by the DOE with the lenses of an MLA, the focus spacing can be increased to the targeted value d_{focus}. Since each beamlet is precisely relayed on the corresponding MLA lens, the power-limiting disadvantages of the MLA are overcome, too.

In this work, a DOE design with $M = 3$ was used together with an MLA lens design that complements the rest of the rest of the optical setup. The design consideration of both micro-optical components will be discussed in detail in the following section of this chapter.

Together with the parameters of the employed laser system $\Delta\lambda = 4.7\,\text{nm}$ and $\lambda = 790\,\text{nm}$, the PSF distortion of the hybrid approach presented can be estimated to

$$\frac{\Delta d}{d_{\text{FWHM}}} = 1.78\,\%. \tag{5.7}$$

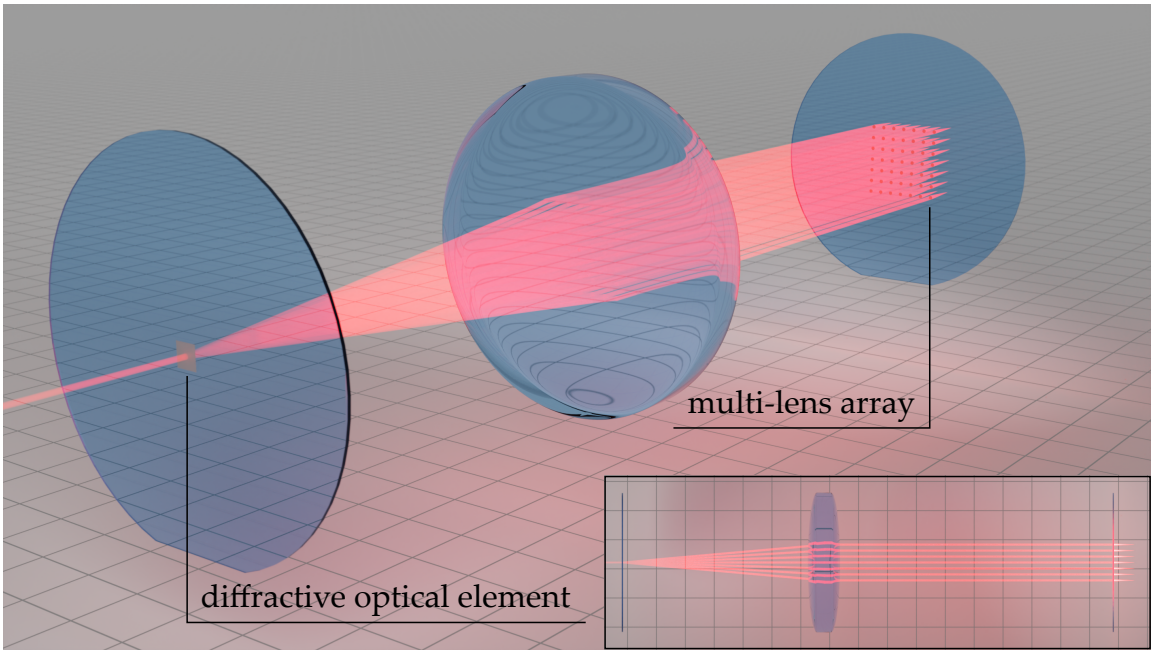

Figure 5.3: Rendering of hybrid diffractive-refractive beam-splitting by a diffractive optical element (DOE) and a multi-lens array (MLA). The incident red Gaussian laser beam gets diffracted into $7 \times 7 = 49$ individual beamlets by a DOE with low diffraction orders. A macroscopic lens guides them onto their respective lenses of the MLA consisting $7 \times 7 = 49$ individual mini-lenses that focus these beamlets and create the focus array that will later be used for 3D laser printing. The inset on the lower right shows a top view of the arrangement. Adapted from [58].

By combining the DOE and MLA, the PSF distortion can thus be decreased by two orders of magnitude. Therefore, this technique will be employed in the next-generation multi-focus 3D laser printing setup described in this thesis and allows for a large number of foci in a large FOV. In the next section, the design of both micro-optical elements is discussed.

5.2 Component Design for Hybrid Diffractive-Refractive Beam Splitting

In the last section, I have discussed the advantages and disadvantages of refractive and diffractive beam splitting and presented the hybrid approach of both methods that will be employed in this thesis. In this section, I will focus on the calculations of the designs of both micro-optical elements that match this approach.

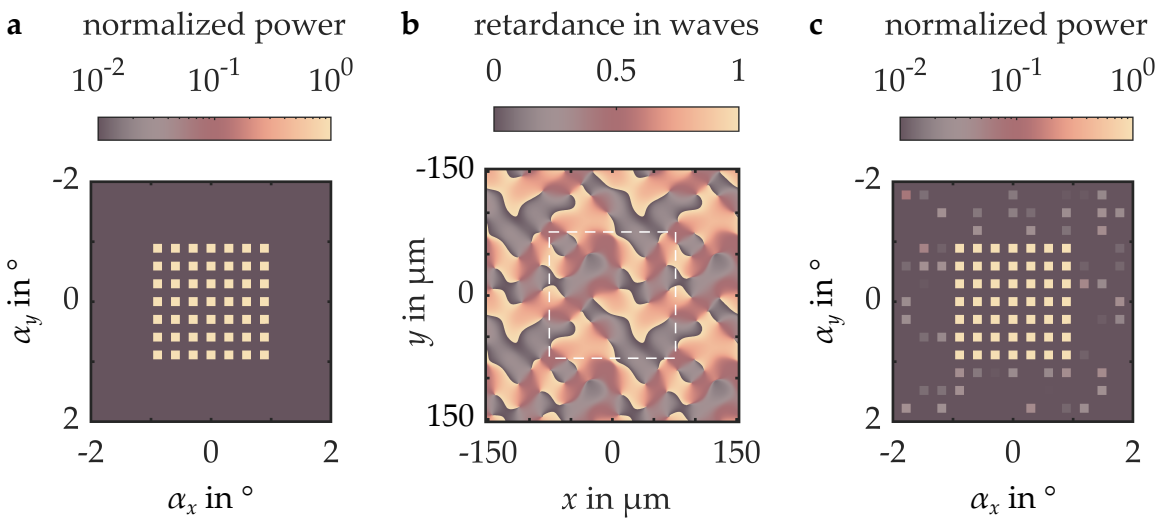

Figure 5.4: Design of the diffractive optical element (DOE). a, normalized target power distribution in a false-color diagram defined by an array of $7 \times 7 = 49$ diffraction orders with a homogeneous power distribution. **b,** DOE design. The white dashed line highlights a single unit cell. **c,** computed far-field diffraction pattern of the DOE design shown in **b** assuming an incident uniform illumination with wavelength $\lambda = 790\,\text{nm}$. The logarithmic color scale reveals weak higher orders. The power diffracted in the desired orders versus the incident power, hence, the diffraction efficiency, calculates to 92.3 %. Based on [56].

5.2.1 *Diffractive Optical Elements With Low Diffraction Orders*

The phase profile design of the diffractive optical element (DOE) was computed by an iterative Fourier transform algorithm first introduced by Gerchberg and Saxton [169]. In the beginning, the algorithm assumes a random phase together with a uniform amplitude as an initial guess and calculates its diffraction pattern by Fourier transformation. The amplitude of this first diffraction pattern is usually far from the target amplitude. By replacing the obtained amplitude by the target amplitude, a new term consisting of the computed phase of the diffraction pattern and the target amplitude then gets propagated back into the DOE plane by inverse Fourier transformation. After this operation, the amplitude is replaced by the uniform amplitude to conclude the first iteration of the algorithm with a very similar term in comparison to the initial guess. The amplitude is still uniform, however, the phase has slightly changed in contrast to the random initial guess. By repeating this cycle, the phase profile will slowly approach a solution that yields a diffraction pattern close to the desired target diffraction pattern.

In this application of hybrid diffractive-refractive beam splitting, a diffraction pattern consisting of $7 \times 7 = 49$ diffraction orders of equal power is desired.

Figure 5.4a shows the target power distribution. For illustration purposes, a DOE design parameter $M = 2$ was chosen here to separate the individual diffraction orders. The computed DOE phase profile to approximate this target power distribution is shown in Figure 5.4b. Here, a single unit cell is highlighted by a white dashed line. Its lateral size defines the largest grating constant in the DOE structure and will therefore set the distance between the center focus and its four neighbors. Note that even though this particular design is used throughout this thesis, there are many other phase profiles that will yield an equally well approximated intensity profile. Figure 5.4c shows the computed far-field diffraction pattern of the DOE design presented in Figure 5.4b by assuming uniform illumination. Each DOE design solution to this proposed problem will feature weak higher orders that are revealed by the logarithmic color scale. However, the diffraction efficiency, which is the power diffracted in the desired diffraction orders versus the incident power, calculates to 92.3 %, which is satisfyingly high. Loosing too much power by limited diffraction efficiencies would otherwise lead to voxels with low intensities that might not be able to overcome the polymerization threshold.

Since the DOE will not be used with a uniform illumination in the actual optical setup but rather with a Gaussian beam, it is not sufficient to only simulate its performance with a uniform illumination when deciding on its design properties, especially when dealing with low diffraction orders or DOE design parameters M. To decide on the DOE design parameter M, i.e. the focus spacing before the multi-lens array (MLA), the far-field diffraction pattern of the DOE design presented in Figure 5.4 was simulated for different values M. For this simulation, a Gaussian beam with a beam diameter $d_{1/e^2} = 571.3\,\mu m$ and wavelength $\lambda = 790\,nm$ that fits to the beam parameters of the actual optical setup was chosen. While keeping the beam size constant, the DOE design quantity M was varied by changing the lateral size of the DOE unit cell. The resulting far-field diffraction patterns are presented in Figure 5.5.

Low DOE design quantities $M \approx 1$ lead to undesired interference effects among the individual foci due to their laterally overlapping tails of the electric fields. Figure 5.5a demonstrates this effect by showing a perturbed far-field intensity profile with foci of unequal intensity and size, depending whether they interfere constructively or destructively with their neighbors. A subsequent MLA will not erase this effect since the tails of neighboring Gaussian foci will be focused as well and lead to an inhomogeneous focus array. This perturbation already decreases tremendously when increasing the DOE design parameter to $M \approx 2$ as depicted in Figure 5.5b. The increased separation of the individual foci reduces the discussed lateral overlap and allows for a more homogeneous diffraction pattern. Higher values M will also lead to higher diffraction angles, which is why the individual

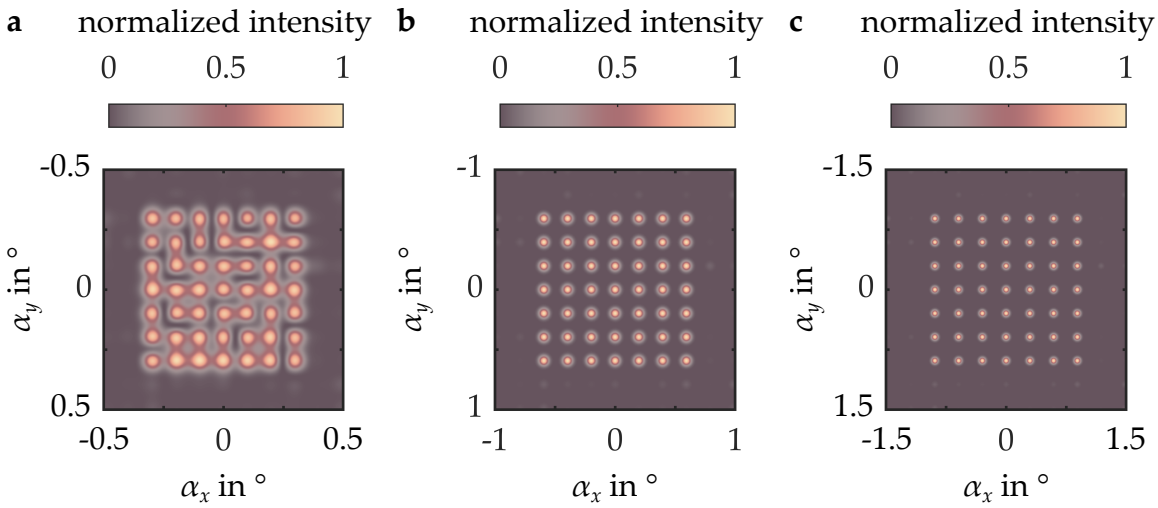

Figure 5.5: Computed far-field diffraction patterns for diffractive optical elements (DOEs) with varying DOE design quantities M**.** For the simulation, a Gaussian beam with beam diameter $d_{1/e^2} = 571.3\,\mu m$ and wavelength $\lambda = 790\,nm$ was chosen. The DOE design quantity M was varied by changing the lateral size of the DOE unit cell shown in Figure 5.4b. **a,** far-field diffraction pattern for a DOE unit cell side length $l_{UC} = 458.3\,\mu m$ yielding $M \approx 1$. The lateral tails of the individual Gaussian foci overlap and interfere, impairing the diffraction pattern. **b,** far-field diffraction pattern for a DOE unit cell side length $l_{UC} = 305.5\,\mu m$ yielding $M \approx 2$. The foci are further separated, reducing the overlap and yielding a more homogeneous diffraction pattern. Note that the foci feature a similar diameter as in **a** but appear smaller due to the larger plot range. **c,** far-field diffraction pattern for a DOE unit cell side length $l_{UC} = 152.8\,\mu m$ yielding $M \approx 3$. The foci are well separated and show a homogeneous distribution of the incident power.

diffraction orders appear smaller than in Figure 5.5a due to the larger lateral angle range covered. To minimize the overlap between neighboring foci further, the far-field diffraction pattern employing $M \approx 3$ is shown in Figure 5.5c. The individual foci are well separated and allow for a homogeneous focus array.

Like previously discussed, the DOE design parameter M should be kept low to minimize broadening of the point-spread function (PSF) due to angular dispersion. The PSF broadening for the discussed DOE designs calculate to:

$$\frac{\Delta d_{M\approx1}}{d_{FWHM}} = 0.59\,\%, \tag{5.8}$$

$$\frac{\Delta d_{M\approx2}}{d_{FWHM}} = 1.19\,\%, \tag{5.9}$$

$$\frac{\Delta d_{M\approx3}}{d_{FWHM}} = 1.78\,\%. \tag{5.10}$$

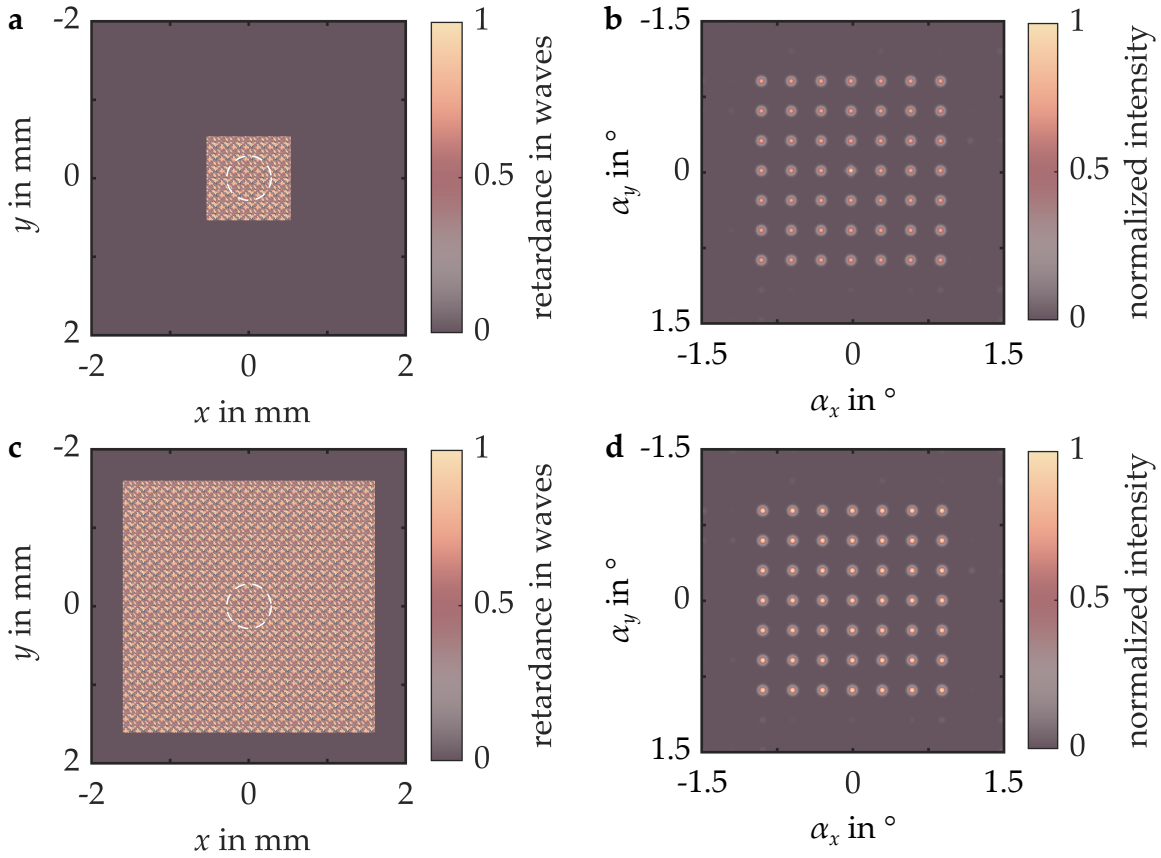

Figure 5.6: Computed far-field diffraction patterns for diffractive optical elements (DOEs) with different lateral sizes. For the simulation, a Gaussian beam with beam diameter $d_{1/e^2} = 571.3\,\mu m$ and wavelength $\lambda = 790\,nm$ was chosen. The lateral DOE size was varied by changing the number of DOE unit cells with side length $l_{UC} = 152.8\,\mu m$ shown in Figure 5.4b. **a,** DOE design featuring $7 \times 7 = 49$ unit cells resulting in a DOE side length of 1.1 mm. The beam diameter d_{1/e^2} of the laser illuminating the DOE is indicated by the white dashed line. **b,** resulting far-field diffraction pattern. Incident laser radiation beyond the DOE contributes to the zeroth order, increasing its intensity and therefore impairing the diffraction pattern. **c,** DOE design featuring $21 \times 21 = 441$ unit cells resulting in a DOE side length of 3.2 mm. The beam diameter d_{1/e^2} of the laser illuminating the DOE is indicated by the white dashed line. **d,** resulting far-field diffraction pattern. The incident laser radiation beyond the DOE is so small that its contribution to the zeroth order is negligible.

Even though the PSF broadening differences among these designs is minuscule, the consequences of Gaussian-beam interferences is severe. To highly minimize this effect while only sacrificing very little PSF broadening, a DOE design featuring $M \approx 3$ was used throughout this thesis.

With the phase profile design of the DOE and the size of one DOE unit cell, i.e. the value M, defined, the last open design parameter is the number of DOE unit cells, i.e. the lateral size of the complete DOE. Until now, all simulations assumed that the fraction of the incident illumination that does not transmit the DOE is zero. To elevate these computations closer to reality, Figure 5.6 shows two DOEs along with their calculated far-field diffraction patterns. The design and size of the DOE unit cell $l_{\mathrm{UC}} = 152.8\,\mu\mathrm{m}$ is equal for both instances but the number of unit cells building up the micro-optical device is different. Figure 5.6a shows a DOE featuring $7 \times 7 = 49$ individual unit cells contributing to a DOE size of $1.1 \times 1.1\,\mathrm{mm}^2$ whereas Figure 5.6c shows a DOE $21 \times 21 = 441$ individual unit cells contributing to a DOE size of $3.2 \times 3.2\,\mathrm{mm}^2$. In both instances, the beam diameter $d_{1/\mathrm{e}^2} = 571.3\,\mu\mathrm{m}$ of the $\lambda = 790\,\mathrm{nm}$ incident Gaussian beam fits inside the DOE. Nevertheless, the far-field diffraction patterns of both micro-optical devices differ. For the small DOE, the fraction of the Gaussian beam not being transmitted through the DOE is non-negligible and contributes to the strength of the zeroth order like shown in Figure 5.6b, leading to an inhomogeneous diffraction pattern. In Figure 5.6d, the far-field diffraction pattern appears homogeneous due to the fraction of the Gaussian beam leaking beyond the DOE being negligibly small and the perturbing contribution to the zeroth order therefore being minuscule. For this reason, the large DOE configuration shown in Figure 5.6c and Figure 5.6d is used.

For the manufacturing of the DOE, the phase retardance topography is finally converted to a height topography depending on the difference of refractive index of the polymer building up the DOE [170] to the refractive index of air $\Delta n = n_{\mathrm{IP-S}} - n_{\mathrm{air}} = 1.507 - 1 = 0.507$ and the employed wavelength $\lambda = 790\,\mathrm{nm}$ assuming the thin-element approximation [171]

$$h_{\mathrm{DOE}} = \frac{\Delta\phi_{\mathrm{DOE}}}{2\pi}\frac{\lambda}{\Delta n}. \tag{5.11}$$

To summarize, the final parameters for the fabrication of the diffractive optical element consist of a unit cell size of $152.8 \times 152.8\,\mu\mathrm{m}^2$ and $21 \times 21 = 441$ unit cells in lateral direction contributing to a total DOE size of $3.2 \times 3.2\,\mathrm{mm}^2$.

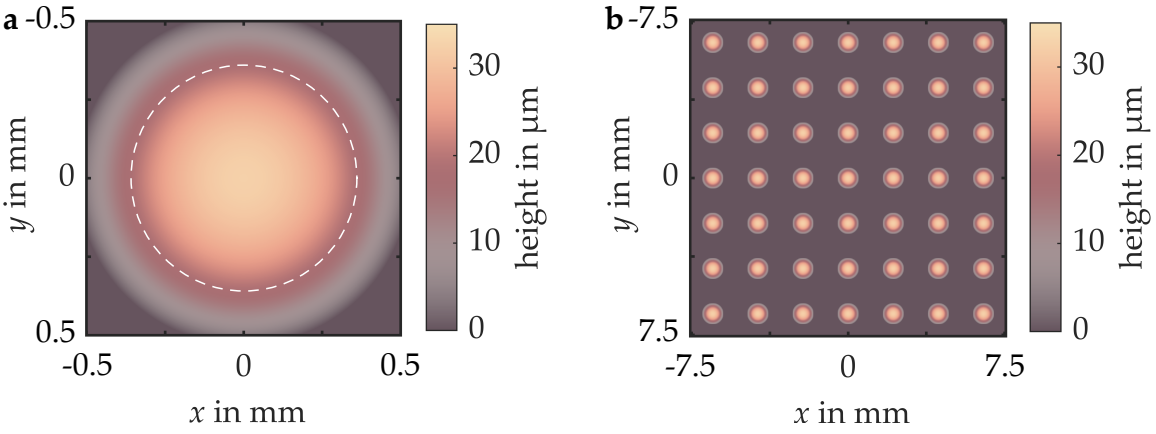

Figure 5.7: Design of the multi-lens array (MLA). a, false-color diagram showing the height profile of a single lens design of the MLA. The design features a lateral size of $l_{\text{lens}} = 1\,\text{mm}$ with the beam diameter of the incident Gaussian beam $d_{1/e^2} = 720\,\mu\text{m}$ indicated by a white dashed line. The radius of curvature $R = 4.64\,\text{mm}$ and conic constant $K = 17.50$ lead to a total lens height of SAG $= 32.6\,\mu\text{m}$. **b,** Total MLA featuring $7 \times 7 = 49$ individual lenses that have a center distance of 2.2 mm, which will later translate into a focus center distance of 60 µm in the writing plane.

5.2.2 *A Matching Aspheric Multi-Lens Array*

The design of the MLA was computed by ray-tracing calculations in the optical design software Zemax OpticStudio. Since the fabrication of the lens array allows for freedom of design, very little boundary conditions have to be set for the computation. The design mostly depends on the remaining optical setup and shall translate the beam diameter at the MLA $d_{1/e^2} = 720\,\mu\text{m}$ to the conjugate entrance pupil diameter of the microscope objective lens $D = 11.55\,\text{mm}$ that will be used for final focusing into the writing plane. The freedom in design allows for the fabrication of aspheric lenses with almost arbitrary radii of curvature and conic constants, which is used to compensate for aberrations introduced by the remaining optical components of the optical setup.

Figure 5.7a shows the design for a single MLA lens resulting from these ray-tracing calculations in a false-color diagram of its height profile with the beam diameter of the incident Gaussian beam d_{1/e^2} being indicated by a white dashed line. The lateral size of the lens $l_{\text{lens}} = 1\,\text{mm}$ was chosen larger than the beam diameter to not introduce edge effects and collect as much light as possible. A larger lens design would require stitching in manufacturing, potentially introducing unwanted imperfections in the lens profile and increasing the fabrication time. Together with the lens radius of curvature $R = 4.64\,\text{mm}$ and conic constant $K = 17.50$, the lens features a total height or sagitta of SAG $= 32.6\,\mu\text{m}$. Figure 5.7b

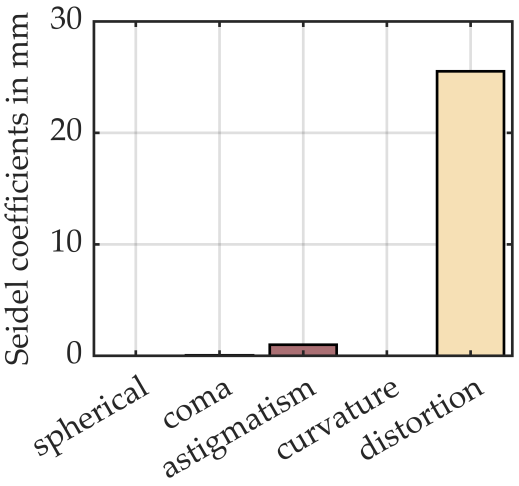

Figure 5.8: Seidel coefficients introduced by one lens of the multi-lens array (MLA). The wavefront error scales with these coefficients. The astigmatism and large distortion aberration are intended by design and will compensate for (opposite) astigmatism and distortion aberrations of a specific lens in the remaining optical setup, which is described in chapter 6. Lateral and longitudinal color aberrations are zero and therefore not shown in this plot.

shows the resulting multi-lens array comprising $7 \times 7 = 49$ individual lenses with equal design that have a center distance of 2.2 mm. Given a certain magnification of the remaining optical setup after the MLA described in chapter 6, this center distance will later translate into a focus distance of 60 µm in the writing plane. The distance was chosen such that all foci fit into the field of view of the used microscope objective lens but still have a large enough distance to allow for printing individual structures of up to 60 µm size. During manufacturing, which will be described in detail in section 5.3, each lens will be fabricated within one writing field of the manufacturing device.

The MLA lens was not designed to have minimum aberrations but intentionally features a strong distortion aberration as well as some astigmatism. Figure 5.8 gives an overview of aberrations introduced by the MLA lens design. These aberrations are introduced to slightly compensate for (opposite) aberrations introduced by macroscopic lenses of the remaining optical setup behind the MLA to improve the overall quality of the focus array in the printing plane. By using this design, aberrations of the optical setup can therefore be reduced. A more detailed overview of all aberrations in the complete optical setup can be found in chapter 6. With the designs of both micro-optical elements being set, the following section discusses the impact of systematic errors in manufacturing by two-photon lithography that will later be compensated for to improve the optical quality of both the DOE and MLA.

5.3 Maximizing Optical Quality by Iterative Pre-compensation

With the designs of the micro-optical components presented in section 5.2 and their manufacturing methods explained in section 3.2, this section discusses challenges in fabrication. 3D laser printed structures suffer from various imperfections. The micro-optical components needed for the envisioned optical setup impose high requirements for their shape accuracy. Thus, already small deviations from the design influence their performance. Naturally, these manufacturing imperfections should be reduced as much as possible to maximize optical performance. To give an understanding, the first part of this section outlines some of these manufacturing imperfections and their impact on the DOE diffraction pattern. They can be of statistical and of systematical nature. For the subsequent optimization, it is important to understand that only systematical errors can be reduced.

Afterwards, a workflow to improve the optical quality of both the diffractive optical element (DOE) and the multi-lens array (MLA) by minimizing these systematic manufacturing imperfections is presented. First, the basic idea of this iterative process to adapt the sample design to the systematic errors during fabrication is explained. After presenting the individual steps of this pre-compensation workflow, the improved results and the analysis of the micro-optical components are shown. Notably, the workflow was automated in an open-access software for arbitrary 2.5D structures [172],

5.3.1 Impact of Manufacturing Imperfections on Diffraction Efficiency

The fully designed micro-optical components are manufactured by two-photon lithography, which allows for high resolution but comes with some statistical and systematical errors like stitching, writing field inhomogeneities, and shrinkage [173, 174]. In the following, some prominent examples are discussed. In reality, a 3D structure is always suffering from a superposition of many errors.

Stitching

In two-photon lithography, fabrication can only happen within the writing field of the used microscope objective lens which is finite. For the manufacturing conditions of the micro-optical components a writing field size of $500 \times 500\,\mu m^2$ is typical. Since the DOE features a total lateral size of $3.2 \times 3.2\,mm^2$, it has to be fabricated by stitching where the structure is divided into many writing fields that will be printed sequentially. In between the completion of two individual writing fields, the sample stage moves to position the next writing field under the objective lens.

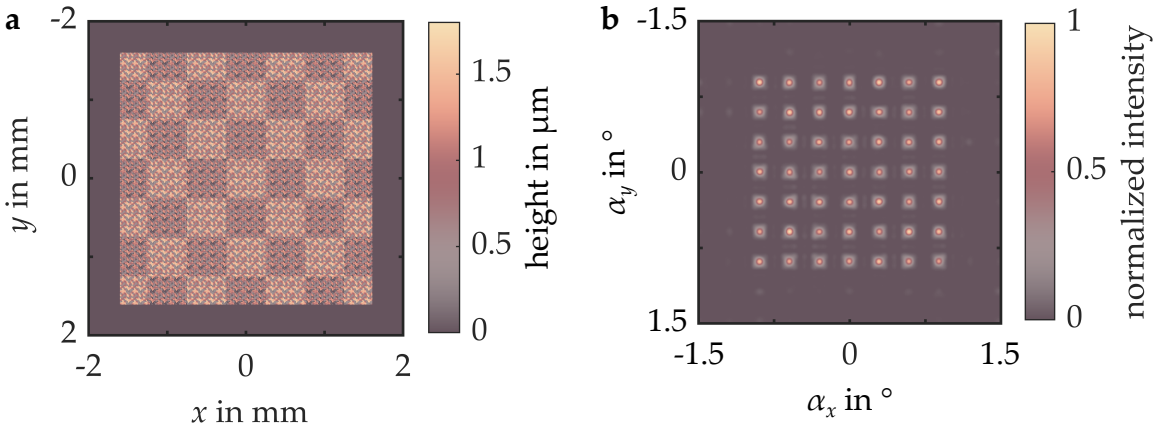

Figure 5.9: Computed far-field diffraction pattern for a diffractive optical element (DOE) with different writing field height offsets. For the simulation, a Gaussian beam with beam diameter $d_{1/e^2} = 571.3\,\mu m$ and wavelength $\lambda = 790\,nm$ was chosen. **a,** DOE design featuring individual writing fields for stitching. The side length of one writing field is $l_{WF} = 500\,\mu m$. Neighboring writing fields are offset by $z_{offset} = \pm 150\,nm$. **b,** resulting far-field diffraction pattern. The varying writing field height offsets impair the diffraction pattern. It shows no homogeneous power distribution anymore.

Usually, for each writing field, the lithography device determines the z-position of the interface between the sample substrate and the photoresist on top. However, this measurement has a residual error and typically varies by approximately 150 nm. This statistical imperfection already has a severe impact on the quality of the diffraction pattern. Figure 5.9a shows a DOE that is dissected into many writing fields for stitching with a single writing field size of $500 \times 500\,\mu m^2$. Neighboring writing fields are offset in height by $z_{offset} = \pm 150\,nm$. The distortion of the otherwise homogeneous far-field diffraction pattern is displayed in Figure 5.9b. Individual foci lost their Gaussian shape and show varying intensities. This imperfection is of statistical nature and can not be compensated by adjusting the print job accordingly. However, in modern two-photon-lithography machines the interface-finding precision is usually slightly better than shown in Figure 5.9, where it was chosen such that the effect on the diffraction pattern is clearly visible. To further reduce this error, the interface finding routine as a whole would need improvements.

Even if the error from finding the interface position is neglected, systematic imperfections can still occur when having slight sample tilts with respect to the writing plane. Figure 5.10a shows a DOE suffering from a sample tilt of $\alpha = 0.05°$ in both x- and y-direction while being manufactured using $500 \times 500\,\mu m^2$-sized

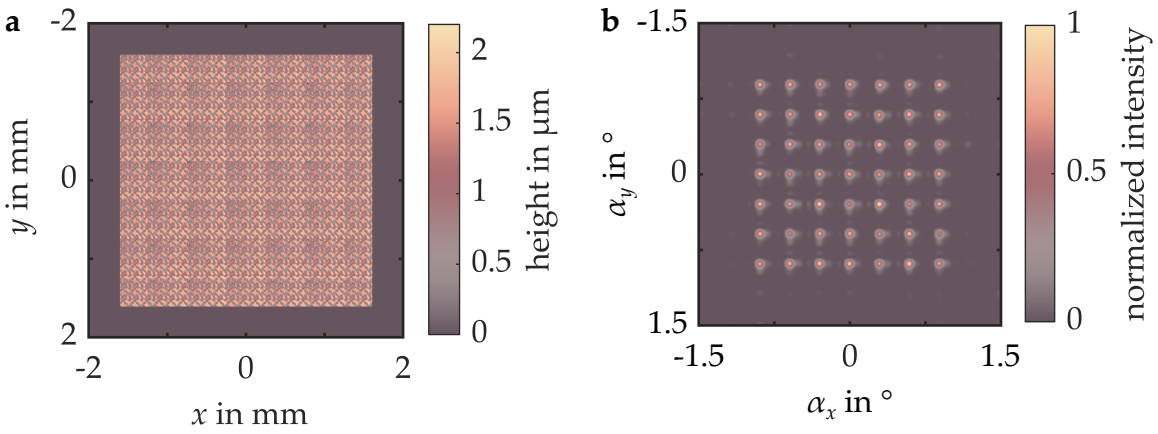

Figure 5.10: Computed far-field diffraction pattern for a diffractive optical element (DOE) with tilted writing fields. For the simulation, a Gaussian beam with beam diameter $d_{1/e^2} = 571.3\,\mu m$ and wavelength $\lambda = 790\,nm$ was chosen. **a,** DOE design featuring individual writing fields for stitching. The side length of one writing field is $l_{WF} = 500\,\mu m$. Individual writing fields are tilted along x- and y-direction following a respective tilt of $\alpha = 0.05°$. **b,** resulting far-field diffraction pattern. The tilted writing fields impair the diffraction pattern. It shows no homogeneous power distribution anymore.

writing fields with ideal interface finding. The tilted sample leads to each writing field being tilted with the center of each writing field being at the desired height $z_{offset} = 0\,nm$. Figure 5.10b shows the deteriorated far-field diffraction pattern. The individual foci show varying intensities and distorted shapes. Compensation for this effect is therefore highly desirable and possible with the introduced routine in subsection 5.3.2.

Writing Field Inhomogeneities

Next to imperfections in stitching many writing fields together, the writing field itself can have systematic errors, too. When scanning a laser focus, the intensity is not always constant at every location of the writing field. The microscope objective lenses used for focusing introduce aberrations that depend on the laser focus position. Usually, towards the edges of the writing field, aberrations increase and deteriorate the intensity of the laser focus. This leads to lower intensities towards to edges and higher intensities in the center. As explained in section 2.2, varying focus intensities lead to varying voxel sizes which in turn will lead to smaller sample heights towards the edges of the writing field.

Figure 5.11a shows a DOE suffering from these intensity inhomogeneities inside each $500 \times 500\,\mu m^2$-sized writing field. In the center of each field, the structure

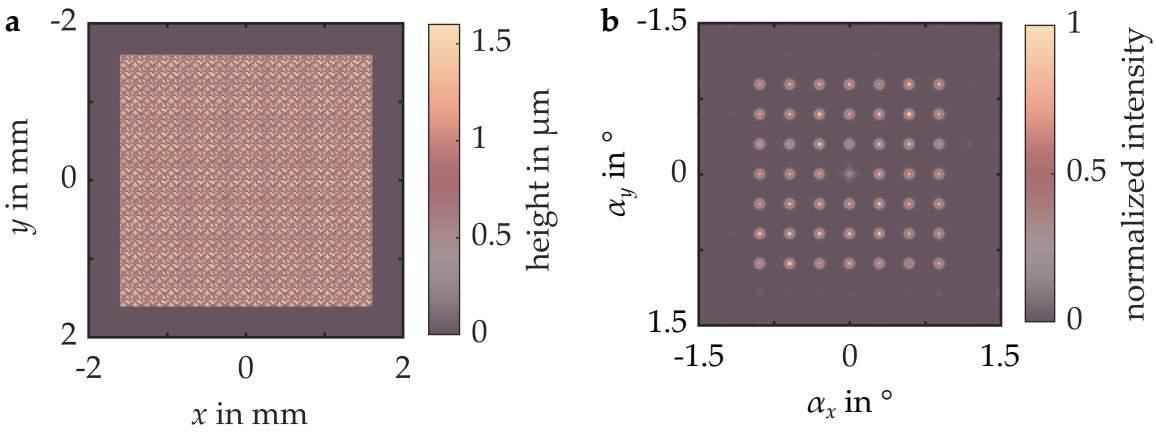

Figure 5.11: Computed far-field diffraction pattern for a diffractive optical element (DOE) with inhomogeneous intensity distributions inside each writing field. For the simulation, a Gaussian beam with beam diameter $d_{1/e^2} = 571.3\,\mu m$ and wavelength $\lambda = 790\,nm$ was chosen. **a,** DOE design featuring individual writing fields for stitching. The side length of one writing field is $l_{WF} = 500\,\mu m$. Each writing field features an inhomegenous intensity distribution, which varies the voxel size along the writing field. This leads to structures that become smaller towards the edges of the writing field. In the center of each writing field, the structure shows the desired height h_{design} and, at the corner of each writing field, declines to a height of $80\,\% \times h_{design}$. **b,** resulting far-field diffraction pattern. The varying voxel sizes inside each writing field impair the diffraction pattern. The power distribution is no longer homogeneous.

shows the desired height h_{design} while it decays parabolically to a assumed height of $80\,\% \times h_{design}$ at the corners of each writing field. Assuming a Gaussian beam with beam diameter $d_{1/e^2} = 571.3\,\mu m$ and wavelength $\lambda = 790\,nm$, the far-field diffraction pattern shown in Figure 5.11b results from these imperfections. Here, the zeroth order almost vanished while the remaining foci show varying intensities. Since these imperfections appear systematically, they can be compensated for.

Shrinkage

Even under perfect conditions during the manufacturing process, all structures fabricated by two-photon lithography are suffering from a prominent systematic imperfection in form of shrinkage [173, 174]. After printing, all remaining liquid photoresist has to be washed off in a development step as explained in section 2.1. During this procedure, samples usually end up smaller than they used to be before development. While the common explanation to this effect lies in the washing out of unreacted photoresist from solidified material, the process hat not been completely understood. In principle, this shrinkage occurs along all coordinate

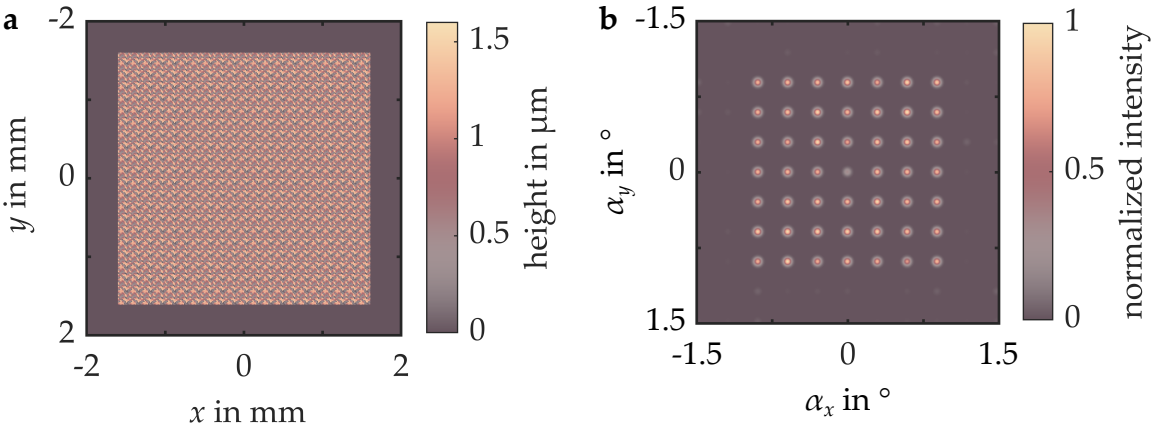

Figure 5.12: Computed far-field diffraction pattern for a diffractive optical element (DOE) that suffered from shrinkage. For the simulation, a Gaussian beam with beam diameter $d_{1/e^2} = 571.3\,\mu m$ and wavelength $\lambda = 790\,nm$ was chosen. **a,** DOE design that suffered from $S = 5\,\%$ shrinkage. The height profile was multiplied by $1 - S$. The resulting design therefore is slightly smaller than intended. **b,** resulting far-field diffraction pattern. The diffraction pattern was impaired by the height-altering shrinkage S. It shows no homogeneous power distribution anymore.

axes. However, since the bottom of the DOE is connected to the substrate, it will mainly shrink perpendicular to the substrate surface, i.e. in its height, which modifies the local phase change of the incident wavefront and therefore alters the diffraction pattern.

Figure 5.12a shows a DOE suffering shrinkage that decreased the height profile by $S = 5\,\%$. Typically, a shrinkage between $S = 2\,\%$ and $S = 12\,\%$ is observed for the used photoresist[170]. Assuming a Gaussian beam with beam diameter $d_{1/e^2} = 571.3\,\mu m$ and wavelength $\lambda = 790\,nm$, the far-field diffraction pattern shown in Figure 5.12b shows a weak zeroth order together with slight variations in the remaining intensity profile, which has to be compensated. Notably, this effect also can occur when assuming the wrong refractive index of the polymerized material when calculating the absolute height of the DOE from its phase profile.

5.3.2 *Tackling 3D Printing Imperfections by Design*

Simply printing the target design of any micro-optical component will result in a structure suffering from many different manufacturing imperfections, some of which being explained in subsection 5.3.1 and altering the desired performance of the micro-optical device [108]. Here, it is not directly clear which kinds of manufacturing imperfections contribute to the result since in most of the cases a superposition of many different errors impair the structure. When characterizing

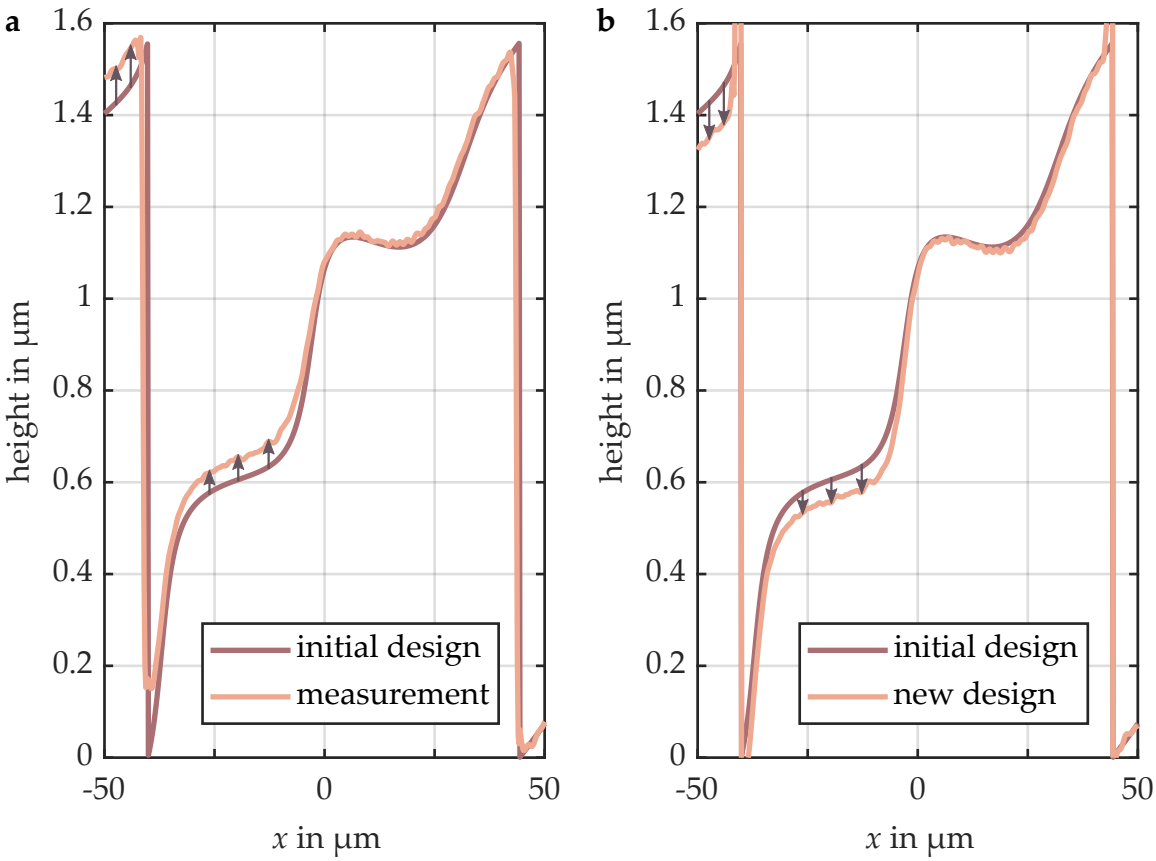

Figure 5.13: Concept of pre-compensation to improve shape accuracy. a, section of the initial design of the diffractive optical element (DOE) and measurement of its fabricated sample. In this initial print, the sample was printed slightly too high at some positions, indicated by the gray arrows. **b,** section of the initial design of the DOE and the computed new design. At sample locations where the sample was initially printed too high, the new design is intentionally modified to be slightly smaller to pre-compensate for this systematic error.

the sample topography *via* optical spinning-disc confocal microscopy, it becomes apparent that it deviates from its design. By precisely overlaying this measured topography with the design topography *via* digital image cross-correlation as explained in subsection 3.2.6, a difference map can be calculated. This 2D image quantifies the deviation of the fabricated structure from its design for every point in space.

This is illustrated in Figure 5.13a by plotting a section of an x-cut through the DOE profile for both the initial design and the measurement of its initial print. At certain positions, the DOE was printed too high and will therefore exhibit a diffraction pattern that deviates from the target diffraction pattern. It should be

noted that the used Quantum X lithography device already features many routines to minimize these imperfections, e.g., by measuring the sample tilt for each writing field and automatically compensating for this tilt within the precision of the measurement. However, in this chapter it will become apparent that this is not sufficient for the shape accuracy that is needed for a satisfactory DOE performance.

Figure 5.13b shows the same section of an x-cut through the DOE profile. This time, however, the initial design is plotted together with a potential new design for a second iteration of printing. At positions where the DOE was printed too large in the first print, the new design $\mathrm{DES}_{\mathrm{v2}}(x,y)$ intentionally features smaller features by subtracting the difference between the measurement of the first printed structure $\mathrm{MEA}_{\mathrm{v1}}(x,y)$ and the initial design $\mathrm{DES}_{\mathrm{v1}}(x,y)$ from the initial design:

$$\mathrm{DES}_{\mathrm{v2}}(x,y) = \mathrm{DES}_{\mathrm{v1}}(x,y) - (\mathrm{MEA}_{\mathrm{v1}}(x,y) - \mathrm{DES}_{\mathrm{v1}}(x,y)). \tag{5.12}$$

This is the basic idea behind iterative pre-compensation [172, 173]. Given that the errors altering the sample print are systematic, the second print iteration will result in a sample that is closer to the initial design than the initial print. If the results are not satisfactory by then, the loop can be repeated to minimize the difference between measurement and design:

$$\mathrm{DES}_{\mathrm{v}n+1}(x,y) = \mathrm{DES}_{\mathrm{v}n}(x,y) - (\mathrm{MEA}_{\mathrm{v}n}(x,y) - \mathrm{DES}_{\mathrm{v1}}(x,y)). \tag{5.13}$$

Notably, completely reaching the initial design is not possible since some manufacturing imperfections are of statistical nature and not systematic.

5.3.3 *Iterative Pre-compensation Using Digital Image Cross-Correlation*

To automate iterative pre-compensation *via* digital image cross-correlation, a homemade software was developed that takes over the import of measurement and design and all necessary data handling steps to eventually compute a new, pre-compensated design. After an initial version of this algorithm featuring the basic ideas was programmed, a more general and refined software was developed from scratch by the author together with Jannis Weinacker, Sebastian Kalt, and Pascal Rietz [172]. Figure 5.14 shows the corresponding workflow.

First, the very initial design $\mathrm{DES}_{\mathrm{v1}}(x,y)$ is imported together with the current version of the pre-compensated design $\mathrm{DES}_{\mathrm{v}n}(x,y)$ and the measurement of its printed structure $\mathrm{MEA}_{\mathrm{v}n}(x,y)$. To allow for a statistical analysis, a structure is printed four times with every sample characterized by optical spinning-disc confocal microscopy. During the measurement of the printed structure certain errors of different sources can occur. For instance, the sample substrate could have a small

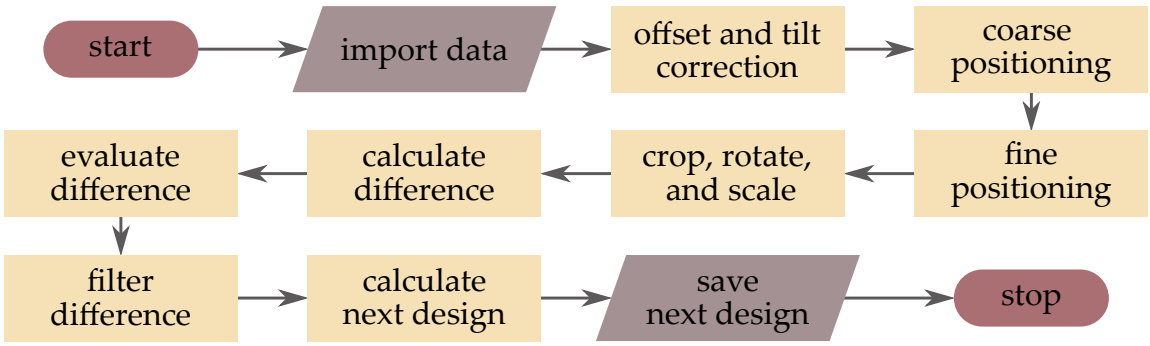

Figure 5.14: Workflow of our homemade software automating design pre-compensation. After importing both the design and measurement data, the software levels the measurement and coarsely positions the measured structure to overlay with the design. Employing digital image cross-correlation, the measured structure gets rotated and laterally scaled to maximize overlay precision. Afterwards, the measurement data gets positioned more precisely. After cropping and resizing the structure to match the pixel size of the design, the difference is calculated and evaluated by two figures of merit. To get rid of unwanted measurement or print errors in the difference data, a filtering algorithm refines the retrieved data to not introduce more imperfections in the next print iteration. Eventually, using the filtered difference data, the next design is calculated and exported for the upcoming fabrication step. Adapted from [172].

tilt with respect to the measurement plane. To take these errors into account, a plane is fitted through measured parts of the substrate outside of the structure to calculate the tilt and correct and level the entire measurement. Afterwards, a software routine performs a quick and coarse positioning of the measured structure with respect to the initial design. Although this step is not necessary all the time, it improves the degree of resilience of the subsequent fine positioning step utilizing digital image cross-correlation and allows for deleting parts of the measurement that do not include the analyzed structure, increasing performance. After finding the correct positioning of the measurement, a further step maximizes this maximum value of the 2D cross-correlation function $C(\Delta x, \Delta y)$ for correct positioning by rotating and scaling the measurement data. By this variation of arbitrary rotation angles β and lateral scales S_x and S_y, a new maximum is found. This step is performed to minimize the introduction of artificial artifacts to the new design. If the measurement is rotated or scaled with respect to the design, the difference is not calculated between two corresponding locations of the structure. Figure 5.15 visualizes this problem by showing design data in the background and measurement data with exaggerated scaling and rotation errors in the foreground. The maximum of the cross-correlation function $C(\Delta x, \Delta y, \beta, S_x, S_y)$ is found for the correct shift, rotation, and scale.

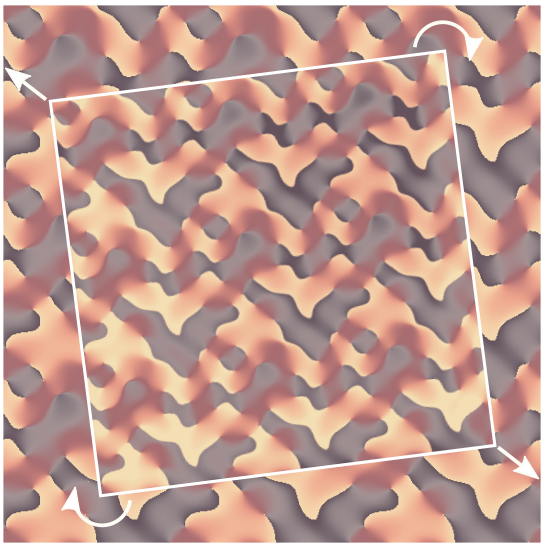

Figure 5.15: Schematic exaggerated depiction of data modifications to maximize overlay precision using digital image cross-correlation. The design of the diffractive optical element (DOE) is shown in the background. A measurement of the fabricated structure of the initial design of this DOE is visible in the foreground. Without rotating and scaling the measurement data, the overlay with the design data is insufficient for pre-compensation. By iteratively rotating and scaling the measured structure and evaluating the strength of the cross-correlation peak in a nonlinear programming solver, the necessary rotation angle and scaling factor can be found and applied.

After ensuring that the alignment of the measurement of the printed structure $\mathrm{MEA}_{vn}(x,y)$ to the very initial design $\mathrm{DES}_{v1}(x,y)$ is optimized by these steps, the measurement data is cropped to only include the structure and no substrate data to afterwards calculate the difference

$$\mathrm{DIF}_{vn}(x,y) = \mathrm{MEA}_{vn}(x,y) - \mathrm{DES}_{v1}(x,y). \tag{5.14}$$

This difference is then evaluated to quantify how well the printed structure fits to the target design by calculating two figures of merit. To calculate these, the pixels containing the structure $\mathrm{STR}_{vn}(x,y)$ are computed first if the structure is, e.g., circular and not rectangular:

$$\mathrm{STR}_{vn}(x,y) = \begin{cases} 1 & \text{structure,} \\ 0 & \text{no structure.} \end{cases} \tag{5.15}$$

Now, the two figures-of-merit can be calculated. The first one calculates to the mean-absolute difference of all pixels containing structure data [172]

$$\mu = \frac{\sum_{\text{pixels}} |\mathrm{DIF}_{vn}(x,y)\mathrm{STR}_{vn}(x,y)|}{\sum_{\text{pixels}} \mathrm{STR}_{vn}(x,y)}. \tag{5.16}$$

The second one calculates to the standard deviation (root-mean-square) of the same pixels [172]

$$\sigma = \sqrt{\frac{\sum_{\text{pixels}} \left[\mathrm{DIF}_{vn}(x,y) - \langle \mathrm{DIF}_{vn}(x,y) \rangle\right]^2 \mathrm{STR}_{vn}(x,y)}{\sum_{\text{pixels}} \mathrm{STR}_{vn}(x,y)}}. \tag{5.17}$$

Both of these figures-of-merit contain information about the quality of the printed structure. For a print that perfectly matches the design, the entire difference matrix should only contain zeros and therefore yield $\mu = 0$ and $\sigma = 0$. In reality, these values will be finite and decrease with increasing print quality.

The computed and evaluated difference data features a minimum of artificial artifacts due to errors in alignment. However, further artifacts introduced by the measurement itself can impair the difference data. These errors can include measurement noise, unwanted dust particles on the structure, or wrong height data in steep regions of the sample where the available numerical aperture of the employed objective lens is not sufficient to resolve the topography. Calculating a new designs from these impaired data will not only correct for systematic errors but introduce new errors, which will prevent the iterative pre-compensation algorithm from converging to a high-quality micro-optical component. Therefore, these difference data is filtered to minimize these errors.

Systematic errors like shrinkage usually lead to smooth variations in the difference data. To exclude them, a first filtering step detects all difference data pixels that correspond to either a large difference value or large gradients

$$|\mathrm{DIF}_{\mathrm{v}n}(x,y)| > 2\,\mu\mathrm{m}, \tag{5.18}$$

$$|\nabla\mathrm{DIF}_{\mathrm{v}n}(x,y)| > 0.3\,\mu\mathrm{m}. \tag{5.19}$$

These large local deviations in the difference data typically arise from unwanted features like damaged parts of the structure or dirt particles. To cover the whole area in question, the marked areas are expanded by a default circle with radius $r = 2\,\mu\mathrm{m}$. The expanded areas are then deleted and replaced by interpolated values using the surrounding areas of the difference data. Generally, only small areas are affected by this step. If the measurement data of a printed structure is so deteriorated that large areas have to be excluded, the whole measurement should be excluded.

Pixels located at the border of the structure defined by a frame of thickness $d = 5\,\mu\mathrm{m}$ are generally excluded [172]. Their values are not replaced by interpolating from the surrounding area but rather by extruding from the pixel values further inside the sample. This step is executed since already slight lateral shrinkage will render any effort to overlap the borders with the design impossible. A pre-compensation of these regions without the described filtering step therefore makes no sense.

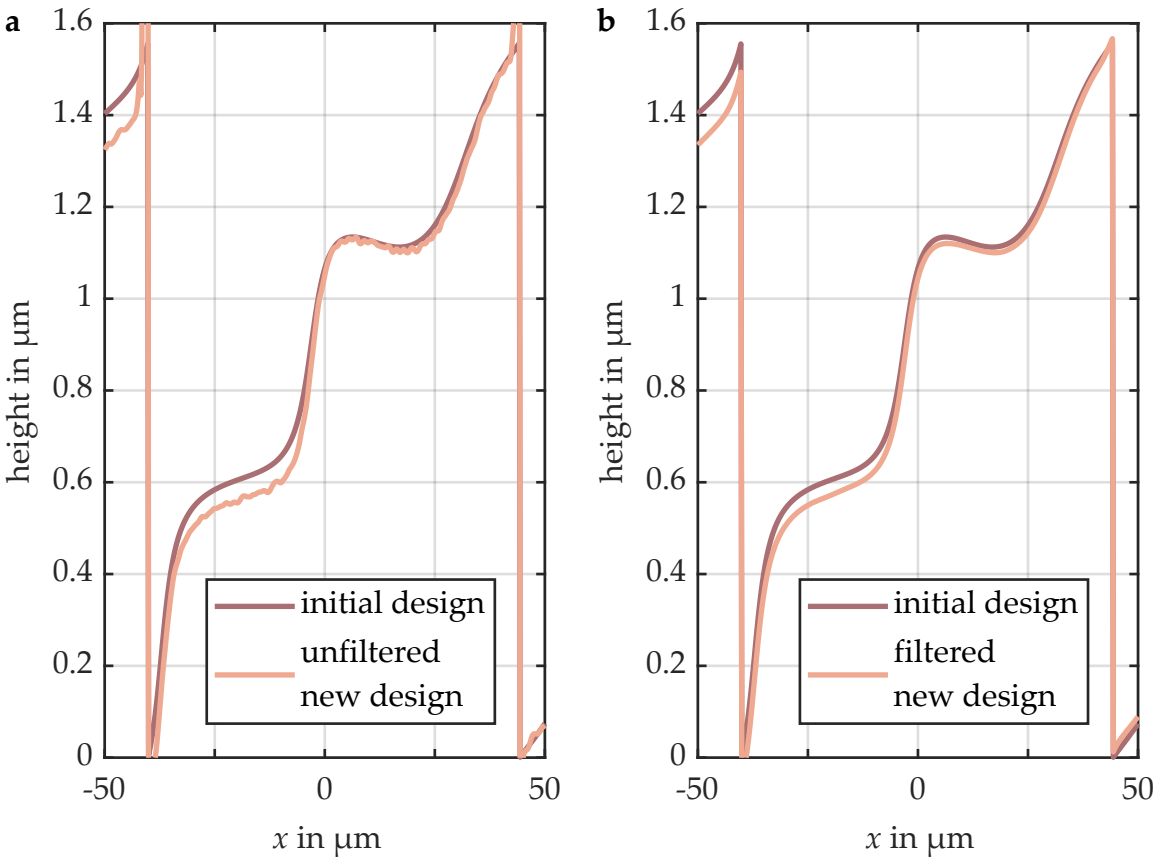

Figure 5.16: Comparison of unfiltered and filtered data. **a,** section of the initial design of the diffractive optical element (DOE) and the computed new design, calculated by adding the difference between the initial design and the measurement of its printed sample. Regions near steep edges tend to have large differences to the design, which makes the new design overshoot the pre-compensation. Furthermore, grainy details in otherwise smooth sections are visible and will increase the surface roughness of the next print. **b,** section of the initial design of the DOE and the filtered new design. The applied filtering algorithm recognizes errors occurring at steep edges and allows for a new design without drastic jumps in height. Furthermore, grainy details in otherwise smooth section are filtered out.

In a last step, a Gaussian filter with a defined standard deviation $\sigma_{\text{filt}} = 2\,\mu\text{m}$ is applied on the measurement data to suppress all artifacts originating from noise [172]. Systematic errors that have to be pre-compensated usually stretch over a large spatial range and not small areas of a few micrometers length. Therefore, the Gaussian filtering does not have a perceivable influence on the pre-compensation quality but significantly reduces noise in data.

Using this filtered difference data $\tilde{\mathrm{DIF}}_{\mathrm{v}n}(x,y)$, a new design for the next print iteration can be calculated:

$$\mathrm{DES}_{\mathrm{v}n+1}(x,y) = \mathrm{DES}_{\mathrm{v}n}(x,y) - \tilde{\mathrm{DIF}}_{\mathrm{v}n}(x,y). \tag{5.20}$$

Figure 5.16 demonstrates the positive impact of the described filtering algorithm on the calculated new design. A new design computed from unfiltered difference data depicted in Figure 5.16a shows noisy regions of the topography as well as sample regions which are far too high. The new design computed from filtered difference data depicted in Figure 5.16b features a smooth topography and heights that stay in the region of the original design and do not suffer from errors originating from the measurement.

The effectiveness of this workflow is presented in Figure 5.17 [172]. The already described design of the diffractive optical element was manufactured by Jannis Weinacker and optically analyzed by me in three iterations: an initial print without pre-compensation, a design with a first pre-compensation and afterwards a design with a second pre-compensation. Figure 5.17a and Figure 5.17b show the topography of the initial design and the measurements of the three print iterations as well as the difference to the design. Without any pre-compensation many artifacts that make the structure deviate from its design can be observed. The measurement features clear lines from stitching with tilted writing fields. Designs featuring one or two iterations of pre-compensation show significantly smoother difference data as well as topographies that are much closer to the initial design. Obviously, the difference of the design to itself is zero. Figure 5.17c plots the difference data in a histogram in the style of relative occurrence in percent versus the actual difference of any point of the topography to its designed height. Since the design fits perfectly to itself, the histogram has one sharp peak at 0 µm difference containing all difference data. In general, the closer the histogram is to this shape, the closer the printed structure is to its design. These plots also reveal the gradually improving quality of the measured samples after pre-compensation: The initial print features a broad peak with high values for the mean difference $\mu = 178.3\,\mathrm{nm}$ and the standard deviation $\sigma = 262.1\,\mathrm{nm}$. For increasing iterations of pre-compensation the shape of the histogram gets more narrow, indicating a structure of higher quality. The best result after two iterations of pre-compensation features a mean difference $\mu = 78.8\,\mathrm{nm}$ and a standard deviation $\sigma = 154.6\,\mathrm{nm}$.

These diffractive optical elements were also analyzed optically by illuminating them with a $\lambda = 790\,\mathrm{nm}$ wavelength laser and positioning them in the front focal plane and a CMOS camera in the back focal plane of a 150 mm focal length lens to capture the diffraction pattern. In the case of the initial print, several regions of high intensity in between the individual foci can be observed with

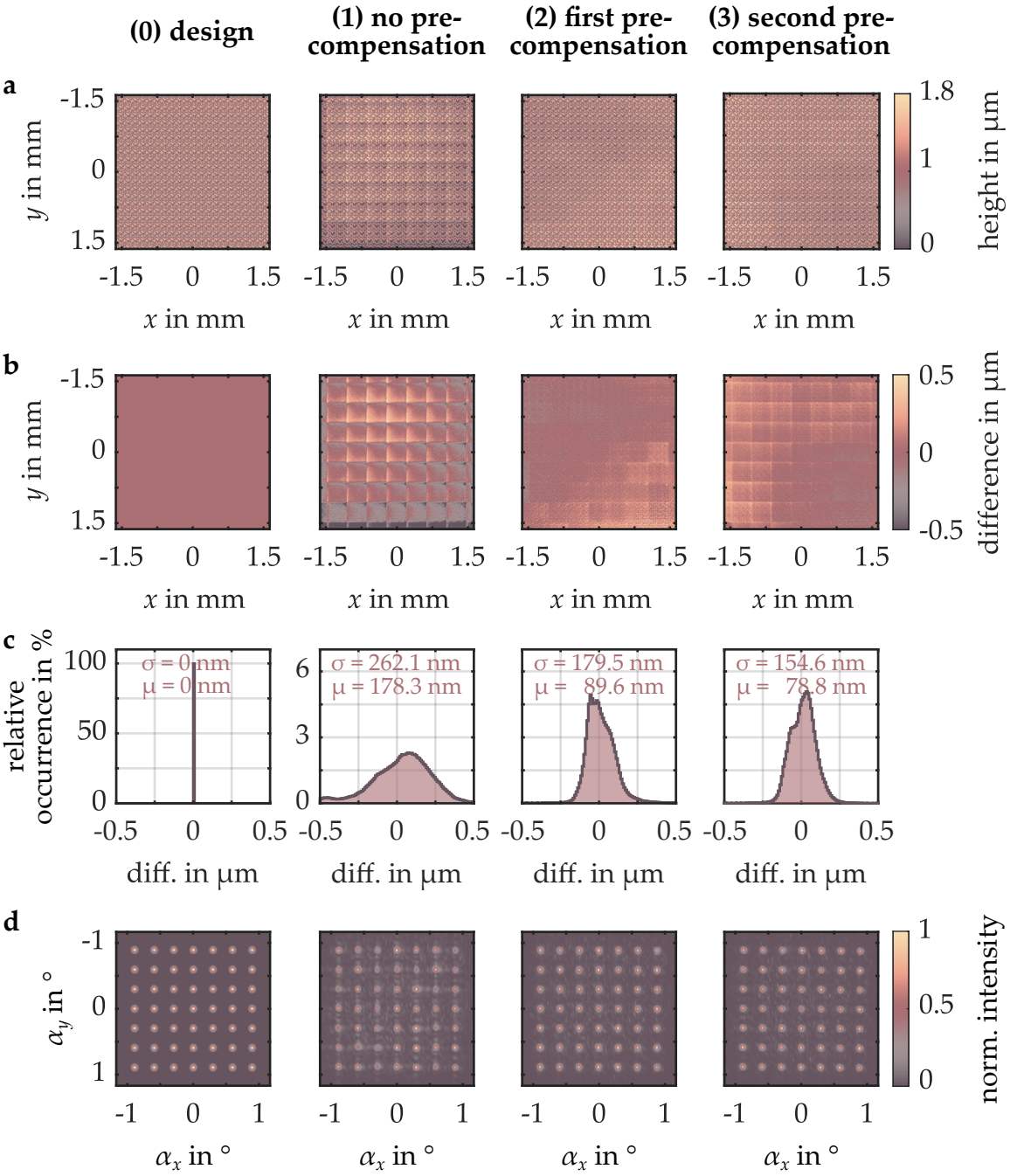

Figure 5.17: Pre-compensation overview of the diffractive optical element (DOE). The four columns show data of (0) the initial DOE design and (1-3) three different 3D laser printed samples. The three samples were printed (1) without any pre-compensation and hence using the initial design, (2) with a first pre-compensation based on data of the first print, and (3) with a second pre-compensation. **a,** DOE topography. **b,** difference of the DOE topography to the initial design. **c,** corresponding histograms of the difference data. **d,** corresponding far-field diffraction pattern. For the design, the computed diffraction pattern is shown. For the three samples, the diffraction pattern was measured using a camera. Adapted from [172].

the pattern showing no homogeneous power distribution. Already with the first pre-compensation, the diffraction pattern shows more resemblance to the target diffraction pattern, which is plotted in the left column. The absolute improvements in the second pre-compensation are smaller but still contribute to reduce the deviation to the desired design further.

To summarize, already one iteration of pre-compensation with careful handling of the measurement data shows significant improvements to the diffraction pattern of the diffractive optical element. Subsequent iterations of pre-compensation further enhance the quality. This procedure is a very powerful tool to significantly improve printing results.

5.3.4 Quality Assessment of Compensated Micro-Optical Components

Using the iterative workflow presented in section 5.3, the final structures for the next-generation multi-focus 3D laser printing setup planned and applied in this thesis were manufactured. Figure 5.18 gives an overview of the final DOE and MLA sample. Figure 5.18a shows four DOEs printed on a 2-inch diameter glass wafer. One of these DOEs will be used to initially split the incident laser beam into $7 \times 7 = 49$ beamlets. A close-up image of one of these DOEs taken with a digital microscope is depicted in Figure 5.18b. No visible stitching artifacts and an overall homogeneous topography can be observed even though the DOE was fabricated using $9 \times 9 = 81$ writing fields. An even closer perspective view of the quasi-continuous 16-bit topography is shown in Figure 5.18c, captured by a scanning-electron microscope.

An optical photograph of the complete MLA featuring $7 \times 7 = 49$ individual lenses printed on a 2-inch diameter glass wafer is depicted in Figure 5.18d. This lens array is used in the final optical setup to focus the incoming beamlets relayed at their respective lens to create the initial focus array. Figure 5.18e shows a close-up view of the lens array, captured by a light microscope. Each lens was fabricated subsequently without stitching. A light-microscopy image showing a single lens of the MLA and highlighting its smooth surface is presented in Figure 5.18f. To minimize reflection losses, both elements were anti-reflection coated as described in subsection 3.2.7.

The confocal analysis of the final versions of both micro-optical components is depicted in Figure 5.19. For both the DOE and MLA, the initial design, the topography resulting from the measurement of the final printed structure, and the calculated difference of both are displayed. Next to its design, Figure 5.19a

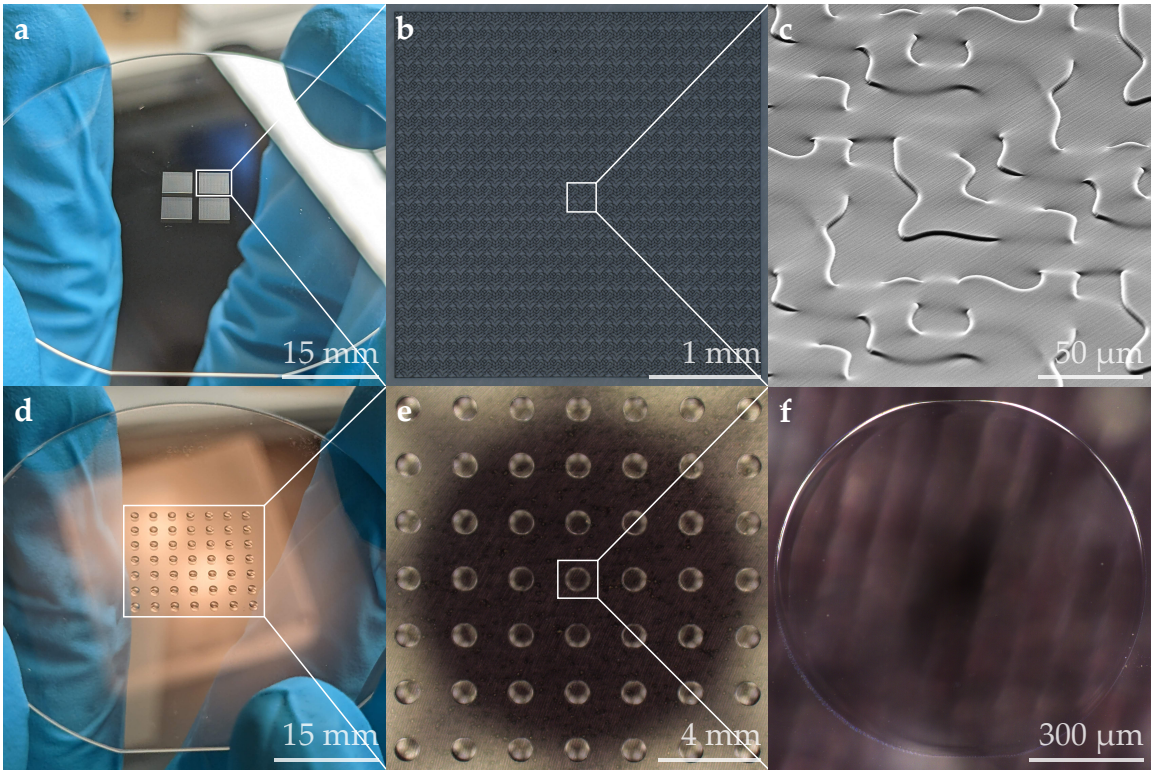

Figure 5.18: Final fabricated micro-optical components for next-generation multi-focus 3D laser printing. a, optical photograph of four diffractive optical elements (DOEs) manufactured on a 2-inch diameter glass wafer by 2-photon grayscale lithography. One of these DOEs will be used in the optical setup described in chapter 6 to split an incoming laser beam into $7 \times 7 = 49$ beamlets. **b,** light-microscopy image showing one of the four DOEs, which was manufactured by stitching using $9 \times 9 = 81$ writing fields. However, no artifacts due to stitching are observed. **c,** close-up perspective view of the DOE with its quasi-continuous 16-bit topography, captured with a scanning-electron microscope. **d,** optical photograph of a multi-lens array (MLA) comprising $7 \times 7 = 49$ lenses that was manufactured on a 2-inch diameter glass wafer by 2-photon grayscale lithography. This MLA will be used in the optical setup described in chapter 6 to individually focus $7 \times 7 = 49$ beamlets into an array of foci. **e,** light-microscopy image displaying the full MLA. For the individual lenses no stitching was applied. **f,** close-up light microscopy view of a single lens of the MLA, revealing its smooth surface. Adapted from [58].

shows the measurement of the final DOE sample that went through three iterations of pre-compensation. Interface finding during fabrication is one source of imperfection and can be spotted by the small squares in the measurement and calculated difference to the design. Other than that, the structure shows a high optical quality with a mean deviation of $\mu = 71\,\text{nm}$, which is less than one-tenth of the incident wavelength.

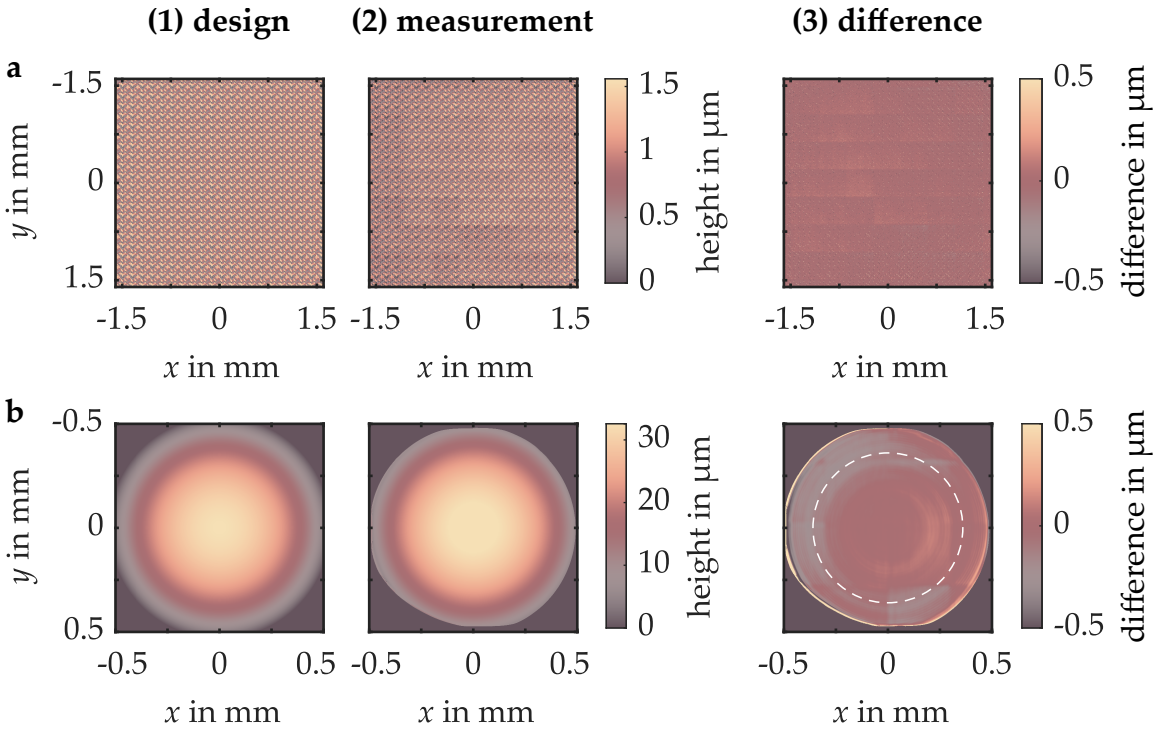

Figure 5.19: Confocal analysis of the final fabricated micro-optical components for next-generation multi-focus 3D laser printing. a, The three columns show data of (1) the initial micro-optical component design in a false-color height profile, (2) a spinning-disk confocal-optical-microscope measurement of the final pre-compensated version of this design, and (3) the calculated difference between this final structure and its initial design. **a,** the design of the diffractive optical element (DOE) shows $21 \times 21 = 441$ individual DOE unit cells. The measured sample went through three iterations of pre-compensation from the design. The calculated difference demonstrates a mean deviation $\mu = 71\,\text{nm}$. A main source of imperfection can be spotted by the small squares, which are caused by the interface finding during fabrication. **b,** design of a single lens of the multi-lens array (MLA). The measured sample went through two iterations of pre-compensation from the design. The calculated difference demonstrates a mean deviation $\mu = 142\,\text{nm}$. To avoid imperfections due to stitching, the individual lenses were printed within single writing fields. This causes imperfections near the edges of the scanning area of the laser focus that contribute to the mean deviation. However, their impact on the wavefront is small since they lie outside of the conjugated objective lens pupil diameter, indicated by a white dashed circle. Adapted from [58].

The MLA sample shown in Figure 5.19b next to its design went through two iterations of pre-compensation. For printing the single lenses, as much of the available writing field was used as possible without stitching. This is why the lens shows strong deviations from its design at its edges. However, the impact of these errors on the final focus array is negligible since they lie outside the conjugated objective lens pupil diameter. This diameter is indicated by a white dashed circle in the difference data plot. The mean deviation calculates to $\mu = 142\,\text{nm}$, which is two times larger than the mean deviation of the DOE. This can be traced back to the fact that perfectly aligning a lens to its design is much harder than aligning a DOE to its design, since the latter has many sharp features for the algorithm to recognize. A lens is a very smooth structure and does not offer these features. Furthermore, the rotation symmetry makes it hard to find the right rotation angle in alignment. One could argue that the rotation of the lens measurement data is not important, however, the writing field inhomogeneities of the objective lens used for fabrication are not rotationally symmetric. Correcting for these systematic errors therefore requires nicely aligning the lens measurement data also with respect to its rotation. Intentionally adding a feature to break rotation symmetry could further support this process in the future.

While small imperfections in the topography of the MLA lenses do not introduce severe impairments to the focus array, the DOE is especially sensitive like demonstrated in subsection 5.3.1. Thus, the diffraction pattern of the initial and final DOE was analyzed optically as well. In Figure 5.20a and Figure 5.20c, the false-color plots of the normalized intensity of the DOE far-field diffraction pattern is shown for the initial print and the final sample, respectively. This data was acquired by placing the DOEs in the front focal plane and a CMOS camera in the back focal plane of a 150 mm focal lenth lens. The micro-optical component was illuminated with the same $\lambda = 790\,\text{nm}$ laser source that is also employed in the final version of the complete optical setup described in chapter 6.

The diffraction pattern shows many inhomogeneities for the initial print and a seemingly homogeneous pattern of Gaussian-like foci with only weak interference in between neighboring foci. By applying a 2D-Gaussian fit to each individual focus, the power diffracted into each focus was estimated from the resulting fit parameters. Figure 5.20b and Figure 5.20d show these powers in a false-color bar plot as their deviation from the mean power across the whole focus array. Both the height and the color of each bar represents the power deviation. This representation reveals inhomogeneities of the focus array that are hard to identify from the camera image. For the initial print in Figure 5.20b, the foci show a large power deviation of up to 60 % and a root-mean-square power deviation of 22.9 %.

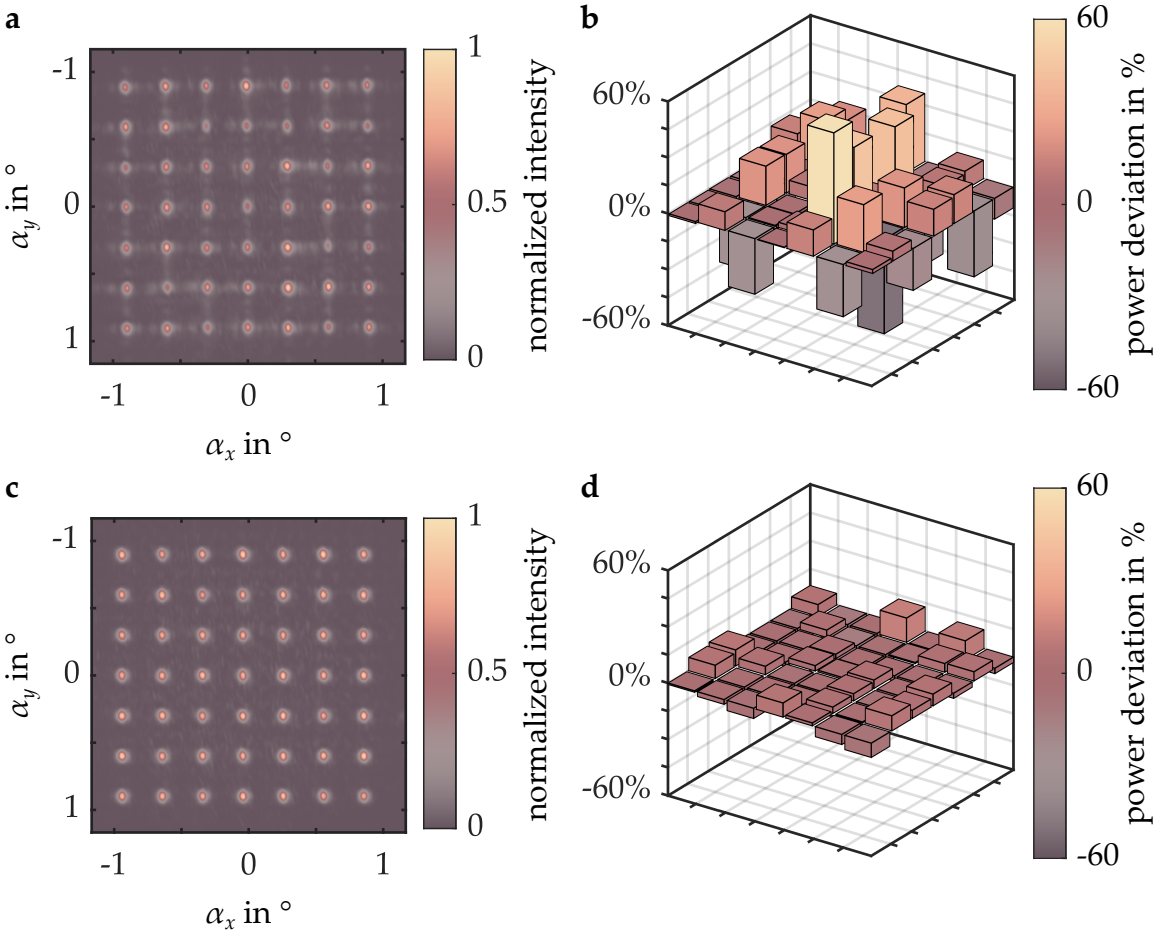

Figure 5.20: Optical analysis of the initial print and final diffractive optical element (DOE) sample. **a,** false-color plot of the normalized intensity of the DOE far-field diffraction pattern for the initial print. The measurement was performed by respectively placing the DOE and a CMOS camera in the front and back focal plane of a 150 mm focal length lens. The sample was illuminated with the same $\lambda = 790\,\text{nm}$ laser source as used in the final optical setup, which is described in chapter 6. **b,** false-color bar plot of the calculated power deviation of each individual focus from the mean power across the focus array. For the intensity profile of each individual focus in **a**, a 2D-Gaussian fit was applied to calculate the power from the fit parameters. The root-mean-square (RMS) power deviation is 22.9 %. **c,** false-color plot of the normalized intensity of the DOE far-field diffraction pattern for the final DOE sample. **d,** calculated power deviation of each individual focus from the mean power across the focus array for the intensity profile of each individual focus in **c**. The root-mean-square (RMS) power deviation is 5.4 %. Adapted from [58].

The final print in Figure 5.20d shows a significant improvement. The foci only differ in their power in a range of 13 %, which will later translate into varying voxel sizes. Obviously, foci of the exact same power would be highly desirable, however, with a root-mean-square power deviation of 5.4 %, the DOE already offers a satisfactory power distribution for the fabrication of the targeted structures by multi-focus 3D laser printing presented in this thesis.

5.4 Discussion and Conclusion

After overcoming one of the major limitations on further enhancing multi-focus 3D laser printing by developing a highly sensitive photoresist, this chapter described how the additional and equally important limitation of beam splitting was successfully overcome. Different approaches of beam splitting were discussed and the new approach of hybrid diffractive-refractive beam splitting presented. By combining both diffractive and refractive beam splitting, many disadvantages of either technique can be circumvented. Diffractive beam splitting is taken over by a diffractive optical element (DOE) while refractive beam splitting is achieved by a multi-lens array (MLA).

To combine both for this hybrid approach with high efficiency, the considerations going into and the computation of their designs was presented. A DOE with low diffraction orders utilizing a design value $M \approx 3$ was developed by also simulating its performance towards varying design values M and unit cell numbers to justify a high-quality design. The MLA was computed by ray-tracing calculations in an optical design software and designed such that it can partly compensate aberrations introduced by further optical components in the optical setup.

To understand and motivate the importance of high-quality fabrication of these micro-optical components as well as the iterative pre-compensation workflow, several simulations studying the impact of different systematic imperfections of the manufacturing process on the DOE diffraction pattern were presented. Without compensating for these problems of, e.g., tilted writing fields in stitching, writing field intensity inhomogeneities, or shrinkage, high optical quality cannot be obtained easily.

To automatically compensate for these problems, an iterative process pre-compensating for many systematic errors in printing using the design data and the retrieved topography of the printed sample by confocal-optical microscopy was presented. The open-source software can be applied to any 2.5D structure and exploits image cross-correlation for precisely overlaying the design and measurement data. This

is important not only for lateral positioning but also for scaling and rotating the measurement data to minimize the introduction of further errors to the computed difference data, which would otherwise possibly degrade a next iteration. Preventing additional artifacts was further supported by a filtering algorithm that reduces noise and filters out unwanted features in the difference data originating from objects like dust particles. The presented workflow offers much more flexibility than just working on shrinkage by global compensation [173] or advanced development methods [175, 176] or rather approximating the imperfect structure topography by a function fit [109, 177]. In the future, machine learning might help to reduce the required steps of pre-compensation iterations [178].

To demonstrate the capabilities of this process, data from three iterations of printing a DOE are analyzed by calculating the difference data histogram as well as measuring the optical diffraction pattern. Finally, the micro-optical components that are used in the next-generation multi-focus 3D laser printing setup presented in this thesis are presented and thoroughly analyzed. Their retrieved topography shows a close resemblance to their design with a mean deviation of $\mu = 71\,\mathrm{nm}$ for the DOE and $\mu = 142\,\mathrm{nm}$ for the MLA. An even closer look on the performance on the DOE was taken by optically analyzing its diffraction pattern and calculating the power diffracted into each individual focus of the $7 \times 7 = 49$ focus array. The computed root-mean-square power deviation of 5.4 % is sufficiently small for the application in multi-focus 3D laser printing.

Further improving the quality of micro-optical components could not be achieved by software compensations alone but would require further hardware adaptions. With the given process, only systematic errors can be handled. Every statistical error contributing to the imperfection of the sample will introduce a barrier that stops the user from further enhancing the optical quality. Therefore, the source of these statistical errors should be handled. One very prominent problem is the statistical nature of interface finding. In the case of the employed Quantum X lithography device, the interface is found by detecting the fluorescence signal. An array of laser foci is swept through the photoresist towards the interface between the glass substrate surface and the photoresist. The laser illumination excites the molecules in the photoresist which in turn emit fluorescence light. As soon as the array of laser foci enters the substrate, the signal vanishes and the device obtains its information about the position of the interface. However, measurement results will vary around the real value with a precision of a few 100 nm. This variation can not be pre-compensated for, which makes an improvement of the interface finding process highly desirable.

Furthermore, some artifacts that impair the measurement data do not originate from printing but from the confocal-optical-microscopy measurement itself.

Similar to the fabrication process, the measurement field of the confocal-optical microscope is limited as well. To measure a full MLA lens or the DOE, many measurement fields have to be stitched together. This process is also affected by statistical errors which, together with interface finding problems, form the most prominent sources of imperfection. Using a more precise measurement instrument to retrieve the sample topography would therefore also improve the overall quality that can be reached by iterative pre-compensation. Nonetheless, the optical quality accomplished for the structures shown in this chapter is of very high standard and the automated pre-compensation process variable enough to translate it to any 2.5D structure, which will hopefully be of great benefit for the community.

Chapter 6

6 A Next-Generation Multi-Focus 3D Laser Printer

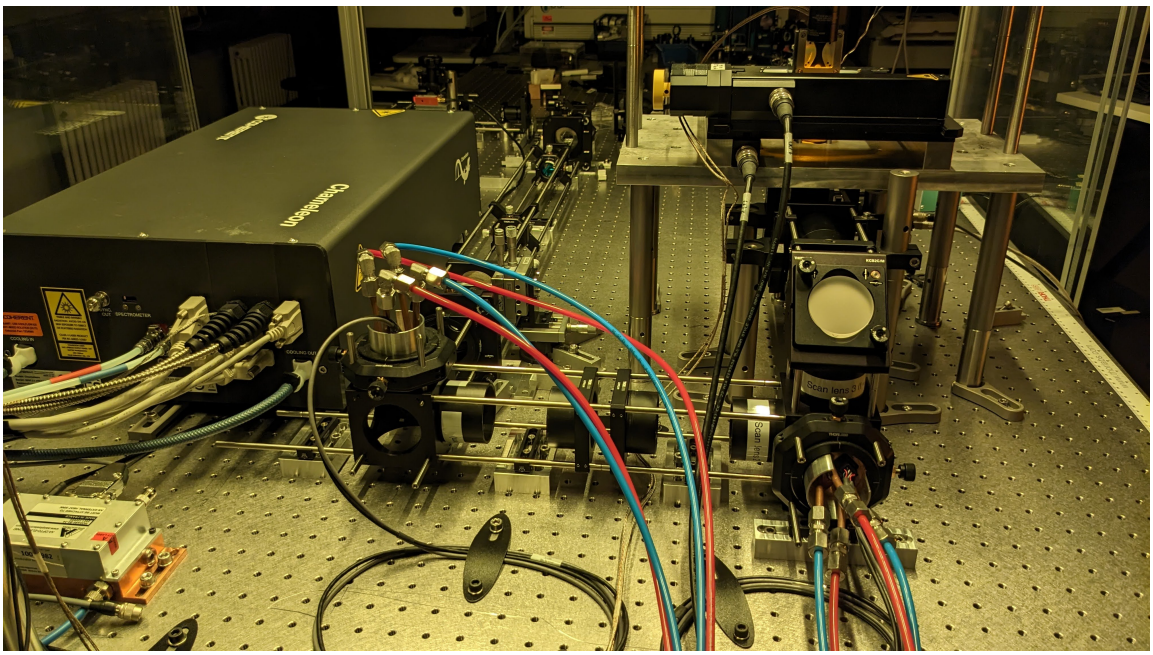

Photograph of the next-generation multi-focus 3D laser printing setup.

In this chapter, I will present the optical setup used for next-generation multi-focus 3D laser printing. For realizing the envisioned machine, the efforts described in the preceding chapters are combined by employing a sensitive photoresist and high-quality micro-optical components for hybrid beam splitting. First, a scheme of the optical setup with all components will be presented. The employed low-aberration scan optics will be described and the focusing quality of the entire setup will be simulated by computing the focus profile for different foci in the focus array. Lastly, I will highlight an experiment to characterize the voxel size that can be effectively used for printing.

6.1 An Optical Setup for High-Speed Multi-Focus 3D Laser Printing

With a sensitive photoresist and high-quality micro-optical components for low-aberration beam splitting at hand, the completion of next-generation multi-focus 3D laser printing is within reach. To allow for fast printing, a suitable optical setup with a powerful laser source, fast laser scanning capabilities, low-aberration optics and sufficient modularity for the implementation of hybrid diffractive-refractive beam splitting is needed. These requirements were combined in the assembly of a custom-built optical setup.

Figure 6.1 shows a schematic overview of the optical setup built for multi-focus 3D laser printing with a basic arrangement based on earlier works [33, 179]. The femtosecond-pulsed output beam of a Ti:Sa laser (Chameleon Ultra II, Coherent) with a pulse duration of $t_p = 140\,\mathrm{fs}$ and a repetition rate of $R_p = 80\,\mathrm{MHz}$ is set to the wavelength $\lambda = 790\,\mathrm{nm}$ featuring an output power of 3.7 W. Using a telescope comprising lenses L1 and L2, the beam is 1.25× demagnified and imaged into an acousto-optic modulator's (AOM's, MT80-A1.5-IR, AA Opto Electronic) TeO_2 crystal, which allows for fast power modulation.

The zeroth order is directed into a beam dump while the first diffraction order is imaged onto the diffractive optical element (DOE) via a telescope comprising lenses L3 and L4 with a 1.6× demagnification. The DOE design is shown in subsection 5.2.1. The manufacturing and optimization of the DOE used in the optical setup is described in section 5.3. Without the enhanced performance the optical setup could not scan as many laser foci and would potentially expose light in between foci. Matching the target beam diameter $d_{1/e^2} = 571.3\,\mu\mathrm{m}$ with a flat wavefront at the DOE is vital since the DOE design value M depends on the number of grating periods per beam diameter like explained in section 5.1. Therefore, the beam parameters at this location are of great importance for the performance of the whole optical setup.

Next, the incident beam is diffracted and split by the DOE into 7×7 beamlets that pass a telescope comprising lenses L5 and L6 with a 3.33× magnification to increase beamlet spacing without introducing too much optical path. Lens L7 then telecentrically collimates the individual beamlets and relays them onto their respective lens of the multi-lens array (MLA). The MLA design is shown in subsection 5.2.2. To reduce additional wavefront errors, the manufacturing of the MLA was optimized, which is described in section 5.3. At the MLA, the beamlets feature a beam diameter $d_{1/e^2} = 720\,\mu\mathrm{m}$ with a flat wavefront and get

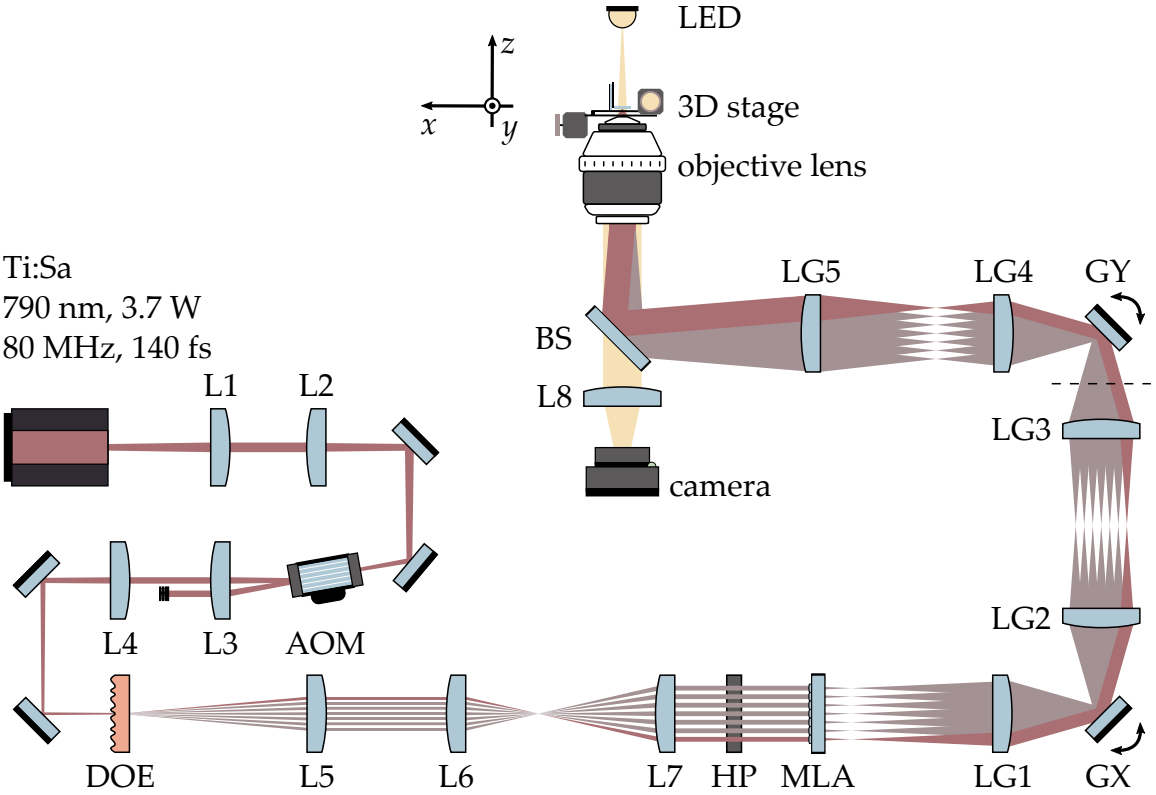

Figure 6.1: Scheme of the optical setup employed for next-generation multi-focus 3D laser printing. A Ti:Sa laser beam (Coherent Chameleon Ultra II) gets directed onto an acousto-optic modulator (AA MT80-A1.5-IR), which allows for fast power modulation. A low-diffraction-order diffractive optical element (DOE) splits the incident laser beam into an array of $7 \times 7 = 49$ laser beamlets and is located at the beam waist. After adjusting the diffraction angles with a telescope, the beamlets are then relayed onto the $7 \times 7 = 49$ individual lenses of a multi-lens array (MLA), creating the focus array, which is imaged onto the writing plane and will be used for printing. Beam steering is enabled by two galvanometric mirrors (GX and GY) in combination with their corresponding lens groups LG1, LG2, LG3, and LG4 before the beam eventually passes a relay comprising the tube lens (LG5) and the objective lens (Zeiss Plan-Apochromat 40x/NA1.4 Oil DIC). A microscope stage (Märzhäuser-Wetzlar Scan IM 120×100) and a piezoelectric inertia stage (PI Q-545.140) enable the translation of the mounted sample in xy- and z-direction, respectively. A yellow-light LED together with a camera and a suitable lens for imaging (L8) allows for monitoring the printing process. To be able to discriminate the many diffraction orders, the outermost beam is highlighted in red. The black dashed line before GY indicates a flip in the coordinate system. Adapted from [58].

focused individually to create the initial focus array with an effectively higher value $M_{\text{eff}} \approx 300$ than initially introduced by the DOE $M_{\text{DOE}} \approx 3$ without increasing angular dispersion. In front of the MLA, an aluminum plate with $7 \times 7 = 49$ holes of 900 µm diameter (HP) is positioned such that the center of the beamlets can pass through but the lateral tails of the respective beamlets are clipped. Not introducing this vignetting would lead to light not focused by the MLA lenses to get focused on the first galvanometric mirror (GX), potentially destroying its coating.

The initial focus array is then imaged into the writing plane with an approximate effective 36× demagnification of the remaining setup. To allow for scanning of the focus array, two galvanometric mirros (GX and GY; 6215H, 6 mm mirror diameter, Cambridge Technology) are inserted in between the initial focus array and the objective lens. A first scan lens group (LG1) collimates the first focus array on the first galvanometric mirror GX. A telescope comprising the lens groups LG2 and LG3 then 1 : 1 images the first galvanometric miror onto the second galvanometric mirror GY. Notably, the coordinate system in Figure 6.1 is flipped here, indicated by a black dashed line. In order to use both galvanometric mirrors at high scanning frequencies for long manufacturing times, they are water-cooled. The water-cooling system was already used by Vincent Hahn and taken over for the new version of the setup.

A last scan lens group (LG4) then restores the focus array by focusing the individual collimated beamlets coming from the second galvanometric mirror. A telescope comprising the tube lens group LG5 and the objective lens (Plan-Apochromat 40x/NA1.4 Oil DIC, Carl Zeiss AG) finally images the intermediate $7 \times 7 = 49$ focus array into the writing plane with a final focus distance $d_{\text{focus}} = 60\,\mu\text{m}$. The optical power entering the microscope objective lens entrance pupil was measured to be $P_{\text{total}} = 954\,\text{mW}$, which translates into roughly $P_{1/49} = 19.5\,\text{mW}$ per focus. Assuming Gaussian foci, this power allows for estimating an average intensity of $13.5\,\text{MW}\,\text{cm}^{-2}$ and a peak intensity of $1.2\,\text{TW}\,\text{cm}^{-2}$ per focus in the focus array.

In chapter 5, great care was taken to create a homogeneous focus array. These efforts are quickly in vain if this initial focus array is not imaged properly through the optical setup. Employing lens systems with high aberrations towards the edges of their field of view (FOV) would impair the focus array and not allow for achieving a homogeneous focus array in the writing plane. Therefore, lens systems with low aberrations even for large FOVs are used. They are based on Ref. [179] with their details discussed in section 6.2.

The micro-optical components presented in chapter 5 allow for printing with $7 \times 7 = 49$ foci with a focus-to-focus distance of 60 µm. Should a different number

of foci, a different focus pattern, or a different focus-to-focus distance be needed in the future, the micro-optical components can easily be exchanged for a modified version. The only fixed parameter is the focal length of the MLA lenses, which determines the beam diameter at the entrance pupil of the microscope objective lens. Therefore, the optical setup is designed to be highly modular.

The sample is mounted on a piezoelectric inertia stage (Q-545.140, Physik Instrumente GmbH & Co. KG) which in turn is mounted on a microscope stage (Scan IM 120 × 100, Märzhäuser-Wetzlar). Both facilitate the translation of the mounted sample in z- and xy-direction, respectively. A yellow-light LED illuminates the sample and, together with a suitable lens for imaging (L8) and a CMOS camera, allows for monitoring the printing process. Between L7 and the MLA, an aluminum plate featuring $7 \times 7 = 49$ individual holes of 900 µm diameter is inserted to only letting the center of each beamlet pass and cut off any lateral Gaussian tails that otherwise would not get collected by the MLA lenses and thereby focused on the first galvanometric mirror GX, potentially damaging it.

To maximize the available maximum focus scanning speed in the writing plane, the setup is designed such that it uses almost the full aperture of the galvanometric mirrors GX and GY by illuminating them with a beam diameter $d_{1/e^2} = 5.775\,\mathrm{mm}$. This enables using a telescope comprising lens groups LG4 and LG5 with a small $2\times$ magnification while still fully illuminating the microscope objective lens entrance pupil $D = 11.55\,\mathrm{mm}$. The smaller the magnification of this very telescope, the higher the translated spatial deflection in the writing plane from the angular deflection of both galvanometric mirrors becomes. Since the maximum scanning speed is ultimately limited by the galvanometric mirror's resonance frequency, this maximizes the available focus scanning velocity and facilitates writing speeds of up to $v = 1\,\mathrm{m\,s^{-1}}$. Hybrid diffractive-refractive beam splitting allows for using large fields of view due to the absence of limiting optics compensating for angular dispersion. The used field of view has a diameter of 594 µm, which is close to what the objective lens can handle. This emphasizes the importance of low-aberration scan optics all the way towards the edges of the available field of view.

The electronic control of the setup must offer short response times to synchronize the AOM and galvanometric mirrors for fast printing. This task was taken over by a real-time computer and a field-programmable gate array (FPGA) (7931R, NI Corp.), which was equipped with a transceiver module (5783, NI Corp.). An initial setup control software was developed during my Master's thesis [180] and later updated by Vincent Hahn for printing large metamaterials [33].

6.2 Low-Aberration Scan Optics

In this section, the design, assembly, and simulated quality of the macroscopic lens systems shown in Figure 6.1 and denoted as LG1, LG2, LG3, LG4, and LG5 is shown. The lens systems are based on Ref. [179]. However, the system used in the referenced work is not able to properly image the full FOV used by the $7 \times 7 = 49$ focus array properly and would deteriorate the outermost foci. To further decrease aberrations for this specific setup, LG2, LG3, and LG4 were therefore tweaked slightly while LG5 was newly developed and LG1 reworked for the different required focal length. The ray-tracing simulations for development and analysis were performed in the optical design software OpticStudio (Zemax LLC).

6.2.1 Lens Group Designs

Figure 6.2 depicts the five macroscopic lens groups shown in the setup overview Figure 6.1. All constituting lenses were bought individually and assembled together by the author. The ray-tracing computations of the depicted simplified beams were performed in OpticStudio. For clarity, only the central and the two outermost beamlets are shown in the side view instead of all seven beamlets otherwise visible. The detailed lens data can be found in section A.2 in the appendix.

LG1 is shown in Figure 6.2a and collimates the beamlets coming from the initial focus array created by the MLA onto the first galvanometric mirror. It was reworked from the versions published in Refs. [33, 179] to feature the suitable effective focal length $f_{\mathrm{LG1}} = 73.9\,\mathrm{mm}$ to illuminate the galvanometric mirror with the required beam diameter and to minimize aberrations for the large FOV in use. Lens groups 2 and 3 (LG2 and LG3) shown in Figure 6.2c $1:1$ image the first onto the second galvanometric mirror with effective focal lengths $f_{\mathrm{LG2+3}} = 74.4\,\mathrm{mm}$. The lenses of this setup are identical to the versions in Refs. [33, 179] with slight changes in their positioning to minimize aberrations for this specific setup. From the second galvanometric mirror, lens group 4 (LG4), shown in Figure 6.2b creates an intermediate focus array. It features the effective focal length $f_{\mathrm{SL4}} = 58.3\,\mathrm{mm}$ and was used like in Refs. [33, 179]. A completely new tube lens system was developed as lens group 5 (LG5) shown in Figure 6.2d to collimate the beamlets coming from the intermediate focus array into the entrance pupil of the objective lens. In comparison to previous versions of this this optical design, the aperture of the galvanometric mirrors is almost fully illuminated, which requires a shorter effective tube lens focal length $f_{\mathrm{TL}} = 117.3\,\mathrm{mm}$ to properly illuminate the objective lens entrance pupil. Together with LG4, this lens group forms a $2\times$ telescope. The design was optimized for low aberrations in large FOVs.

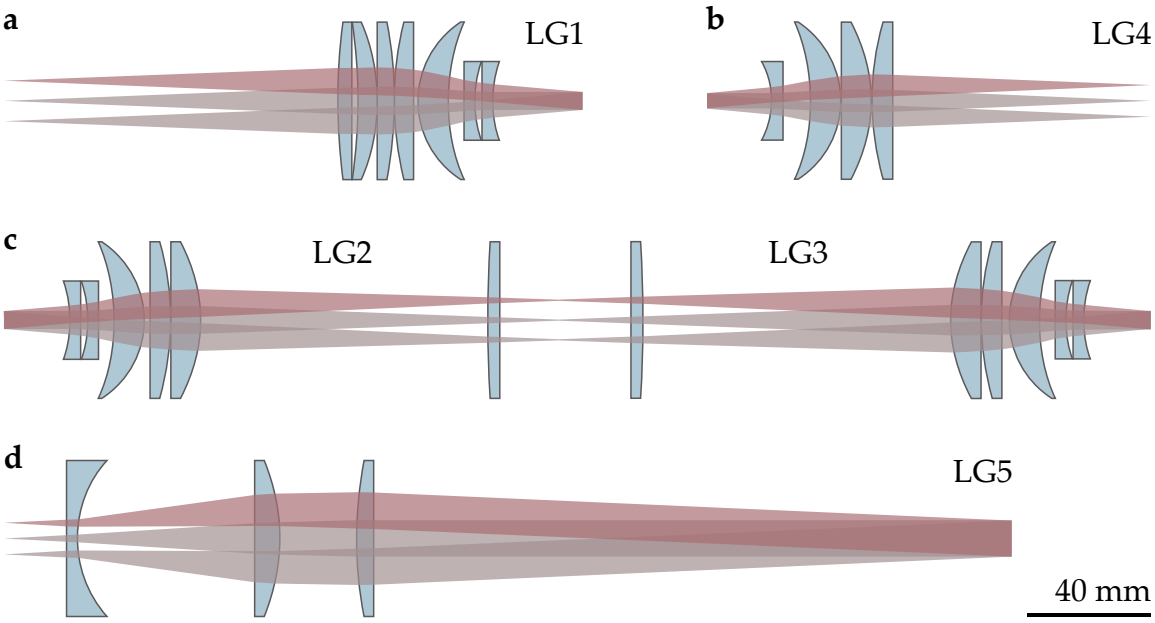

Figure 6.2: Schematic overview of the different lens systems employed in the optical setup shown in Figure 6.1. The outermost beam is highlighted in red. **a,** depiction of the first lens group, which images the focus array and was improved for low aberrations. **b,** depiction of the fourth lens group, which creates the final macroscopic focus array before it is imaged down onto the writing plane. **c,** depiction of the 1 : 1 telescope comprising lens groups two and three, imaging the first onto the second galvanometric mirror. **d,** depiction of the fifth lens group acting as a tube lens. This lens group was newly designed for a short focal length and low aberrations. Adapted from [58].

To ensure correct positioning of the individual lenses inside the respective lens tube for each lens system, spacer rings were used. The required thickness was calculated using Autodesk Inventor (Autodesk, Inc.) and the spacer rings manufactured by CNC cutting. This was necessary since small errors in thickness could cause the interfaces of neighboring lenses to touch. Later fixing the whole lens system with a retaining ring would then damage the lens glasses. Figure 6.3 depicts this arrangement in two examples. Figure 6.3a shows LG1 in a lens tube with spacer rings marked in red. The two small-diameter lenses on the right-hand side are held with a CNC-cut polymer housing. Figure 6.3b shows LG5 in an arrangement of two combined lens tubes, which was taken into account in the spacer ring design.

Figure 6.4 shows some exemplary optical photographs of assembled lens systems by methods described above. Figure 6.4a shows LG1 from the side later

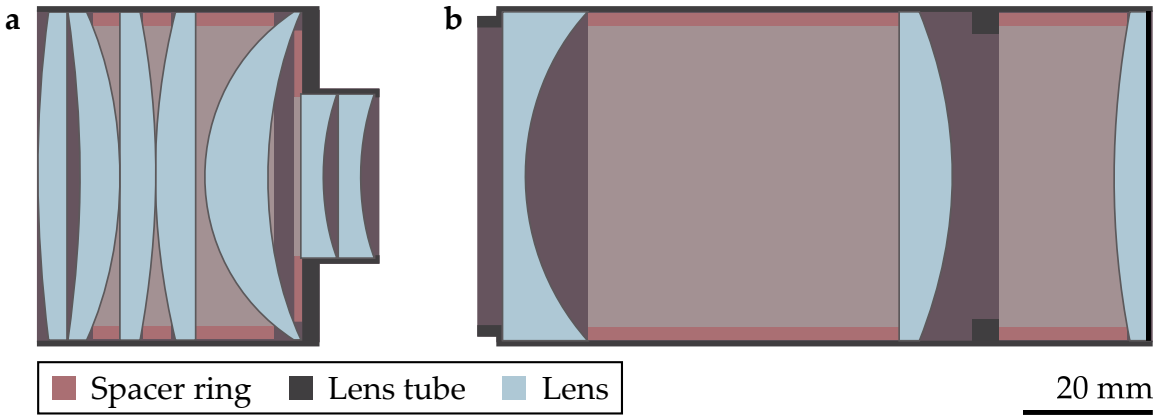

Figure 6.3: Selection of two lens systems featuring spacer rings. The CNC-cut spacer rings depicted in red ensure correct positioning of the individual lenses. **a,** schematic drawing of lens group 1 (LG1) in a lens tube. The spacer rings are especially important in regions where the surfaces could potentially damage each other. **b,** schematic drawing of lens group 5 (LG5) in a lens tube. For this long lens systems, two individual lens tubes are screwed together, which was taken into account in the spacer rings design.

facing the galvanometric mirror. The lenses are positioned inside a lens tube and a CNC-cut polymer housing. The arrangement is screwed in a 60 mm cage cube that has been cut such that the corresponding lens groups hit a mechanical stop when they are at the designed position. This is shown in Figure 6.4b, which displays an optical photograph of LG1 and five lenses of LG2 inside the first cage cube, which later holds the first galvanometric mirror. Figure 6.4c shows LG5 featuring the longest housing.

In the following, the simulated optical performance of the optical setup is discussed. Simulating important parameters as a feedback for the design is vital to minimize aberrations and ensure that the quality of the focus array is sufficient for printing.

6.2.2 *Optical Imaging Quality*

The most important boundary condition for the developed lens systems was the deterioration of the initial homogeneous focus array. To demonstrate the low aberrations within the large FOV occupied by the several foci, optical ray-tracing simulations were performed in OpticStudio (Zemax LLC). The resulting spot diagrams and point spread functions (PSFs) are shown in Figure 6.5.

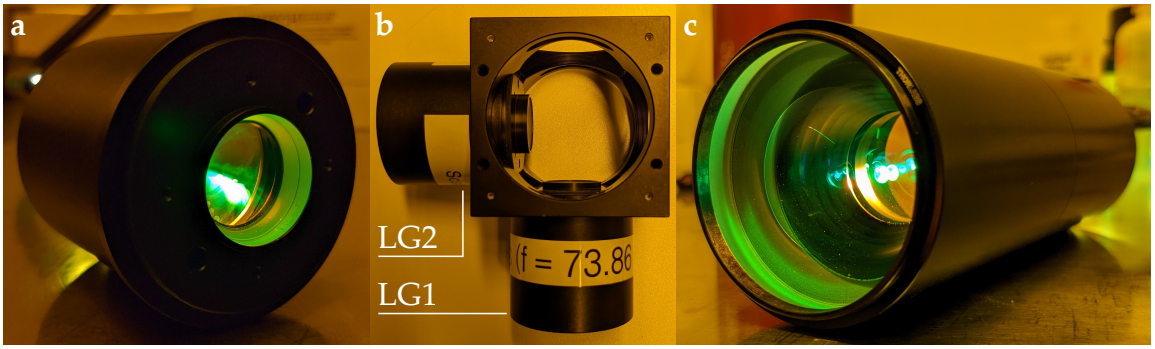

Figure 6.4: Selection of home-built lens systems for next-generation multi-focus 3D laser printing. a, optical photograph of assembled lens group 1 (LG1) comprising seven lenses. CNC-cut spacer rings ensure correct positioning. **b,** optical photograph of the first galvanometric-mirror unit including LG1 and lens group 2 (LG2). The cube made out of anodized aluminum was cut such that the threads for LG1 and LG2 end at the correct position. **c,** optical photograph of assembled lens group 5 (LG5) comprising 3 lenses. Similar to LG1, CNC-cut spacer rings ensure correct positioning.

Obtaining good imaging quality in (1) the center of the focus array is possible for many optical systems while areas towards the edges of the available FOV, e.g., at (2) the edge of the focus array or (3) at the corner of the focus array need suitable optical systems. In Figure 6.5a, the location of the three foci selected as examples for this study within the focus array are highlighted. In the writing plane, the distance between neighboring foci is $d_{\text{focus}} = 60\,\mu\text{m}$.

The computed spot diagrams in the writing plane for these examples are shown in Figure 6.5b. In optical ray-tracing simulations, many rays are launched from a single source point that are traced throughout the optical system [181]. The spot diagram then plots the (x, y)-coordinates of these rays in an arbitrary plane with respect to a reference point, e.g., the center of the focus as plotted in Figure 6.5. In this case, the chosen plane is the writing plane where later 3D objects shall be printed. With zero aberrations in the optical setup the spot diagram would yield rays converging at one singular point in space. Finite aberrations in a real setup lead to spot diagrams forming patterns that deviate from that. Observing these patterns without a reference offers only little information. Therefore, the spot diagrams are plotted with an Airy Disk reference ellipse centered around the chief ray that allows for comparison to the diffraction limit [181].

The spot diagrams for the three examples displayed in Figure 6.5b show a finite size, which is smaller than the respective Airy ellipse drawn in black in all three cases. This suggests diffraction-limited focusing, which, for a FOV size like applied here, was not possible with earlier versions of the optical system.

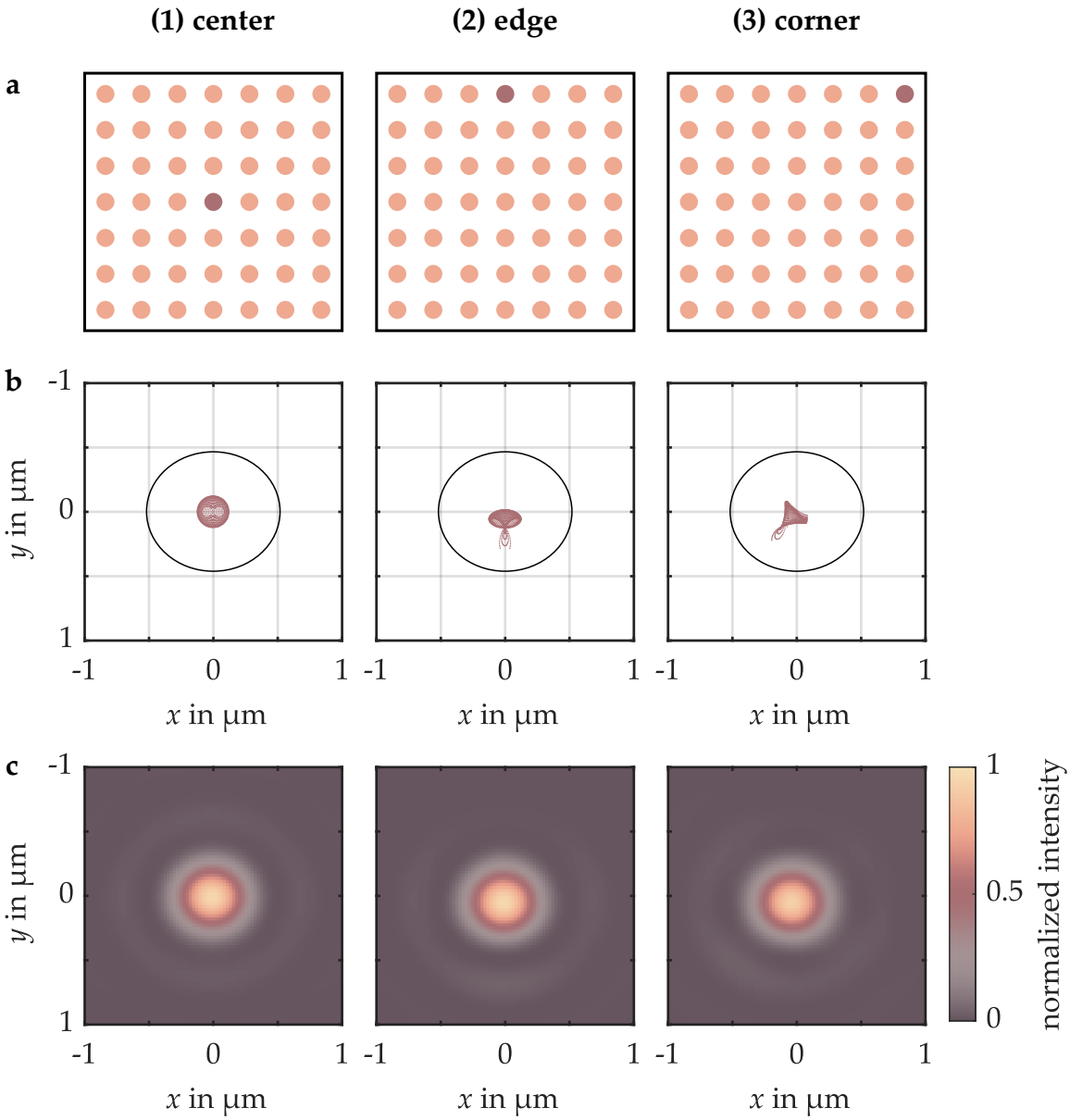

Figure 6.5: Overview of optical focusing quality in the writing plane. The three columns show data in the writing plane for (1) the focus in the center of the focus array, (2) a focus in the center of an edge of the focus array, and (3) a focus at the corner of the focus array. **a,** schematic depiction of the focus position within the focus array. **b,** simulated spot diagram computed *via* optical ray tracing. The black ellipse denotes the Airy ellipse. All spot diagrams show diffraction-limited foci. **c,** simulated point-spread function (PSF) computed *via* optical ray tracing. Adapted from [58].

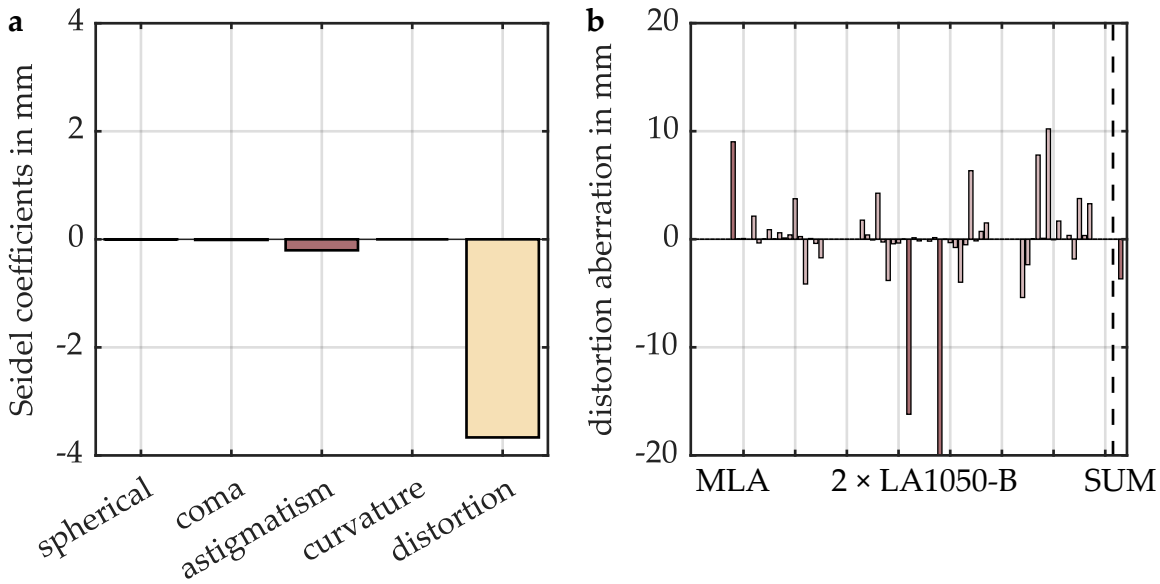

Figure 6.6: Overview of optical aberrations in the setup described in Figure 6.1. **a,** computed Seidel coefficients for the whole setup that are mostly dominated by distortion aberration. Lateral and longitudinal color aberrations are zero and therefore not shown in this plot. **b,** computed Seidel coefficients of the distortion aberration for every surface in the optical setup. The highlighted surfaces are those of the lenses of the multi-lens array (MLA), of the lens LA1050-B, which appears twice in the setup, and the total distortion aberration through the whole setup. Lens LA1050-B marks the main contribution to the overall distortion aberration and is partly compensated by design of the MLA lenses.

In Figure 6.5c, the respective simulated fast-Fourier-transform PSFs are plotted in a false-color diagram. Thereby, the amplitude and optical path difference of each ray originating from a single source point and traced through the setup is used to calculate the complex amplitude of the respective points on the wavefront grid at the position of the exit pupil [181]. The obtained grid is then Fourier transformed and squared to result in the PSF [181]. The PSFs for the analyzed optical setup show good focus quality. Based on these simulations, the optical system shown should be sufficient for next-generation multi-focus 3D laser printing.

The simulated spot diagrams and PSFs in Figure 6.5 indicate good imaging with low aberrations unable to strongly deteriorate the focus quality. However, aberrations still exist in the optical setup. To estimate the magnitude of different optical aberrations, the computed Seidel coefficients are plotted in Figure 6.6. They characterize the aberrations for the object, which is located at the largest distance to the optical axis, i.e., the edge of the exit pupil. Seidel coefficients

appear in fourth-order term of the wavefront error and describe the magnitude of spherical aberration, coma, astigmatism, field curvature, and distortion [182]. Larger Seidel coefficients contribute to larger wavefront errors.

Figure 6.6a shows the five Seidel coefficients for the whole optical setup. The most prominent contribution can be attributed to the distortion aberration. Distortion does not necessarily deteriorate the quality of individual foci but slightly changes their location. Since the aberration is proportional to the third power of the field height, optical systems with large FOVs typically feature larger distortion aberrations [182]. In this case, the sign of the corresponding Seidel coefficient is negative, indicating a barrel distortion where the outermost foci are slightly positioned towards the center of the focus array. This shift can already be seen in the spot diagrams shown in Figure 6.5b where the spot diagrams for the foci at the edge or corner of the focus array are slightly shifted towards the center of the focus array. In the writing plane, this shift of the focus location is less than 100 nm even for the outermost focus. This displacement is smaller than the voxel size and the aberration therefore sufficiently small for the application of next-generation multi-focus 3D laser printing.

Figure 6.6b allows for analyzing the contribution of various components of the optical setup to the total distortion aberration by plotting the computed Seidel coefficients for every surface starting from the MLA. Interestingly, the largest contribution to the total distortion aberration stems from lens LA1050-B, which is used in LG2 and LG3 and highlighted in this plot. The design of the MLA lenses allows for partly compensating for these aberration by introducing a distortion aberration with opposite sign to the setup. This allows for mitigating the aberration and building a setup with sufficient imaging quality even for large FOVs.

6.3 Voxel Size Characterization

Simulating the performance of the optical setup is vital for the development of the underlying lens systems. However, actual printing tests can lead to results that deviate from the simulation. At the end, the most important metric is the voxel size that can be applied for each focus within the focus array. To characterize this property, a sample featuring suspended single voxel lines was 3D printed with the introduced optical setup. The sample was printed with a laser power set at a level that allowed the focus array to barely print every suspended line. This way the structures do not get overexposed and do not print with potentially larger voxels than possible since the size of the voxels depends on the applied two-photon

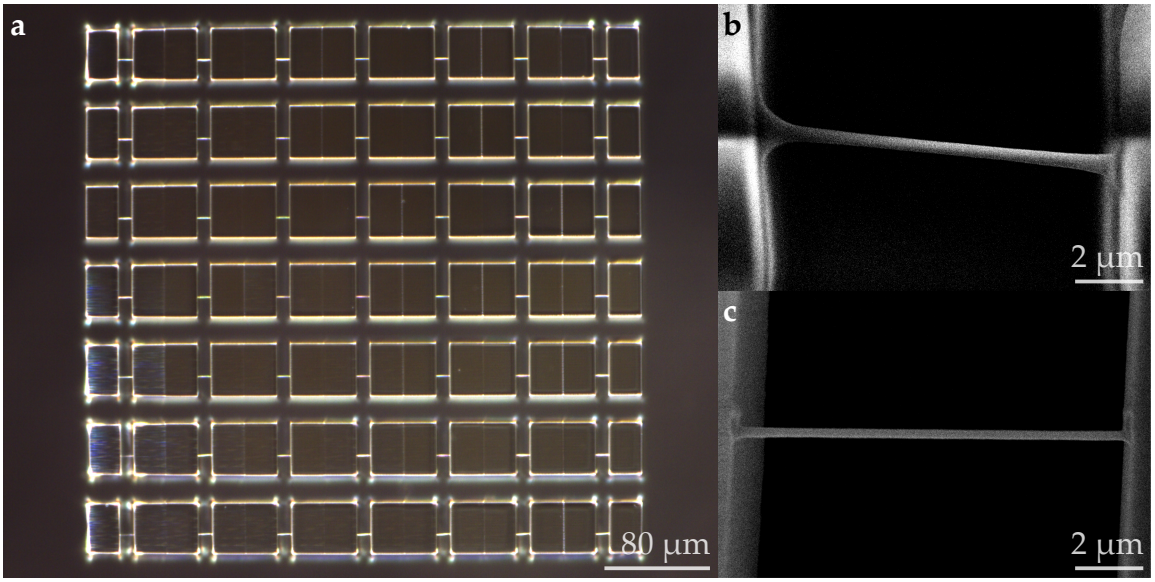

Figure 6.7: Suspended single voxel lines manufactured by the next-generation multi-focus 3D laser printing setup described in Figure 6.1. a, light-microscopy image displaying the structure fabricated by the $7 \times 7 = 49$ focus array. The cuboids are interconnected by single voxel lines. **b,** scanning-electron microscopy image showing a single suspended voxel line from the side. The image has been acquired at an angle $\phi = 85°$ and, together with the remaining voxel lines, is used to determine the axial voxel size by image analysis after correcting for the 5° angle deviation from 90°. **c,** scanning-electron microscopy image showing a single suspended voxel line from the top. The image has been acquired at an angle $\theta = 0°$ and, together with the remaining voxel lines, is used to determine the lateral voxel size by image analysis. Adapted from [58].

exposure dose D_{exp} as explained in section 2.2. The $7 \times 7 = 49$ individual single voxel lines were analyzed with the through-lens detector of a focused-ion-beam scanning-electron microscope (Strate 400S dual-beam system, FEI) to measure the lateral and axial dimensions of the voxels.

Figure 6.7a shows a light-microscope image of the printed sample. Each focus of the array 3D prints a single suspended line, which is supported by cuboids on either side. The cuboids are fabricated together with the suspended lines in one print job and feature a height of 30 µm while the suspended line features a length of 10 µm. Figure 6.7b depicts a scanning-electron microscope image of an exemplary single suspended voxel line. This side view, obtained at a $\phi = 85°$ angle, allows for measuring the axial voxel size of that very focus of the focus array. This procedure is repeated for all 49 lines corresponding to the 49 individual voxels of the array. Figure 6.7c displays the scanning-electron microscope image of a suspended voxel line from the top, acquired at a $\theta = 0°$ angle. All

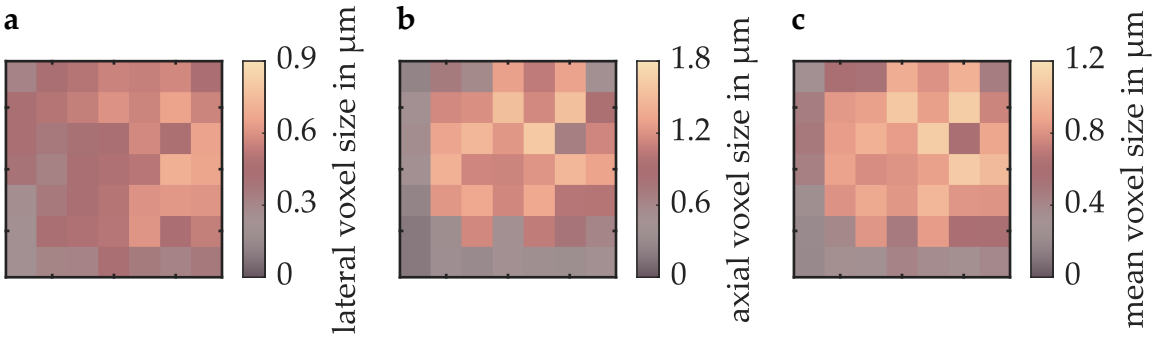

Figure 6.8: Voxel size analysis across the whole focus array. false-color plot of the measured voxel size of each individual voxel in the focus array, obtained by SEM image analysis. **a,** overview of the measured lateral voxel sizes across the focus array. The mean lateral voxel size is $a_{xy,\text{mean}} = (475 \pm 117)$ nm. **b,** overview of the measured axial voxel sizes across the focus array. The mean axial voxel size is $a_{z,\text{mean}} = (905 \pm 435)$ nm. **c,** overview of the calculated mean voxel sizes across the focus array, calculated using the data from **a** and **b**. The mean (lateral and axial) voxel size is $a_{\text{mean}} = (690 \pm 260)$ nm. Adapted from [58].

scanning-electron-microscopy images for the analysis of the $7 \times 7 = 49$ voxel sizes were taken by Qing Sun under the supervision of Yolita Eggeler within a collaboration with the Laboratory for Electron Microscopy at the Karlsruhe Institute of Technology. This data was used to measure the lateral voxel size.

The $7 \times 7 = 49$ individual measurements of both the lateral and axial voxel size by image analysis are summarized in Figure 6.8. The lateral voxel size shown in Figure 6.8a strongly decreases towards the edges of the focus array, calculating to a mean lateral voxel size $a_{xy,\text{mean}} = (475 \pm 117)$ nm. The deviation among the individual foci is more distinct for the axial voxel size depicted in Figure 6.8b. Again, the voxels towards the edges of the focus array show a smaller axial extent. The mean axial voxel size is $a_{z,\text{mean}} = (905 \pm 435)$ nm. Figure 6.8c summarizes both respective measurements by depicting a mean voxel size calculated by the mean value between the lateral and axial measurement. The mean voxel size equals to $a_{\text{mean}} = (690 \pm 260)$ nm.

In general, a smaller voxel size means that the respective focus features a weaker intensity profile. This can, e.g., be caused by a lower laser power for the respective beamlet in comparison to beamlets towards the center of the array. However, the power diffracted in the different orders by the DOE was characterized in subsection 5.3.4. There, no decrease in diffracted laser power towards the edges alone was seen. Loss in laser power can also happen after the diffractive optical element. The hole plate in front of the MLA clips the incoming beamlets to suppress the

tails of their Gaussian intensity profile. If the grating constant of the DOE deviates from its design by, e.g., shrinkage, the beamlet spacing does not perfectly fit to the hole spacing anymore, clipping the outermost beamlets and leading to a loss in power. Furthermore, clipping at the objective lens entrance pupil is possible, too, which can lead to decreased effective numerical apertures.

In addition, aberrations of the optical setup can also lead to impaired focus intensity profiles. In the previous section, the imaging quality of the optical setup was simulated to be sufficient. However, slight deviations of lens spacings from their design or small beam misalignments can add up and introduce aberrations that were not visible in the simulation. The various aberrations introduced by these reasons do not deteriorate all foci equally but show the greatest effect towards the edges of the available FOV due to the large field heights.

Lastly, the microscope objective lens used in the optical setup was not taken into account in any simulation and could introduce aberrations, too. Microscope objective lenses are a complex combination of many lenses and therefore show differences in imaging quality among different assembly batches. The influence of this component was not characterized and could have some influence on the focus array as well.

To summarize, the characterized voxel size shows some inhomogeneities across the focus array. Nevertheless, the individual voxel sizes are very much sufficient for the fabrication of the targeted samples and are still significantly smaller compared to competing approaches of fast 3D laser printing [30, 62].

6.4 Summary and Discussion

With all the ingredients for highly-parallelized and swift multi-focus 3D laser printing in the form of a sensitive photoresist and high-quality micro-optical elements for hybrid diffractive-refractive beam-splitting at hand, this chapter presented an optical setup that combined said ingredients as well as low-aberration optics, a high-power femtosecond-pulsed laser, and fast electronics to a functioning next-generation 3D printer.

The underlying optical setup was thoroughly described and its various components explained. After highlighting the importance of low-aberration scan optics to properly image the initial focus array created by the DOE and MLA, the designs employed in the optical setup were shown and their assembly from a total of 27 individual macroscopic lenses described. To enhance and tailor the imaging quality to the optical setup, the first lens group was reworked and the last one

was developed from scratch by optical ray-tracing simulations, while the rest was adapted from already published results [33, 179].

To simulate the optical performance of the optical setup, the spot diagram and point spread function of exemplary foci across the focus array were computed *via* optical ray-tracing simulations, showing diffraction-limited results. Furthermore, aberrations throughout the optical setup were computed to be low and discussed. The impact of the main contribution to the overall aberration in distortion aberration was discussed. For future modifications of the setup, this could be an entry point for optical improvements. By identifying the optical components mainly contributing to this aberration, a first building block for this potential future development was set.

To close off the chapter, an experiment characterizing the voxel size for each focus across the focus array was presented and analyzed. The $7 \times 7 = 49$ focus array fabricated suspended lines that were imaged by scanning-electron microscopy and analyzed by image analysis to measure the lateral and axial voxel size. Summarizing the acquired data allowed for determining the mean voxel size for the setup and voxel size inhomogeneities between different laser foci. The potential origin of these imperfections in beam clipping at the hole plate in front of the MLA as well as the objective lens, aberrations by misalignments and small errors in the lens system assembly, and aberrations introduced by the microscope objective lens were discussed.

Improving the homogeneity of the focus array could be an avenue to further improve the printing setup. By characterizing clipping at the specified locations in the optical setup, the reduction in laser power and loss in effective numerical aperture for various foci could be minimized. Furthermore, inhomogeneities in voxel size that cannot be resolved could potentially be compensated by adapting the design of the diffractive optical element. Foci that show small voxel sizes could intentionally receive more laser power in diffraction to counteract the losses of the remaining setup.

To summarize, a functioning next-generation 3D laser printing setup was successfully developed, characterized, and employed. In the following chapter, sub-micron resolved 3D structures with unprecedented voxel numbers fabricated by this setup are presented.

Chapter 7

7 Multi-Focus Manufacturing of Large-Scale Microstructures

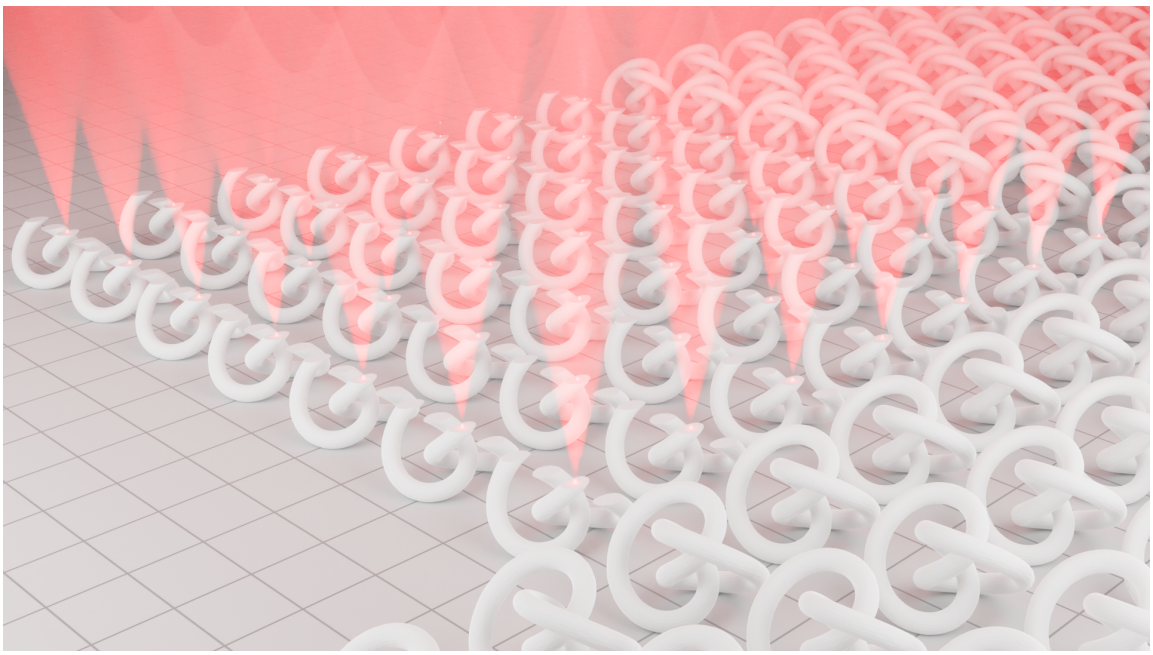

Artistic render of the multi-focus manufacturing of many identical 3D structures.

In this chapter, I will demonstrate the capabilities of the newly developed home-built multi-focus 3D laser printing setup by showcasing successful applications in the fields of respiratory sciences, material sciences, and particle physics. The sample properties demanded for these various research projects could not have been met with previous printing rates. All presented results have been achieved with the photoresist presented in chapter 4 and using the full laser power as specified in chapter 6.

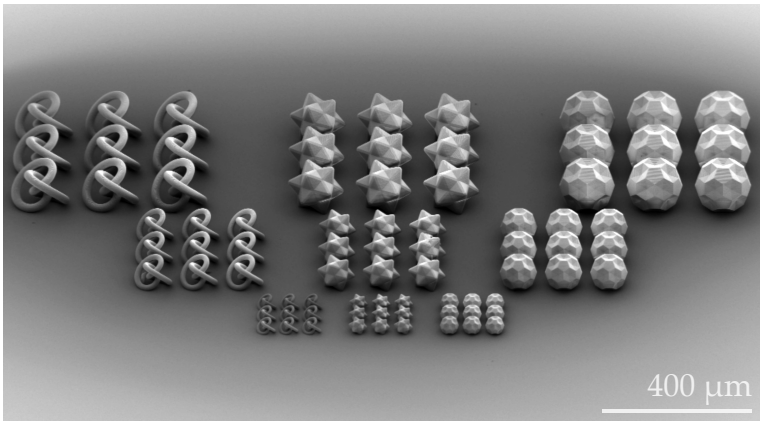

Figure 7.1: A glimpse of next-generation particle engineering in respiratory sciences. Scanning-electron micrograph showing arrays of carrier particles for dry-powder inhalation in different geometries and sizes. From left to right, the name of the designs are (1) rolling knot, (2) pharmacone, and (3) soccer ball. Adapted from [183].

7.1 Millions of Carrier Particles for Respiratory Drug Delivery

The first application of the next-generation multi-focus 3D laser printing setup described in this thesis lies in the field of respiratory sciences. With the new printing rate of 10^8 voxels s^{-1} achieved, the fabrication of the necessary amount of carrier particles for dry-powder inhalation on the lab scale is possible for the first time. In the following, the need for these structures is discussed and the manufacturing results presented. The employed method to release the particles from the substrate damage-free is shown in subsection 3.3.1 of chapter 3.

7.1.1 Tailored Structures for Dry-Powder Inhalation

Treating systematic and especially respiratory diseases by drug inhalation is a well-established and wide-spread approach [184]. To implement this approach, inhalable, pulmonary formulations are needed to deliver the medication to the desired location in the lung [184]. These pulmonary formulations have to fulfill two requirements [184, 185]:

1. the formulation needs to get aerosolized in-situ (usually by a device),
2. the formulation must be able to disperse into small droplets or particles with a size $s_{aero} < 5\,\mu m$.

The latter is important to stay in the inhalable size range. However, some therapies like, e.g., antibiotic treatment require especially high dose applications, which complicates fulfilling the described requirements [184, 186]. In general, meeting these prerequisites can be achieved by different combinations of formulation approaches and matching devices [184, 187]:

1. liquid formulations dispersed by nebulizers or soft mist inhalers forming small droplets with their size governed by the device,
2. liquid-dry formulations dissolved or dispersed in a pressure-liquefied propellant with the propellant quickly evaporating after dispersion and the remaining material forming the aerosol,
3. dry-powder formulations, which benefit from high durability but suffer from low fluidity and uncontrolled agglomeration [188]. Here, three different formulation approaches can be chosen from [184]:
    a) large carrier particle and micrometer-sized active ingredients,
    b) soft agglomerates of the micrometer-sized drug in spherical shapes,
    c) spray-dried low-density particles engineered for high porosity.

In general, dry-powder formulations require development to balance interactions and forces between individual particles of the dry-powder bulk to guarantee high stability both in storage and during processing [184, 189]. Furthermore, dispersion during processing and the generation of fine particles in the inhalation step must fulfill the necessary requirements as well [184, 189].

Especially for low-dose respiratory therapies, blends consisting of large carrier particles and micrometer-sized drugs like mentioned in 3a) are still the preferred formulation [184, 188], making the preparation of the blend easier than determining the weight of the drug in the microgram regime. For these dry powders with large carrier particles, micrometer-sized drug particles are blended with and adhere to larger carrier particles [184]. During inhalation, the drug is released from the carrier upon impact. In the past, lactose was used as a carrier particle, however, perfect control over the shapes and sizes of the various chunks of lactose was hard to achieve, severely limiting the efficiency of the method. Ideally, the size distribution of the individual carrier particles should be as small as possible [183]. Therefore, additive manufacturing is an attractive avenue for supplying tailor-made carrier particles to greatly enhance the performance of the formulations incorporating large carrier particles to potentially tailor aerosol behavior [183, 184]. Figure 7.1 depicts three different potential tailor-made carrier particle designs created by our collaborators for next-generation particle engineering in respiratory sciences. The different structures were fabricated with a Photonic Professional GT lithography device (Nanoscribe GmbH & Co. KG).

While the sole fabrication of carrier particles with, e.g., a size of $s_{\text{carrier}} = 50\,\mu\text{m}$ is attainable for multi-photon 3D laser printing, (1) the biocompatibility of the manufactured polymer and (2) the sheer amount of particles necessary to form a macroscopic powder poses a challenge. A small amount of powder $m_{\text{powder}} = 100\,\text{mg}$

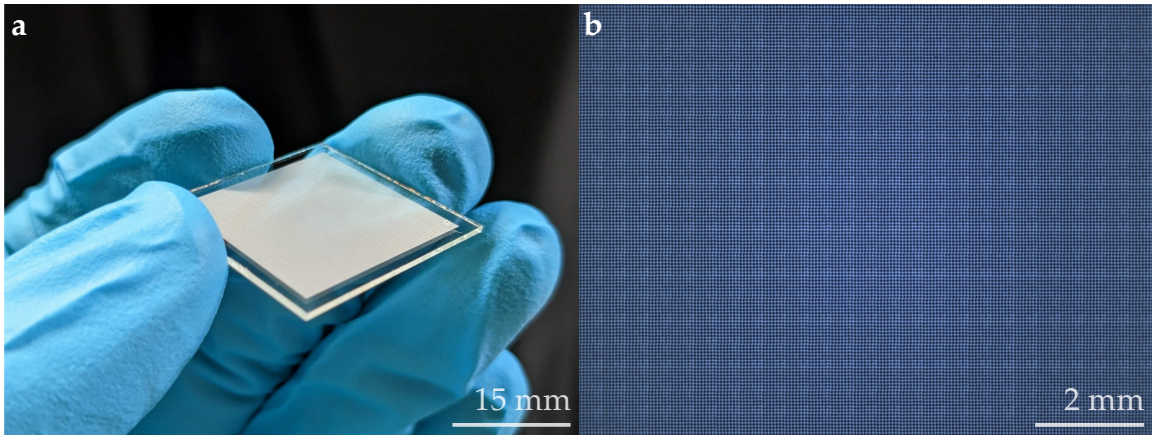

Figure 7.2: Overview of large scale manufacturing of rolling-knot carrier particles by the next-generation multi-focus 3D laser printing setup presented in this thesis. In total, 122,500 individual structures with equidistant center distance $d_{\text{focus}} = 60\,\mu\text{m}$ were manufactured on a $25 \times 25\,\text{mm}^2$ glass substrate in less than 4 h print time. The side length of a single particle is 50 µm. **a,** optical photograph of the full glass substrate with carrier particles printed onto it. In total, $50 \times 50 = 2500$ writing fields were fabricated using the $7 \times 7 = 49$ focus array resulting in a printed area of $21 \times 21\,\text{mm}^2$. **b,** light microscopy image showing a section of the sample, revealing a large number of carrier particles.

for early-stage research projects quickly exceeds particle numbers over 1 million. For state-of-the-art multi-photon 3D printers, manufacturing these particles in the required amount would take months of print time, which makes the development of swift multi-photon 3D laser printing setups highly desirable [183, 190]. In this section, this aspect is addressed by fabricating millions of tailor-made carrier particles of different designs for dry-powder inhalation in a few days by the next-generation multi-focus 3D laser printing setup described in this thesis. This was previously impossible due to the lack of sufficient printing rate in the required resolution regime. For the first stage of a collaboration with the group of Regina Scherließ working in respiratory sciences in Kiel, the three designs "rolling knot", "pharmacone", and "soccer ball" shown in Figure 7.1 were manufactured for investigation.

7.1.2 Results

To demonstrate the capabilities of next-generation multi-focus 3D laser printing, the rolling-knot design was printed on a conventional $25 \times 25\,\text{mm}^2$ glass substrate. Thereby, 122,500 individual 50 µm-sized structures were 3D printed in less than 4 h print time using $50 \times 50 = 2500$ writing fields contributing to a printed area of

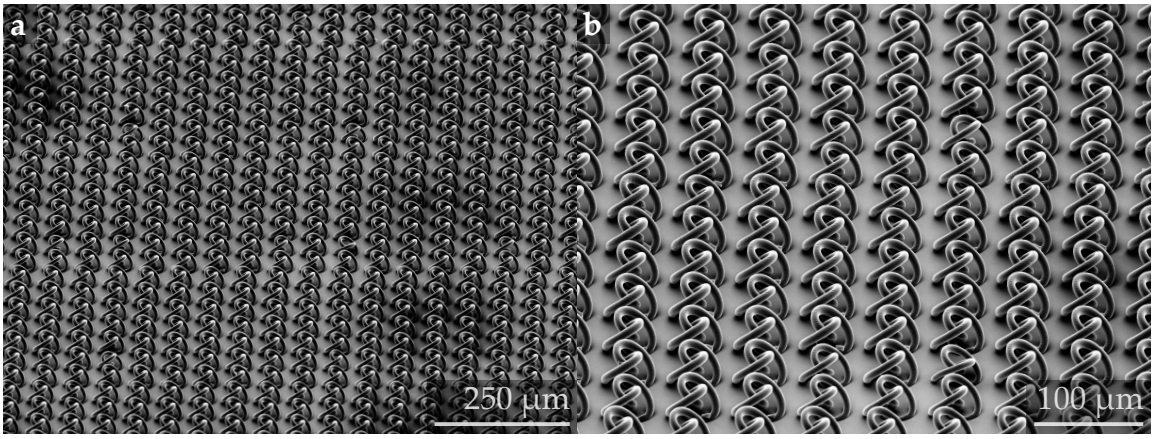

Figure 7.3: Scanning-electron microscope overview of many rolling-knot carrier particles fabricated by multi-focus 3D laser printing. Both images show a closer view of the same sample presented in Figure 7.2. **a,** scanning-electron micrograph showing a large scene of rolling-knot carrier particles 3D printed on a glass substrate using the $7 \times 7 = 49$ focus array. **b,** scanning-electron micrograph revealing a close-by view of individual rolling-knot structures with a knot-to-knot center distance of 60 µm. Adapted from [58].

$21 \times 21\,\mathrm{mm}^2$. They were printed with a hatching distance of 200 nm and a slicing distance of 300 nm. Figure 7.2 depicts the resulting sample on a large scale. An overview of the substrate with a large number of 3D-printed carrier particles is shown in Figure 7.2a. Macroscopically, the tightly fabricated structures look like a dense layer of homogeneous color, making them indistinguishable to the naked eye. A light-microscopy image shown in Figure 7.2b reveals many individual carrier particles in a section of the sample.

To further resolve the large array of microstructures, Figure 7.3 depicts scanning-electron-microscopy images revealing the individual rolling-knot carrier particles. In Figure 7.3a, a large amount of carrier particles is shown while Figure 7.3b offers a more close-by view, resolving individual rolling-knot structures.

Next to the sheer mass production of the required carrier particle designs, the available freedom in design was used to tailor macroscopic surface roughnesses to enhance drug adhesion on the carrier particle. To achieve this, the rolling-knot carrier particles were fabricated using different hatching- and slicing parameters varying between 200 nm and 700 nm. Figure 7.4 gives an overview of this experiment by showing the different combinations of manufacturing parameters together with the scanning-electron-microscopy images of a respective 3D printed rolling-knot particle. Together with our collaborators in the field of respiratory

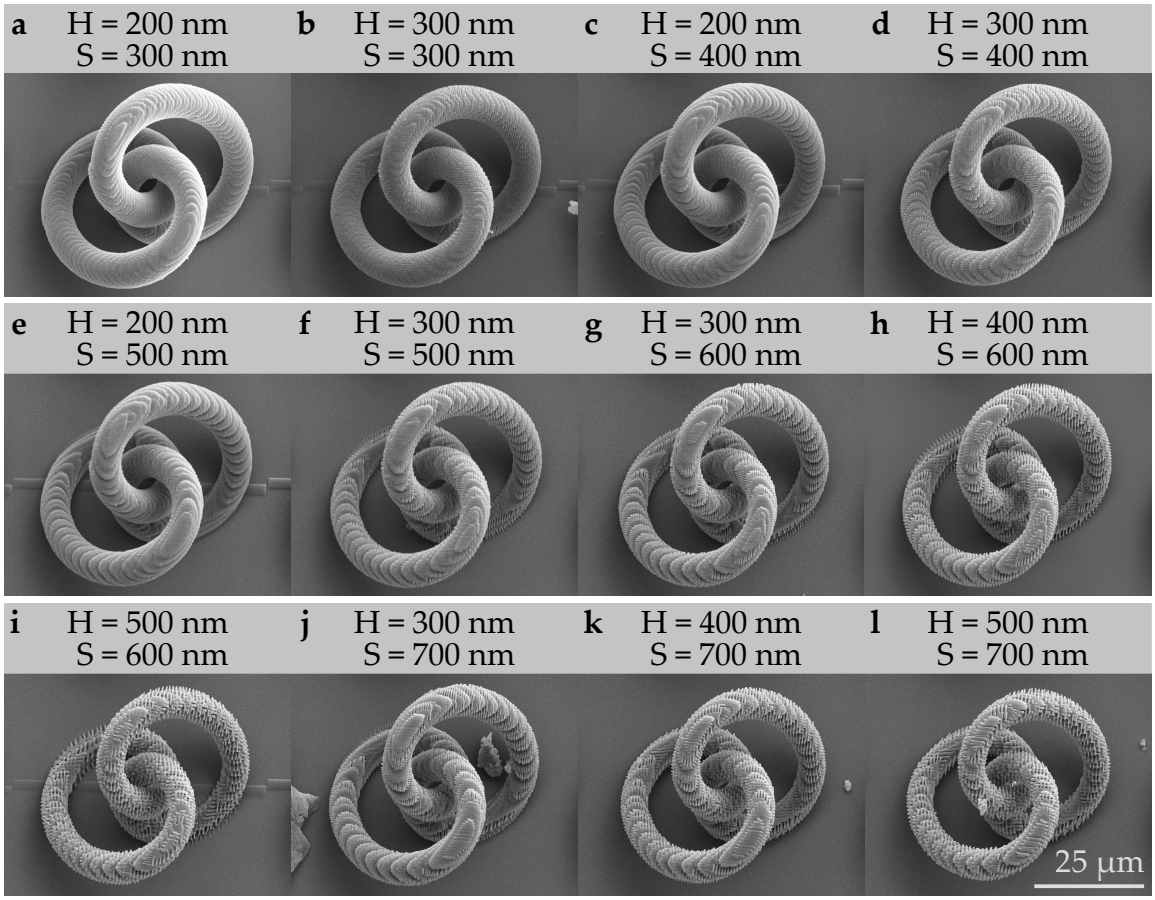

Figure 7.4: Overview of rolling-knot carrier particles 3D printed with varying hatching (H) and slicing (S) parameters. a-l, scanning-electron micrographs showing single carrier particles. To enhance drug adhesion, the degree of macroscopic surface roughness can be controlled by adjusting hatching and slicing. For the following experiments, a hatching $H = 300\,\text{nm}$ and slicing $S = 400\,\text{nm}$ was chosen.

sciences, the combination shown in Figure 7.4d comprising a hatching distance $H = 300\,\text{nm}$ and a slicing distance $S = 400\,\text{nm}$ was chosen as a compromise between structural stability and macroscopic surface roughness for enhanced adhesion properties for the drug particles with a few 1 µm in size. This set of parameters is used for the large-scale manufacturing presented in the following.

To fit more carrier particles on one substrate and therefore decrease the number of individual print jobs necessary for the required amount of structures, 2-inch diameter glass wafers were used for large-scale 3D laser printing of the three carrier-particle designs. Figure 7.5 shows the results of fabricating over 1 million carrier particles in the requested geometries. Figure 7.5a depicts three 2-inch

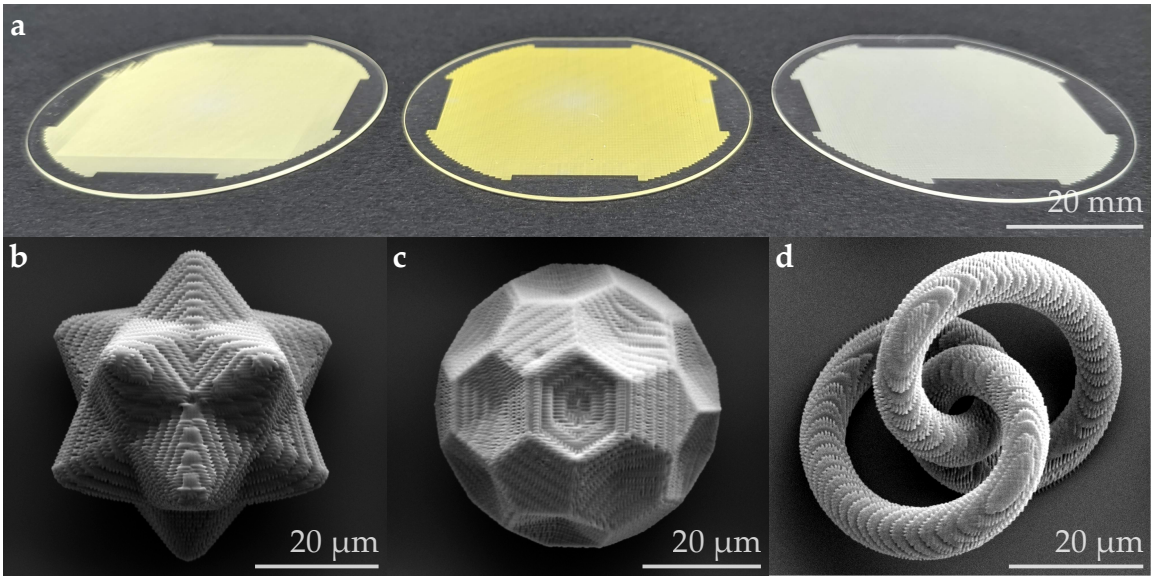

Figure 7.5: Overview of over 1 million carrier particles featuring different geometries. a, optical photograph showing three 2-inch diameter glass wafers with carrier particles of different designs manufactured onto them by the next-generation multi-focus 3D laser printing setup presented in this thesis. From left to right, the designs printed on these wafers are the so-called (1) pharmacone, (2) soccer ball, and (3) rolling knot. Each wafer contains more than 400,000 individual structures, which have been printed on a sacrificial layer for lift-off. The print time per wafer was 8 h. In total, approximately 7 million carrier particles were manufactured on 18 wafers in 144 h. **b-d,** scanning-electron micrograph revealing a single **b** pharmacone, **c** soccer ball, and **d** rolling knot carrier particle. The surface roughness was intentionally increased by hatching and slicing to potentially enhance drug adhesion. Adapted from [58].

diameter glass wafers with more than 400,000 individual structures printed on each wafer with a sacrificial layer, fabricated with a focus velocity $v = 1\,\mathrm{m\,s^{-1}}$ in 8 h print time. Macroscopically, the 3D printed areas appear in different shades of yellow. This color is due to residual photoinitiator molecules incorporated in the polymer network. Since the different geometries feature different volume filling fractions, the respective shade of yellow is slightly different. The scanning-electron-microscope images shown in Figure 7.5b-d reveal a close-up view of the individual carrier particles making up the large print areas, printed with the hatching- and slicing parameters defined above.

In total, approximately 7 million carrier particles were manufactured on 18 wafers. This accounts to a total print time of approximately 144 h. Figure 7.6 shows $3 \times 5 = 15$ of these samples. For some sample positions, a few carrier particles are

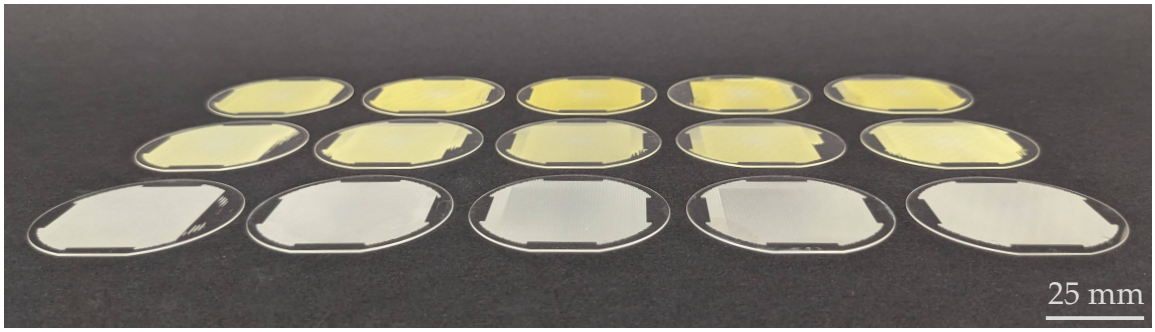

Figure 7.6: Overview of over 6 million carrier particles featuring different geometries. optical photograph showing $3 \times 5 = 15$ 2-inch diameter glass wafers with carrier particles of different designs manufactured onto them by the next-generation multi-focus 3D laser printing setup presented in this thesis. From top to bottom, the designs printed on these wafers are the so-called (1) soccer ball, (2) pharmacone, and (3) rolling knot. Each wafer contains more than 400,000 individual structures, which have been printed on a sacrificial layer for lift-off. The print time per wafer was 8 h.

missing. This can happen when they are not printed perfectly at the glass interface but somewhere in the photoresist without a substrate to attach to. To reduce this incidence, the tilt of the sample is computed by measuring the interface position at different locations before starting the print job. During printing, this tilt is then compensated for by appropriately moving the sample without finding the interface multiple times during printing. This saves manufacturing time, however, the sample becomes sensitive to drifts during fabrication. These can happen because of, e.g., gravity pulling on the substrate which is mounted upside down and fixed by tape, forces applied by the photoresist connecting the microscope objective lens and the substrate, or forces applied by the multiple strips of tape on the glass wafer. Some of the fabricated wafers depicted in Figure 7.6 show regions of missing samples. Here, the particles were not printed at the correct z-position at the interface between the sacrificial layer and the photoresist due to a drift along the optical axis and therefore did not have sufficient connection to the sample substrate. As a result, these particles are lost in the development step. Fortunately, this effected less than 5 % of the printed carrier particles and did not greatly increase the amount of required samples to match the requested total number of carrier particles.

The results of a first study testing the adhesion capabilities of the large-scale manufactured and released carrier particles with a test drug is shown in Figure 7.7. All fabricated samples with intact sacrificial layers shown before were shipped to the research group of Regina Scherließ in Kiel. Melvin Wostry performed the lift-off and filtered out the carrier particles from the used de-ionized water. Afterwards

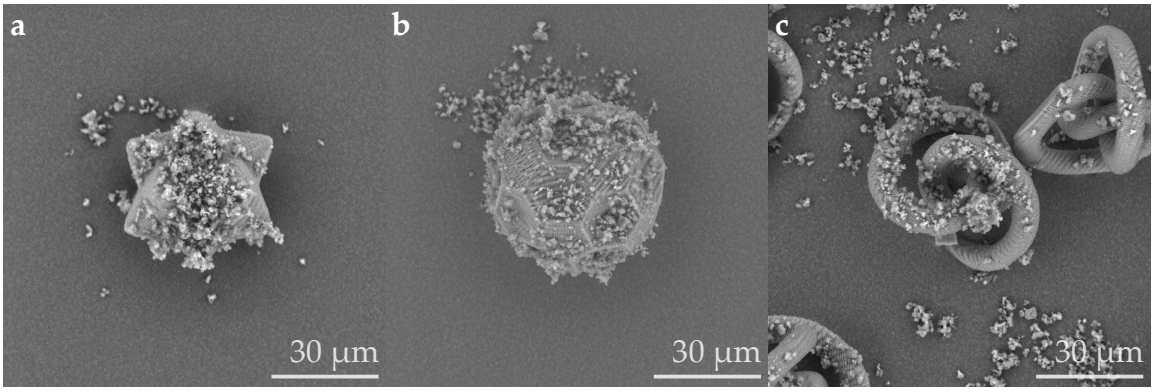

Figure 7.7: Overview of lift-off carrier particles with the active agent budesonid attached. The lift-off, further sample processing including the attachment of the active agent, as well as the scanning-electron microscope analysis was performed by Melvin Wostry in Kiel. **a-c,** carrier particles after lift-off covered with budesonid: **a** pharmacone, **b** soccer ball, **c** rolling knot. The used polymer for fabrication seems to allow for attachment of the active agent. The images have been kindly provided with permission of Melvin Wostry.

he applied the test drug budesonide with an approximate size $x_{50} = 1.37\,\mu m$ (measured at 3 bar dispersion pressure with a HELOS plus RODOS device, Sympatec GmbH). For each carrier particle design, the same number of budesonide particles was used. Their mass was defined to be 10 wt% with respect to the total mass of the used soccer-ball carrier particles.

Figure 7.7a-c show exemplary carrier particles of the three discussed designs with budesonide attached to them. The scanning-electron-microscope pictures were taken by Melvin Wostry. The test drug successfully adheres to the polymer structure of all designs. For this test experiment, small differences among the geometries can already be observed. Budesonide forms large clusters in the dimples of the soccer-ball carrier particle while a smaller amount of particles adheres to the rolling-knot structure. The pharmacone structure shows densely-packed regions of budesnoide on top but only few particles at the sides.

To systematically study the influence of different carrier-particle parameters like geometry, macroscopic surface roughness, or the polymer material used for printing, further studies facilitated by next-generation multi-focus 3D laser printing will be performed in the future.

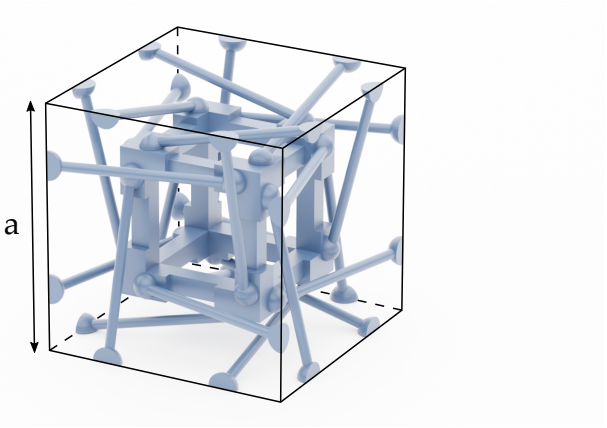

Figure 7.8: Design of a cubic metamaterial unit cell potentially exhibiting a roton-like dispersion relation in a large metamaterial. It comprises a hollowed-out cube with rods connected to it. To fit to the $7 \times 7 = 49$ focus array, the unit cell size was set to $a = 60\,\mu\text{m}$. Adapted from [191].

7.2 Centimeter-Scale Metamaterial Samples

Apart from printing multiple individual, i.e. disconnected, structures at once, multi-focus 3D laser printing is also well suited for printing samples with a lateral periodicity that fits to the focus-to-focus distance $d_{\text{focus}} = 60\,\mu\text{m}$, i.e. connected structures. In the following, two metamaterial samples with a previously unparalleled total size and number of unit cells are shown. One unit cell design was previously proven to exhibit a roton-like dispersion relation [191] while the other lies in the regime of high compressive strengths and was pursued in the framework of a collaboration with the University of Toronto, Canada.

7.2.1 A Mechanical Metamaterial With a Roton-Like Dispersion Relation

Metamaterials are rationally designed structures with effective material properties that exceed the properties of the bulk material [192]. In recent years, chiral metamaterials were shown to exhibit extraordinary effective material properties [191, 193–198], some of which already manufactured by the previous, slower version of this multi-focus 3D laser printing setup [199].

In the next section, a printed metamaterial sample is presented that is based on a recently published design to exhibit a roton-like dispersion relation [191]. Figure 7.8 depicts the metamaterial unit cell made up of a hollowed-out cube with four rods connected to each its sides. These rods do not connect the center cube to its six nearest neighbors along the principal directions but to the twelve neighbors along the cube's face-diagonal direction [191]. The final metamaterial sample which was printed results from a simple-cubic periodic arrangement of these cubes [191].

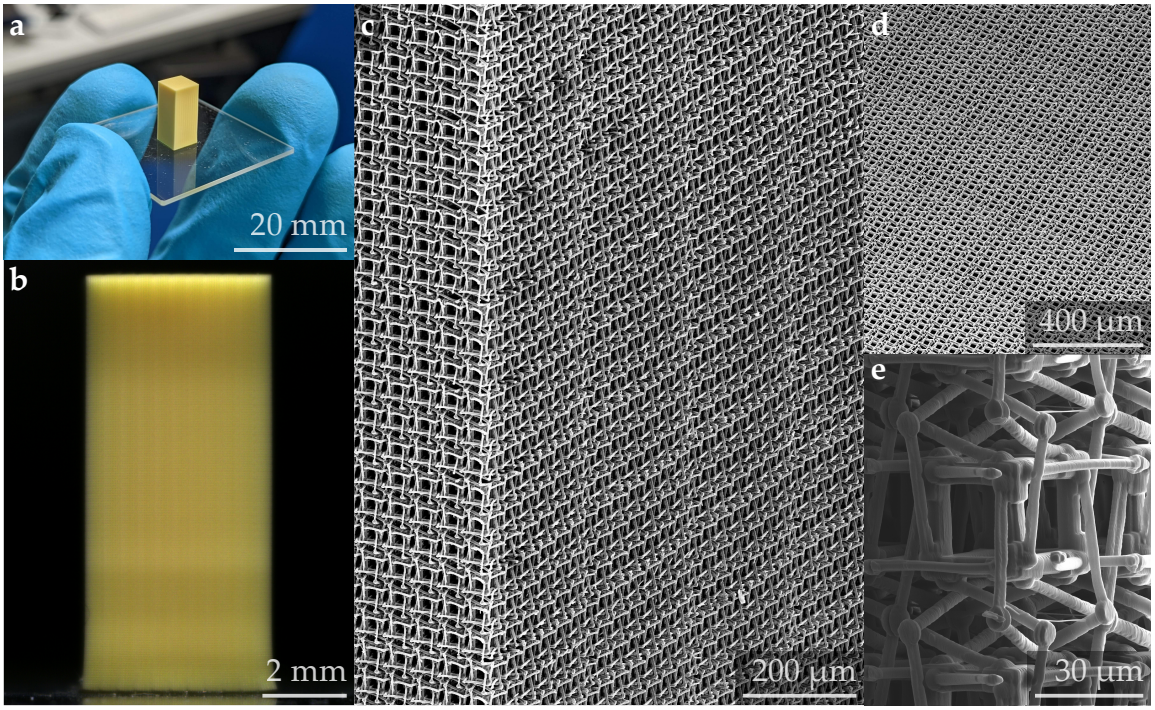

Figure 7.9: Large chiral-roton metamaterial comprising more than 1 million individual unit cells. The structure was fabricated with the next-generation multi-focus 3D laser printing setup presented in this thesis. **a,** optical photograph showing the printed structure on a $25 \times 25\,\mathrm{mm}^2$ glass substrate. The metamaterial comprises $77 \times 77 \times 171 = 1,013,859$ individual unit cells with a unit cell size of $60 \times 60 \times 60\,\mu\mathrm{m}^3$. It makes up a volume of $4.6 \times 4.6 \times 10.3\,\mathrm{mm}^3$ and contains more than 1.7×10^{12} voxels (voids not counted). **b,** light-microscope image showing the full metamaterial tower from a side view. **c,** scanning-electron micrograph revealing the individual unit cells that build up the material. **d,** scanning-electron micrograph depicting the top of the structure, showing a sea of unit cells. **e,** scanning-electron micrograph highlighting a single metamaterial unit cell. Adapted from [58].

The total size of any metamaterial sample is ultimately limited by the required manufacturing time. Printed metamaterial samples in Ref. [191] were severely limited in their number of unit cells and thus their total size due to the manufacturing with a commercial system unable to reach the high peak printing rates of the new setup presented in chapter 6. With the availability of the next-generation multi-focus setup developed within this thesis, these limitations can be exceeded by several orders of magnitude. To fit one metamaterial unit cell inside each focus of the focus array, the unit cell size was set to $a = d_{\mathrm{focus}} = 60\,\mu\mathrm{m}$.

Results

A metamaterial sample featuring the unit cell design shown in Figure 7.8 and manufactured by next-generation multi-focus 3D laser printing is shown in Figure 7.9. With a total size of $4.6 \times 4.6 \times 10.3\,\mathrm{mm}^3$ comprising $77 \times 77 \times 171 = 1,013,859$ individual unit cells and counting approximately 1.7×10^{12} voxels, it exceeds sizes normally accustomed to structures with sub-micron resolution by far while being printed in just two days print time due to a more than $10\times$ higher peak printing rate than the previous version of the setup [33] and a more than $100\times$ higher peak printing rate than commercial systems [24].

Figure 7.9a depicts the macroscopic sample printed on a $25 \times 25\,\mathrm{mm}^2$ glass substrate. It was printed with a hatching distance of 200 nm and a slicing distance of 300 nm. The yellow color stems from residual photoinitiator molecules embedded in the polymer matrix during printing. Figure 7.9b shows a face view of the metamaterial tower captured with an optical light microscope.

To further resolve the sample, Figure 7.9c and Figure 7.9d depict scanning-electron-microscopy images from the sides and the top of the metamaterial crystal. The fragile arms connecting different unit cell cubes were correctly attached during printing to form a stable sample. Figure 7.9e shows a close-up view of one unit cell.

This sample is built up of about 10 times more unit cells than a comparable metamaterial sample fabricated with the previously fastest multi-focus 3D laser printing setup in the same time [33], demonstrating the proposed printing rate enhancement of the next generation developed in this thesis.

In addition to the larger number of foci 3D laser printing in parallel, the setup utilizes a maximum focus velocity of $v = 1\,\mathrm{m\,s}^{-1}$. This allowed printing the shown metamaterial sample with only one print job. Previously, the metamaterial unit cell had to be dissected into more than 50 individual print sub-jobs executed sequentially because the used focus velocity $v = 0.145\,\mathrm{m\,s}^{-1}$ was too slow to connect the fabricated rods properly to the neighboring structures before it swam away in the liquid photoresist [191]. With the high focus velocities now available, this manual splitting is not required anymore. Therefore, the setup developed in this thesis is well-suited to also print other complex metamaterial samples like the one shown in the next section.

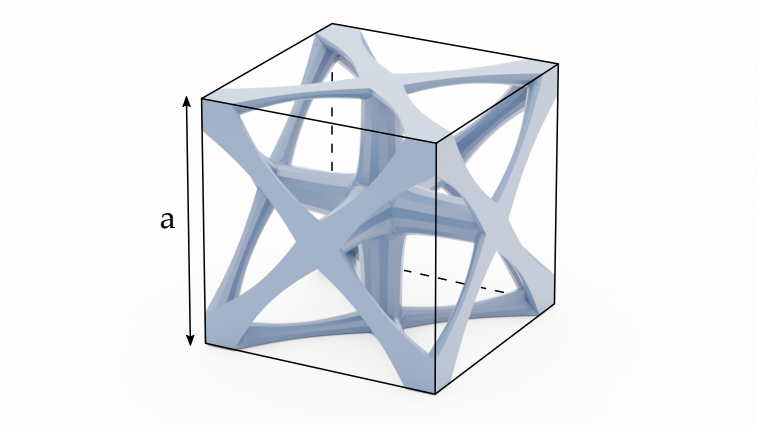

Figure 7.10: Metamaterial unit cell for high compressive strengths. The unit cell was designed by Peter Serles within his PhD research. Its size $a = 20\,\mu m$ will shrink during the pyrolysis step after the manufacturing.

7.2.2 *A Lightweight Metamaterial With High Compressive Strength*

To reach the next level in lightweight metamaterials with high compressive strengths, samples with sub-micron-resolved unit cells are required. By using the machine learning algorithm *Multi-Objective Bayesian Optimization*, a face-centered cubic nanolattice was developed by Peter Serles from the University of Toronto to maximize compressive stiffness and strength with minimum density [200]. The resulting metamaterial unit cell is shown in Figure 7.10 with the lattice struts contributing to a stable crystal.

To arrive at the final sample, the 3D printed metamaterial needs to be pyrolyzed [201–206], where the organic polymer precursor is thermo-chemically decomposed while excluding the ambient atmosphere of oxygen [201]. During this step, the smallest structures shrink fivefold [201], making the lattice struts even thinner. The result is a lightweight metamaterial with a relative densitv of styrofoam (approximately $100 - 200\,g\,cm^{-3}$) and the compressive strength of steel ($100 - 400\,MPa$) [200]. The metamaterial unit cell design shown in Figure 7.10 was printed with a unit cell size $a = d_{focus}/3 = 20\,\mu m$ to laterally fit $3 \times 3 = 9$ unit cells in the writing area of a single focus of the focus array. The entire array thus produces $21 \times 21 = 441$ unit cells in one writing field in a matter of seconds. After pyrolysis, the size of an individual unit cell shrinks down to approximately $a_{final} = 4\,\mu m$.

This pyrolysis step is necessary to arrive at sub-micrometer strut cross-sections, which are necessary to obtain the maximum strength of the material [207]. Since the entire sample shrinks during this step, exceedingly large metamaterial samples are needed. Since the shrinkage drastically reduces the final structure size, the initial printed metamaterial dimensions must be adapted accordingly to still be able to perform mechanical experiments after the pyrolysis. Furthermore, these large samples still need sub-micron resolution to fabricate the thin lattice struts to a satisfactory degree, which cannot be obtained with other 3D laser printing

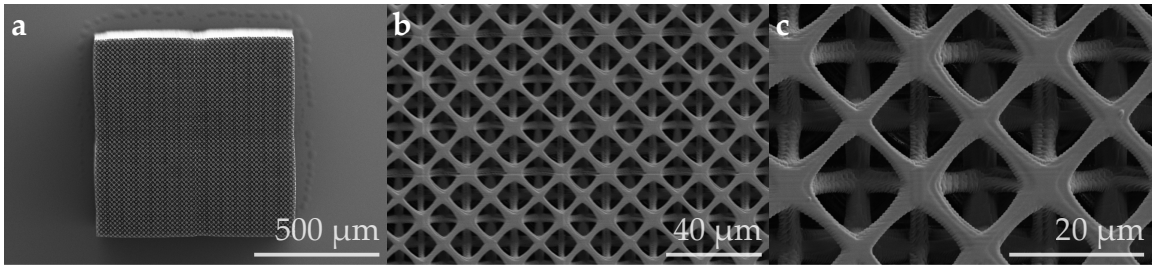

Figure 7.11: Several print quality characterization samples with high compressive strength. The structures were fabricated with the next-generation multi-focus 3D laser printing setup presented in this thesis. **a-c,** scanning-electron micrographs **a** depicting a test sample that was printed with $2 \times 2 = 4$ writing fields, **b** revealing the single $20 \times 20 \times 20\,\mu m^3$-sized unit cells, and **c** showing the single lattice struts that build up the material.

technologies like stereolithography or continuous liquid interface production, which are typically employed for larger structures in the centimeter regime.

Results

To study if the achievable lattice strut resolution by next-generation multi-focus 3D laser printing is sufficient, a small test sample comprising only a few thousand unit cells was 3D printed using $2 \times 2 = 4$ writing fields. Figure 7.11 shows scanning-electron-microscopy images of said sample. It was printed with a hatching distance of 200 nm and a slicing distance of 300 nm. The whole structure shown in Figure 7.11a shows slight shrinkage at the outer corners of the metamaterial crystal at writing field edge regions. Furthermore, slight artifacts from stitching are visible in the form of straight lines crossing the bulk material. These artifacts were minimized by adjusting lateral stage movements for stitching in the final print. Figure 7.11b reveals single unit cells connected by the lattice struts. The close-up view in Figure 7.11c further resolves the fine details of the metamaterial. Slight thickness variations of the lattice struts can be observed that stem from differences in voxel size across the focus array, which was explored in section 6.3.

With the structure parameters described above, a large metamaterial crystal was fabricated. Figure 7.12 gives an overview of the final sample. Since this material was manufactured for a collaboration and shipped to Canada for pyrolysis and further experiments, no scanning-electron-microscopy images were taken to avoid altering the sample by sputtering a thin layer of gold on it. Figure 7.12a shows the macroscopic metamaterial sample featuring $315 \times 315 \times 189 = 18,753,525$ individual unit cells and filling a volume of $6.3 \times 6.3 \times 3.8\,mm^3$ while only requiring

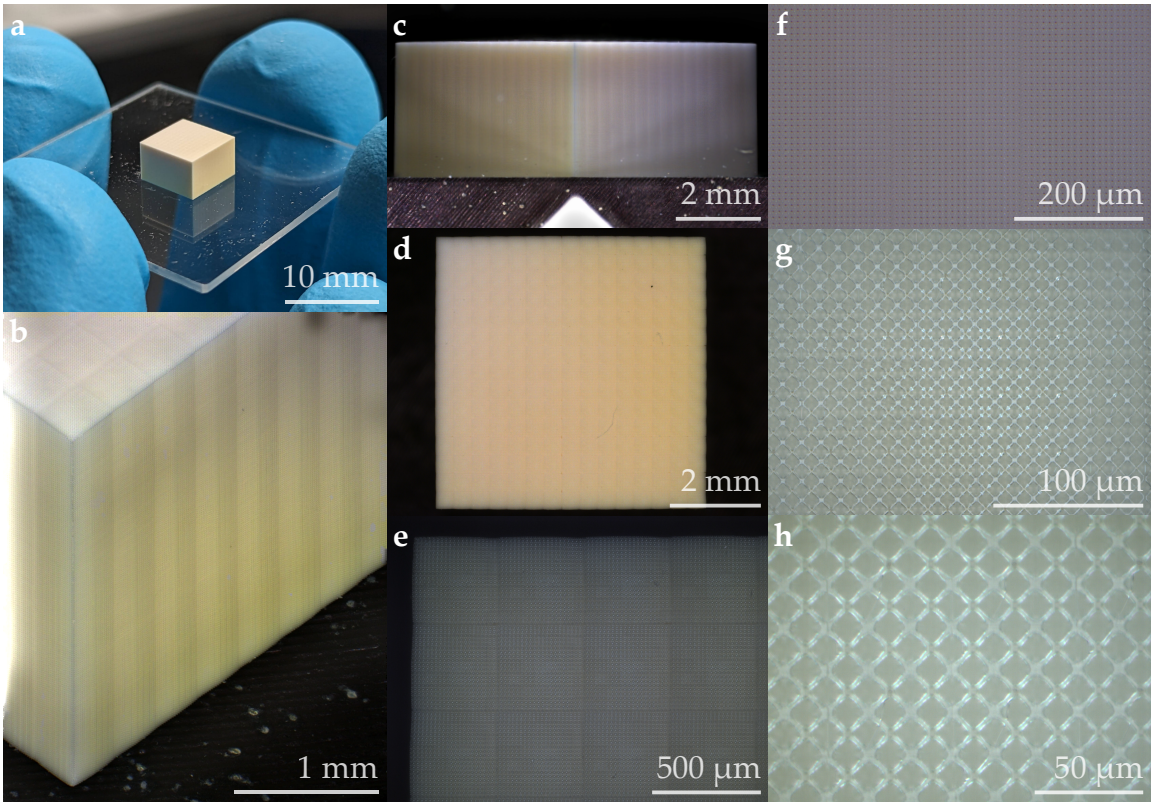

Figure 7.12: Large metamaterial with high compressive strength comprising more than 10 million individual unit cells. The structure was fabricated with the next-generation multi-focus 3D laser printing setup presented in this thesis. **a,** optical photograph showing the structure printed on a $25 \times 25\,\mathrm{mm}^2$ glass substrate. The metamaterial comprises $315 \times 315 \times 189 = 18,753,525$ individual unit cells with a unit cell size of $20 \times 20 \times 20\,\mu\mathrm{m}^3$. It makes up a volume of $6.3 \times 6.3 \times 3.8\,\mathrm{mm}^3$. **b-h,** light-microscope images of different views and magnifications showing **b** an oblique and **c** side view of the metamaterial block, **d** the top of the metamaterial with **e** its upper left corner, **f** a small section of the top of the metamaterial, **g** individual unit cells, and **h** single lattice struts.

two days print time. For the pyrolysis step following afterwards, the sample needs to be detached from the substrate to prevent damage during shrinkage. Therefore, it was printed on a sacrificial layer analogously to the carrier particles presented in section 7.1.

Figure 7.12b-d show light-microscopy images of the sides and the top of the metamaterial crystal. The sample is too large to resolve any individual unit cells in this mode. Figure 7.12e offers a closer view of the top left corner of the top side of the sample, revealing artifacts from stitching in form of straight lines at writing field edges. This is due to the smaller voxel sizes characterized in section 6.3,

leading to more loosely cross-linked polymer networks that are more prone to shrinkage during development than highly cross-linked materials like in the center of each writing field. This aspect can be improved in the future like described in section 6.4 but poses no inherent problem for the application of this material in pyrolysis and the subsequent mechanical experiments.

Figure 7.12f-h further resolve the top of the sample, revealing both the sheer number of unit cells and the individual lattice struts making up the material. Figure 7.12h resolves the small features in a degree light microscopy can offer and shows the sufficient sample quality. With a typical commercially available device, the print time would have been approximately 6 months compared to the 2 days that were needed here.

Subsequent to the optical analysis of the printed sample, it was detached from the substrate and shipped to our collaboration partner Peter Serles in Toronto, Canada. After arrival, the sample was pyrolyzed and tested in preliminary experiments, all performed by Peter Serles. Figure 7.13 gives an overview of the metamaterial crystal shown after pyrolysis. All optical photographs were kindly supplied with permission from Peter Serles.

Figure 7.13a shows the pyrolyzed sample next to a canadian 5-cent coin. Its previous size $6.3 \times 6.3 \times 3.8\,\mathrm{mm}^3$ is reduced to a volume of $2.9 \times 2.8 \times 1.8\,\mathrm{mm}^3$ with its yellow color vanished and turned to black. The structure is light enough to be balanced on a soap bubble like shown in Figure 7.13b. A first experiment examining compressive strength is shown in Figure 7.13c. Here, the sample was sandwiched between two glass substrates and subjected to a weight $m = 1\,\mathrm{kg}$. Despite the thin lattice struts after pyrolysis, the material does not break, being able to support over $1,000,000\times$ of its own weight. Figure 7.13d depicts a second sample of the same design after pyrolysis. More experiments with larger masses and more metamaterial samples will be performed in the future.

7.3 Large-Scale Structures for Potential Scintillator Applications in Particle Physics

The last application of next-generation multi-focus 3D laser printing shown in this thesis lies in the field of particle physics. Within a collaboration with the group of Guido Drexlin working at the KATRIN research facility of the Karlsruhe Institute of Technology, a periodic structure needs to be fabricated on an area of approximately $64\,\mathrm{cm}^2$ for a potential scintillation application.

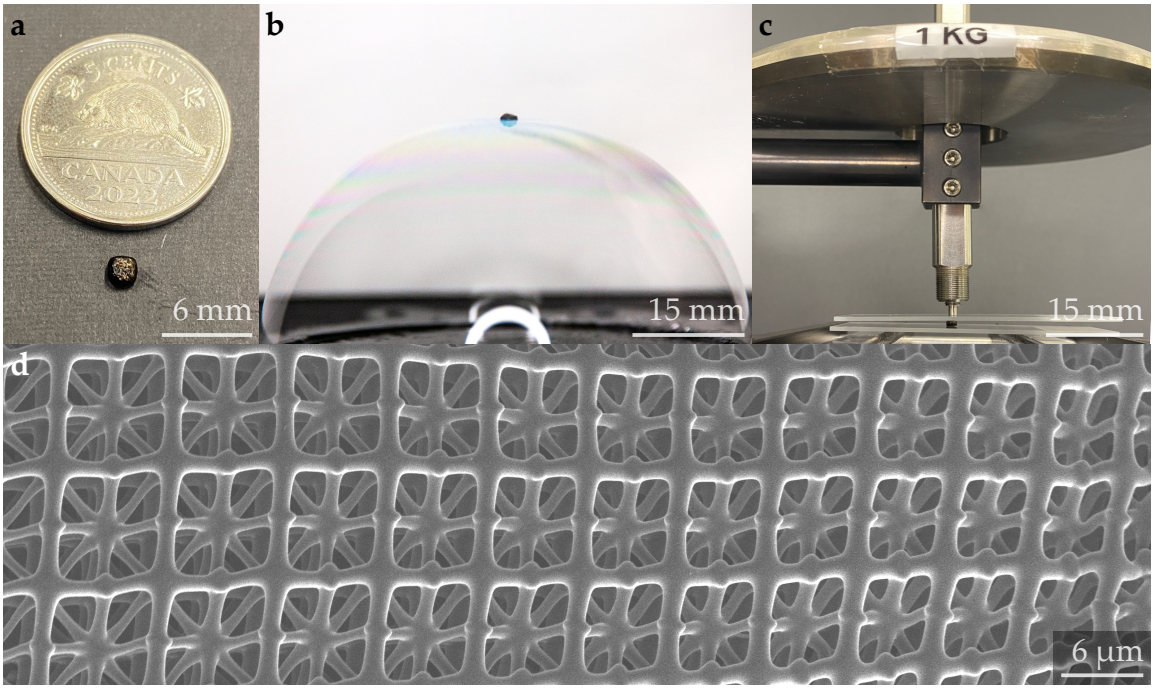

Figure 7.13: Overview of the full-size metamaterial sample after pyrolysis. The pyrolysis was performed and the images were taken by Peter Serles. **a,** optical photograph of the pyrolyzed sample next to a canadian 5-cent coin. The volume before pyrolysis $6.3 \times 6.3 \times 3.8\,\mathrm{mm}^3$ shrunk approximately tenfold to a volume of $2.9 \times 2.8 \times 1.8\,\mathrm{mm}^3$. This leads to thin lattice struts and an overall low sample weight. **b,** optical photograph of the sample after pyrolysis balanced on a soap bubble. The metamaterial is so lightweight that it does not break the bubble. **c,** optical photograph of the pyrolyzed sample between two glass cover slips, withstanding the weight of 1 kg. Even though the lattice struts become very thin after pyrolysis, the metamaterial sample does not break. **d,** Scanning-electron micrograph of a second sample after pyrolysis. The images have been kindly provided with permission of Peter Serles.

7.3.1 Motivation

The main goal of the KATRIN research facility is to determine the effective mass of the electron antineutrino. Reaching this goal is confronted with many challenges and an important one are high spectrometer background rates. Their design value is targeted to be 0.01 counts per second and is currently exceeded by a factor of 100 [208]. With a technique developed within the KATRIN collaboration called *active transverse energy filtering* (aTEF), signal electrons with large angles $\theta_{\mathrm{signal}} < 50°$ with respect to the detector can be detected while background electrons with small angles $\theta_{\mathrm{background}} < 20°$ are blocked in an insensitive layer [209, 210].

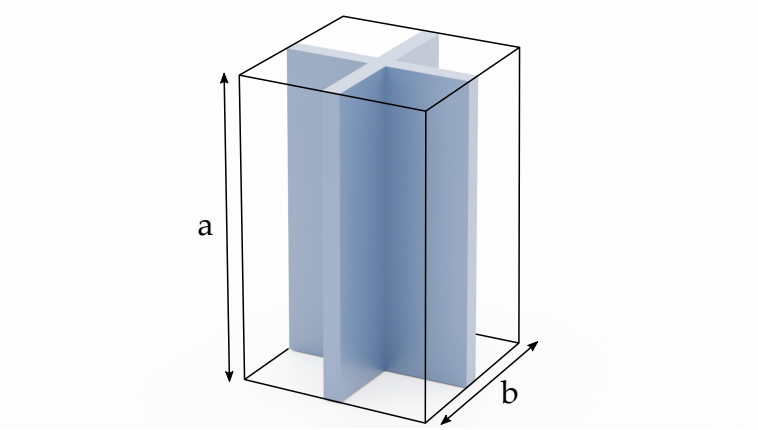

Figure 7.14: Unit cell of a potential structure for scintillator applications. The unit cell was designed within a collaboration of Dr. Anton Huber and Jannis Weinacker. A height $a = 100\,\mu m$ was chosen while the side length $b = 60\,\mu m$ was defined to fit to the $7 \times 7 = 49$ focus array.

Within the KATRIN experiment, this approach is pursued by two implementation strategies. One of them is a combination of a micro-structured polymer scintillator and an array of single-photon avalanche diodes (SPADs), called *scintillating-aTEF* [208, 210]. Here, the scintillating structure consists of arrays of quadratic cells with the top and bottom covered with layers featuring no scintillation. Large-angle electrons get the chance to interact with the scintillating material while small-angle electrons are mostly blocked. Absorbed electrons trigger the emission of optical photons, optically guided through the scintillator structure and eventually detected by the SPAD array at the bottom [208, 210].

The unit cell design of these proposed scintillating structures is shown in Figure 7.14. Laterally arranging these unit cells periodically yields the described large scintillator structure.

Notably, the photoresist this structure was printed with does not feature scintillating properties. Furthermore, the focus-to-focus distance $d_{\text{focus}} = 60\,\mu m$ does not yet fit to the designed periodicity of the final structure which requires side lengths of up to $300\,\mu m$. However, the goal is to fabricate these large samples by multi-photon 3D laser printing, which requires high printing rates. The challenge here lies in the required throughput of the manufacturing technology to enable the fabrication of the necessary samples in a reasonable time. Therefore, multi-focus 3D laser printing is a highly attractive avenue for reaching that goal. In the following section, a first proof of concept is shown with a large structure containing many unit cells of slightly altered height $a = 100\,\mu m$ and lateral size $b = 60\,\mu m$ as depicted in Figure 7.14. It was 3D printed with the sensitive photoresist described in subsection 3.3.2. In the future, the focus array could be adapted to the periodicity of the design and a scintillating photoresist, which is already in development, employed.

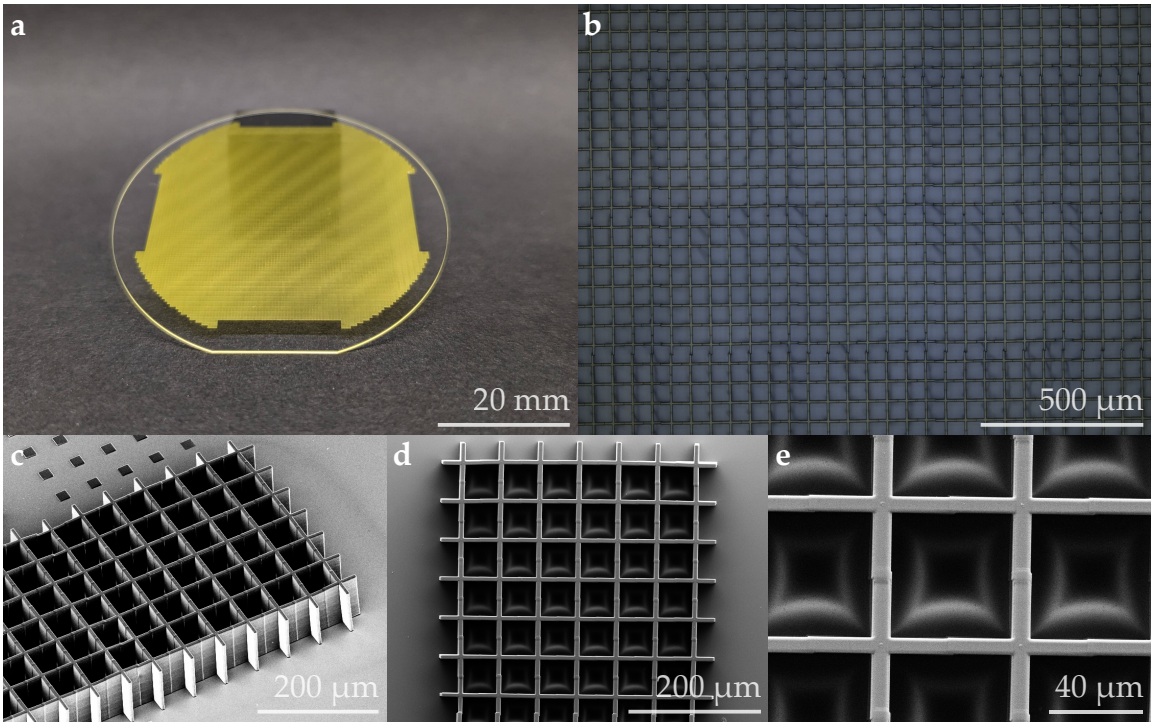

Figure 7.15: Overview of a potential structure for scintillator applications in particle physics. a, optical photograph depicting a 2-inch diameter glass wafer with 415,373 unit cells of the wall structure presented in Figure 7.14 printed onto it. The wafer is elevated by a small polymer block behind. **b,** light-microscope image showing a zoom in into the structure, revealing individual walls that build up the material. **c-e,** scanning-electron microscope images of the characterization sample with reduced sizes showing **c** smooth side walls, **d** a top view of the structure, and **e** a zoomed-in view, revealing small artifacts due to stitching.

7.3.2 *Results*

A first proof-of-concept manufacturing result of the wall structure described in Figure 7.14 on a large area as well as a characterization sample with reduced sizes for the analysis at a scanning-electron microscope is shown in Figure 7.15. An optical photograph of 415,373 individual unit cells fabricated in 2 days on a 2-inch diameter glass wafer is shown in Figure 7.15a. It was printed with a hatching distance of 200 nm and a slicing distance of 300 nm. Figure 7.15b shows a top view of this sample acquired by an light microscope, revealing the individual walls of the unit cell building up the material. Small imperfections in stitching are especially visible when fabricating thin walls that connect to each other. Therefore, stage movements and the rotation of the focus array for printing have to be aligned precisely. Some of these artifacts can be seen in slightly misplaced opposing walls.

Figure 7.15c-d show scanning-electron-microscope images of the small characterization sample with reduced sizes of the same design. Figure 7.15d shows a section of the structure that was printed using one writing field and the $7 \times 7 = 49$ focus array. The close-up view in Figure 7.15e reveals small artifacts due to stitching.

7.4 Discussion

In this chapter, the capabilities of the next-generation multi-focus 3D laser printing setup described in this thesis were demonstrated in four applications in the fields of pharmacy, material science, and particle physics. With previous generations of multi-focus printing and light-sheet 3D laser printing performing at $10\times$ lower [33, 62] and commercial systems offering $100\times$ lower [24] total peak printing rates, the demands of the described research projects could not have been met. New technologies combining beam splitting with acousto-optical deflection and digital mirror devices recently started to offer similar manufacturing speeds as well [75]. However, the field of view in this published approach is only $34 \times 68\,\mu m^2$ (compared to $420 \times 420\,\mu m^2$). Stage movements already made up a significant part of the print time for structures presented in this chapter. Therefore, a large fraction of manufacturing time would be lost in stage movements with samples having significantly more stitching artifacts with the cited approach.

Employing the high printing rates achieved, collaborators working in respiratory drug delivery could be successfully supplied with over 7 million individual carrier particles for potential pharmaceutical applications. The proposal for these structures was formulated some years ago but only the setup described in this thesis is now able to meet the requirements. By manufacturing all carrier particles on sacrificial layers, easy and damage-free detachment of the structures from the substrate could be facilitated. Furthermore, the manufacturing allowed for tuning the macroscopic surface roughness of the large number of samples to a desired degree. Finally, preliminary results of the manufactured carrier particles in contact with first drugs obtained by collaborating scientists were presented as well.

In the field of material science, two metamaterial samples with unprecedented numbers of individual unit cells were fabricated. A demanding chiral design featuring roton-like dispersion relations could not only be successfully 3D printed featuring over 1 million single unit cells, it also benefited from the high employed focus velocity, rendering previous dissections of the unit cell in many print sub-jobs unnecessary. Within a collaboration with the University of Toronto, a large lightweight metamaterial design with potentially high compressive strenghts could be manufactured with over 18 million individual unit cells. The research project includes pyrolysis of the 3D printed structure, which greatly benefits from

the new size dimensions enabled by next-generation multi-focus 3D laser printing while still maintaining sub-micron resolution. In addition to the characterization of the 3D printed sample, some preliminary results obtained by the collaborating party were presented.

To take a first step in the proof-of-concept fabrication of potentially scintillating structures to possibly minimize detector noise, a large sample comprising 100 µm-high walls filling up an area of roughly 20 cm^2 was presented. This project is a collaboration within the scope of the KATRIN research facility at the Karlsruhe Institute of Technology in the field of particle physics. The early prints demonstrate the utility of multi-focus 3D laser printing for this application. As soon as the corresponding photoresist development yields a system to fabricate sufficiently scintillating structures, this could be combined with the photoinitiator BBK presented in chapter 4 to match the necessary photoresist sensitivity. By printing a new diffractive optical element and potentially a new multi-lens array with the workflow described in chapter 5, arbitrary focus patterns can be created. If a larger field of view is required, the microscope objective lens used in this thesis could be replaced by one with a lower numerical aperture. The setup presented in chapter 6 offers the required flexibility to simply exchange the addressed components.

8 Chapter 8
Conclusions and Outlook

In the scope of this thesis, I have successfully reached a new technology level of 3D laser printing by boosting the print rate of multi-focus 3D laser printing by an order of magnitude. For this advancement, I have developed a novel sensitive photoresist and fabricated high-quality micro-optical components for a hybrid beam-splitting method. Using the new possibilities of high manufacturing speeds, I was able to address current problems in respiratory sciences, material sciences, and particle physics in promising collaborations that exceed the scope of this thesis. In the following, I will summarize and contextualize the contents of this thesis and give a short outlook on the future of multi-focus 3D laser printing.

In chapter 2, I have explained the necessary basics of 3D laser printing for fast, power-efficient manufacturing. After outlining the basic methodology and underlying chemical reactions, I introduced the important quantity of two-photon exposure dose that describes many characteristics of fast 3D laser printing. In doing so, I introduced the threshold and accumulation model and used the presented assumptions to extract the impact of photoresist nonlinearity on print quality. Using examples exploring the impact of various parameters, I have demonstrated that the models assumed for 3D laser printing can yield simulations that closely resemble printed samples. As this thesis aimed to enhance the print rate while staying within a limited power budget, I explained the impact of photoresist nonlinearity and the type of parallelization on the necessary total average laser power. By doing that, I pointed out the reasons for the pursued parallelization method by static beam splitting using a DOE. To close off the chapter, I have given an overview of various 3D printing technologies in literature and discussed the fastest currently available approaches while integrating my own work.

The methods applied within this thesis have been summarized in chapter 3. The first section summarized the characterized photoresists, the optical setup used for characterization, and sample handling, while the second section introduced concepts necessary for optimizing the quality of the fabricated micro-optical components. This included the concept of two-photon grayscale lithography, the

photoresist used for these micro-optics, information on sample handling and coating, and details on digital image cross-correlation. The last section described methods regarding the multi-focus manufacturing of different samples using the newly developed setup. I explained the approach used for damage-free sample lift-off and summarized details on sample handling.

In chapter 4, I have presented the development of a highly sensitive photoresist, which marks the first advancement to make the next generation of multi-focus 3D laser printing possible. To give an overview of the sensitivity of more than 80 different photoresist systems in literature, I have introduced a dimensionless photoresist-sensitivity figure-of-merit and compared the available data on these various photoresists. In doing so, I extracted five promising photoresist systems and discussed their potential for further improvements. Thereby, I identified the two photoinitiators DETC and MBK as promising candidates and presented further experiments with photoresists containing these initiators in the following sections. In the case of DETC, I showed that adding additional photoinitiators next to DETC at the solubility limit does not significantly boost the sensitivity. Consequently, I studied the impact of DBA- and onium-salt coinitiators on the sensitivity of DETC-containing photoresists but showed that increased sensitivities can only be achieved for slow focus velocities, which are not suited for fast 3D laser printing. For MBK, I identified its limited solubility as the most limiting factor of this otherwise efficiently working photoinitiator. By synthesizing a new molecule with longer alkyl chains as side groups, the MBK derivative BBK could be obtained. I demonstrated that due to the increased solubility of the new photoinitiator BBK, the resulting photoresists show a significant boost in sensitivity, marking the currently highest sensitivity at high focus velocities. I closed the chapter by characterizing the absorption spectrum and showing a first experiment on the potential biocompatibility of BBK as well as summarizing and discussing the results.

In chapter 5, I have presented the second improvement contributing to the high print rate of next-generation multi-focus 3D laser printing. After explaining the advantages and disadvantages of diffractive and refractive beam splitting, I have introduced the novel hybrid diffractive-refractive beam-splitting method applied in this thesis. In the second section, I have shown the various calculations and simulations that contributed to the design of the two micro-optical components of the DOE and MLA. Since the fabrication with commercial systems did not yield samples of sufficient quality, I pursued the optimization of their optical quality in the third section. First, I showed simulations demonstrating the impact of various manufacturing imperfections on the diffraction pattern of the DOE. Finally, I presented a workflow developed to iteratively enhance the shape accuracy of the printed samples to their design. To demonstrate the impact of this workflow, I have

characterized many generations of DOE samples by both confocal-topography- and optical analysis and presented the quality of the final samples used for multi-focus 3D laser printing. In the fourth section, I have discussed and concluded the presented achievements.

The two advancements in photoresist sensitivity and high-quality micro-optical components came together in chapter 6. I have presented the optical setup for the next generation of multi-focus 3D laser printing. It uses a large field of view and was designed such that it can use the maximum available focus scan speed for the given galvanometric mirror unit. In the second section, I have presented the low-aberration scan optics that image the original focus array into the writing plane without distorting the outermost foci. I based the optical system on previous works and further improved the imaging quality by optical ray-tracing simulations to come up with an updated version of the applied lens systems. Furthermore, I described the assembly of these components and presented the simulated performance. In the third section, I characterized the voxel size that can effectively be used with the described setup and summarized and discussed the contents of this chapter in the fourth section.

In chapter 7, I demonstrated the capabilities of this new setup with high print rates in the three disciplines of respiratory sciences, material sciences, and particle physics. In the first section, I have presented the need for millions of carrier particles for respiratory drug delivery and addressed the previously unmet demand by fabricating over 7 million carrier particles in less than one week of print time. I have further shown the first results of subsequent pharmaceutical experiments with these carrier particles in the ongoing collaboration with pharmacists at the University of Kiel. In the second section, I have presented two examples in the field of metamaterials to demonstrate the setup's capability to not only print individual, disconnected structures, but also continuous, connected structures. In a first example, I have shown a chiral mechanical metamaterial structure comprising over 1 million unit cells of more than 1.7×10^{12} voxels that was printed within two days. The second example comprised a lightweight metamaterial with high compressive strength consisting of over 18 million unit cells, which was printed in two days and has met the demand of material scientists at the University of Toronto. To close off the section on material science, I presented early results of the lightweight metamaterial after pyrolysis. In the third section, I have shown structures for a potential scintillation application in the field of neutrino-mass research and demonstrated that the demand for large areas built up by the corresponding design can be met by multi-focus 3D laser printing. In the fourth section, I have discussed and contextualized the presented results.

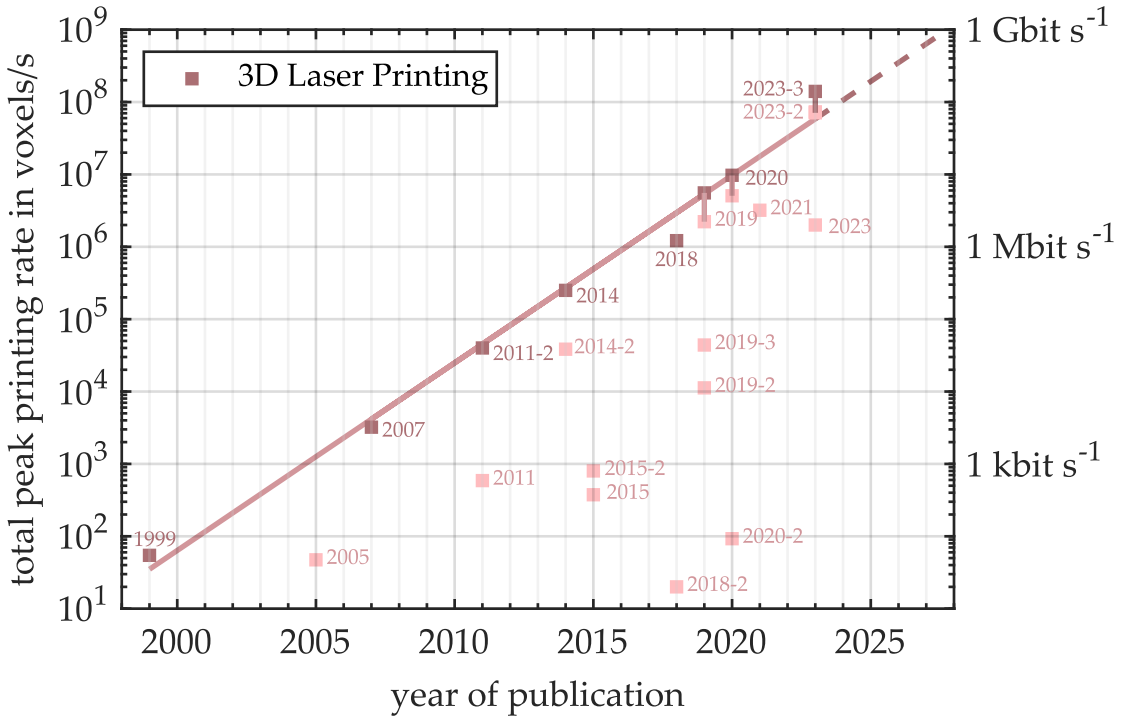

Figure 8.1: Printing speed evolution of 3D laser printing. The data is sorted by peak printing rate and publication year. Data points in dark red mark technology leaps that increased the total peak printing rate of the field. Data points in light red mark publications that used 3D laser printers which did not employ the highest possible printing rate at the time but were added for the sake of completeness. Therefore, only data points in dark red were considered for the linear fit. The printing rate has increased annually by a factor of 1.82, reaching an increase by a total factor of 1.6×10^6 between 1999 and 2023; one order of magnitude higher than 2020.
References: 1999 [19], 2005 [20], 2007 [21], 2011 [22], 2011-2 [23], 2014 [24], 2014-2 [25], 2015 [26], 2015-2 [27], 2018 [28], 2018-2 [29], 2019 [30], 2019-2 [31], 2019-3 [32], 2020 [33], 2020-2 [34], 2021 [64], 2023 [63], 2023-2 [75], and 2023-3 [58].

Outlook

In chapter 1, I introduced the equivalent of Moore's law in 3D laser printing and showed that the development of peak printing rate followed a clear trend between the years 1999 and 2020 and projected a peak printing rate of 10^8 voxels s^{-1}, i.e., 100 million voxels per second, before 2025. With the advancements in photoresist sensitivity, beam splitting with shape-accurate micro-optical components, and low-aberration large-FOV imaging, I was able to successfully achieve the predicted technology leap for multi-focus 3D laser printing that now allows for an order of magnitude higher print rates than previously possible. The updated equivalent of Moore's law in 3D laser printing is shown in Figure 8.1. Based on the updated

fit including the new data point connected to this work (2023-3), the total peak printing rate is now projected to annually increase by 82 % or double roughly every 14 months. Following this trend, a peak printing rate of 10^9 voxels s^{-1} should be possible by 2028. This again opens the question whether the current print rate will mark the end of this trend.

To increase throughput further, the straightforward approach would be to work on the respective fields of advancement and continue to optimize the underlying aspects. In the case of photoresist sensitivity, BBK-containing photoresists might mark the currently best-performing photoresist for high-speed printing [38], however, there seems to be no fundamental limit that prevents photoinitiator development from yielding yet more efficient molecules in the future. Very little is currently known about the underlying quantum-chemical processes of both BBK and DETC [49, 144–147]. Therefore, a better understanding of the core mechanisms could provide new possibilities in enhancing their efficiency. Furthermore, the photoresist-sensitivity overview presented in chapter 4 showed no clear correlation between photoresist sensitivity and the underlying chemical structure. The top-performing photoinitiators feature vastly different chemical groups, therefore, it is highly likely that photoinitiators with a completely new composition might soon take over the lead, allowing for even higher degrees of parallelization.

While many setups in high-speed 3D laser printing follow different parallelization approaches, they all suffer from limited efficiency. I have explained the disadvantages of parallelization by LCDs, DMDs, or SLMs in chapter 2 and presented DOEs as very efficient in chapter 5. Even though a new hybrid diffractive-refractive approach was pursued in this work, the resulting focus array in the writing plane still showed voxel-size inhomogeneities as presented in chapter 6 despite visible improvements in the DOE's diffraction pattern using the presented algorithm in chapter 5 and low-aberration imaging. Homogenizing the focus array further is possible by individually weakening the strongest diffraction orders. However, this comes at a loss in total laser power. Therefore, improvements in beam-splitting efficiency and subsequent imaging into the writing plane are still possible but will most likely not result in a quantum leap.

Naturally, one could employ even stronger laser systems offering higher total average laser powers to allow for more foci. However, with the microscope objective lenses that are typically in use for 3D laser printing, this is currently not an option. The laser power used in this work was already close to the microscope-objective-lens damage threshold [58]. Without new developments of high-power microscope objective lenses, stronger lasers will, therefore, doom the setup from the start, leaving no way to tightly focus the incident light into small foci.

Even when combining potential advancements in photoresist sensitivity and beam-splitting efficiency to allow for more foci in the future, they likely would not fit inside the microscope objective lens' FOV when applying similar focus-to-focus distances $d_{\text{focus}} = 60\,\mu\text{m}$ as in this thesis. With a focus-array size of $7 \cdot 60\,\mu\text{m} \times 7 \cdot 60\,\mu\text{m} = 420 \times 420\,\mu\text{m}^2$, the available FOV is almost fully occupied. Without larger available FOVs of high-NA microscope objective lenses, more foci are therefore only possible when decreasing the focus-to-focus distance d_{focus}. However, as each focus fabricates one individual sub-structure, the maximum possible size of this sub-structure will decrease as well, limiting the flexibility of the setup. Dynamic beam splitting might therefore take over the lead in peak print rate if it either overcomes its low power efficiency or utilizes even more sensitive photoresists. Using dynamic beam splitting, the focus pattern can be adjusted during printing and therefore more foci can be employed without sacrificing flexibility.

Considering the second leading 3D laser printer in this field (data point 2023-2 in Figure 8.1) [75], the importance of fast scanning in comparison to high parallelization degrees becomes evident again. Even though the authors used only 8 foci in parallel instead of 49 as in this work, they were able to match the print rate achieved in this thesis by scanning these laser foci faster. As already explained in chapter 2, power scaling is more beneficial for scanning one or a few laser foci very fast instead of using a high degree of parallelization with slow scanning. However, their beam-scanning method of acousto-optic scanning comes with the disadvantage of small scan angles and therefore limits the writing-field area that can be addressed. Hence, they suffered from a small $34 \times 68\,\mu\text{m}^2$ FOV instead of, e.g., $420 \times 420\,\mu\text{m}^2$ like in this work. However, if this combination of extremely fast scanning by, e.g., acousto-optic scanning combined with the highest possible degree of parallelization is developed further, the current disadvantages could be eliminated, allowing for a new technology leap.

Beyond two-photon printing, the use of two-step photoresists combined by current parallelization technologies could yield higher print rates as well. These photoresists feature extremely low polymerization threshold powers and can perform with continuous-wave lasers instead of pulsed lasers but currently only offer the necessary nonlinearity exponent for printing real 3D structures at comparatively low focus velocities [60]. New resist formulations for two-step absorption at high focus velocities, therefore, might be another potential advancement in photoresist chemistry [211].

In the end, every future advancement in increasing the print rate of 3D laser printing will eventually demand for novel solutions in defining the printing of 3D structures. Currently, 3D designs are divided into typically equidistant layers

and these layers are further divided into typically equidistant lines that comprise the structure-defining voxels of typically constant size. However, this naive approach has its limits. A $1\,m^3$ sized cube alone comprises 10^{21} voxels when following the approach of filling it with equisized voxels of 100 nm [38]. Manufacturing this cube with the print rate achieved in this thesis would therefore take more than 300,000 years. As a potential solution to this problem, directed self-assembly was already proposed in the past [38]. Another solution could be to apply 3D laser printing setups with truly scalable voxel sizes. For bulky parts of the structure, a 100 nm voxel-size resolution is not needed and will increase the print time unnecessarily. A smart subdivision of the 3D design in parts that need high resolution and those that don't therefore reduces data sizes and print times. Some recent manufacturing approaches already move in this direction [106].

For almost 25 years, the equivalent of Moore's law in 3D laser printing held true with an approximate print rate doubling every 14 months. In the field of integrated circuits, some industry experts consider Moore's law as dead [212]. However, the number of transistors in an integrated circuits keeps on increasing as the achievable size of MOSFET devices keeps decreasing [213]. In this thesis, I have increased the print rate of 3D laser printing further than originally deemed possible. To follow this trend and enhance throughput further, new challenges will have to be overcome. However, I am confident that new approaches to current problems will allow for a new technology leap again and produce fascinating new applications in the future.

A Appendix

Appendix A

A.1 Further Data on Sensitive Photoresists

Sym.	Label	Ref.	Photoresist	FOM	v (m/s)	P_{th} (W)	λ_0 (m)	t_p (s)	R_p (Hz)	NA	n_{PI} (wt%)
▼	2003-1	[122]	BSB-S_2 + SU-8 + GBL	4.03E-1	5.00E-5	3.50E-3	7.45E-7	8.0E-14	8.2E+7	1.40	2.500
☆	2005-1	[123]	Irg369 + ORMOCER I	1.74E-3	1.42E-5	3.00E-2	7.80E-7	8.0E-14	8.0E+7	1.40	0.250
◁	2006-1	[124]	BMPyPCbzTos + MA + DEP-6A	2.01E-1	1.77E-4	1.00E-2	7.80E-7	8.0E-14	8.2E+7	1.40	0.100
◁	2007-1	[125]	BCPhPnCbz + MAA + DEP-6A	2.29E-2	1.00E-5	1.01E-2	8.00E-7	8.0E-14	8.0E+7	1.42	0.720
◁	2007-1	[125]	BCPhBnCbz + MAA + DEP-6A	9.12E-1	1.00E-5	1.60E-3	8.00E-7	8.0E-14	8.0E+7	1.42	0.750
◁	2007-1	[125]	BNPhPnCbz + MAA + DEP-6A	5.72E-1	1.00E-5	2.02E-3	8.00E-7	8.0E-14	8.0E+7	1.42	0.770
◁	2007-1	[125]	BNPhBnCbz + MAA + DEP-6A	3.65E+0	1.00E-5	8.00E-4	8.00E-7	8.0E-14	8.0E+7	1.42	0.800
▷	2007-2	[126]	BPnDPhAnt + MAA + DPHA	5.70E+0	1.00E-5	6.40E-4	8.00E-7	8.0E-14	8.0E+7	1.42	0.367
▶	2009-1	[127]	BTPhAQ + MAA + DPHA	3.81E+0	1.00E-5	8.00E-4	8.00E-7	8.0E-14	8.0E+7	1.40	0.500
▶	2009-1	[127]	BTPhABnQ + MAA + DPHA	3.61E-1	1.00E-5	2.60E-3	8.00E-7	8.0E-14	8.0E+7	1.40	0.500
✸	2010-1	[128]	SU-8	4.52E-2	9.92E-5	1.57E-2	5.32E-7	cw	cw	1.40	?
✡	2010-1	[128]	IP-L	4.75E-3	2.00E-4	6.87E-2	5.32E-7	cw	cw	1.40	?
★	2010-2	[129]	Irg369 + SZ2080	2.21E+2	1.00E-4	2.33E-6	1.03E-6	3.0E-13	1.0E+3	1.40	1.000
★	2010-2	[129]	DABP + SZ2080	3.45E+2	1.00E-4	1.86E-6	1.03E-6	3.0E-13	1.0E+3	1.40	1.000
★	2010-2	[129]	Pure SZ2080	2.86E+1	1.00E-4	6.46E-6	1.03E-6	3.0E-13	1.0E+3	1.40	0.000
◁	2011-1	[130]	BNPhBnC + MAA	1.61E-1	1.00E-5	4.02E-3	7.80E-7	1.0E-13	8.2E+7	1.45	0.100
◁	2011-1	[130]	BNPhBnC/PhOMe + MAA	1.42E-1	1.00E-5	4.28E-3	7.80E-7	1.0E-13	8.2E+7	1.45	0.100
◁	2011-1	[130]	BNPhMBnC + MAA	1.27E-1	1.00E-5	4.53E-3	7.80E-7	1.0E-13	8.2E+7	1.45	0.100
★	2011-2	[42]	DETX + SZ2080	9.02E+1	1.00E-4	2.21E-4	5.32E-7	8.0E-12	1.0E+6	1.40	1.000

Figure A.1: Overview of all photoresist data contributing to the overviews shown in Figure 4.1 and Figure 4.2. The symbols and labels shown in the first two columns correspond to the symbols and labels shown in the overview graphs. The photoresist composition is shown in the fourth column in abbreviated form. The fifth and seventh column show the values of the photoresist-sensitivity figure-of-merit FOM and the polymerization threshold power P_{th}, which are depicted in the vertical axes of the respective overview figures. The focus velocity v corresponding to the horizontal axes of both overview figures is shown in the sixth column. The remaining parameters needed for calculating the FOM (wavelength λ_0, pulse duration t_p, repetition rate R_p, and numerical aperture of the microscope objective lens NA) are shown in columns eight to eleven. The last column specifies the used photoinitiator concentration n_{PI}. Adapted and updated from [38].

Sym.	Label	Ref.	Photoresist	FOM	v (m/s)	P_{th} (W)	λ_0 (m)	t_p (s)	R_p (Hz)	NA	n_{PI} (wt%)
▷	2012-1	[131]	BDAPhPnOAnt + MAA + DPHA	3.65E+1	1.00E-3	2.53E-3	8.00E-7	8.0E-14	8.0E+7	1.42	0.940
▷	2012-1	[131]	BPTPnOAnt + MAA + DPHA	9.12E-1	1.00E-5	1.60E-3	8.00E-7	8.0E-14	8.0E+7	1.42	0.867
▷	2012-1	[131]	BCPhPnOAnt + MAA + DPHA	3.33E-2	1.00E-5	8.37E-3	8.00E-7	8.0E-14	8.0E+7	1.42	0.899
▼	2013-1	[132]	DBAn2PhOMe + TTA + ETA	1.47E-1	5.00E-5	6.87E-3	7.80E-7	1.0E-13	8.0E+7	1.40	0.377
▽	2013-1	[132]	BDBAn3FL + TTA + ETA	6.76E-2	5.00E-5	1.01E-2	7.80E-7	1.0E-13	8.0E+7	1.40	0.400
△	2013-1	[132]	BDMAnPhPn + TTA + ETA	9.59E-2	5.00E-5	8.49E-3	7.80E-7	1.0E-13	8.0E+7	1.40	0.202
△	2013-1	[132]	BDABnCPn + TTA + ETA	7.99E-2	5.00E-5	9.30E-3	7.80E-7	1.0E-13	8.0E+7	1.40	0.324
△	2013-1	[132]	BDABnCHx + TTA + ETA	6.75E-2	5.00E-5	1.01E-2	7.80E-7	1.0E-13	8.0E+7	1.40	0.200
◇	2014-1	[49]	Irg819 + PETA	4.70E+0	3.72E-2	5.00E-2	8.10E-7	1.0E-13	8.0E+7	1.40	1.397
◇	2014-1	[49]	Irg819 + DPEPA	8.13E+0	3.68E-2	3.78E-2	8.10E-7	1.0E-13	8.0E+7	1.40	0.799
◇	2014-1	[49]	Irg819 + TMPTA	1.49E+0	3.68E-2	8.84E-2	8.10E-7	1.0E-13	8.0E+7	1.40	1.406
□	2014-1	[49]	DETC + PETA	3.09E+1	3.72E-2	1.95E-2	8.10E-7	1.0E-13	8.0E+7	1.40	0.286
▲	2014-1	[49]	ITX + PETA	6.27E+0	3.68E-2	4.31E-2	8.10E-7	1.0E-13	8.0E+7	1.40	0.845
☆	2015-1	[133]	Irg242 + ORMOCER	2.15E+1	1.00E-3	9.00E-4	5.15E-7	3.5E-13	1.0E+7	1.40	?
◇	2016-1	[134]	Irg369 + DTMPTA	4.52E-1	4.00E-3	5.00E-2	7.80E-7	1.0E-13	8.0E+7	1.40	1.000
♦	2016-1	[134]	Irg369 + DTMPTA + PETMP	1.57E+0	5.00E-3	3.00E-2	7.80E-7	1.0E-13	8.0E+7	1.40	1.000
★	2017-1	[135]	Irg369 + SZ2080	2.47E+2	5.00E-4	6.00E-5	5.15E-7	3.0E-13	2.0E+5	1.40	1.000
★	2017-1	[135]	Pure SZ2080	1.39E+2	5.00E-4	8.00E-5	5.15E-7	3.0E-13	2.0E+5	1.40	0.000
□	2019-1	[43]	DETC + PETA	2.29E+2	1.82E-1	1.84E-2	8.00E-7	1.4E-13	8.0E+7	1.40	0.250
□	2019-1	[43]	DETC + TMPETA	2.31E+1	1.82E-1	5.80E-2	8.00E-7	1.4E-13	8.0E+7	1.40	0.250
□	2019-1	[43]	DETC + BPFDA	1.35E+2	1.82E-1	2.40E-2	8.00E-7	1.4E-13	8.0E+7	1.40	0.250
□	2019-1	[43]	DETC + THICTA	1.60E+2	7.28E-3	4.40E-3	8.00E-7	1.4E-13	8.0E+7	1.40	0.250
◇	2019-1	[43]	Irg369 + PETA	5.61E+1	1.82E-1	3.72E-2	8.00E-7	1.4E-13	8.0E+7	1.40	2.000
◇	2019-1	[43]	Irg819 + PETA	3.04E+1	1.82E-1	5.05E-2	8.00E-7	1.4E-13	8.0E+7	1.40	2.000
○	2019-1	[43]	Pure PETA	6.18E+0	1.82E-1	1.12E-1	8.00E-7	1.4E-13	8.0E+7	1.40	0.000
◀	2019-2	[136]	BMOA-1T + TTA + ETA	2.03E+1	3.16E-1	9.00E-2	7.98E-7	7.2E-14	7.3E+7	0.80	0.345
◀	2019-2	[136]	BtBuA-1T + TTA + ETA	2.57E+1	3.16E-1	8.00E-2	7.98E-7	7.2E-14	7.3E+7	0.80	0.398
◀	2019-2	[136]	BMA-1T + TTA + ETA	4.57E+1	3.16E-1	6.00E-2	7.98E-7	7.2E-14	7.3E+7	0.80	0.313
◀	2019-2	[136]	BTMSA-1T + TTA + ETA	4.57E+0	3.16E-2	6.00E-2	7.98E-7	7.2E-14	7.3E+7	0.80	0.430
◀	2019-2	[136]	BHA-1T + TTA + ETA	3.36E+1	3.16E-1	7.00E-2	7.98E-7	7.2E-14	7.3E+7	0.80	0.285
◀	2019-2	[136]	BFA-1T + TTA + ETA	3.36E+1	3.16E-1	7.00E-2	7.98E-7	7.2E-14	7.3E+7	0.80	0.321
◀	2019-2	[136]	BCNA-1T + TTA + ETA	3.36E+0	3.16E-2	7.00E-2	7.98E-7	7.2E-14	7.3E+7	0.80	0.335
◀	2019-2	[136]	BSO_2MA-1T + TTA + ETA	6.58E+0	3.16E-2	5.00E-2	7.98E-7	7.2E-14	7.3E+7	0.80	0.442
▽	2019-2	[136]	BDBAn3FL + TTA + ETA	6.43E+0	1.00E-1	9.00E-2	7.98E-7	7.2E-14	7.3E+7	0.80	0.317
▲	2019-3	[137]	BDAPhTX + PETA	2.09E-1	1.00E-4	5.50E-3	8.00E-7	2.5E-14	8.0E+7	1.49	0.250
▲	2019-3	[137]	DANTX + PETA	2.56E-1	1.00E-4	4.97E-3	8.00E-7	2.5E-14	8.0E+7	1.49	0.500
▲	2019-3	[137]	ITX + PETA	5.95E-2	1.00E-4	1.03E-2	8.00E-7	2.5E-14	8.0E+7	1.49	1.500
◁	2019-4	[138]	36CbzDBOx + TMPTA + TMP3EOTA	1.12E+0	7.50E-4	1.40E-2	8.00E-7	1.0E-13	8.0E+7	1.42	0.100
◁	2019-4	[138]	36CbzDAOx + TMPTA + TMP3EOTA	1.52E+0	7.50E-4	1.20E-2	8.00E-7	1.0E-13	8.0E+7	1.42	0.087
◁	2019-4	[138]	27CbzDBOx + TMPTA + TMP3EOTA	1.52E+0	7.50E-4	1.20E-2	8.00E-7	1.0E-13	8.0E+7	1.42	0.100
◁	2019-4	[138]	27CbzDAOx + TMPTA + TMP3EOTA	4.47E+0	7.50E-4	7.00E-3	8.00E-7	1.0E-13	8.0E+7	1.42	0.087
●	2019-4	[138]	TPO + TMPTA + TMP3EOTA	1.28E+0	7.50E-4	1.31E-2	8.00E-7	1.0E-13	8.0E+7	1.42	0.045
✡	2019-4	[138]	IP-L	1.30E+0	7.50E-4	1.30E-2	8.00E-7	1.0E-13	8.0E+7	1.42	?
◁	2019-5	[139]	OXE + PETA	1.37E+3	4.00E-5	2.20E-4	7.40E-7	1.4E-13	8.0E+7	0.65	0.101
★	2019-6	[32]	Pure SZ2080	1.41E+2	1.00E-2	1.46E-4	5.15E-7	3.0E-13	2.0E+5	1.40	0.000

Figure A.2: Continuation of Figure A.1.

Sym.	Label	Ref.	Photoresist	FOM	v (m/s)	P_{th} (W)	λ_0 (m)	t_p (s)	R_p (Hz)	NA	n_{PI} (wt%)
	2020-1	[38]	DETC + PETA	4.74E+1	1.24E-1	2.93E-2	8.20E-7	1.0E-13	8.0E+7	1.40	0.500
	2020-1	[38]	DETC + PETA + TEA	9.00E+1	1.24E-1	2.13E-2	8.20E-7	1.0E-13	8.0E+7	1.40	0.500
	2020-1	[38]	DETC + PETA + DBAm	9.00E+1	1.24E-1	2.13E-2	8.20E-7	1.0E-13	8.0E+7	1.40	0.500
	2020-1	[38]	DETC + PETA + DPIHFP	9.00E+1	1.24E-1	2.13E-2	8.20E-7	1.0E-13	8.0E+7	1.40	0.500
	2020-1	[38]	DETC + PETA + DBA + DPIHFP	1.45E+2	1.24E-1	1.68E-2	8.20E-7	1.0E-13	8.0E+7	1.40	0.500
	2020-1	[38]	Pure PETA	1.91E+1	6.14E-2	1.13E-2	4.05E-7	1.0E-13	8.0E+7	1.40	0.000
	2020-1	[38]	Pure DPHA	2.95E+1	6.14E-2	9.07E-3	4.05E-7	1.0E-13	8.0E+7	1.40	0.000
	2020-1	[38]	Pure BPADA	5.67E+1	6.14E-2	6.54E-3	4.05E-7	1.0E-13	8.0E+7	1.40	0.000
	2020-1	[38]	Pure BPAGMA	4.23E+1	6.14E-2	7.57E-3	4.05E-7	1.0E-13	8.0E+7	1.40	0.000
	2020-1	[38]	IP-DIP	3.33E+1	1.24E-1	3.50E-2	8.20E-7	1.0E-13	8.0E+7	1.40	?
	2020-1	[38]	IP-L	3.33E+1	1.24E-1	3.50E-2	8.20E-7	1.0E-13	8.0E+7	1.40	?
	2020-1	[38]	IP-S	5.92E-1	2.21E-3	3.50E-2	8.20E-7	1.0E-13	8.0E+7	1.40	?
	2020-1	[38]	DETC + BPADA	5.37E+1	1.24E-1	2.76E-2	8.20E-7	1.0E-13	8.0E+7	1.40	0.500
	2020-1	[38]	DETC + DPHA	7.92E+1	1.24E-1	2.27E-2	8.20E-7	1.0E-13	8.0E+7	1.40	0.500
	2020-1	[38]	DETC + UDMA	3.33E+0	1.24E-2	3.50E-2	8.20E-7	1.0E-13	8.0E+7	1.40	0.500
	2020-1	[38]	DETC + BPAGMA	1.87E+1	6.99E-2	3.50E-2	8.20E-7	1.0E-13	8.0E+7	1.40	0.500
	2020-1	[38]	DETC + PETA + PETMP	6.26E+1	6.99E-2	1.91E-2	8.20E-7	1.0E-13	8.0E+7	1.40	0.500
	2020-1	[38]	DMBMCH + PETA	1.12E+2	1.24E-1	1.91E-2	8.20E-7	1.0E-13	8.0E+7	1.40	0.100
	2020-1	[38]	DMBMCH + BPADA	2.13E+2	1.24E-1	1.38E-2	8.20E-7	1.0E-13	8.0E+7	1.40	0.400
	2020-1	[38]	BDBuABnCHx (BBK) + PETA	9.05E+2	1.24E-1	6.71E-3	8.20E-7	1.0E-13	8.0E+7	1.40	0.700
	2020-2	[121]	V-Shape + DDA + DPPHA	2.04E+2	4.00E-5	1.20E-4	5.32E-7	5.6E-10	1.2E+4	1.40	1.000
	2020-2	[121]	Oct + DDA + DPPHA	3.62E+2	4.00E-5	9.00E-5	5.32E-7	5.6E-10	1.2E+4	1.40	0.660
	2020-2	[121]	BDEBP	9.70E+0	4.00E-5	5.50E-4	5.32E-7	5.6E-10	1.2E+4	1.40	?
	2020-2	[121]	ITX	6.16E+0	4.00E-5	6.90E-4	5.32E-7	5.6E-10	1.2E+4	1.40	?
	2020-2	[121]	OXE2	1.27E+1	4.00E-5	4.80E-4	5.32E-7	5.6E-10	1.2E+4	1.40	?
	2021-1	[140]	Compound 1 + TEA + PETA	5.06E+1	1.00E-4	3.50E-3	7.80E-7	1.0E-13	8.0E+7	0.50	0.063
	2021-1	[140]	Compound 2 + TEA + PETA	1.10E+1	1.00E-4	7.50E-3	7.80E-7	1.0E-13	8.0E+7	0.50	0.062
	2021-1	[140]	Compound 3 + TEA + PETA	3.40E+0	1.00E-4	1.35E-2	7.80E-7	1.0E-13	8.0E+7	0.50	0.098
	2021-2	[141]	ITX-phenyl-CN + PETA	2.93E+0	1.00E-4	5.80E-3	8.00E-7	3.9E-13	8.0E+7	1.49	0.294
	2021-2	[141]	ITX-pyridine + PETA	2.74E+0	1.00E-4	6.00E-3	8.00E-7	3.9E-13	8.0E+7	1.49	0.274
	2021-2	[141]	ITX-phenyl + PETA	2.41E+0	1.00E-4	6.40E-3	8.00E-7	3.9E-13	8.0E+7	1.49	0.273
	2021-2	[141]	ITX-phenyl-F + PETA	2.48E+0	1.00E-4	6.30E-3	8.00E-7	3.9E-13	8.0E+7	1.49	0.289
	2021-2	[141]	ITX-phenyl-OCH3 + PETA	3.79E+0	1.00E-4	5.10E-3	8.00E-7	3.9E-13	8.0E+7	1.49	0.299
	2021-2	[141]	ITX-thiophene + PETA	2.65E+0	1.00E-4	6.10E-3	8.00E-7	3.9E-13	8.0E+7	1.49	0.279
	2023-1	[142]	Compound 7 + PETA	1.68E+1	3.50E-4	2.52E-3	7.80E-7	1.2E-13	8.0E+7	1.45	0.100
	2023-2	[143]	BHBNB + PETA	4.03E-1	1.00E-5	2.90E-3	7.80E-7	1.2E-13	8.0E+7	1.40	2.000
	2023-2	[143]	BEBNB + PETA + DCM	1.04E-1	1.00E-5	5.70E-3	7.80E-7	1.2E-13	8.0E+7	1.40	0.100

Figure A.3: Continuation of Figure A.2.

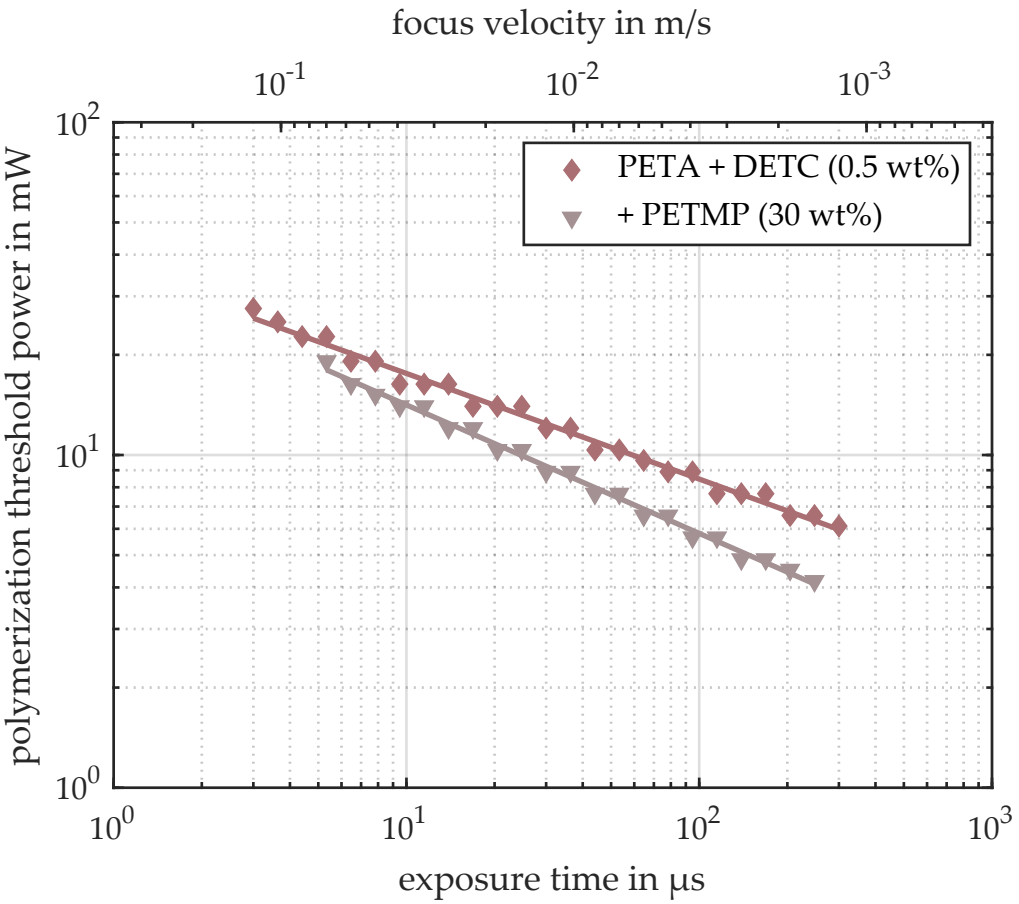

Figure A.4: Polymerization threshold power for various exposure times for two 7-diethylamino-3-thenoylcoumarin (DETC) photoresists, one containing an additional thiol ingredient. The experiment was performed using a $\lambda = 820\,\mathrm{nm}$ wavelength laser with repetition rate $R_\mathrm{p} = 80\,\mathrm{MHz}$ and pulse duration $t_\mathrm{p} = 100\,\mathrm{fs}$ as well as a NA $= 1.4$ microscope objective lens. The effective focus velocity for these parameters is shown in the upper horizontal axis. The basic photoresist contained 0.5 wt% DETC in pentaerythritol triacrylate (PETA). In the additional photoresist, 30 wt% pentaerythritol tetra(3-mercaptopropionate) (PETMP) was added.

A.2 Lens Data for the Next-Generation Setup

Table A.1: Optical design of lens group 1 (LG1). All lenses were purchased from Thorlabs. Hence, the lens name refers to the Thorlabs lens catalog. They are specified by their radius of curvature (ROC), the center distance between two adjacent interfaces (within one lens or between two lenses), and the material making up this distance. Adapted from [58].

lens name	ROC in mm	distance in mm	material
LA1725-B	206.03	4.57	N-BK7
	Inf	1.89	
LE1015-B	-171.60	6.18	N-BK7
	-65.16	0.20	
LA1301-B	Inf	5.52	N-BK7
	-128.77	0.20	
LA1979-B	103.01	6.18	N-BK7
	Inf	1.38	
LE1076-B	30.34	9.70	N-BK7
	65.80	5.13	
LC1582-B	Inf	3.50	N-BK7
	38.59	2.25	
LC1582-B	Inf	3.50	N-BK7
	38.59	0.00	

Table A.2: Optical design of lens group 2 (LG2). All lenses were purchased from Thorlabs. Hence, the lens name refers to the Thorlabs lens catalog. They are specified by their radius of curvature (ROC), the center distance between two adjacent interfaces (within one lens or between two lenses), and the material making up this distance. Adapted from [58].

lens name	ROC in mm	distance in mm	material
LC1582-B	-38.59	3.50	N-BK7
	Inf	2.15	
LC1582-B	-38.59	3.50	N-BK7
	Inf	5.10	
LE1076-B	-65.80	9.70	N-BK7
	-30.34	2.00	
LA1399-B	Inf	6.65	N-BK7
	-90.13	0.10	
LA1050-B	Inf	9.69	N-BK7
	-51.50	93.77	
LA1727-B	386.31	3.83	N-BK7
	Inf	0.00	

Table A.3: Optical design of lens group 3 (LG3). All lenses were purchased from Thorlabs. Hence, the lens name refers to the Thorlabs lens catalog. They are specified by their radius of curvature (ROC), the center distance between two adjacent interfaces (within one lens or between two lenses), and the material making up this distance. Adapted from [58].

lens name	ROC in mm	distance in mm	material
LA1727-B	Inf	3.83	N-BK7
	-386.31	101.14	
LA1050-B	51.50	9.69	N-BK7
	Inf	0.10	
LA1399-B	90.13	6.65	N-BK7
	Inf	2.70	
LE1076-B	30.34	9.70	N-BK7
	65.80	5.10	
LC1582-B	Inf	3.50	N-BK7
	38.59	2.15	
LC1582-B	Inf	3.50	N-BK7
	38.59	0.00	

Table A.4: Optical design of lens group 4 (LG4). All lenses were purchased from Thorlabs. Hence, the lens name refers to the Thorlabs lens catalog. They are specified by their radius of curvature (ROC), the center distance between two adjacent interfaces (within one lens or between two lenses), and the material making up this distance. Adapted from [58].

lens name	ROC in mm	distance in mm	material
LC1715-B	-25.70	3.50	N-BK7
	Inf	9.20	
LE1076-B	-65.80	9.70	N-BK7
	-30.30	0.26	
LA1050-B	Inf	9.70	N-BK7
	-51.50	0.23	
LA1399-B	90.10	6.70	N-BK7
	Inf	0.00	

Table A.5: Optical design of lens group 5 (LG5). All lenses were purchased from Thorlabs. Hence, the lens name refers to the Thorlabs lens catalog. They are specified by their radius of curvature (ROC), the center distance between two adjacent interfaces (within one lens or between two lenses), and the material making up this distance. Adapted from [58].

lens name	ROC in mm	distance in mm	material
LC1315-B	Inf	3.50	N-BK7
	38.59	58.00	
LA1384-B	Inf	8.22	N-BK7
	-64.38	25.35	
LA1301-B	128.77	5.52	N-BK7
	Inf	0.00	

Bibliography

[1] G. E. Moore, *Excerpts from A Conversation with Gordon Moore: Moore's Law*, 2005 (cited on page 3).

[2] G. E. Moore, "Cramming More Components onto Integrated Circuits", Electronics **38**, 114–117 (1965) (cited on page 3).

[3] F. Wanlass and C. Sah, "Nanowatt logic using field-effect metal-oxide semiconductor triodes", in 1963 IEEE International Solid-State Circuits Conference. Digest of Technical Papers, Vol. VI (Feb. 1963), pp. 32–33 (cited on page 3).

[4] F. M. Wanlass, "Low stand-by power complementary field effect circuitry", US3356858A (Dec. 1967) (cited on page 3).

[5] R. H. Dennard, "Field-effect transistor memory", US3387286A (June 1968) (cited on page 3).

[6] H. Ito, C. G. Willson, and J. M. J. Frechet, "Positive- and negative-working resist compositions with acid generating photoinitiator and polymer with acid labile groups pendant from polymer backbone", US4491628A (Jan. 1985) (cited on page 3).

[7] H. Ito and C. G. Willson, "Chemical amplification in the design of dry developing resist materials", Polymer Engineering & Science **23**, 1012–1018 (1983) (cited on page 3).

[8] H. Ito, C. G. Willson, and J. H. J. Frechet, "New UV Resists with Negative or Positive Tone", in 1982 Symposium on VLSI Technology. Digest of Technical Papers (Sept. 1982), pp. 86–87 (cited on page 3).

[9] K. Jain, C. Willson, and B. Lin, "Ultrafast deep UV Lithography with excimer lasers", IEEE Electron Device Letters **3**, 53–55 (1982) (cited on page 3).

[10] K. Jain and G. W. Carlton, "High resolution optical lithography method and apparatus having excimer laser light source and stimulated Raman shifting", US4458994A (July 1984) (cited on page 3).

[11] K. Jain, *Excimer Laser Lithography*, Press Monographs (SPIE Optical Engineering Press, 1990) (cited on page 3).

[12] R. M. Swanson, "A vision for crystalline silicon photovoltaics", Progress in Photovoltaics: Research and Applications **14**, 443–453 (2006) (cited on page 4).

[13] C. Walter, "Kryder's Law", Scientific American **293**, 32–33 (2005) (cited on page 4).

[14] M. H. Kryder and C. S. Kim, "After Hard Drives—What Comes Next?", IEEE Transactions on Magnetics **45**, 3406–3413 (2009) (cited on page 4).

[15] J. Nielsen, "Nielsen's Law of Internet Bandwidth", Nielsen Norman Group (2023) (cited on page 4).

[16] C. L. Benson, G. Triulzi, and C. L. Magee, "Is There a Moore's Law for 3D Printing?", 3D Printing and Additive Manufacturing **5**, 53–62 (2018) (cited on page 4).

[17] I. Kelbassa, T. Wohlers, and T. Caffrey, "Quo vadis, laser additive manufacturing?", Journal of Laser Applications **24**, 050101 (2012) (cited on page 4).

[18] V. Hahn, F. Mayer, M. Thiel, and M. Wegener, "3-D laser nanoprinting", Opt. Photonics News **30**, 28–35 (2019) (cited on page 4).

[19] H.-B. Sun, S. Matsuo, and H. Misawa, "Three-dimensional photonic crystal structures achieved with two-photon-absorption photopolymerization of resin", Applied Physics Letters **74**, 786–788 (1999) (cited on pages 4, 5, 10, 140).

[20] J.-i. Kato, N. Takeyasu, Y. Adachi, H.-B. Sun, and S. Kawata, "Multiple-spot parallel processing for laser micronanofabrication", Applied Physics Letters **86**, 044102 (2005) (cited on pages 5, 30, 64, 140).

[21] X.-Z. Dong, Z.-S. Zhao, and X.-M. Duan, "Micronanofabrication of assembled three-dimensional microstructures by designable multiple beams multiphoton processing", Applied Physics Letters **91**, 124103 (2007) (cited on pages 5, 30, 65, 140).

[22] J. Fischer and M. Wegener, "Three-dimensional direct laser writing inspired by stimulated-emission-depletion microscopy", Optical Materials Express **1**, 614–624 (2011) (cited on pages 5, 30, 140).

[23] S. D. Gittard, A. Nguyen, K. Obata, A. Koroleva, R. J. Narayan, and B. N. Chichkov, "Fabrication of microscale medical devices by two-photon polymerization with multiple foci via a spatial light modulator", Biomedical Optics Express **2**, 3167–3178 (2011) (cited on pages 5, 28, 30, 140).

[24] "Photonic Professional GT", Nanoscribe GmbH & Co. KG (2014) (cited on pages 5, 30, 126, 134, 140).

[25] T. Bückmann, M. Thiel, M. Kadic, R. Schittny, and M. Wegener, "An elasto-mechanical unfeelability cloak made of pentamode metamaterials", Nature Communications **5**, 4130 (2014) (cited on pages 5, 30, 140).

[26] L. Yang, A. El-Tamer, U. Hinze, J. Li, Y. Hu, W. Huang, J. Chu, and B. N. Chichkov, "Parallel direct laser writing of micro-optical and photonic structures using spatial light modulator", Optics and Lasers in Engineering **70**, 26–32 (2015) (cited on pages 5, 28, 30, 140).

[27] W. Yan, B. P. Cumming, and M. Gu, "High-throughput fabrication of micrometer-sized compound parabolic mirror arrays by using parallel laser direct-write processing", Journal of Optics **17**, 075803 (2015) (cited on pages 5, 30, 65, 140).

[28] B. W. Pearre, C. Michas, J.-M. Tsang, T. J. Gardner, and T. M. Otchy, "Fast micron-scale 3D printing with a resonant-scanning two-photon microscope", Additive Manufacturing **30**, 100887 (2019) (cited on pages 5, 30, 140).

[29] W. Chu, Y. Tan, P. Wang, J. Xu, W. Li, J. Qi, and Y. Cheng, "Centimeter-Height 3D Printing with Femtosecond Laser Two-Photon Polymerization", Advanced Materials Technologies **3**, 1700396 (2018) (cited on pages 5, 30, 140).

[30] S. K. Saha, D. Wang, V. H. Nguyen, Y. Chang, J. S. Oakdale, and S.-C. Chen, "Scalable submicrometer additive manufacturing", Science **366**, 105–109 (2019) (cited on pages 5, 30, 113, 140).

[31] Q. Geng, D. Wang, P. Chen, and S.-C. Chen, "Ultrafast multi-focus 3-D nanofabrication based on two-photon polymerization", Nature Communications **10**, 2179 (2019) (cited on pages 5, 27, 30, 65, 140).

[32] L. Jonušauskas, D. Gailevičius, S. Rekštytė, T. Baldacchini, S. Juodkazis, and M. Malinauskas, "Mesoscale laser 3D printing", Optics Express **27**, 15205–15221 (2019) (cited on pages 5, 30, 47, 48, 50, 140).

[33] V. Hahn, P. Kiefer, T. Frenzel, J. Qu, E. Blasco, C. Barner-Kowollik, and M. Wegener, "Rapid Assembly of Small Materials Building Blocks (Voxels) into Large Functional 3D Metamaterials", Advanced Functional Materials **30**, 1907795 (2020) (cited on pages 5, 29, 30, 62, 65, 67, 68, 100, 103, 104, 114, 126, 134, 140).

[34] C. Maibohm, O. F. Silvestre, J. Borme, M. Sinou, K. Heggarty, and J. B. Nieder, "Multi-beam two-photon polymerization for fast large area 3D periodic structure fabrication for bioapplications", Scientific Reports **10**, 8740 (2020) (cited on pages 5, 30, 65, 140).

[35] T. Frenzel, "On 3D Chiral Mechanical Metamaterials", PhD thesis (Karlsruher Institut für Technologie (KIT), Karlsruhe, 2020) (cited on page 10).

[36] J. Fischer, "Three-dimensional optical lithography beyond the diffraction limit", PhD thesis (Karlsruher Institut für Technologie (KIT), Karlsruhe, 2012) (cited on pages 10, 15, 16).

[37] J. O'Brien, P. J. Hughes, M. Brunet, B. O'Neill, J. Alderman, B. Lane, A. O'Riordan, and C. O'Driscoll, "Advanced photoresist technologies for microsystems", Journal of Micromechanics and Microengineering **11**, 353 (2001) (cited on page 10).

[38] P. Kiefer, V. Hahn, M. Nardi, L. Yang, E. Blasco, C. Barner-Kowollik, and M. Wegener, "Sensitive Photoresists for Rapid Multiphoton 3D Laser Micro- and Nanoprinting", Advanced Optical Materials **8**, 2000895 (2020) (cited on pages 10, 12–14, 18, 19, 21, 23–26, 44–51, 54, 57, 60, 62, 64, 141, 143, 145).

[39] C. N. LaFratta, J. T. Fourkas, T. Baldacchini, and R. A. Farrer, "Multiphoton Fabrication", Angewandte Chemie International Edition **46**, 6238–6258 (2007) (cited on page 10).

[40] M. Goppert-Mayer, "Über Elementarakte mit zwei Quantensprungen", Ann. Phys. **9**, 273–295 (1931) (cited on page 10).

[41] W. Kaiser and C. Garrett, "Two-photon excitation in Ca F 2: Eu 2+", Physical review letters **7**, 229 (1961) (cited on page 10).

[42] M. Malinauskas, P. Danilevičius, and S. Juodkazis, "Three-dimensional micro-/nano-structuring via direct write polymerization with picosecond laser pulses", Optics Express **19**, 5602–5610 (2011) (cited on pages 10, 47, 48, 50).

[43] L. Yang, A. Münchinger, M. Kadic, V. Hahn, F. Mayer, E. Blasco, C. Barner-Kowollik, and M. Wegener, "On the Schwarzschild Effect in 3D Two-Photon Laser Lithography", Advanced Optical Materials **7**, 1901040 (2019) (cited on pages 10, 12, 47–49, 51, 54).

[44] A. Münchinger, V. Hahn, D. Beutel, S. Woska, J. Monti, C. Rockstuhl, E. Blasco, and M. Wegener, "Multi-Photon 4D Printing of Complex Liquid Crystalline Microstructures by In Situ Alignment Using Electric Fields", Advanced Materials Technologies **7**, 2100944 (2022) (cited on page 10).

[45] T. Bückmann, N. Stenger, M. Kadic, J. Kaschke, A. Frölich, T. Kennerknecht, C. Eberl, M. Thiel, and M. Wegener, "Tailored 3D Mechanical Metamaterials Made by Dip-in Direct-Laser-Writing Optical Lithography", Advanced Materials **24**, 2710–2714 (2012) (cited on pages 11, 38).

[46] S. Kawata, H.-B. Sun, T. Tanaka, and K. Takada, "Finer features for functional microdevices", Nature **412**, 697–698 (2001) (cited on page 11).

[47] J. Fischer and M. Wegener, "Three-dimensional optical laser lithography beyond the diffraction limit", Laser & Photonics Reviews **7**, 22–44 (2013) (cited on pages 11, 14, 17).

[48] S. Maruo, O. Nakamura, and S. Kawata, "Three-dimensional microfabrication with two-photon-absorbed photopolymerization", Optics Letters **22**, 132–134 (1997) (cited on page 11).

[49] J. B. Mueller, J. Fischer, F. Mayer, M. Kadic, and M. Wegener, "Polymerization Kinetics in Three-Dimensional Direct Laser Writing", Advanced Materials **26**, 6566–6571 (2014) (cited on pages 11, 12, 47–52, 141).

[50] T. Baldacchini, *Three-Dimensional Microfabrication Using Two-Photon Polymerization: Fundamentals, Technology, and Applications* (William Andrew, Sept. 2015) (cited on pages 11, 12, 14).

[51] W. A. Green, *Industrial Photoinitiators: A Technical Guide* (CRC Press, Apr. 2010) (cited on page 11).

[52] B. Tieke, *Makromolekulare Chemie: Eine Einführung* (John Wiley & Sons, Aug. 2014) (cited on page 11).

[53] C. Decker and A. D. Jenkins, "Kinetic approach of oxygen inhibition in ultraviolet- and laser-induced polymerizations", Macromolecules **18**, 1241–1244 (1985) (cited on page 12).

[54] S. C. Ligon, B. Husár, H. Wutzel, R. Holman, and R. Liska, "Strategies to Reduce Oxygen Inhibition in Photoinduced Polymerization", Chemical Reviews **114**, 557–589 (2014) (cited on page 12).

[55] S. Beuermann and M. Buback, "Rate coefficients of free-radical polymerization deduced from pulsed laser experiments", Progress in Polymer Science **27**, 191–254 (2002) (cited on page 12).

[56] V. Hahn, "On 3D Laser Micro- and Nanoprinting: Faster, Finer, and More Affordable", PhD thesis (Karlsruher Institut für Technologie (KIT), Karlsruhe, 2022) (cited on pages 15, 16, 28, 33, 34, 64, 68, 70).

[57] M. Hippler, "3D Laser Lithography of Stimuli-Responsive Hydrogels", PhD thesis (Karlsruher Institut für Technologie (KIT), Karlsruhe, 2020) (cited on pages 17, 33).

[58] P. Kiefer, V. Hahn, S. Kalt, Q. Sun, Y. M. Eggeler, and M. Wegener, "A multi-photon (7×7)-focus 3D laser printer based on a 3D-printed diffractive optical element and a 3D-printed multi-lens array (submitted)", Light: Advanced Manufacturing (2023) (cited on pages 17, 29, 30, 64, 66, 69, 91, 92, 94, 101, 105, 108, 111, 112, 119, 121, 125, 140, 141, 149–151).

[59] R. Wagner, "On the Simulation of Dose Accumulation in 3D Laser Nanoprinting", Bachelor's thesis (Karlsruher Institut für Technologie (KIT), Karlsruhe, 2022) (cited on pages 20–22).

[60] V. Hahn, T. Messer, N. M. Bojanowski, E. R. Curticean, I. Wacker, R. R. Schröder, E. Blasco, and M. Wegener, "Two-step absorption instead of two-photon absorption in 3D nanoprinting", Nature Photonics **15**, 932–938 (2021) (cited on pages 21, 30, 142).

[61] G. Lazarev, P.-J. Chen, J. Strauss, N. Fontaine, and A. Forbes, "Beyond the display: phase-only liquid crystal on Silicon devices and their applications in photonics [Invited]", Optics Express **27**, 16206–16249 (2019) (cited on page 27).

[62] V. Hahn, P. Rietz, F. Hermann, P. Müller, C. Barner-Kowollik, T. Schlöder, W. Wenzel, E. Blasco, and M. Wegener, "Light-sheet 3D microprinting via two-colour two-step absorption", Nature Photonics **16**, 784–791 (2022) (cited on pages 27, 30, 113, 134).

[63] W. Ouyang, X. Xu, W. Lu, N. Zhao, F. Han, and S.-C. Chen, "Ultrafast 3D nanofabrication via digital holography", Nature Communications **14**, 1716 (2023) (cited on pages 27, 30, 140).

[64] P. Somers, Z. Liang, J. E. Johnson, B. W. Boudouris, L. Pan, and X. Xu, "Rapid, continuous projection multi-photon 3D printing enabled by spatiotemporal focusing of femtosecond pulses", Light: Science & Applications **10**, 199 (2021) (cited on pages 27, 30, 62, 140).

[65] T. Kurihara and Y. Takaki, "Using electronic holography to generate speckle-free and shaded reconstructed images", in Practical Holography XXVII: Materials and Applications, Vol. 8644 (Mar. 2013), pp. 97–102 (cited on page 27).

[66] A. Egner and S. W. Hell, "Time multiplexing and parallelization in multifocal multiphoton microscopy", JOSA A **17**, 1192–1201 (2000) (cited on page 27).

[67] A. Egner, V. Andresen, and S. W. Hell, "Comparison of the axial resolution of practical Nipkow-disk confocal fluorescence microscopy with that of multifocal multiphoton microscopy: theory and experiment", Journal of Microscopy **206**, 24–32 (2002) (cited on page 27).

[68] D. Stuart, O. Barter, and A. Kuhn, *Fast algorithms for generating binary holograms*, Sept. 2014 (cited on page 27).

[69] D. Chan, S. G. Narasimhan, and M. O'Toole, "Holocurtains: Programming Light Curtains via Binary Holography", in 2022 IEEE/CVF Conference on Computer Vision and Pattern Recognition (CVPR) (June 2022), pp. 17865–17874 (cited on page 27).

[70] J. W. Goodman, *Introduction to Fourier Optics* (Roberts and Company Publishers, 2005) (cited on pages 27, 28).

[71] R. D. Leonardo, F. Ianni, and G. Ruocco, "Computer generation of optimal holograms for optical trap arrays", Optics Express **15**, 1913–1922 (2007) (cited on page 27).

[72] K. Obata, J. Koch, U. Hinze, and B. N. Chichkov, "Multi-focus two-photon polymerization technique based on individually controlled phase modulation", Optics Express **18**, 17193–17200 (2010) (cited on page 28).

[73] V. Arrizón and M. Testorf, "Efficiency limit of spatially quantized Fourier array illuminators", Optics Letters **22**, 197–199 (1997) (cited on pages 28, 65).

[74] T. D. Ngo, A. Kashani, G. Imbalzano, K. T. Q. Nguyen, and D. Hui, "Additive manufacturing (3D printing): A review of materials, methods, applications and challenges", Composites Part B: Engineering **143**, 172–196 (2018) (cited on page 28).

[75] B. Jiao, F. Chen, Y. Liu, X. Fan, S. Zeng, Q. Dong, L. Deng, H. Gao, and W. Xiong, "Acousto-optic scanning spatial-switching multiphoton lithography", International Journal of Extreme Manufacturing **5**, 035008 (2023) (cited on pages 29, 30, 134, 140, 142).

[76] G. M. Gratson, F. García-Santamaría, V. Lousse, M. Xu, S. Fan, J. A. Lewis, and P. V. Braun, "Direct-Write Assembly of Three-Dimensional Photonic Crystals: Conversion of Polymer Scaffolds to Silicon Hollow-Woodpile Structures", Advanced Materials **18**, 461–465 (2006) (cited on page 30).

[77] E. B. Duoss, M. Twardowski, and J. A. Lewis, "Sol-gel inks for direct-write assembly of functional oxides", Advanced Materials **19**, 3485–3489 (2007) (cited on page 30).

[78] H. Plank, C. Gspan, M. Dienstleder, G. Kothleitner, and F. Hofer, "The influence of beam defocus on volume growth rates for electron beam induced platinum deposition", Nanotechnology **19**, 485302 (2008) (cited on page 30).

[79] "Fortus 360MC", Stratasys Ltd. (2008) (cited on page 30).

[80] "Mojo", Stratasys Ltd. (2012) (cited on page 30).

[81] X. Zheng, H. Lee, T. H. Weisgraber, M. Shusteff, J. DeOtte, E. B. Duoss, J. D. Kuntz, M. M. Biener, Q. Ge, J. A. Jackson, S. O. Kucheyev, N. X. Fang, and C. M. Spadaccini, "Ultralight, ultrastiff mechanical metamaterials", Science **344**, 1373–1377 (2014) (cited on page 30).

[82] X. Zheng, W. Smith, J. Jackson, B. Moran, H. Cui, D. Chen, J. Ye, N. Fang, N. Rodriguez, T. Weisgraber, and C. M. Spadaccini, "Multiscale metallic metamaterials", Nature Materials **15**, 1100–1106 (2016) (cited on page 30).

[83] X. Zheng, J. Deotte, M. P. Alonso, G. R. Farquar, T. H. Weisgraber, S. Gemberling, H. Lee, N. Fang, and C. M. Spadaccini, "Design and optimization of a light-emitting diode projection micro-stereolithography three-dimensional manufacturing system", Review of Scientific Instruments **83**, 125001 (2012) (cited on page 30).

[84] M. Shusteff, A. E. M. Browar, B. E. Kelly, J. Henriksson, T. H. Weisgraber, R. M. Panas, N. X. Fang, and C. M. Spadaccini, "One-step volumetric additive manufacturing of complex polymer structures", Science Advances **3**, eaao5496 (2017) (cited on page 30).

[85] "ProJet 7000 HD, Vendor Information", 3D Systems Corporation (2012) (cited on page 30).

[86] E. B. Duoss, T. H. Weisgraber, K. Hearon, C. Zhu, W. Small IV, T. R. Metz, J. J. Vericella, H. D. Barth, J. D. Kuntz, R. S. Maxwell, C. M. Spadaccini, and T. S. Wilson, "Three-Dimensional Printing of Elastomeric, Cellular Architectures with Negative Stiffness", Advanced Functional Materials **24**, 4905–4913 (2014) (cited on page 30).

[87] "Objet 500 Connex1", Stratasys Ltd. (2014) (cited on page 30).

[88] "Ultimaker 2 Extended", Ultimaker BV (2015) (cited on page 30).

[89] J. R. Tumbleston, D. Shirvanyants, N. Ermoshkin, R. Janusziewicz, A. R. Johnson, D. Kelly, K. Chen, R. Pinschmidt, J. P. Rolland, A. Ermoshkin, E. T. Samulski, and J. M. DeSimone, "Continuous liquid interface production of 3D objects", Science **347**, 1349–1352 (2015) (cited on page 30).

[90] "P 770 with PA 2200 Top Speed 1.0, Datasheet and Vendor Information", EOS GmbH (2016) (cited on page 30).

[91] "FORMIGA P 110 with PA 2200 Top Quality 1.0, Datasheet and Vendor Information", EOS GmbH (2016) (cited on page 30).

[92] "JetFusion 3D 4210", Hewlett-Packard Company (2017) (cited on page 30).

[93] L. Keller and M. Huth, "Pattern generation for direct-write three-dimensional nanoscale structures via focused electron beam induced deposition", Beilstein Journal of Nanotechnology **9**, 2581–2598 (2018) (cited on page 30).

[94] B. E. Kelly, I. Bhattacharya, H. Heidari, M. Shusteff, C. M. Spadaccini, and H. K. Taylor, "Volumetric additive manufacturing via tomographic reconstruction", Science **363**, 1075–1079 (2019) (cited on page 30).

[95] A. Reiser, M. Lindén, P. Rohner, A. Marchand, H. Galinski, A. S. Sologubenko, J. M. Wheeler, R. Zenobi, D. Poulikakos, and R. Spolenak, "Multi-metal electrohydrodynamic redox 3D printing at the submicron scale", Nature Communications **10**, 1853 (2019) (cited on page 30).

[96] D. A. Walker, J. L. Hedrick, and C. A. Mirkin, "Rapid, large-volume, thermally controlled 3D printing using a mobile liquid interface", Science **366**, 360–364 (2019) (cited on page 30).

[97] P. N. Bernal, P. Delrot, D. Loterie, Y. Li, J. Malda, C. Moser, and R. Levato, "Volumetric Bioprinting of Complex Living-Tissue Constructs within Seconds", Advanced Materials **31**, 1904209 (2019) (cited on page 30).

[98] D. Loterie, P. Delrot, and C. Moser, "High-resolution tomographic volumetric additive manufacturing", Nature Communications **11**, 852 (2020) (cited on page 30).

[99] G. Ercolano, T. Zambelli, C. van Nisselroy, D. Momotenko, J. Vörös, T. Merle, and W. W. Koelmans, "Multiscale Additive Manufacturing of Metal Microstructures", Advanced Engineering Materials **22**, 1900961 (2020) (cited on page 30).

[100] M. Regehly, Y. Garmshausen, M. Reuter, N. F. König, E. Israel, D. P. Kelly, C.-Y. Chou, K. Koch, B. Asfari, and S. Hecht, "Xolography for linear volumetric 3D printing", Nature **588**, 620–624 (2020) (cited on page 30).

[101] Y. Chen, J. Zhang, X. Liu, S. Wang, J. Tao, Y. Huang, W. Wu, Y. Li, K. Zhou, X. Wei, S. Chen, X. Li, X. Xu, L. Cardon, Z. Qian, and M. Gou, "Noninvasive in vivo 3D bioprinting", Science Advances **6**, eaba7406 (2020) (cited on page 30).

[102] W. Jung, Y.-H. Jung, P. V. Pikhitsa, J. Feng, Y. Yang, M. Kim, H.-Y. Tsai, T. Tanaka, J. Shin, K.-Y. Kim, H. Choi, J. Rho, and M. Choi, "Three-dimensional nanoprinting via charged aerosol jets", Nature **592**, 54–59 (2021) (cited on page 30).

[103] D. K. Limberg, J.-H. Kang, and R. C. Hayward, "Triplet–Triplet Annihilation Photopolymerization for High-Resolution 3D Printing", Journal of the American Chemical Society **144**, 5226–5232 (2022) (cited on page 30).

[104] S. N. Sanders, T. H. Schloemer, M. K. Gangishetty, D. Anderson, M. Seitz, A. O. Gallegos, R. C. Stokes, and D. N. Congreve, "Triplet fusion upconversion nanocapsules for volumetric 3D printing", Nature **604**, 474–478 (2022) (cited on page 30).

[105] K. Terpilowski and D. Rymuszka, "Surface properties of glass plates activated by air, oxygen, nitrogen and argon plasma", Glass Physics and Chemistry **42**, 535–541 (2016) (cited on page 33).

[106] "Introducing Two-Photon Grayscale Lithography (White paper)", Nanoscribe GmbH & Co. KG (2021) (cited on pages 35, 36, 143).

[107] S. Rodríguez, "Redefining Microfabrication of High-Precision Optics", PhotonicsViews **17**, 36–39 (2020) (cited on page 35).

[108] T. Aderneuer, O. Fernández, and R. Ferrini, "Two-photon grayscale lithography for free-form micro-optical arrays", Optics Express **29**, 39511–39520 (2021) (cited on pages 36, 81).

[109] L. Siegle, S. Ristok, and H. Giessen, "Complex aspherical singlet and doublet microoptics by grayscale 3D printing", Optics Express **31**, 4179–4189 (2023) (cited on pages 36, 96).

[110] J. Köpfler, "On Topological Mechanics of 3D Chiral Metamaterials", PhD thesis (Karlsruher Institut für Technologie (KIT), Karlsruhe, 2022) (cited on page 37).

[111] B. Pan, K. Qian, H. Xie, and A. Asundi, "Two-dimensional digital image correlation for in-plane displacement and strain measurement: a review", Measurement Science and Technology **20**, 062001 (2009) (cited on page 38).

[112] J. Xavier, A. M. R. Sousa, J. J. L. Morais, V. M. J. Filipe, and M. A. Vaz, "Measuring displacement fields by cross-correlation and a differential technique: experimental validation", Optical Engineering **51**, 043602 (2012) (cited on page 38).

[113] J. Zhao, Y. Sang, and F. Duan, "The state of the art of two-dimensional digital image correlation computational method", Engineering Reports **1**, e12038 (2019) (cited on page 38).

[114] T. Frenzel, J. Köpfler, A. Naber, and M. Wegener, "Atomic scale displacements detected by optical image cross-correlation analysis and 3D printed marker arrays", Scientific Reports **11**, 2304 (2021) (cited on page 38).

[115] J. Qu, M. Kadic, A. Naber, and M. Wegener, "Micro-Structured Two-Component 3D Metamaterials with Negative Thermal-Expansion Coefficient from Positive Constituents", Scientific Reports **7**, 40643 (2017) (cited on page 38).

[116] J. Qu, A. Gerber, F. Mayer, M. Kadic, and M. Wegener, "Experiments on Metamaterials with Negative Effective Static Compressibility", Physical Review X **7**, 041060 (2017) (cited on page 38).

[117] J. Chen, W. Cranton, and M. Fihn, *Handbook of Visual Display Technology*, 2012th ed. (Springer, Heidelberg ; New York, Jan. 2012) (cited on page 39).

[118] S. Woska, A. Münchinger, D. Beutel, E. Blasco, J. Hessenauer, O. Karayel, P. Rietz, S. Pfleging, R. Oberle, C. Rockstuhl, et al., "Tunable photonic devices by 3D laser printing of liquid crystal elastomers", Optical Materials Express **10**, 2928–2943 (2020) (cited on page 39).

[119] I. Henkys, "Examination of sacrificial layers for the defined detachment of 3D structures", Bachelor's thesis (Karlsruher Institut für Technologie (KIT), Karlsruhe, 2022) (cited on page 39).

[120] J. Vautz, "Entwicklung von großen, freihängenden Metamaterialnetzen als Grundlage für mechanobiologische Untersuchungen", Master's thesis (Karlsruher Institut für Technologie (KIT), Karlsruhe, 2023) (cited on page 39).

[121] C. Arnoux, T. Konishi, E. Van Elslande, E.-A. Poutougnigni, J.-C. Mulatier, L. Khrouz, C. Bucher, E. Dumont, K. Kamada, C. Andraud, P. Baldeck, A. Banyasz, and C. Monnereau, "Polymerization Photoinitiators with Near-Resonance Enhanced Two-Photon Absorption Cross-Section: Toward High-Resolution Photoresist with Improved Sensitivity", Macromolecules **53**, 9264–9278 (2020) (cited on pages 44, 47, 48, 50).

[122] S. M. Kuebler, K. L. Braun, W. Zhou, J. K. Cammack, T. Yu, C. K. Ober, S. R. Marder, and J. W. Perry, "Design and application of high-sensitivity two-photon initiators for three-dimensional microfabrication", Journal of Photochemistry and Photobiology A: Chemistry, Photoreaction Control and Photofunctional Materials II **158**, 163–170 (2003) (cited on pages 47, 48).

[123] R. Houbertz, "Laser interaction in sol–gel based materials—3-D lithography for photonic applications", Applied Surface Science, Proceedings of the European Materials Research Society 2004 - Symposium N **247**, 504–512 (2005) (cited on pages 47, 48).

[124] J. Gu, W. Yulan, W.-Q. Chen, X.-Z. Dong, X.-M. Duan, and S. Kawata, "Carbazole -based 1D and 2D hemicyanines: synthesis, two- photon absorption properties and application for two- photon photopolymerization 3D lithography", New Journal of Chemistry **31**, 63–68 (2007) (cited on pages 47, 48).

[125] J.-F. Xing, W.-Q. Chen, J. Gu, X.-Z. Dong, N. Takeyasu, T. Tanaka, X.-M. Duan, and S. Kawata, "Design of high efficiency for two- photon polymerization initiator: combination of radical stabilization and large two- photon cross-section achieved by N -benzyl 3,6-bis(phenylethynyl)carbazole derivatives", Journal of Materials Chemistry **17**, 1433–1438 (2007) (cited on pages 47, 48).

[126] J.-F. Xing, X.-Z. Dong, W.-Q. Chen, X.-M. Duan, N. Takeyasu, T. Tanaka, and S. Kawata, "Improving spatial resolution of two-photon microfabrication by using photoinitiator with high initiating efficiency", Applied Physics Letters **90**, 131106 (2007) (cited on pages 47, 48).

[127] X. Cao, F. Jin, Y.-F. Li, W.-Q. Chen, X.-M. Duan, and L.-M. Yang, "Triphenylamine -modified quinoxaline derivatives as two- photon photoinitiators", New Journal of Chemistry **33**, 1578–1582 (2009) (cited on pages 47, 48).

[128] M. Thiel, J. Fischer, G. von Freymann, and M. Wegener, "Direct laser writing of three-dimensional submicron structures using a continuous-wave laser at 532 nm", Applied Physics Letters **97**, 221102 (2010) (cited on pages 47, 48).

[129] M. Malinauskas, A. Žukauskas, G. Bičkauskaitė, R. Gadonas, and S. Juodkazis, "Mechanisms of three-dimensional structuring of photo-polymers by tightly focussed femtosecond laser pulses", Optics Express **18**, 10209–10221 (2010) (cited on pages 47, 48, 50).

[130] W.-E. Lu, X.-Z. Dong, W.-Q. Chen, Z.-S. Zhao, and X.-M. Duan, "Novel photoinitiator with a radical quenching moiety for confining radical diffusion in two-photon induced photopolymerization", Journal of Materials Chemistry **21**, 5650–5659 (2011) (cited on pages 47, 48).

[131] J.-F. Xing, M.-L. Zheng, W.-Q. Chen, X.-Z. Dong, N. Takeyasu, T. Tanaka, Z.-S. Zhao, X.-M. Duan, and S. Kawata, "C 2v symmetrical two-photon polymerization initiators with anthracene core: synthesis, optical and initiating properties", Physical Chemistry Chemical Physics **14**, 15785–15792 (2012) (cited on pages 47, 48).

[132] Z. Li, N. Pucher, K. Cicha, J. Torgersen, S. C. Ligon, A. Ajami, W. Husinsky, A. Rosspeintner, E. Vauthey, S. Naumov, T. Scherzer, J. Stampfl, and R. Liska, "A Straightforward Synthesis and Structure–Activity Relationship of Highly Efficient Initiators for Two-Photon Polymerization", Macromolecules **46**, 352–361 (2013) (cited on pages 47, 48, 51).

[133] S. Steenhusen, F. Burmeister, H.-C. Eckstein, and R. Houbertz, "Two-photon polymerization of hybrid polymers for applications in micro-optics", in Laser 3D Manufacturing II, Vol. 9353 (Mar. 2015), pp. 59–67 (cited on pages 47, 48).

[134] L. Jiang, W. Xiong, Y. Zhou, Y. Liu, X. Huang, D. Li, T. Baldacchini, L. Jiang, and Y. Lu, "Performance comparison of acrylic and thiol-acrylic resins in two-photon polymerization", Optics Express **24**, 13687–13701 (2016) (cited on pages 47, 48, 54, 55).

[135] L. Jonušauskas, D. Gailevičius, L. Mikoliūnaitė, D. Sakalauskas, S. Šakirzanovas, S. Juodkazis, and M. Malinauskas, "Optically Clear and Resilient Free-Form μ-Optics 3D-Printed via Ultrafast Laser Lithography", Materials **10**, 12 (2017) (cited on pages 47, 48, 50).

[136] B. Holzer, M. Lunzer, A. Rosspeintner, G. Licari, M. Tromayer, S. Naumov, D. Lumpi, E. Horkel, C. Hametner, A. Ovsianikov, R. Liska, E. Vauthey, and J. Fröhlich, "Towards efficient initiators for two-photon induced polymerization: fine tuning of the donor/acceptor properties", Molecular Systems Design & Engineering **4**, 437–448 (2019) (cited on pages 47, 48).

[137] T. Chi, P. Somers, D. A. Wilcox, A. J. Schuman, V. Iyer, R. Le, J. Gengler, M. Ferdinandus, C. Liebig, L. Pan, X. Xu, and B. W. Boudouris, "Tailored thioxanthone-based photoinitiators for two-photon-controllable polymerization and nanolithographic printing", Journal of Polymer Science Part B: Polymer Physics **57**, 1462–1475 (2019) (cited on pages 47, 48).

[138] P. Hu, W. Qiu, S. Naumov, T. Scherzer, Z. Hu, Q. Chen, W. Knolle, and Z. Li, "Conjugated Bifunctional Carbazole-Based Oxime Esters: Efficient and Versatile Photoinitiators for 3D Printing under One- and Two-Photon Excitation", ChemPhotoChem **4**, 224–232 (2020) (cited on pages 47, 48).

[139] R. Zhou, J.-P. Malval, M. Jin, A. Spangenberg, H. Pan, D. Wan, F. Morlet-Savary, and S. Knopf, "A two-photon active chevron-shaped type I photoinitiator designed for 3D stereolithography", Chemical Communications **55**, 6233–6236 (2019) (cited on pages 47, 48, 50).

[140] Y. E. Begantsova, R. Zvagelsky, E. V. Baranov, D. A. Chubich, Y. V. Chechet, D. A. Kolymagin, A. V. Pisarenko, A. G. Vitukhnovsky, and S. A. Chesnokov, "Imidazole-containing photoinitiators for fabrication of sub-micron structures by 3D two-photon polymerization", European Polymer Journal **145**, 110209 (2021) (cited on pages 47, 48).

[141] T. Chi, P. Somers, D. A. Wilcox, A. J. Schuman, J. E. Johnson, Z. Liang, L. Pan, X. Xu, and B. W. Boudouris, "Substituted Thioxanthone-Based Photoinitiators for Efficient Two-Photon Direct Laser Writing Polymerization with Two-Color Resolution", ACS Applied Polymer Materials **3**, 1426–1435 (2021) (cited on pages 47, 48).

[142] J. Tang, X. Xu, X. Shen, C. Kuang, H. Chen, M. Shi, and N. Huang, "Ketocoumarin-Based Photoinitiators for High-Sensitivity Two-Photon Lithography", ACS Applied Polymer Materials **5**, 2956–2963 (2023) (cited on pages 47, 48).

[143] C. Cao, X. Shen, S. Chen, M. He, H. Wang, C. Ding, D. Zhu, J. Dong, H. Chen, N. Huang, C. Kuang, M. Jin, and X. Liu, "High-Precision and Rapid Direct Laser Writing Using a Liquid Two-Photon Polymerization Initiator", ACS Applied Materials & Interfaces **15**, 30870–30879 (2023) (cited on pages 47, 48).

[144] J. Fischer, J. B. Mueller, A. S. Quick, J. Kaschke, C. Barner-Kowollik, and M. Wegener, "Exploring the Mechanisms in STED-Enhanced Direct Laser Writing", Advanced Optical Materials **3**, 221–232 (2015) (cited on pages 51, 52, 141).

[145] J. E. Johnson, Y. Chen, and X. Xu, "Model for polymerization and self-deactivation in two-photon nanolithography", Optics Express **30**, 26824–26840 (2022) (cited on pages 52, 141).

[146] A. Mauri, P. Kiefer, P. Neidinger, T. Messer, N. M. Bojanowski, L. Yang, S. Walden, A.-N. Unterreiner, C. Barner-Kowollik, M. Wegener, et al., "Two- and three-photon processes in photoinitiators for 3D laser printing", (2022) (cited on pages 52, 141).

[147] J. Fischer, J. B. Mueller, J. Kaschke, T. J. A. Wolf, A.-N. Unterreiner, and M. Wegener, "Three-dimensional multi-photon direct laser writing with variable repetition rate", Optics Express **21**, 26244–26260 (2013) (cited on pages 52, 141).

[148] F. A. Ogliari, C. Ely, C. L. Petzhold, F. F. Demarco, and E. Piva, "Onium salt improves the polymerization kinetics in an experimental dental adhesive resin", Journal of Dentistry **35**, 583–587 (2007) (cited on page 54).

[149] J.-P. Fouassier, F. Morlet-Savary, J. Lalevée, X. Allonas, and C. Ley, "Dyes as photoinitiators or photosensitizers of polymerization reactions", Materials **3**, 5130–5142 (2010) (cited on page 54).

[150] H. Tsubomura, T. Yagishita, and H. Toi, "Intermediates and Mechanism of Photo-Oxygenation Reaction of Triethylamine", Bulletin of the Chemical Society of Japan **46**, 3051–3055 (1973) (cited on page 54).

[151] R. Sato, T. Kurihara, and M. Takeishi, "Rate enhancement of amines in the photopolymerization of methyl methacrylate under oxygen", Polymer International **47**, 159–164 (1998) (cited on page 54).

[152] Y. Hua, F. Jiang, and J. V. Crivello, "Photosensitized Onium-Salt-Induced Cationic Polymerization with Hydroxymethylated Polynuclear Aromatic Hydrocarbons", Chemistry of Materials **14**, 2369–2377 (2002) (cited on page 54).

[153] T. Rudolph, P. Buehle, and R. Rosskopf, "1,3-dioxan-5-one compounds", US20130309184A1 (Nov. 2013) (cited on page 57).

[154] S. Grebenyuk, A. R. Abdel Fattah, M. Kumar, B. Toprakhisar, G. Rustandi, A. Vananroye, I. Salmon, C. Verfaillie, M. Grillo, and A. Ranga, "Large-scale perfused tissues via synthetic 3D soft microfluidics", Nature Communications **14**, 193 (2023) (cited on page 60).

[155] A. Lüken, L. Stüwe, S. B. Rauer, J. Oelker, J. Linkhorst, and M. Wessling, "Fabrication, Flow Assembly, and Permeation of Microscopic Any-Shape Particles", Small **18**, 2107508 (2022) (cited on page 60).

[156] J. Lölsberg, A. Cinar, D. Felder, G. Linz, S. Djeljadini, and M. Wessling, "Two-Photon Vertical-Flow Lithography for Microtube Synthesis", Small **15**, 1901356 (2019) (cited on page 60).

[157] Q. Akolawala, M. Rovituso, H. H. Versteeg, A. M. R. Rondon, and A. Accardo, "Evaluation of Proton-Induced DNA Damage in 3D-Engineered Glioblastoma Microenvironments", ACS Applied Materials & Interfaces **14**, 20778–20789 (2022) (cited on page 60).

[158] R. K. Jayne, M. Ç. Karakan, K. Zhang, N. Pierce, C. Michas, D. J. Bishop, C. S. Chen, K. L. Ekinci, and A. E. White, "Direct laser writing for cardiac tissue engineering: a microfluidic heart on a chip with integrated transducers", Lab on a Chip **21**, 1724–1737 (2021) (cited on page 60).

[159] P. Somers, Z. Liang, T. Chi, J. E. Johnson, L. Pan, B. W. Boudouris, and X. Xu, "Photo-activated polymerization inhibition process in photoinitiator systems for high-throughput 3D nanoprinting", Nanophotonics **12**, 1571–1580 (2023) (cited on page 62).

[160] B. W. Pearre, C. Michas, J.-M. Tsang, T. J. Gardner, and T. M. Otchy, "Fast micron-scale 3D printing with a resonant-scanning two-photon microscope", Additive Manufacturing **30**, 100887 (2019) (cited on page 64).

[161] N. Streibl, "Beam Shaping with Optical Array Generators", Journal of Modern Optics **36**, 1559–1573 (1989) (cited on page 64).

[162] J. L. Kreuzer, "Coherent light optical system yielding an output beam of desired intensity distribution at a desired equiphase surface", US3476463A (Nov. 1969) (cited on page 65).

[163] D. Shafer, "Gaussian to flat-top intensity distributing lens", Optics & Laser Technology **14**, 159–160 (1982) (cited on page 65).

[164] Q. Hu, Z. Zhou, X. Lv, and S. Zeng, "Compensation of spatial dispersion of an acousto-optic deflector with a special Keplerian telescope", Optics Letters **41**, 207–210 (2016) (cited on pages 66, 67).

[165] H. Urey, "Spot size, depth-of-focus, and diffraction ring intensity formulas for truncated Gaussian beams", Applied Optics **43**, 620–625 (2004) (cited on page 67).

[166] M. Bass, *Handbook of Optics: Volume I - Geometrical and Physical Optics, Polarized Light, Components and Instruments*, 3rd Edition (McGraw-Hill Education, 2010) (cited on page 67).

[167] W. Dietel, J. J. Fontaine, and J.-C. Diels, "Intracavity pulse compression with glass: a new method of generating pulses shorter than 60 fsec", Optics Letters **8**, 4–6 (1983) (cited on page 68).

[168] R. L. Fork, O. E. Martinez, and J. P. Gordon, "Negative dispersion using pairs of prisms", Optics Letters **9**, 150–152 (1984) (cited on page 68).

[169] R. W. Gerchberg and W. O. Saxton, "A Practical Algorithm for the Determination of Phase from Image and Diffraction Plane Pictures", Optik **35**, 237–246 (1972) (cited on page 70).

[170] "NanoGuide", Nanoscribe GmbH & Co. KG (2023) (cited on pages 74, 81).

[171] T. Grossmann, S. Schleede, M. Hauser, T. Beck, M. Thiel, G. v. Freymann, T. Mappes, and H. Kalt, "Direct laser writing for active and passive high-Q polymer microdisks on silicon", Optics Express **19**, 11451–11456 (2011) (cited on page 74).

[172] J. Weinacker, S. Kalt, P. Kiefer, P. Rietz, and M. Wegener, "On Iterative Pre-Compensation of 3D Laser-Printed Micro-Optical Components Using Confocal-Optical Microscopy", Advanced Functional Materials, 2309356 (2023) (cited on pages 77, 83–89).

[173] X. Zhou, Y. Hou, and J. Lin, "A review on the processing accuracy of two-photon polymerization", AIP Advances **5**, 030701 (2015) (cited on pages 77, 80, 83, 96).

[174] R. Zvagelsky, P. Kiefer, J. Weinacker, and M. Wegener, "In-situ Quantitative Phase Imaging during Multi-photon Laser Printing", ACS Photonics **10**, 2901–2908 (2023) (cited on pages 77, 80).

[175] J. Purtov, A. Verch, P. Rogin, and R. Hensel, "Improved development procedure to enhance the stability of microstructures created by two-photon polymerization", Microelectronic Engineering **194**, 45–50 (2018) (cited on page 96).

[176] J. S. Oakdale, J. Ye, W. L. Smith, and J. Biener, "Post-print UV curing method for improving the mechanical properties of prototypes derived from two-photon lithography", Optics Express **24**, 27077–27086 (2016) (cited on page 96).

[177] A. Toulouse, J. Drozella, P. Motzfeld, N. Fahrbach, V. Aslani, S. Thiele, H. Giessen, and A. M. Herkommer, "Ultra-compact 3D-printed wide-angle cameras realized by multi-aperture freeform optical design", Optics Express **30**, 707–720 (2022) (cited on page 96).

[178] N. Lang, S. Enns, J. Hering, and G. v. Freymann, "Towards efficient structure prediction and pre-compensation in multi-photon lithography", Optics Express **30**, 28805–28816 (2022) (cited on page 96).

[179] J. N. Stirman, I. T. Smith, M. W. Kudenov, and S. L. Smith, "Wide field-of-view, multi-region, two-photon imaging of neuronal activity in the mammalian brain", Nature Biotechnology **34**, 857–862 (2016) (cited on pages 100, 102, 104, 114).

[180] P. Kiefer, "Realisation of a Fast 3D Laser Lithography Setup", Master's thesis (Karlsruher Institut für Technologie (KIT), Karlsruhe, 2019) (cited on page 103).

[181] "What is a Point Spread Function?", Zemax Knowledgebase (2021) (cited on pages 107, 109).

[182] H. Gross, H. Zügge, M. Peschka, and F. Blechinger, *Handbook of Optical Systems: Volume 3: Aberration Theory and Correction of Optical Systems*, 1st ed. (Wiley-VCH, Weinheim (Deutschland), Dec. 2006) (cited on page 110).

[183] S. Bock, T. Rades, J. Rantanen, and R. Scherließ, "Additive Manufacturing in respiratory sciences - current applications and future prospects", Advanced Drug Delivery Reviews, 114341 (2022) (cited on pages 116–118).

[184] R. Scherließ, S. Bock, N. Bungert, A. Neustock, and L. Valentin, "Particle engineering in dry powders for inhalation", European Journal of Pharmaceutical Sciences **172**, 106158 (2022) (cited on pages 116, 117).

[185] S. P. Newman, "Drug delivery to the lungs: challenges and opportunities", Therapeutic Delivery **8**, 647–661 (2017) (cited on page 116).

[186] A. Yıldız-Peköz and C. Ehrhardt, "Advances in Pulmonary Drug Delivery", Pharmaceutics **12**, 911 (2020) (cited on page 116).

[187] Q. (Zhou, P. Tang, S. S. Y. Leung, J. G. Y. Chan, and H.-K. Chan, "Emerging inhalation aerosol devices and strategies: Where are we headed?", Advanced Drug Delivery Reviews, Improving the efficacy of inhaled drugs for severe lung diseases: emerging pulmonary delivery strategies **75**, 3–17 (2014) (cited on page 116).

[188] A. H. de Boer, P. Hagedoorn, M. Hoppentocht, F. Buttini, F. Grasmeijer, and H. W. Frijlink, "Dry powder inhalation: past, present and future", Expert Opinion on Drug Delivery **14**, 499–512 (2017) (cited on page 117).

[189] M. Hoppentocht, P. Hagedoorn, H. W. Frijlink, and A. H. de Boer, "Technological and practical challenges of dry powder inhalers and formulations", Advanced Drug Delivery Reviews, Improving the efficacy of inhaled drugs for severe lung diseases: emerging pulmonary delivery strategies **75**, 18–31 (2014) (cited on page 117).

[190] M. Wostry and R. Scherließ, "Possibilities and advantages of additive manufacturing in dry powder formulations for inhalation", European Journal of Pharmaceutical Sciences, 106583 (2023) (cited on page 118).

[191] Y. Chen, J. L. G. Schneider, M. F. Groß, K. Wang, S. Kalt, P. Scott, M. Kadic, and M. Wegener, "Observation of Chirality-Induced Roton-Like Dispersion in a 3D Micropolar Elastic Metamaterial", Advanced Functional Materials, 2302699 (2023) (cited on pages 124–126).

[192] M. Kadic, G. W. Milton, M. van Hecke, and M. Wegener, "3D metamaterials", Nature Reviews Physics **1**, 198–210 (2019) (cited on page 124).

[193] Y. Chen, M. Kadic, and M. Wegener, "Chiral triclinic metamaterial crystals supporting isotropic acoustical activity and isotropic chiral phonons", Proceedings of the Royal Society A: Mathematical, Physical and Engineering Sciences **477**, 20200764 (2021) (cited on page 124).

[194] T. Frenzel, M. Kadic, and M. Wegener, "Three-dimensional mechanical metamaterials with a twist", Science **358**, 1072–1074 (2017) (cited on page 124).

[195] J. Köpfler, T. Frenzel, J. Schmalian, and M. Wegener, "Fused-Silica 3D Chiral Metamaterials via Helium-Assisted Microcasting Supporting Topologically Protected Twist Edge Resonances with High Mechanical Quality Factors", Advanced Materials **33**, 2103205 (2021) (cited on page 124).

[196] J. Reinbold, T. Frenzel, A. Münchinger, and M. Wegener, "The Rise of (Chiral) 3D Mechanical Metamaterials", Materials **12**, 3527 (2019) (cited on page 124).

[197] T. Frenzel, J. Köpfler, E. Jung, M. Kadic, and M. Wegener, "Ultrasound experiments on acoustical activity in chiral mechanical metamaterials", Nature Communications **10**, 3384 (2019) (cited on page 124).

[198] I. Fernandez-Corbaton, C. Rockstuhl, P. Ziemke, P. Gumbsch, A. Albiez, R. Schwaiger, T. Frenzel, M. Kadic, and M. Wegener, "New Twists of 3D Chiral Metamaterials", Advanced Materials **31**, 1807742 (2019) (cited on page 124).

[199] T. Frenzel, V. Hahn, P. Ziemke, J. L. G. Schneider, Y. Chen, P. Kiefer, P. Gumbsch, and M. Wegener, "Large characteristic lengths in 3D chiral elastic metamaterials", Communications Materials **2**, 1–9 (2021) (cited on page 124).

[200] P. Serles, *Collaboration Discussion - Macroscopic Metamaterial Printing (E-Mail)*, Aug. 2023 (cited on page 127).

[201] Y. M. Eggeler, K. C. Chan, Q. Sun, A. D. Lantada, D. Mager, R. Schwaiger, P. Gumbsch, R. Schröder, W. Wenzel, J. G. Korvink, and M. Islam, "A Review on 3D Architected Pyrolytic Carbon Produced by Additive Micro/Nanomanufacturing", Advanced Functional Materials **n/a**, 2302068 (2023) (cited on page 127).

[202] M. Sekar, T. Mathimani, A. Alagumalai, N. T. L. Chi, P. A. Duc, S. K. Bhatia, K. Brindhadevi, and A. Pugazhendhi, "A review on the pyrolysis of algal biomass for biochar and bio-oil – Bottlenecks and scope", Fuel **283**, 119190 (2021) (cited on page 127).

[203] G. Su, H. C. Ong, M. Mofijur, T. M. I. Mahlia, and Y. S. Ok, "Pyrolysis of waste oils for the production of biofuels: A critical review", Journal of Hazardous Materials **424**, 127396 (2022) (cited on page 127).

[204] N. Mishra, G. Das, A. Ansaldo, A. Genovese, M. Malerba, M. Povia, D. Ricci, E. Di Fabrizio, E. Di Zitti, M. Sharon, and M. Sharon, "Pyrolysis of waste polypropylene for the synthesis of carbon nanotubes", Journal of Analytical and Applied Pyrolysis **94**, 91–98 (2012) (cited on page 127).

[205] R. S. Lehrle, "Polymer pyrolysis mechanisms: Experimental approaches for investigating them", Journal of Analytical and Applied Pyrolysis **11**, 55–64 (1987) (cited on page 127).

[206] Q. Sun, C. Dolle, C. Kurpiers, R. Schwaiger, P. Gumbsch, and Y. M. Eggeler, "In Situ Pyrolysis of 3D Printed Microstructures – an ESEM Study", Microscopy and Microanalysis **28**, 2346–2348 (2022) (cited on page 127).

[207] X. Zhang, L. Zhong, A. Mateos, A. Kudo, A. Vyatskikh, H. Gao, J. R. Greer, and X. Li, "Theoretical strength and rubber-like behaviour in micro-sized pyrolytic carbon", Nature Nanotechnology **14**, 762–769 (2019) (cited on page 127).

[208] A. Huber, *Collaboration Discussion - Potentially Scintillating Structures Printing (E-Mail)*, Aug. 2023 (cited on pages 131, 132).

[209] K. Gauda, S. Schneidewind, G. Drexlin, A. Fulst, V. Hannen, T. König, A. Lokhov, P. Oelpmann, H.-W. Ortjohann, W. Pernice, R. G. H. Robertson, R. W. J. Salomon, M. Stappers, and C. Weinheimer, "An active transverse energy filter to differentiate low energy particles with large pitch angles in a strong magnetic field", The European Physical Journal C **82**, 922 (2022) (cited on page 131).

[210] J. N. Lauer, "Application Cases of Transverse Energy Filters in the KATRIN Experiment", Master's thesis (Karlsruher Institut für Technologie (KIT), Karlsruhe, 2022) (cited on pages 131, 132).

[211] N. M. Bojanowski, A. Vranic, V. Hahn, P. Rietz, T. Messer, J. Brückel, C. Barner-Kowollik, E. Blasco, S. Bräse, and M. Wegener, "Search for Alternative Two-Step-Absorption Photoinitiators for 3D Laser Nanoprinting", Advanced Functional Materials 33, 2212482 (2023) (cited on page 142).

[212] W. Witkowski, "'Moore's Law's dead,' Nvidia CEO Jensen Huang says in justifying gaming-card price hike", MarketWatch (2022) (cited on page 143).

[213] D. I. Cutress, "Samsung Foundry: 2nm Silicon in 2025", AnandTech (2021) (cited on page 143).

Acknowledgments

This thesis would not have been possible without the help of many people along its way. In the following, I want to sincerely thank them for their support throughout the past years.

First, I want to thank Prof. Dr. Martin Wegener for granting me the opportunity to work on this exciting topic as my Ph.D. thesis. His excellent supervision and support shaped many aspects of this thesis and allowed me to thrive during my time in his research group.
I further want to thank Prof. Dr. Martin Bastmeyer for the stimulating discussions of my work and kindly agreeing to co-referee this thesis.

The achievements presented in this thesis would not have been possible without my former colleague Dr. Vincent Hahn. He not only laid the groundwork before this project, but also presented ideas and solutions to problems I was facing while continuously educating me in photochemistry and optics, for which I am deeply grateful.
I further want express my sincere gratitude to Dr. Marc Hippler, with whom I shared countless stimulating discussions about this dissertation and many issues during my Ph.D. time. His continuous support and optimism greatly contributed to the outcome of this work and my sanity, and I am grateful for our close friendship.

During my adventures in the field of photochemistry, I was deeply thankful for the long-lasting support and guidance of Prof. Dr. Eva Blasco. In our many discussions about efficient photoinitiators, her expert knowledge and acumen helped in the development of the sensitive photoresist that was urgently needed. Furthermore, she always took the time when I needed professional input in the field of chemistry. I also want to thank Dr. Martina Nardi and Dr. Maximilian Bojanowski for synthesizing, purifying, and analyzing the newly developed molecule for me. I further want to thank Dr. Martina Nardi for helping me measure the necessary extinction spectrum.

Many collaborations have contributed to the results of this thesis. Therefore, I want to start by thanking Qing Sun and TT.-Prof. Dr.-Ing. Yolita Eggeler from KIT for the tedious task of acquiring hundreds of scanning-electron micrographs

for the voxel-size characterization. I further want to thank Melvin Wostry, Dr. Simon Bock, and Prof. Dr. Regina Scherließ from the University of Kiel for the fruitful collaboration in the field of respiratory science and for sharing early research results from pharmaceutical experiments. I also want to thank Peter Serles from the University of Toronto for sharing early research results of our lightweight metamaterials and Dr. Anton Huber from KIT for his expert knowledge of the KATRIN experiment.

In the field of biology, I want to thank Dr. Kai Weißenbruch for taking over all cell-biological work and LSM imaging for the experiments exploring potential cell-cytotoxicities. I further want to thank Magdalena Fladung for enlightening me in many aspects in the field of cell biology, the mutual supervision of our two students, and the joint collaboration. Our countless chats cleared my head many times and I am grateful for our close friendship.

My everyday life at the institute would not have been the same without the many past and present members of the Wegener group. I enjoyed your company every day and will miss the stimulating discussions about various aspects of our work. I never took the supportive atmosphere we share for granted and will definitely miss it in the future. Particularly, I want to thank Sebastian Kalt, Tobias Messer, and Dr. Vincent Hahn for taking many scanning-electron micrographs of my samples; Pascal Rietz for sharing his knowledge of sacrificial layers and our discussions about diffractive optics and parallelization approaches; Jonathan Ludwig Günter Schneider for sharing his PVA and silanized-substrate supply with me; and Dr. Alexander Münchinger for teaching me how to use our EVAP machine. Furthermore, I want to thank Jannis Weinacker, Sebastian Kalt, and Pascal Rietz for their work in our joint effort of developing our QUANDALF software. In the last eleven years, I battled through studies and Ph.D. thesis together with Michael Groß, who shared countless discussions about physics and other struggles with me. I am grateful for our joint journey and appreciated our exchanges during the writing of our dissertations. I further want to thank Richard Wagner, Ivo Henkys, and Julia Vautz for their hard work during their Bachelor's and Master's theses. I am grateful for many learning opportunities as their supervisor.

Thanks to the exceptional backbone of the Institute of Applied Physics, many hardships were lifted off my shoulders. I want to start by thanking Claudia Alaya, Petra Bauer, Monika Brenkman, Ursula Mösle, and Gloria Zanda for taking care of many administrative matters. Furthermore I want to thank the people behind the mechanical workshop under the direction of Maik Nothdurft and formerly Frank Landhäußer for manufacturing the many parts a custom-made setup desperately needs. I am also indebted to the members of the exceptional electronic workshop Werner Gilde, Michael Hippe, and Helmuth Lay for helping with various issues

concerning electronic devices and IT. Lastly, I want to thank Johann Westhauser for helping me with the great amount of purchase orders I had to go through in the last years and his technical help in the lab. I further want to express my gratitude towards the administrative staff of the Nanostructure Service Laboratory under the direction of Prof. Dr. Gernot Goll.

The cluster of excellence "3D Matter Made to Order" guaranteed carefree conditions for my work at all times. For the funding I received throughout my whole Ph.D. thesis I am greatly thankful.

Furthermore, I am indebted to the many people that agreed to proofread this thesis and successfully contributed to polishing it. Therefore, I want to thank Dr. Marc Hippler, Melanie Dörr, Dr. Paul Somers, Jannis Weinacker, Pascal Rietz, Josephine Spiegelberg, Phil Scott, Dr. Vincent Hahn, Roman Zvagelsky, Magdalena Fladung, Sebastian Kalt, Jonathan Ludwig Günter Schneider, Prof. Dr. Eva Blasco, Melvin Wostry, Dr. Anton Huber, and Peter Serles.

Finally, I would like to thank my family and friends for their unconditional support throughout the years. I am deeply grateful to my mother, Rosalinde, for her continuous, undying, and loving support, and to my father, Karlheinz, who was always the greatest fan of my path. Most of all, I want to thank my girlfriend Melanie for her unwavering love and support. Her infectious and sparkling excitement never failed to chase any dark clouds away.